2D Materials Focus Topic
Room: 212C - Session 2D+EM+NS+PS+SP+SS+TF-MoM

2D Materials: Growth and Fabrication
Moderator: Cory Dean, Columbia University, Peide Ye, Purdue University

8:20am **2D+EM+NS+PS+SP+SS+TF-MoM1 Growth and FTIR Characterization of 2D Hexagonal Boron Nitride on Metal Substrates**, ***Boris Feigelson***, *V.M. Bermudez, J.K. Hite, Z.R. Robinson, V.D. Wheeler, K. Sridhara, S.C. Hernández*, US Naval Research Laboratory

Atomically thin two dimensional hexagonal boron nitride (2D h-BN) is one of the key materials in the development of new van der Waals heterostructures due to its outstanding properties including an atomically smooth surface, high thermal conductivity, high mechanical strength, chemical inertness and high electrical resistance. The development of 2D h-BN growth is still in the early stages and largely depends on rapid and accurate characterization of the grown monolayer or few layers h-BN films.

In this work, the IR-active out-of-plane vibrational mode of 2D h-BN films grown in vertical reactor by atmospheric-pressure CVD on metal substrates (mainly Cu but also Ni) is exploited to identify 2D h-BN directly on substrates and studied both computationally and experimentally.

Fourier transform grazing-incidence infrared reflection absorption spectroscopy (FT-IRRAS) data have been used to characterize monolayer and few-layer h-BN films directly on metal substrates. Two sub-bands of the A_{2u}(LO) vibrational mode were, for the first time, found for thin 2D h-BN films in contact with Cu and Ni [1]. To unveil the nature of the discovered sub-bands, ab-initio calculations were performed and verified using 2D h-BN films grown on various Cu substrates with varying coverage and with individual crystallites of different shapes and size up to 4 mm. It was shown that the lower-energy A_{2u}(LO)1 sub-band around 819 cm^{-1} is related to 2D h-BN coupled with Cu substrate, while the higher energy A_{2u}(LO)2 sub-band around 824 cm^{-1} is related to decoupled (essentially free standing) 2D h-BN. These findings demonstrate not only a new and facile method for immediate 2D h-BN identification and characterization, but also a method that provides a simple means to characterize the degree of coupling between 2D h-BN and the substrate. This approach also provides an opportunity to determine which growth conditions lead to the absorption of foreign species on the substrate prior to the h-BN deposition and which conditions can prevent the formation of the interfacial layer between h-BN and the substrate. Such interfacial layers, like oxidized Cu, were shown to result in easily-recognizable shifts in the A_{2u}(LO) peak. The degree to which the interaction of the h BN layer with the substrate is uniform and homogenous can also be assessed easily by examining the width and fine structure of the A_{2u}(LO) band. The developed approach can also be used to study growth and formation of h-BN/graphene and other 2D heterostructures.

References

1. B. N. Feigelson, V. M. Bermudez, J. K. Hite, Z. R. Robinson, V. D. Wheeler, K. Sridhara, and S. C. Hernandez, Nanoscale **7,** 3694 (2015)

8:40am **2D+EM+NS+PS+SP+SS+TF-MoM2 Effect of Surface Termination on the Growth of Graphene on Cu Single Crystal Substrates**, ***Tyler Mowll***, *E.W. Ong,* University at Albany-SUNY*, P. Tyagi,* GLOBALFOUNDRIES*, Z.R. Robinson,* College at Brockport-SUNY*, C.A. Ventrice, Jr.*, SUNY Polytechnic Institute

The most common technique for synthesizing single-layer graphene films with large lateral dimensions is chemical vapor deposition (CVD) on Cu foil substrates. The primary reasons for choosing Cu substrates are the extremely low solubility of carbon in Cu, which allows a self-limited growth of graphene, and the relatively low cost of the Cu foil substrates. However, the transport properties of the CVD grown graphene films are typically a couple of orders of magnitude lower than for graphene flakes mechanically exfoliated from graphite. One of the reasons for the reduction in transport properties is the presence of crystalline defects in the CVD grown films. These structural defects arise in part from the multidomain structure of the Cu films. In order to achieve a better understanding of the influence of the surface termination of the Cu substrate on the crystallization of graphene during the CVD growth process, a systematic study of graphene growth on Cu(100), Cu(110), and Cu(111) crystals has been performed. The growth process is performed in an ultra-high vacuum (UHV) chamber that has been modified to perform CVD growth at pressures as high as 100 mTorr. The precursor gas used is ethylene. This growth procedure allows for the preparation of the clean surfaces in UHV, growth under typical CVD conditions, and characterization of the surface structure in UHV, without exposing the sample to atmospheric contaminants. Our results indicate that the Cu(111) surface has the lowest catalytic activity of the three surfaces for the decomposition of ethylene. In fact, the decomposition rate is so low that graphene growth is suppressed because of the sublimation of Cu at the elevated temperatures used to grow the graphene. By using an Ar overpressure, it was found that graphene could be grown on that surface. The surface symmetry of the Cu substrate has a strong influence on the rotational alignment of the graphene grains as they nucleate on each surface. For Cu(111), single-domain graphene growth can be achieved for ethylene pressures of 5 mTorr or less. For both Cu(100) and Cu(110), a minimum of two graphene domains is always observed.

9:00am **2D+EM+NS+PS+SP+SS+TF-MoM3 Thermally Annealed and Electropolished Cu Substrates for CVD Growth of 2D Materials: Graphene, h-BN and MoS_2**, ***Karthik Sridhara,*** Texas A&M University*, B.N. Feigelson, J.K. Hite,* US Naval Research Laboratory*, A. Nath,* George Mason University*, M. Fuhrer,* Monash University, Australia*, D.K. Gaskill,* US Naval Research Laboratory*, H. Castaneda, L.O. Nyakiti*, Texas A&M University

The growth of two dimensional (2D) materials such as graphene, hexagonal boron nitride (h-BN) and molybdenum disulphide (MoS_2) have been demonstrated by chemical vapor deposition (CVD) on polycrystalline catalytic copper substrates. These Cu foil substrates (25 µm thick) are produced by metallurgical rolling leading to the formation of irregular ridges on the foil surface along with a film of native oxide on the surface. These processing artifacts are a limiting factor for controlled and reproducible large area (several cm^2) growth of 2D materials. Greater control of growth can be achieved by controlling the density of nucleation sites and improving the catalytic activity of Cu by removing the Cu native oxide on the surface. Previous attempts to pre-treat the Cu substrate by using wet chemistry or thermal annealing to control growth has been weakly addressed.

In this work, electropolishing combined with prior thermal annealing at 1030°C for 5 hrs under H_2 is used to control the degree of roughness of cold rolled polycrystalline Cu foils, and subsequently, to explore the influence of electropolishing on the growth of 2D materials: graphene, h-BN and MoS_2. Electropolishing dissolves a thin surface layer of Cu, which contains surface defects and contaminants. This helps in decreasing the density of spontaneous nucleation sites by producing a morphologically uniform and contaminant-free surface. Secondary effects, etch pits which are ascribed to O_2 bubbling at random nucleation sites on Cu surface, are mitigated by using additives, such as acetic acid and ethylene glycol, in the H_3PO_4 electrolyte. Thermal annealing and electropolishing results in this work reveal that a roughness of ~1.2 nm (R_q) can be achieved as measured by Atomic Force Microscope (AFM) along with a greatly planarized Cu foil. AFM will also be used to establish the Cu substrate morphology and its relationship to the growth of 2D materials. Fourier Transform Infrared, and Raman spectroscopy will be used to confirm the existence of the 2D material. Preliminary growth studies of h-BN on these high quality Cu substrates demonstrate improved growth, as assessed by the metrics of size and count of h-BN crystals from Scanning Electron Microscopy (SEM) micrographs [1]. This work will demonstrate that thermal annealing followed by electropolishing leads to optimization of Cu foil surface resulting in the larger crystal size and a reduction in nucleation sites that induce 2D material crystal growth [1].

[1] K. Sridhara. "Growth of hexagonal boron nitride on electrochemically prepared polycrystalline Cu substrates." M.S. Thesis, University of Maryland, College Park, MD, 2014.

9:20am **2D+EM+NS+PS+SP+SS+TF-MoM4 *In Situ* Optical Diagnostics During Molybdenum Disulfide Chemical Vapor Deposition**, ***Berc Kalanyan***, *J.E. Maslar, W.A. Kimes, B.A. Sperling,* National Institute of Standards and Technology (NIST)*, R. Tieckelmann, T. Orzali,* SEMATECH*, R. Beams, S.J. Stranick, A.V. Davydov*, National Institute of Standards and Technology (NIST)

Two dimensional (2D), layered transition-metal dichalcogenides (TMDs), e.g., MoS_2, are of increasing interest for next-generation nanoelectronic and optoelectronic devices. These materials have thickness dependent optical and electrical properties that make them suitable for a variety of applications including integrated circuits. For many applications, high volume manufacturing (HVM) of devices based on TMDs will require deposition techniques that are capable of reproducibly growing wafer-scale, 2D TMD films with monolayer control. To date, such a capability has not been widely demonstrated with typical TMD deposition processes.

This work aims to identify promising chemistries for HVM TMD chemical vapor deposition (CVD) processes. We focus on MoS_2 CVD using a variety of precursors (including organometallics, elemental sulfur, and organosulfur compounds) in a research grade single-wafer deposition system equipped with *in situ* optical diagnostics. The precursor flux is measured using optical mass flow meters installed on the delivery lines while deposition chemistry is characterized in the reactor volume above the deposition surface using *in situ* Fourier transform infrared (FR-IR) spectroscopy. As-deposited and annealed films are characterized with *ex situ* techniques, including Raman and photoluminescence spectroscopy, scanning and transmission electron microscopy, and X-ray photoelectron spectroscopy.

Stoichiometric MoS_2 films have been prepared from (η^5-ethylcyclopentadienyl)-dicarbonylnitrosyl molybdenum and elemental sulfur. As-grown films are smooth and continuous with major MoS_2 Raman modes present. Film thickness scales approximately with Mo precursor exposure time and few-layer films can be produced using pulsed injection mode. Furthermore, optical *in situ* diagnostics allow us to relate metal precursor flux to film crystallinity and facilitate the study of precursor decomposition in the thermal boundary layer.

9:40am **2D+EM+NS+PS+SP+SS+TF-MoM5 Controlled Interfaces in 2D Materials**, ***Arend van der Zande***, University of Illinois at Urbana Champaign **INVITED**

Interfaces are ubiquitous in material science and technologies. For example, grain boundaries often dominate the mechanical and electrical properties in crystalline materials, while interfaces between dissimilar materials form the fundamental building blocks to diverse technologies, such as building electrical contacts in transistors and PN diodes in solar cells. Interfaces become even more important in 2D materials such as graphene and transition metal dichalcogenides, where the lack of dangling bonds enables material stability down to a single monolayer. In this entirely surface-dominated limit, the usual rules governing 3D interface devices, such as depletion regions, break down.

In this talk, we will discuss our work on engineering in- and out-of-plane 2D materials interfaces. We will first examine the structure of atomically-thin membranes and the impact of defects such as grain boundaries on the mechanical, optical, and electronic properties. We fabricate out-of-plane interfaces by stacking 2D materials to form heterostructures, which we utilize to tailor the bandgap in 2D materials and build new optoelectronic devices such as tunable photodiodes. Looking to the future, the rapidly expanding family of 2D materials with a diverse set of electronic properties provide a promising palette for discovering emergent phenomena and a motivation for developing overarching design principles for understanding and controlling interfaces in 2D.

10:40am **2D+EM+NS+PS+SP+SS+TF-MoM8 Obtaining Clean Suspended CVD Graphene: Comparative Examination of Few Transfer and Cleaning Protocols**, ***Alexander Yulaev***, National Institute of Standards and Technology (NIST), University of Maryland (UMD), *G. Cheng, A. Hight Walker,* National Institute of Standards and Technology (NIST), *M. Leite,* University of Maryland (UMD), *A. Kolmakov*, NIST

Clean suspended graphene is used as supporting media in TEM, filtering membranes, and as electron transparent windows in ambient pressure electron spectroscopy and microscopy. CVD grown graphene is the most popular material for these applications due to its large-scale and high yield production. Multiple approaches such as sacrificial layer based methods [1] and direct transfer method on perforated carbon mesh by IPA droplet [2] have been implemented to transport graphene from copper or nickel foil onto a target substrate. However, the cleanness of the suspended graphene remains to be an issue, and controversial results on lateral size of atomically clean graphene domains have been reported [2-5]. We conduct the comparative analysis of the most widely-used CVD graphene transfer and cleaning protocols. In particular, using extreme surface sensitivity of low energy SEM, we compare the standard PMMA based approach with direct graphene transfer method. We also propose alternative graphene transfer protocol which is based on employment of polycyclic aromatic hydrocarbon (PAH) as a sacrificial layer. The advantage of PAH method over others consists in facile sublimation of sacrificial layer upon heating PAH material within moderate temperature range of 100-150 ^oC. All three methods of graphene transfer were compared under the same conditions followed by similar graphene cleaning procedures by platinum catalysis [4] and activated carbon adsorption [5]. Both SEM and TEM study revealed the superiority of PAH method to achieve cleaner suspended CVD graphene. We envision that novel approach of graphene transfer can be employed under conditions when exposure of the sample to moisture is prohibited such as in battery research.

[1] "Transfer of CVD-Grown Monolayer Graphene onto Arbitrary Substrates", Ji Won Suk *et al*., ACS Nano, 2011, 5 (9), pp. 6916.

[2] "A direct transfer of layer-area graphene", William Regan *et al*., Appl. Phys. Lett., 2010, 96, 113102.

[3] "Low-energy electron holographic imaging of gold nanorods supported by ultraclean graphene", Jean-Nicolas Longchamp *et al*., Ultramicroscopy 145 (2014) 80.

[4] "Ultraclean freestanding graphene by platinum-metal catalysis", Jean-Nicolas Longchamp *et al*., J. Vac. Sci. Technol. B 31, 020605 (2013).

[5] "Dry-cleaning of graphene", Gerardo Algara-Siller *et al*., Applied Physics Letters 104, 153115 (2014).

11:00am **2D+EM+NS+PS+SP+SS+TF-MoM9 Low-Energy Electron Microscopy of Transition Metal Dichalcogenides Prepared by Various Methods**, ***Sergio de la Barrera***, *S. Satpathy, R. Feenstra,* Carnegie Mellon University, *S. Wu, X.D. Xu,* University of Washington, *S. Vishwanath, X. Liu, J. Furdyna, D. Jena, H. Xing,* University of Notre Dame, *Y.-C. Lin, S.M. Eichfeld, J.A. Robinson,* Pennsylvania State University, *P. Mende*, Carnegie Mellon University

Recent work on two-dimensional materials has focused on transition metal dichalcogenides (TMDs), owing to their semiconducting behavior. Characterizing as-grown TMDs is crucial in improving the understanding of the effects of growth conditions, and ultimately improving material quality. Low-energy electron microscopy (LEEM) is a powerful tool for this purpose, providing real-space images with ~10 nm spatial resolution as well as selected-area low-energy electron diffraction (µLEED) of local crystal orientation at length scales down to ~ 1 µm. Additionally, by varying the incident electron beam energy, low-energy electron reflectivity (LEER) spectra are extracted.

In this work, comparative LEEM results are presented from three TMD materials: MoS_2 prepared by exfoliation (onto Si), $MoSe_2$ grown by molecular beam epitaxy (MBE) (on epitaxial graphene), and WSe_2 grown by chemical vapor deposition (CVD) (also on epitaxial graphene). It is found that for TMDs generally, the LEER spectra do not exhibit the oscillatory behavior (in the 0 – 6 eV range) that is seen for both graphene and hexagonal boron nitride (h-BN) for various numbers of monolayers (MLs). This lack of oscillatory behavior is interpreted as being due to the weak coupling of the interlayer states localized in between the MLs, which is itself a result of the relatively large out-of-plane lattice parameter. Nevertheless, additional "band structure" features in the LEER spectra permit clear identification of the TMD materials relative to the substrates. The exfoliated flakes are seen to extend over many 10's of mm, the MBE-grown $MoSe_2$ forms a nearly continuous film, and the CVD-grown WSe_2 forms triangular islands several mm in extent. µLEED studies of the MBE-grown $MoSe_2$ and CVD-grown WSe_2 reveal preferential orientation with the underlying graphene substrates.

The reduced work functions of the TMD materials relative to the underlying substrate are clearly evident in the onset voltages for the LEER spectra (i.e. the onset shifts in accordance with the local work function of the surface). Most significantly, for the WSe_2 islands, a predominant "tail" is observed in this onset, extending about 5V below the usual onset location. This tail is tentatively interpreted as arising from charging of the islands, perhaps due to polar termination at the edges of the TMD islands. Comparison of the data with simulated LEER spectra will be presented, as a test of this model for edge charge of the islands.

Work supported by the Center for Low Energy Systems Technology (LEAST), one of six SRC STARnet Centers sponsored by MARCO and DARPA, and by NSF-EFRI-1433496.

11:20am **2D+EM+NS+PS+SP+SS+TF-MoM10 Atomically-Thin 2D Layers of Group IV Semiconductors**, ***Joshua Goldberger***, The Ohio State University **INVITED**

Similar to how carbon networks can be sculpted into low-dimensional allotropes such as fullerenes, nanotubes, and graphene with fundamentally different properties, it is possible to create similar "allotropes" of Ge or Sn with unique optoelectronic properties as well. Here, we will describe our recent success in the creation of hydrogen and organic-terminated group 14 graphane analogues, from the topochemical deintercalation of precursor Zintl phases, such as $CaGe_2$. We will discuss how the optical, electronic, and thermal properties of these materials can be systematically controlled by substituting either the surface ligand or via alloying with other Group 14 elements. Additionally, we have also developed an epitopotaxial approach for integrating precise thicknesses of Germanane layers onto Ge wafers that combines the epitaxial deposition of $CaGe_2$ precursor phases with the topotactic interconversion into the 2D material. Finally, we will describe

our recent efforts on the synthesis and crystal structures of Sn-containing graphane alloys in order to access novel topological phenomena predicted to occur in these graphanes.

Electronic Materials and Processing
Room: 211A - Session EM+AS+SS-MoM

Rectenna Solar Cells, MIM Diodes, and Oxide Interfaces
Moderator: John Conley, Oregon State University, Dale Kotter, RedWave Energy, Inc.

8:20am **EM+AS+SS-MoM1 Harvesting Energy with Optical Rectennas: Challenges and Innovations**, ***Garret Moddel***, University of Colorado and RedWave Energy, Inc., *S. Joshi, B. Pelz, A. Belkadi, S. Yuan,* University of Colorado at Boulder, *P. Brady, D. Kotter*, RedWave Energy, Inc. **INVITED**

Optical rectennas are of interest for radiant heat and light energy harvesting, and ultra-fast detectors that work for terahertz waves up through visible-light wavelengths. The devices work under constraints that are different from those of either microwave rectennas or conventional solar cells. These antenna-coupled diodes incorporate micron-scale antennas and diodes that must operate at frequencies in the tens to hundreds of terahertz, but the antenna size and diode speed are not the most daunting challenges. The current produced by the antenna – particularly for rectennas operating at close to visible-light frequencies – samples the diode at discrete voltages described by a quantum approach instead of at continuously varying voltages described by classical electromagnetic theory – which makes for a fascinating theory of operation. The consequence is a quantum limit to the power conversion efficiency, similar to the Shockley-Queisser limit for conventional solar cells. The optical frequency and intensity determine whether the rectenna operation can be described classically or must involve a quantum analysis. Because rectennas gather current from the entire antenna, if the light is not spatially coherent cancellation occurs, resulting in reduced efficiency. This limits the amount of power received by each diode, which further limits the diode rectification efficiency. Over the last decade the number of groups investigating various parts of rectenna technology has grown from almost none to at least 50. This growing community of researchers, with innovative solutions, is needed to meet optical rectenna challenges and enable a practical technology. Some emerging solutions will be presented.

9:00am **EM+AS+SS-MoM3 Demonstration of Traveling-Wave Metal-Insulator-Metal Diodes for 28 THz (10.6 μ m) Rectennas**, ***Bradley Pelz***, University of Colorado at Boulder, *G. Moddel*, University of Colorado at Boulder and Redwave Energy

Lumped element rectennas encounter an efficiency limitation above several terahertz due to the RC time constant of an MIM diode. A traveling-wave diode (TWD) takes advantage of nanoscale geometries to achieve a lower capacitance than that of a lumped element diode. The TWD behaves as a MIM transmission line for surface plasmons in which the rectification occurs as the wave travels down its length. Due to the distributed nature of the rectifier, the impedance seen by the antenna is the characteristic impedance of the transmission line. COMSOL simulations have shown this gives a reactive component of diode impedance that is substantially smaller than either the real component of the characteristic impedance for the TWD or the reactance from the parallel plate capacitance of an equivalently sized lumped element MIM diode. This allows for a much higher coupling efficiency from the antenna than in the case of a lumped element diode, and a substantially reduced RC time constant.

To obtain a resistance that matches that of the antenna simulations show that the TWD requires a width of 100 nm or less, which is too small for conventional lithography techniques. This small critical dimension was achieved using a germanium shadow mask technique. After fabrication, the DC junction characteristics were measured using a four-point technique. The open circuit voltage of these unbiased devices was measured under 28 THz illumination using a CO_2 laser and a lock-in amplifier. The TWD coupled to a bow tie antenna showed both polarization and power dependence. Since these measurements were completed at zero bias, the response could not have been bolometric, and the device must have been operating in energy harvesting mode.

9:20am **EM+AS+SS-MoM4 Basic Efficiency Limits for Rectenna Solar Power Conversion**, ***Heylal Mashaal***, *J.M. Gordon*, Ben-Gurion University of the Negev, Israel

The prospect of employing aperture rectennas for solar power conversion will be explored in this presentation. Sunlight is commonly viewed as incoherent – hence seemingly unsuitable for antenna harvesting – but all electromagnetic radiation exhibits spatial coherence on a sufficiently small scale. The first direct measurement of the spatial coherence of sunlight will be presented, and the ramifications for using optical concentrators that can effectively replace orders of magnitude of antenna and rectifier elements will be discussed.

Rooted in the partial spatial coherence of sunlight, a derivation of the thermodynamic limit for coherence-limited solar power conversion will be presented – an expansion of Landsberg's elegant basic bound, originally limited to incoherent converters at maximum flux concentration. The results do not depend on a particular conversion strategy. As such, they pertain to systems that span geometric to physical optics.

Last, a basic upper bound will be presented for the ability to rectify the broadband signals using a full wave rectification scheme.

Our findings indicate promising potential for rectenna power conversion.

9:40am **EM+AS+SS-MoM5 Coherence Effects in Periodic Arrays of Nano-Antennas used for Energy Harvesting and Self-Imaging**, ***Peter Lerner***, SciTech Associates, LLC, *P.H. Culter, N.M. Miskovsky*, Penn State University

Coherence effects in periodic arrays of nano-antennas used for energy harvesting and self-imaging

P. B. Lerner [1] , N. M. Miskovsky[1,2] , P. H. Cutler[1,2]

Modern technology allows the fabrication of antennas with a characteristic size comparable to the electromagnetic wavelength in the optical region. [1] This has led to the development of new technologies using nanoscale rectifying antennas (rectennas) for solar energy conversion and sensing of terahertz, IR and visible radiation. For example, a rectenna array can collect incident radiation from an emitting source and the resulting conversion efficiency and operating characteristics of the device will depend on the spatial and temporal coherence properties of the absorbed radiation. For solar radiation, the intercepted radiation by a micro- or nano-scale array of devices has a relatively narrow spatial and angular distribution. Using the Van Cittert-Zernicke Theorem, we show that the coherence length (or radius) of solar radiation on an antenna array is, or can be, tens of times larger than the characteristic wavelength of the solar spectrum, i.e., the thermal wavelength, $\lambda_T=2\pi\hbar c/(k_B T)$, which for T=5000K is about 2 microns. Such an effect is advantageous, making possible the rectification of solar radiation with nanoscale rectenna arrays, whose size is commensurate with the coherence length. Furthermore, using the van Cittert-Zernicke Theorem, we also examine the blackbody radiation emitted from an array of antennas at temperature T, which can be quasi-coherent and lead to a modified self-image, analogous to the Talbot-Lau self-imaging process [2] but with thermal rather than monochromatic radiation. This coherence of the antennas' blackbody radiation can also introduce an angular spectrum, which may be concentrated (enhanced) along certain spatial directions, giving rise to additional features not present in the original array. The self-emitted thermal radiation may be important as a non-destructive means for quality control of the array.

[1] Miskovsky, N. M., P. H. Cutler, A. Mayer, B. L. Weiss, B. Willis, T. E. Sullivan, and P. B. Lerner (2012) Nanoscale Devices for Rectification of High Frequency Radiation from the Infrared through the Visible: A New Approach, *Journal of Nanotechnology*, Article ID 512379, 19 pages, http://dx.doi.org/10.1155/2012/512379 .

[2] Gori, F. (1979) Lau Effect and Coherence Theory, *Optics Communications*, 31(1), 4.

---

1 SciTech Associates, Woodland Drive, State College, 16803.

2 Physics Department (emeritus), Penn State University, University Park, 16802.

10:00am **EM+AS+SS-MoM6 Metamaterial Enhanced Rectenna for Efficient Energy Harvesting**, *D. Lu*, ***Won Park***, University of Colorado Boulder, *P. Brady*, Redwave Energy Inc.

Rectenna solar cell offers an important alternative to the conventional semiconductor solar cell technology. Direct rectification of electromagnetic radiation faces many challenges one of which is the high frequency of operation. Thermal emission from hot bodies peaks at 10 ~ 100 THz while solar radiation has its maximum at around 600 THz. One may circumvent this difficulty if sufficiently strong thermal radiation is available at lower frequencies. In general, thermal emission is described well by the theory of blackbody radiation while the property of the non-black surface is characterized by its emissivity. When the surface supports surface waves, however, the properties of thermal emission can deviate substantially from the blackbody radiation, offering a new avenue for engineering thermal emission. For example, spatially coherent and spectrally selective thermal emission may be achieved. The presence of surface waves also means

enhanced local density of states near the surface, which consequently leads to strongly modified thermal emission intensity and spectrum in the near field. In this paper, we report a metamaterial design to achieve enhanced thermal emission at 1 THz.

Two types of metamaterial designs were investigated: a 1D array of parallel trenches and a 2D array of holes etched on copper. The metamaterial surface was designed to support surface waves resembling the surface plasmon on metal surface. Numerical simulations by the finite element method confirmed the presence of surface waves and strong electric field near the surface at 1 THz. The strongly enhanced electric field is the direct consequence of enhanced local density of states. To further confirm the surface modes can be excited by thermal emission, we also conducted finite-difference time-domain simulations in which thermal emission was calculated by using the fluctuation dissipation theorem. Once the enhanced thermal emission is confirmed, a bowtie antenna was placed close to the metamaterial surface to capture the enhanced thermal emission in the near field. The antenna was optimized to maximize the electromagnetic energy delivered to the antenna gap. Since the antenna should couple efficiently with the surface modes, the optimal antenna design became quite different from the free space bowtie antenna operating at the same frequency. The optimized metamaterial and antenna design resulted in an antenna voltage of 10 mV at 1 THz, three orders of magnitude larger than the free space antenna. Such a large enhancement makes the metamaterial approach a highly promising route to efficient energy harvesting with rectenna.

11:00am **EM+AS+SS-MoM9 Modeling of and Power from Nb-NbOx-based Nanorectenna Arrays**, ***Richard M. Osgood***, US Army NSRDEC, *J. Xu, G.E. Fernandes*, Brown University, *M. Rothschild, K. Diest*, MIT Lincoln Laboratory, *M. Kang, K.B. Kim*, Seoul National University, Republic of Korea, *L. Parameswaran*, MIT Lincoln Laboratory, *P. Periasamy*, IBM, *M. Chin*, Army Research Laboratory, *S. Kooi*, MIT Institute for Soldier Nanotechnologies, *S. Giardini*, US Army NSRDEC, *R. O'Hayre, P. Joghee*, Colorado School of Mines

We investigate arrays of "microrectennas" (with sub-micron features tuned for the near-and short-wave infrared) consisting of "stripe-teeth" metamaterial antennasconducting vertically through the coupled, underlying metal-insulator-metal (MIM) diode into a metallic substrate. Stripes, with cross-stripe resonances, conduct current out of the array, while antenna-like teeth break left-right symmetry and concentrate a high vertical electric field (E_z) at the end of the teeth at their antenna resonance. If plasmonic field enhancement and concentration reduce the capacitance and/or increase the effective voltage across the MIM diode, new research and development of large-area ultrafast optical rectennas will be enabled, requiring patterning and alignment of only the top metal layer.

Stripe-teeth arrays were designed, fabricated, and analyzed both experimentally and theoretically. Substrates were layers ("ground planes") of Nb and Al, and a Au nanowire array patterned using novel high-throughput e-beam technology.[1] Substrates were oxidized/anodized, or had oxides deposited, to form microantenna-coupled MIM diodes consisting of Al-Al_2O_3-Al, Au/Ti-NbO_x-Nb, Al-Al_2O_3-Au, Ag/Ti-NbO_x-Nb, Ag/Ti-NiO-Ni, Pt-NbO_x-Nb, after deposition of top metal layers of Ag/Ti, Au/Ti, Pt, and Al (only a few nm of Ti). Conduction through 10-25 nm thick oxide layers in the MIM diodes occurred via quantum mechanical tunneling and thermionic emission, with asymmetric barrier heights all less than 1 V except for the Al-Al_2O_3-Al diodes. The Au-Al_2O_3-Al system required modeling the "hot spot" from top metal protrusions into the Al_2O_3barrier layers and in close (tunneling) proximity to the ground plane, probably because of the surface roughness and variation in Al_2O_3 thickness; the planar-planar MIM diode model was inapplicable in this case.

The top metal was patterned into the stripe-teeth arrays. Reflective Al substrates provided sharp optical antenna resonances while Nb layers produced broader, weaker antenna resonances due to Nb absorption, similar to stripe-only arrays reported in Ref. 2. We also report the result of visible light (514 nm – 630 nm) laser illumination of Nb/NbO_x/Ag(Ti) stripe-teeth arrays, including the observation of a short-circuit current and open-circuit voltage, in response to power densities in the range 80 W/cm^2.

1. H. S. Lee, *et. al.*, "Electron beam projection nanopatterning using crystal lattice images obtained from high resolution transmission electron microscopy", Adv. Mats. **19** 4189 (2007).

2. Wu, C., *et.al*." Large-area wide-angle spectrally selective plasmonic absorber," *Phys. Rev. B*, Vol. 84, 075102-7, 2011.

11:20am **EM+AS+SS-MoM10 Metal-Insulator-Insulator-Metal Diodes for Rectenna Applications**, ***Shijia Lin***, *N. Murari, J.F. Conley, Jr.*, Oregon State University

A metal-insulator-metal (MIM) tunnel diode has a capacitor-like structure with a thin insulating layer sandwiched by two metals. Because of their potential for femtosecond-fast transport when dominated by tunnel transport, MIMs are of interest for rectenna based solar cells, hot electron transistors, and IR detectors. The common strategy to achieving rectification in MIM devices relies on the use of dissimilar work function metal electrodes to produce an asymmetric electron tunneling barrier with polarity dependent tunneling probability. The performance of single layer MIM devices is limited by the workfuction difference that can be achieved between the electrodes and the metal-insulator band offsets. Small electron affinity oxides are limited by high V_{ON}. Large electron affinity dielectrics have small V_{ON}, but tend to have limited asymmetry due to thermal emission dominated conduction. An alternative approach to controlling asymmetry is to use nanolaminate pairs of insulators with different bandgaps and band offsets to produce asymmetric tunnel barrier metal-insulator-insulator-metal (MIIM) diodes. Asymmetry in MIIM devices may be enhanced by step tunneling[1] or defect enhanced direct tunneling.[2]

In this work, we investigate asymmetry in HfO_2/ Nb_2O_5 bilayer insulator MIIM diodes. HfO_2 and Nb_2O_5 were deposited via atomic layer deposition (ALD) using tetrakis (ethylmethylamino) hafnium (TDMAHf) and niobium ethoxide metal precursors, respectively with H_2O as the oxidant. Nanolaminate films were deposited at a chamber temperature of 250°C in one continuous run without breaking vacuum. Sputtered TaN or amorphous metals were used as the bottom electrode and evaporated Al dots were used as a top electrode. MIIM I-V asymmetry and non-linearity are shown to be a function of stack thickness, relative layer thickness, and insulator layer position with respect to the electrodes. Overall, bilayer insulators are shown to be an effective method of enhancing the performance of MIIM tunnel diodes.

1. N. Alimardani and J.F. Conley Jr, Appl. Phys. Lett. 102, 143501 (2013).

2. N. Alimardani and J.F. Conley, Jr., Appl. Phys. Lett. 105, 082902 (2014).

11:40am **EM+AS+SS-MoM11 Built-in Potential in Fe_2O_3-Cr_2O_3 Superlattices for Improved Photoexcited Carrier Separation**, ***Tiffany Kaspar***, *D.K. Schreiber, S.R. Spurgeon, S.A. Chambers*, Pacific Northwest National Laboratory

Hematite, α-Fe_2O_3, is an ideal photocatalyst to split water as a source of H_2 fuel because it is non-toxic, Earth-abundant, stable in aqueous environments, and possesses a bandgap in the visible wavelength range (~2.1 eV). However, fast photogenerated electron-hole recombination, facilitated in part by slow carrier transport kinetics, has long been identified as a major obstacle in the utilization of hematite photocatalysts. A direct method to reduce photogenerated carrier recombination is to employ heterojunctions to spatially separate excited electrons and holes. Our approach is to engineer built-in electric fields by exploiting the band alignment characteristics of epitaxial Fe_2O_3/Cr_2O_3 heterojunctions. The Fe_2O_3-Cr_2O_3 system exhibits non-commutative band offsets which differ by approximately 0.4 eV depending on the order of deposition. The non-commutative band offset properties of Fe_2O_3-Cr_2O_3 interfaces can be utilized in a superlattice structure, deposited by oxide molecular beam epitaxy, to build up an intrinsic electric field; this potential may be sufficient to spatially separate photogenerated electrons and holes. We demonstrate precise control over the Fe_2O_3-Cr_2O_3 interface structure with atomic-resolution atom probe tomography and scanning transmission electron microscopy. Direct evidence that Fe_2O_3-Cr_2O_3 superlattice layers generate an intrinsic built-in potential is observed with x-ray photoelectron spectroscopy. The individual interfacial band offset values, and thus the overall potential, can be tailored by altering the cation stoichiometry at the interfaces. Doping the component layers to improve transport characteristics requires a deep understanding of the dopant-induced electronic structure changes. To illustrate how the built-in potential in optimized Fe_2O_3-Cr_2O_3 superlattice structures can be harnessed to drive holes to the surface and electrons into the bulk, photoconductivity and photochemical degradation results will be presented.

Electronic Materials and Processing
Room: 210E - Session EM+NS+PS-MoM

More Moore! Materials and Processes to Extend CMOS Another Decade

Moderator: Christopher Hinkle, University of Texas at Dallas

8:20am **EM+NS+PS-MoM1 Effects of Deposition Temperature and Pre-rapid Thermal Process on Electrical and Interfacial Characteristics of Alumina on GaSb**, ***Seongkyung Kim***, *H.J. kim*, Seoul National University, Korea, Republic of Korea

Recently Ⅲ-Ⅴ compound materials have attracted significant attention as promising channel materials for sub-10 nm logic MOSFET due to their high mobility. GaSb is a strong candidate for pMOSFETs because of its high

hole mobility in addition to the insolubility of its native oxides. Even with the outstanding electrical properties of GaSb, there are some drawbacks related to the instability of its native oxides and metallic layer of elemental Sb. The native oxides and metallic layer of elemental Sb are considered to be sources of Fermi level pinning and flat C-V curves. Therefore, it is necessary to improve surface treatment methods. Since it is possible to eliminate its native oxides and elemental Sb by heating them, it is essential to research temperature related surface treatments.

In this study, various ALD temperatures from 190 ^oC to 310 ^oC and pre-RTP(Rapid Thermal Process), which is first introduced here as a pre-deposition treatment, have been adopted for eliminating the remaining native oxides after cleaning. N_2 gas atmosphere is used to suppress the oxygen to interact with GaSb surface for the pre-RTP. GaSb metal-oxide-semiconductor capacitors were fabricated on p-type GaSb, which has a carrier concentration of 1.0~2.0 x 10^{17} cm^{-3}. GaSb was degreased with acetone, ethanol, and isopropane for 5 minutes each and then etched by HCl. 10 nm of Al_2O_3 has been deposited as a gate dielectric with TMA and DI water by thermal ALD. For the metal gate, a Pt electrode has been deposited with an electron-beam evaporator.

When the deposition temperature increases, the Ga_2O_3 peak increases and the substrate peak decreases under XPS analysis. It is observed that the amount of Sb increases at the GaSb/Al_2O_3 interface as the deposition temperature increases in AES depth profiles. Both Ga2O3 and elemental Sb have increased generation as the deposition temperature increases, since the surface chemical reactions are accelerated by increased temperature. The CV curve becomes flat as the deposition temperature increases. It indicates that Ga_2O_3 has a flattening effect of the CV curve and the more amount of Ga_2O_3 that is generated, the flatter the CV curve will become.

Desorption of the native oxides and elemental Sb should occur by annealing the substrate. After the pre-RTP, the amount of elemental Sb increases, since the remaining native oxide, after cleaning, is reduced by increased temperatures. The remaining native oxide Sb_2O_3, after cleaning, supplies oxygen to the substrate and becomes elemental Sb. The leakage current increases with pre-RTP. It shows that the elemental Sb increases the leakage current. Further study on optimizing pre-RTP conditions is needed.

8:40am **EM+NS+PS-MoM2 Selective Wet Etching of III-V Semiconductors with HCl and H_2O_2**, ***Pablo Mancheno-Posso***, *. Jain, A.J. Muscat*, University of Arizona

The etching of III-V semiconductors is needed to insert these materials into current device flows to extend CMOS transistor technology. III-V oxides are detrimental to electrical performance and must be removed, because they adopt different oxidation states and can be soluble in water. Plasma etching to create profiles can damage and change the stoichiometry of the surface. Wet etching of these oxides can control the roughness and chemical termination of the surface by choice of oxidant and etchant, concentration, and pH. Wet etching of III-V semiconductors is accomplished by oxidizing acid and base chemistries that can preferentially remove group III or V atoms. In new 3 D transistor architectures, the formation of the channel fin requires a low etching rate to ensure a smooth surface and a highly selective etching bath with respect to other materials or crystal faces that are exposed. In this work, we varied the group III and V atoms across five binaries (GaAs, InAs, InP, GaSb, and InSb) and measured etching rates. These materials were etched using mixtures of HCl (0.01 M) and H_2O_2 (0.0001-5 M). The etching rate was measured using profilometry on wafers patterned with conventional photolithography. The chemical composition was monitored using X-ray photoelectron spectroscopy (XPS). The etching rate of GaAs and InAs (same group V atom) exhibited a volcano-shaped dependence on H_2O_2 concentration. At H_2O_2 concentrations of 5 to 100 mM, the etching rate increased linearly from 0.08±0.03 to 1.1±0.1 nm/s for GaAs and from 0.06±0.04 to 0.9±0.3 nm/s for InAs. The rate decreased to 0.04±0.01 nm/s for GaAs and 0.26±0.13 nm/s for InAs at 1 M H_2O_2. InP, which is often exposed during etching of another III-V, showed a linear dependence on H_2O_2 concentration (0.01 to 5 M), increasing from 0.003±0.001 to 0.012±0.009 nm/s. The selectivity of etching GaAs to InP at three points along the volcano was about 55, 140, and 4 at H_2O_2 concentrations of 0.01, 0.1, and 1 M. Like the arsenides, the antimonides etched at about the same rate, but the volcano dependence moved to lower peroxide concentrations. The etching rate of GaSb increased from 0.07±0.04 to 0.21±0.04 nm/s and InSb from 0.09±0.03 to 0.38±0.09 nm/s for H_2O_2 concentrations from 0.1 to 1 mM. The group V atom determined the etching rate and is involved in the rate determining step in the reaction. The presence of As-Cl bonds on the surface after etching GaAs in HCl was confirmed by temperature programmed desorption (TPD) experiments after immersion in 1.7 M HCl. The mechanism for etching III-V semiconductors will be discussed based on the etching rate data and chemical composition of the surface.

9:00am **EM+NS+PS-MoM3 Border Trap Analysis and Reduction for ALD High-k InGaAs Gate Stacks**, ***Kechao Tang***, Stanford Univ., *R. Winter,* Technion – Israel Inst. of Tech., *T. Kent,* UC, San Diego, *M. Negara,* Stanford Unive., *R. Droopad,* Texas State Univ., *A.C. Kummel,* UC, San Diego, *M. Eizenberg,* Technion – Israel Inst. of Tech., *P. McIntyre*, Stanford Univ.

For future high performance III-V n-channel MOS devices, $In_{0.53}Ga_{0.47}As$ is a promising material for the channel due to its high electron mobility. Atomic layer deposited (ALD) Al_2O_3 has a large conduction band offset to InGaAs and can form a low defect-density interface with InGaAs [1]. ALD-HfO_2 can achieve a very low EOT (effective oxide thickness) with low gate leakage [2]. Therefore, both of these oxides have received extensive attention as candidate dielectric layers for InGaAs nMOSFETs. Apart from the well-known oxide/InGaAs interface charge traps that may pin the Fermi level of the channel, traps in the oxide layer, called border traps, may also reduce the charge in the channel and thus degrade the on-state performance of InGaAs MOSFET devices. We report a study of the effects of various approaches to reduce the density of border traps (N_{bt}), such as variation of the ALD temperature, and of post-gate metal forming gas (5% H_2/95% N_2) anneal (FGA) conditions.

Experimental methods employed include quantitative interface trap and oxide trap modeling [3, 4] of MOS capacitor data obtained over a range of frequencies and temperatures. We find that MOS capacitors fabricated using trimethylaluminum (TMA)/H_2O at an ALD temperature of 120°C have a considerably lower border trap density while maintaining a low interface trap density (D_{it}) compared to samples prepared with a more standard 270°C Al_2O_3 ALD temperature. It is also found that large-dose (~6,000 L) exposure of the $In_{0.53}Ga_{0.47}As$ (100) surface to TMA immediately after thermal desorption of a protective As_2 capping layer in the ALD chamber is an important step to guarantee the repeatability of high quality Al_2O_3/InGaAs samples made at Al_2O_3 ALD temperatures much lower than 270°C. The reduction of N_{bt} is consistent with time-of-flight secondary ion mass spectrometry depth profiles that show more effective hydrogen incorporation in the low-temperature ALD-grown Al_2O_3 films during post-gate FGA.

The N_{bt} of Al_2O_3 under various conditions will be compared with that of low-temperature ALD-grown HfO_2 films on InGaAs substrates. For the HfO_2 case, we also confirm the independence of border trap response on the electrical measurement temperature and check the influence of the crystal orientation of the InGaAs surface on MOS interface characteristics.

This work was supported by the US-Israel Binational Science Foundation.

References

[1] J. Ahn et al., Appl. Phys. Lett. 103 (2013), 071602

[2] V. Chobpattana et al., J. Appl. Phys. 114 (2013), 154108

[3] H. Chen et al., IEEE TED 59 (2012), 2383-2389

[4] Y. Yuan et al., IEEE TED 59 (2012), 2100-2106

9:20am **EM+NS+PS-MoM4 Self-LIMITING CVD of an Air Stable Silicon Oxide Bilayer for Preparation of Subsequent Silicon or Gate Oxide ALD on InGaAs(001)-(2x4)**, ***Mary Edmonds***, *T. Kent, S. Wolf,* University of California at San Diego, *J. Kachian, N. Yoshida, M. Chang,* Applied Materials, *D. Alverez,* Rasirc, Inc, *R. Droopad,* Texas State University, *A.C. Kummel*, University of California at San Diego

A broader range of channel materials allowing better carrier confinement and mobility could be employed if a universal control monolayer (UCM) could be ALD or self-limiting CVD deposited on multiple materials and crystallographic faces. Si-OH is a leading candidate for use as the UCM, as silicon uniquely bonds strongly to all crystallographic faces of $InGa_{1-x}As$, $In_xGa_{1-x}Sb$, $In_xGa_{1-x}N$, SiGe, and Ge enabling transfer of substrate dangling bonds to silicon, which may then subsequently be functionalized with an oxidant such as HOOH(g) in order to create the UCM terminating Si-OH layer. This study focuses on depositing a saturated Si-OH seed layer on InGaAs(001)-(2x4) at a substrate temperature of 350°C. XPS in combination with STS/STM were employed to characterize the electrical and surface properties of the saturated Si-OH seed layer on InGaAs(001)-(2x4).

The 350°C self-limiting CVD procedure includes a decapped $In_{0.53}Ga_{0.47}As$(001)-(2x4) surface dosed with total 87.6 MegaLangmuir Si_2Cl_6 followed by 210.55 MegaLangmuir total anhydrous HOOH(g). Complete saturation of silicon coverage is determined to occur once further dosing with Si_2Cl_6 leads to no further increase in the silicon 2p or further decrease in the substrate gallium 3p peak areas. Complete surface saturation of Si-O_x on InGaAs(001)-(2x4) was determined to occur once no further increase in the O 1s peak was seen with additional anhydrous HOOH(g) doses. Following Si-OH surface saturation, 300,000 L TMA was dosed at 250°C, and XPS shows the emergence of Al 2p and C 1s peaks indicative of TMA surface nucleation. The surface was then dosed with 500 L atomic H at 250°C to remove the methyl groups on the surface aluminum and replace

with -H termination as well as remove any residual chlorine left on the surface. The surface was then exposed to air for 30 minutes, dosed with an additional 500 L atomic H at 250°C, and then STS measurements were performed. STM measurements of the $Si-O_x$ surface show uniform surface coverage. STS measurements show the surface Fermi level position moves towards midgap due to a surface dipole formation from –OH groups and oxygen bonding to the surface. TMA dosed on the $Si-O_x$ surface shifts the Fermi level back towards the conduction band, consistent with unpinning and the -OH induced surface dipole being lessened through surface bonding with dimethylaluminum groups. Following hydrogen dosing and air exposure, the surface Fermi level remains near the conduction band edge consistent with the surface being stable and unreactive in air. Preliminary MOSFET studies on InGaAs(001) show equivalent performance with Si_2Cl_6 predosing compared to in-situ cleaning with atomic H.

9:40am **EM+NS+PS-MoM5 Going Big in Two-Dimensions*, Joshua Robinson***, The Pennsylvania State University **INVITED**

The last decade has seen nearly exponential growth in the science and technology of two-dimensional materials. Beyond graphene, there are a variety of layered materials that provide a broad range of electronic characteristics useful for transistors, flexible electronics, sensors, and photodetectors, to name a few. However, bridging the gap between science and teechnology often lies in one's ability to synthesize materials on the wafer scale (or bigger). In this talk, I will discuss recent breakthroughs for direct growth of two-dimensional atomic layers and heterostructures with scalable techniues such as metal-organic chemical vapor deposition. We have demonstrated the direct growth of MoS_2, WSe_2, MoS_2/WSe_2, and hBN on epitaxial graphene to form large area van der Waals heterostructures. We reveal that the properties of the underlying substrate dictate properties of the layers and heterostructures, and that the direct synthesis of TMDs on epitaxial graphene exhibits atomically sharp interfaces. Our work has lead to a better understanding of vertical transport in 2D heterostructures, and we have identified new phenomenon in multi-junction heterostructures that has lead to resonance tunneling between layers and ultimately negative differential resistance.

1. Eichfeld, S. M.; Hossain, L.; Lin, Y.-C.; Piasecki, A. F.; Kupp, B.; Birdwell, A. G. G.; Burke, R. A.; Lu, N.; Peng, X.; Li, J.; et al. Highly Scalable, Atomically Thin WSe2 Grown via Metal-Organic Chemical Vapor Deposition. ACS Nano 2015.

2. Y.C. Lin, C.-Y. Chang, R. Ghosh,J.Li, H.Zhu, R.Addou, B.Diaconescu, T.Ohta, X.Peng, N.Lu, M.J. Kim, J.T. Robinson, R.M.Wallace, T.Mayer, S.Datta, L.J. Li, J.A. Robinson; Atomically Thin Heterostructures based on Single-Layer Tungsten Diselenide and Graphene; *Nano Letters*

3. M. S. Bresnehan, G. Bhimanapati, K. Wang, D.Snyder, J.A.Robinson; Impact of Copper Overpressure on the Synthesis of Hexagonal Boron Nitride Atomic Layers; *ACS Appl. Mater. Interfaces*, 6, 16755–16762 (2014)

4. S.M. Eichfeld, C.M. Eichfeld, Y.C. Lin, L. Hossain, J.A. Robinson; Rapid, non-destructive evaluation of ultrathin WSe2 using spectroscopic ellipsometry; *APL Materials* 2 (9), 092508

5. Y.C. Lin, N. Lu, N. Perea-Lopez, J. Li, C.H. Lee, Z.Lin, P.N. Browning, M.S. Bresnehan, L. Calderin, M.J. Kim, T.S. Mayer, M. Terrones, J.A. Robinson; Direct Synthesis of van der Waals Solids on Epitaxial Graphene; *ACS Nano* 8 (4), 3715-3723 (2014)

10:40am **EM+NS+PS-MoM8 2D Bipolar Devices for Novel Logic Applications: Fabrication, Characterization and Applications*, Ji Ung Lee***, SUNY Polytechnic Institute **INVITED**

The three pillars in semiconductor device technologies are (1) the p-n diode, (2) the MOSFET and (3) the Bipolar Junction Transistor (BJT). They have enabled the unprecedented growth in information technology that see today. For any new material, therefore, the development of these three devices is critical for providing benchmark performance against highly scaled Si-based technologies. Here, we will describe our efforts to fabricate and characterize these three benchmark devices in 2D materials, including graphene and transition metal dichalcogenide semiconductors (TMDs).

Although graphene is gapless, we will describe device concepts based on graphene p-n junctions that can lead to steep subthreshold slope devices. Critical to realizing such devices is the demonstration of relativistic Klein tunneling, a property of chiral carriers that arise from the unique electronic structure of graphene. Here, we will describe the fabrication and characterization of graphene p-n junctions, and discuss the unique tunneling properties that arise in these junctions and our efforts to realize high efficiency switching devices.

Using TMD materials, we have fabricated a single device that can reconfigure into p-n, MOSFET, and BJT devices. The reconfigurable device allows us to provide fundamental linkages between material properties and device performance not possible by fabricating the three devices individually. We will provide our method of fabrication and describe electrical and optical properties of the reconfigurable device.

11:20am **EM+NS+PS-MoM10 Electron Transport and Tunneling in Graphene-based Heterostructures*, Emanuel Tutuc***, The University of Texas at Austin **INVITED**

Vertical heterostructures consisting of atomic layers separated by insulators can open a window to explore the role of electron interaction in these materials, otherwise not accessible in single layer samples, as well as to explore device applications.

We describe here the realization of vertical heterostructures consisting of graphene, hexagonal boron nitride (hBN), and transition metal dichalcogenides realized using a layer-by-layer transfer. In double bilayer graphene heterostructures separated by hBN dielectric [1] where the two layers are rotationally aligned the interlayer tunneling current measured as a function of interlayer bias reveals a gate-tunable resonance thanks to momentum conserving tunneling. [2, 3] We discuss potential device application based on these experimental observations, as well as metrics that allow a benchmarking of their performance.

We also discuss the realization and characterization of graphene-MoS_2 heterostructures, which reveal a strong negative compressibility in the MoS_2 layer as a result of electron-electron interaction. [4]

Work done in collaboration with Kayoung Lee, Babak Fallahazad, Sangwoo Kang, Stefano Larentis, Hema C. P. Movva, Sanjay K. Banerjee, Leonard F. Register, Takashi Taniguchi, and Kenji Watanabe, and with support from the NRI-SWAN Center, Office of Naval Research, and Intel Corp.

[1] "Chemical potential and quantum Hall ferromagnetism in bilayer graphene", K. Lee, B. Fallahazad, J. Xue, D. C. Dillen, K. Kim, T. Taniguchi, K. Watanabe, E. Tutuc, Science 345, 58 (2014).

[2] "Gate-Tunable Resonant Tunneling in Double Bilayer Graphene Heterostructures", B. Fallahazad, K. Lee, S. Kang, J. Xue, S. Larentis, C. Corbet, K. Kim, H. C. P. Movva, T. Taniguchi, K. Watanabe, L. F. Register, S. K. Banerjee, E. Tutuc, Nano Letters 15, 428 (2015).

[3] "Bilayer Graphene-Hexagonal Boron Nitride Heterostructure Negative Differential Resistance Interlayer Tunnel FET", S. Kang, B. Fallahazad, K. Lee, H. C. P. Movva, K. Kim, C. Corbet, T. Taniguchi, K. Watanabe, L. Colombo, L. F. Register, E. Tutuc, S. K. Banerjee, IEEE Electron Device Letters 36, 405 (2015)

[4] "Band Offset and Negative Compressibility in Graphene-MoS_2 Heterostructures", S. Larentis, J. R. Tolsma, B. Fallahazad, D. C. Dillen, K. Kim, A. H. MacDonald, E. Tutuc, Nano Letters 14, 2039 (2014).

Energy Frontiers Focus Topic
Room: 211B - Session EN+AS+EM+NS+SE+SS+TF-MoM

Solar Cells I
Moderator: Jason Baxter, Drexel University, Chintalapalle Ramana, University of Texas at El Paso

8:20am **EN+AS+EM+NS+SE+SS+TF-MoM1 Elevated Temperature Phase Stability of CZTS-Se Thin Films for Solar Cells**, *E. Chagarov, K. Sardashti,* University of California at San Diego, *D.B. Mitzi,* Duke University, *R.A. Haight,* IBM T.J. Watson Research Center, ***Andrew C. Kummel***, University of California at San Diego

Density-functional theory simulations of CZTS, CZTSe and $CZTS_{0.25}Se_{0.75}$ photovoltaic compounds have been performed to investigate stability of $CZTS_{0.25}Se_{0.75}$ alloy vs. decomposition to CZTS, CZTSe and other secondary compounds. The Gibbs energy for vibration contribution was estimated by calculating phonon spectra and thermodynamic properties at finite temperatures. It was demonstrated that $CZTS_{0.25}Se_{0.75}$ alloy is stabilized not by enthalpy of formation but by vibration and mixing contributions to the Gibbs energy. A set of phase diagrams was built in multidimensional space of chemical potentials at 300K and 900K temperatures to demonstrate alloy stability and boundary compounds at various chemical conditions. The Gibbs energy gain/loss for several decomposition reactions was calculated as a function of temperature with/without Cu/Zn intermixing and vibration contributions to the Gibbs energy demonstrating $CZTS_{0.25}Se_{0.75}$ that even defect-free (no Cu/Zn intermixing) $CZTS_{0.25}Se_{0.75}$ can be stable at typical processing temperatures.

8:40am **EN+AS+EM+NS+SE+SS+TF-MoM2 Chemical and Electrical Characterization of Polycrystalline CZTS,Se and CIGS,Se Grain Boundaries by NanoAuger and Kelvin Probe Force Microscopy (KPFM)**, ***Kasra Sardashti***, UC San Diego, *P.D. Antunez, R.A. Haight,* IBM T.J. Watson Research Center, *A.C. Kummel*, UC San Diego

Polycrystalline Copper-zinc-tin-sulfide/selenide (CZTS,Se) compounds have received wide research interest due to their potential as inexpensive absorber materials composed of earth-abundant elements. Photovoltaic devices fabricated on CZTS,Se have reached conversion efficiencies of 12.6 %. One of the key parameters to further boost the conversion efficiency is to control the concentration of recombination sites at the surface, secondary phase interfaces and in the grain boundaries. To determine the presence of secondary phases on the surface and composition of grain boundaries, this work has employed Auger nanoprobe electron spectroscopy (NanoAuger) with 8nm lateral resolution combined with high resolution ambient Kelvin Probe Force Microscopy (KPFM) with dual-lock-in setup. NanoAuger was performed in planar and cross-sectional modes on CZTS,Se surfaces before and after top surface oxide removal by NH_4OH clean. Elemental maps before and after NH_4OH clean show Sn-/O-rich and Cu-poor grain boundaries suggesting that grain boundaries are terminated by tin-oxide (SnOx). Secondary phases such as SnSe and ZnSe were observed in the cross-sectional maps. Kelvin probe force microscopy (KPFM) on the cleaned surfaces showed that SnOx-terminated grain boundaries have 80-200 mV larger work function than grains, resulting in upward band bending between grains and grain boundaries. The upward band bending accompanied by the large valence band offset between the SnOx and CZTS,Se lead to relatively large energy barriers for both electrons and holes to travel into the grain boundaries and recombine. Comparison with the elemental maps for CIGSe (with device efficiencies as high as 18%) revealed the absence of the grain boundary oxide passivation.

9:40am **EN+AS+EM+NS+SE+SS+TF-MoM5 Spin Coating Thin Film CZTS for Efficient, Low-Cost Solar Cells on Flexible Glass Substrates**, *D. Kava, J. Galindo, C.O. Sana, S. Shahriar,* ***Deidra Hodges***, University of Texas at El Paso

Photovoltaic's contribution to energy production continues to grow as costs continue to decrease. As silicon cells approach their limits, other materials are emerging. The development of Cu_2ZnSnS_4 (CZTS) thin film solar cells using non-vacuum liquid-based spin coating techniques have been previously investigated. The focus of this paper is the optimization of p-type CZTS thin film solar cells onto flexible substrates. Flexible solar panel costs are higher than their traditional counterparts. CZTS currently reports only a 3.2% efficiency on flexible glass, while the record for CZTS on non-flexible substrates is 12.6%. The cells are created using a single solution ink sol–gel method. All metals are dissolved in a single step prior to deposition onto substrates (nickel foil and corning willow glass) as a thin film. Corning Willow glass is a new material introduced recently to the market, while nickel is a inexpensive flexible reflective foil. The Corning Willow glass is coated with a molybdenum layer as a reflective back contact layer. By using a single step and a solution deposition method, lower production cost are achievable. For thin film deposition, we used a non-vacuum spin coater (WS650 spin processor, Laurell Technologies) with an optimized spin coat programming. Annealing took place under vacuum in a RTP furnace while time, temperature and ramp functions were varied. The other layers of the device consists of cadmium sulfide n-type window layer and a zinc oxide doped with aluminum transparent top contact layer. Characterization and analysis of the thin films were performed using Raman spectroscopy, scanning election microscope (Zeiss NEON 40), X-ray diffraction (Philipps X'Pert), proflimeter (Veeco Dektak 150), UV-Vis-NIR Spectrophotometer (Carry 5000), Hall Effect measurement system (HMS3000) and 4 point probe (Lucas Labs) measurements. Results show CZTS thin film solar cells on flexible glass is obtainable.

10:00am **EN+AS+EM+NS+SE+SS+TF-MoM6 Band Gap Profile of Cu(In,Ga)(Se,S) 2 Thin Films via High-Resolution Reflection Electron Energy Loss Spectroscopy**, ***Sung Heo***, *H.I. Lee, J.B. Park, G.S. Park,* Samsung Advanced Institute of Technology, Republic of Korea, *D.H. Lee, J.G. Nam,* Samsung, Republic of Korea, *H.J. Kang,* Chungbuk National University, Republic of Korea, *B.D. Choi*, Sungkyunkwan University, Republic of Korea

$Cu(In,Ga)Se_2$ (CIGS)-based solar cells was investigated with an aim of enhancing cell performance because these cells provided high conversion efficiency at relatively low cost. The efficiency of CIGS cells has recently approached 19.7% at small sizes. In general, $Cu(In_{1-x},Ga_x)(Se_{1-y}S_y)_2$(CIGSS) composition profiles are double-graded, and they can improve the open-circuit voltage (V_{OC}) and the efficiency of solar cells because band gaps increase toward both the surface (i.e., with the increase of sulfur) and the bottom (i.e., with the increase of gallium). It is important to accurately measure the band gap at the top and the bottom of the CIGSS cell. Nevertheless, the band gap profile measurement of the CIGSS as a function of depth is challenging.

In this study, we obtained the depth profile of the CIGSS cell using the quantitative Auger Electron Spectroscopy method, for which the relative sensitivity factor was corrected using the inductively coupled plasma-atomic emission spectrometry (ICP-AES) method. We also measured the band gap directly using high-resolution reflection electron energy loss spectroscopy (HR-REELS) with a monochromatic electron gun, which has low electron energy at 300 eV.

For the direct measurement of a band gap profile, HR-REELS spectra were obtained as a function of depth during Ar ion sputtering at 3.0 kV. The band gap profile shows a double-graded band gap as a function of depth. The band gap values are 1.32 eV at the surface (E_{g1}), 1.08 eV at the depth between 0.3 and 0.7μm ($E_{g\ min.position}$), and 1.50 eV at the depth of about 2.2 μm (E_{g2}), respectively. Our findings suggest a new analytical method which directly determines the band gap profile as function of depth.

10:40am **EN+AS+EM+NS+SE+SS+TF-MoM8 Spatial Atmospheric ALD of Zinc Oxysulfide Buffer Layers for CIGS Solar Cells**, *C. Frijters, P.J. Bolt, P. Poodt,* ***Andrea Illiberi***, Solliance/TNO, Netherlands

Copper Indium Gallium di-Selenide (CIGS) solar cells are a promising approach in photovoltaic technology, having low production costs, high conversion efficiencies (> 20 %), as well as the possibility to manufacture them on flexible substrates. State-of-the-art in CIGS solar cells manufacturing is to use a stack of CdS, intrinsic ZnO (*i*-ZnO) and an Al-doped ZnO TCO on top of the CIGS film. Replacement of CdS by a non-toxic Cd-free layer with wider band gap (> 2.4 eV) would *a)* decrease the production cost by avoiding the expensive treatment of toxic wastes and *b)* increase the overall cell efficiency by enhancing the quantum efficiency in the blue range. Moreover, the use of a "soft" and highly conformal deposition technique is preferred to improve the electrical properties of the buffer layer/CIGS interface.

In this paper we present spatial atmospheric atomic layer deposition of a Zn(O,S) buffer layer as CdS replacement for CIGS solar cells. Spatial ALD is emerging as an industrially scalable deposition technique at atmospheric pressure which combines the advantages of temporal ALD, i.e. excellent control of film composition and uniformity on large area substrates, with high growth rates (up to nm/s). Films are grown by sequentially exposing the substrate to oxygen and sulfur precursors (H_2O, H_2S) and the zinc metal precursor (i.e., DEZn). By controlling the kinetics of surface reactions between evaporated precursors and reactive sites at the film surface, the composition of Zn(O,S) can be precisely tuned. The incorporation of S into ZnO results in a bowing of the band gap in the range from 3.3 eV (ZnO) to 2.7 (S/O+S ~ 0.5) and 3.4 eV (ZnS), as measured by spectrophotometry. The morphology of the $Zn(O_{x-1},S_x)$ films varies from polycrystalline (for $0<x<30$ and $70<x<100$) to amorphous ($30<x<70$), as measured by X-ray diffraction. CIGS solar cells with a Spatial ALD Zn(O,S) buffer layer show an increased spectral response around 400 nm compared to solar cells with a CdS buffer layer. The solar cells with the Zn(O,S) buffer layer had an efficiency of 15.9 %, compared to 15.5 % for the reference solar cells with a CdS buffer layer.

11:00am **EN+AS+EM+NS+SE+SS+TF-MoM9 Deep Level Electron Traps in Epitaxial $CuInSe_2$ Probed using Photo-Modulated X-ray Photoelectron Spectroscopy**, ***Nicole Johnson,*** University of Illinois at Urbana-Champaign, *P. Aydogan,* Bilkent University, Turkey, *A. Rockett,* University of Illinois at Urbana-Champaign, *S. Suzer*, Bilkent University, Turkey

Performance in a variety of electronic devices is largely controalled by minority carrier charge capture on point defects. To date there is no experimental method to directly identify these point defects in a chemically specific fashion. Photo-modulated X-ray Photoelectron Spectroscopy (XPS) utilizes the chemical and charge sensitivity of XPS to identify changes in peak shape due to changing atomic charge state from capture of light-generated minority carriers. Epitaxial thin films of $CuInSe_2$ (CIS) were chosen as a case study for this technique because their defect chemistry is still relatively unknown as compared to traditional solar cell materials. The 500-1000nm thick films were grown by a hybrid sputtering and evaporation technique on GaAs(001) substrates at600-700°C. Aligned surface morphology features matching the substrate geometry in scanning electron microscopy (SEM) images indicate epitaxial growth, which was confirmed by x-ray diffraction (XRD).A layer of CdS was deposited on the CIS via chemical bath deposition to protect the CIS surface from oxidation in storage and to duplicate the heterojunction used in solar cells. Prior to loading in the XPS, the CdS was etched off to expose a Cd doped CIS surface for analysis. The photo-modulated XPS used monochromatic AlKα x-rays with a 532 nm laser as the illumination source. Under illumination, each film constituent was observed to exhibit unique binding energy shifts.

Based on their peak shifts relative to the surface photovoltage profile, Cd and In were found to be right at the surface while Cu and Se were deeper into the film, consistent with a Cd-doped, In-rich surface. The technique is therefore shown to provide a chemically-sensitive depth profile non-destructively that can be obtained even on a relatively rough sample. Additionally, shape changes in the Se 3d doublet spectra indicate electron capture in a deep trap state that is likely due to cation vacancies. Measurements at varying temperatures indicate air-induced surface recombination states are passivated by annealing at 80C, allowing the surface photovoltage to persist. At 230C, an irreversible change happens in the surface properties such that the surface photovoltage gets much smaller and reverses sign. This work was supported by a joint NSF-TUBITAK collaborative research project (NSF Grant No: 1312539 TUBITAK Grant No: 212M051).

11:20am **EN+AS+EM+NS+SE+SS+TF-MoM10 The Role of ZnTe Buffer Layers on the Performance and Stability of CdTe Solar Cells**, ***Jiaojiao Li***, Colorado School of Mines, *A. Abbas,* Loughborough University, UK, *D.M. Meysing, J.D. Beach, D.R. Diercks,* Colorado School of Mines, *M.O. Reese, T.M. Barnes,* National Renewable Energy Laboratory, *C.A. Wolden,* Colorado School of Mines, *J.M. Walls*, Loughborough University, UK

The use of ZnTe buffer layers at the back contact of CdTe solar cells has been credited with contributing to recent improvements in both record cell efficiency and module stability. To better understand the underlying reasons high resolution transmission microscopy (HR-TEM) and atom probe tomography (APT) were used to study the evolution of the back contact region before and after rapid thermal activation of this layer. During activation the 150 nm ZnTe layer, initially nanocrystalline and homogenous, transforms into a bilayer structure consisting of an amorphous region in contact with CdTe characterized by significant Cd-Zn interdiffusion, and a crystalline layer that shows evidence of grain growth and twin formation. This graded layer may passivate interface defects and account fo the improved open circuit voltage and fill factor that accompanies the RTP activation step. Copper, co-evaporated uniformly within ZnTe, is found to segregate dramatically after rapid thermal activation, either collecting near the ZnTe|Au interface or forming Cu_xTe clusters in CdTe at defects or grain boundaries near the interface. Further examination of the Cu_xTe clusters revealed that they are encased in a thin layer of Zn, and it is postulated that this structure may limit the extent of diffusion into CdTe and play an important role in device stability.

11:40am **EN+AS+EM+NS+SE+SS+TF-MoM11 The Performance and Durability of Broadband Anti-Reflection Coatings for Thin Film CdTe Solar Cells**, *G. Womack, P.M. Kaminski,* ***John Walls***, Loughborough University, UK

Light reflection from the glass surface of a photovoltaic (PV) module is a significant source of energy loss for crystalline silicon and all types of thin film PV devices. The reflection at the glass and air interface accounts for ~4% of the total energy. Single layer anti-reflection coatings using magnesium fluoride or porous silica with sufficiently low refractive index have been reported but these are only effective over a narrow range of wavelengths. In this paper we report on the design, deposition and testing of multilayer broadband anti-reflection coatings that reduce the weighted average reflection over the wavelength range used by thin film CdTe devices to ~1.22% resulting in a useful 3.6% increase in photocurrent. In this study we have used multilayer stacks consisting of silica and zirconia layers deposited using a reactive magnetron sputtering process. Details of the stack design, sputtering process parameters and the optical and micro-structural properties of the layers are provided.

Thin film CdTe devices pose a special problem because the anti-reflection coating is applied to one side of the glass while device layers are deposited directly on to the opposite glass surface in the superstrate configuration In thin film CdTe production, the glass is exposed to high temperature processes during the absorber deposition and during the cadmium chloride activation treatment. If glass pre-coated with a broadband anti-reflection coating is to be used then the coating must withstand temperatures of up to ~550°C. Surprisingly, our studies have shown that multilayer silica/zirconia anti-reflection coatings on soda lime glass remain unaffected by temperatures up to 600 ^{o}C at which point mild crazing is observed. This is an important observation since it means that low cost glass which is pre-processed with a broadband anti-reflection coating by glass manufacturers is potentially useable in thin film CdTe module production

2D Materials Focus Topic
Room: 212C - Session 2D+EM+MC+MS+NS-MoA

2D Materials: Devices and Applications
Moderator: Joshua Goldberger, The Ohio State University, Arend van der Zande, University of Illinois at Urbana Champaign

2:20pm **2D+EM+MC+MS+NS-MoA1 Designer Materials from the Assembly of 2D Layered Heterostructures**, ***Cory Dean***, Columbia University **INVITED**

The capability to assemble two-dimensional (2D) materials into layered heterogeneous structures presents an exciting new opportunity in materials design. For example, encapsulating graphene with hexagonal BN yields enhanced transport properties with reduced environmental sensitivity, and allows for complex band structure engineering. This has enabled graphene to be exploited as a model experimental platform to study a wide range of fundamental physics arising both from conventional single-particle considerations, as well as more exotic emergent behaviour in the strongly interacting regime. Graphene however represents just one of a larger subset of layered materials, which are now receiving growing attention due to their diverse array of intrinsic properties. The opportunity to "mix and match" these disparate crystals to realize fundamentally new hybrid material properties provides an almost unbounded new direction as we look for quantum materials beyond graphene. In this talk I will outline some of the fundamental questions, and technical challenges facing these efforts and highlight some of our recent innovations in this direction. Implications for the development of new device geometries and scientific pursuits will be discussed.

3:00pm **2D+EM+MC+MS+NS-MoA3 Structural Semiconducting-to-Metallic Phase Transition in Monolayer Transition Metal Dichalcogenides Induced by Electrostatic Gating**, ***Yao Li***, *K.-A. Duerloo, E.J. Reed*, Stanford University

Dynamic electrical control of conductivity in two-dimensional (2D) materials is one of the most promising schemes for realizing energy-efficient electronic devices. Monolayer transition metal dichalcogenides (TMDs) are 2D materials that can exist in multiple crystal structures, each of different electrical conductivity. Using density functional approaches, we discover that a structural semiconducting-to-metallic phase transition in some monolayer TMDs can be driven by electrical stimuli, including change of charge density and bias voltage. We find that a bias voltage approximately 0.5~1 V can trigger the phase transition in $MoTe_2$, while a larger voltage is required for the transition in other monolayer TMDs. The threshold bias voltage is strongly influenced by the substrate on which the monolayer is placed. Carefully choosing the substrate could greatly reduce the threshold bias voltage for the phase transition, and therefore consume much less energy, suggesting potential applications in electronics with very high energy efficiency. The dynamic control of this semiconducting-to-metallic phase transition can be achieved utilizing standard electronic devices like the electrostatic gating employed in a field-effect transistor. We have also calculated the phase boundary of a reported metallic-to-metallic phase transition in $TaSe_2$ to compare with earlier STM experimental results and reasonable agreement is observed. Our findings open up the possibility of manufacturing ultrathin flexible two-dimensional phase change electronic devices with potential for higher energy efficiency than conventional electronic devices.

3:20pm **2D+EM+MC+MS+NS-MoA4 Use of Voltage-Contrast and Dynamical XPS for Characterization of Graphene-Based Devices in Operation**, ***Sefik Suzer***, Bilkent University, Turkey

A noncontact chemical and electrical technique of XPS is performed to investigate a number of deviecs under operation. The main objective of the technique is to trace chemical and location specified surface potential variations as shifts of the XPS peak positions under operating conditions. To implement the measurements we apply D.C. (Voltage-Contrast) and/or A.C. (Dynamical) voltage biases externally to the sample, while recording XPS data. Accordingly, we extract chemically resolved static and/or time-resolved information related with certain electrical properties of materials and devices made from them. Details of the technique and applications to a number of graphene-based devices, configured in a transistor geometry with and without gating, will be presented.

4:00pm **2D+EM+MC+MS+NS-MoA6 Avalanche Photodiodes based on MoS_2/Si Heterojunctions**, ***Oriol López Sánchez***, Ecole Polytechnique Fédérale de Lausanne (EPFL), Switzerland, *G. Fiori, G. Iannaccone*, Università di Pisa, Italy, *D. Dumenco*, Ecole Polytechnique Fédérale de Lausanne (EPFL), Switzerland, *E. Charbon*, Delft University of Technology, Netherlands

Avalanche photodiodes (APDs) are the semiconducting analogue of photomultiplier tubes offering very high internal current gain and fast response. APDs are interesting for a wide range of applications in communications, laser ranging, biological imaging, and medical imaging where they offer speed and sensitivity superior to those of classical p-n junction-based photodetectors. The APD principle of operation is based on photocurrent multiplication through impact ionization in reverse-biased p-n junctions. Here, we demonstrate APDs based on vertically stacked monolayer MoS_2 and p-Si, forming an abrupt p-n heterojunction. With this device, we demonstrate carrier multiplication exceeding 1000 at 10 V reverse bias . Our devices show little degradation of SNR at high gains. These heterostructures allow the realization of simple and inexpensive high-performance and low-noise photon counters based on transition metal dichalcogenides.

4:20pm **2D+EM+MC+MS+NS-MoA7 From Black Phosphrus to Phosphorene**, ***Peide Ye***, Purdue University **INVITED**

Phosphorus is one of the most abundant elements preserved in earth, constructing with a fraction of ~0.1% of the earth crust. In general, phosphorus has several allotropes. The two most commonly seen allotropes, white and red phosphorus, are widely used in explosives and safety matches. In addition, black phosphorus, though rarely mentioned, is a layered semiconductor and has great potentials in optical and electronic applications. Remarkably, this layered material can be reduced to one single atomic layer in the vertical direction owing to the van der Waals structure, known as phosphorene, where the physical properties can be tremendously different from its bulk counterpart. In this talk, we trace back to the 100 years research history on black phosphorus from the synthesis to material properties, and extend the topic from black phosphorus to phosphorene. The physical and transport properties are highlighted, aiming at further applications in electronic and optoelectronics devices.

5:00pm **2D+EM+MC+MS+NS-MoA9 Ambient Oxidation and Alumina Passivation of Exfoliated Black Phosphorus Transistors**, ***Joshua Wood***, *S. Wells, D. Jariwala, K.-S. Chen, X. Liu, V. Sangwan, E. Cho, L. Lauhon, T.J. Marks, M.C. Hersam*, Northwestern University

Exfoliated black phosphorus (BP) is an elemental, two-dimensional (2D) nanomaterial with high carrier mobility (~100 $cm^2V^{-1}s^{-1}$), a layer-dependent band gap (~0.3 to 2.0 eV), and in-plane anisotropy. Further, 2D BP is air sensitive, culminating in undesirable surface reactions that degrade device performance. We find that unencapsulated, exfoliated BP flakes form oxidized derivatives following ambient exposure, as ascertained by X-ray photoelectron spectroscopy, atomic force microscopy, Fourier transform infrared spectroscopy, transmission electron microscopy, and electrostatic force microscopy measurements. BP ambient oxidation is driven by oxygen-saturated H_2O, as we observe two-fold faster degradation for BP on hydrophobic substrates versus hydrophilic ones. After 48 hours of ambient oxidation, unencapsulated BP field-effect transistors (FETs) decline in mobility and current on/off ratio by factors of over 1000. In contrast, alumina (i.e., AlO_x) passivated BP flakes and FETs are robust and unoxidized for over seven months in ambient conditions. Alumina-passivated BP FETs possess mobilities of ~100 $cm^2V^{-1}s^{-1}$, on/off ratios of 1000, and ambipolar transport, even following extensive ambient exposure [1]. This understanding of BP ambient oxidation—and how to prevent it—is also impacting ongoing work in solution-phase BP separation [2], BP chemical modification, and high-performance BP optoelectronic applications.

[1] J. D. Wood *et al.*, *Nano Lett.* **14**, 6964 (2014); [2] J. Kang *et al.*, *ACS Nano* **9**, 3596 (2015).

5:20pm **2D+EM+MC+MS+NS-MoA10 Electro-Acoustic Characterization of Transition Metal Dichalcogenide Films on $LiNbO_3$**, ***Edwin Preciado***, UC Riverside, *F.J.R. Schülein, A. Wixforth*, Universität Augsburg, Germany, *A. Nguyen, D. Barroso, M. Isarraraz, G. von Son, I. Lu, L. Bartels*, UC Riverside, *H. Krenner*, Universität Augsburg, Germany

We demonstrate mm-scale CVD growth of single layer molybdenum disulfide directly onto piezoelectric lithium niobate and present the fabrication of a hybrid FET – SAW (field effect transistor – surface acoustic

wave) device. Our experiments reveal close agreement between transport measurements utilizing conventional contacts and SAW spectroscopy. This approach will ultimately provide for a contact free transport characterization of 2D TMD films, avoiding concerns about the role of charge transfer at contacts as an artifact of such measurements.

Electronic Materials and Processing
Room: 211A - Session EM+AS+SS-MoA

MIM Diodes, Functional Oxides, and TFTs
Moderator: Pat Brady, RedWave Energy, Inc., John Conley, Oregon State University

2:20pm **EM+AS+SS-MoA1 Engineered Tunnel-Barrier Terahertz Rectifiers for Optical Nantennas**, ***Ivona Mitrovic***, *N. Sedghi, A.D. Weerakkody, J.F. Ralph, S. Hall, J.S. Wrench, P.R. Chalker,* University of Liverpool, UK, *Z. Luo, S. Beeby*, University of Southampton, UK

Thin film metal-insulator-metal rectifying devices using double, triple or quadruple insulator layers are currently the focus of attention for the development of next-generation optical nantennas for infrared energy harvesting. The interest is driven by their distinctive attributes, such as nanoscale footprint, room temperature operation, zero bias voltage requirement, and ease of integration with Complementary Metal Oxide Semiconductor technology. Highly asymmetric and nonlinear current-voltage (IV) behaviour at low applied voltages is critical for this application. In this paper, we present comprehensive experimental and theoretical work on tunnel-barrier rectifiers comprising double (Ta_2O_5/Al_2O_3 and Nb_2O_5/Al_2O_3) and triple ($Ta_2O_5/Nb_2O_5/Al_2O_3$) insulator configurations engineered to enhance low voltage nonlinearity. There are two mechanisms that allow metal-insulator-insulator-metal (MIIM) rectifiers to have a high nonlinearity while keeping the resistance low: (i) resonant tunnelling, and (ii) step tunnelling. This paper focuses on the former approach. A modified multi-layer Tsu-Esaki method has been used for IV calculations from the transmission coefficient by the transmission matrix method. The theoretical work indicates that the onset of resonant tunneling in MIIM and MIIIM rectifiers can be adjusted to be close to zero volts by appropriate choice of work function difference of the metal contacts, the thickness of insulator layers, and the depth of the quantum well. The double and triple insulator rectifiers were fabricated using atomic layer deposition (ALD) and rf magnetron sputtering, while different metal contacts including Al, Ta, W, Nb, Cr and Ag were defined by photolithography or shadow mask and deposited by e-beam and thermal evaporation. The thickness, band gap, surface roughness, band offsets and work functions have been extracted from variable angle spectroscopic ellipsometry, atomic force microscopy, x-ray and inverse photoelectron spectroscopy on fabricated devices to ascertain the quality of the interfaces and to measure barriers. The key rectifier properties, asymmetry, nonlinearity and responsivity have been assessed from current voltage measurements performed in the range 293-370 K. A superior low voltage asymmetry (18 at 0.35 V) and responsivity (9 A/W at 0.2 V) has been observed for fabricated bilayer Ta_2O_5/Al_2O_3 and Nb_2O_5/Al_2O_3 MIIM devices respectively, in advance of state-of-the-art experimental values. The results demonstrate ALD and rf sputtered tunnel-barrier rectifiers which enhance low voltage nonlinearity and have the potential to be employed in optical nantennas for infrared energy harvesting.

2:40pm **EM+AS+SS-MoA2 MIM Diodes for RF Energy Harvesting**, *A.A. Khan, A. Syed, F. Ghaffar,* ***Atif Shamim***, King Abdullah University of Science and Technology

Metal Insulator Metal (MIM) diodes that work on fast mechanism of tunneling have been used in a number of very high frequency applications such as (Infra Red) IR detectors and optical Rectennas for energy harvesting. Their ability to operate under zero bias condition as well as the possibility of realizing them through additive techniques makes them attractive for (Radio Frequency) RF applications. However, two major issues namely, high surface roughness at the metal-insulator junction which effects the reliability of the diode, and very high resistance (typically in Mega Ohms) which complicates its matching with RF antenna have prevented its wide spread use in RF rectennas.

In this work, various metal deposition methods such as sputtering and electron beam evaporation are compared in pursuit of achieving low surface roughness. Amorphous metal alloy has also been investigated in terms of its low surface roughness. Zinc oxide has been studied for its suitability as a thin dielectric layer for MIM diodes. Finally, comprehensive RF characterization of MIM diodes has been performed in two ways: 1) by standard S-parameter methods, and 2) by investigating their rectification ability under zero bias operation.

It is concluded from the Atomic Force Microscopy (AFM) imaging that surface roughness as low as sub 1 nm can be achieved reliably from crystalline metals such as copper and platinum. This value is comparable to surface roughness achieved from amorphous alloys, which are non-crystalline structures and have orders of magnitude lower conductivities. Relatively lower resistances of the order of 1 Kilo Ohm with a sensitivity of 1.5 V^{-1} have been obtained through DC testing of devices with MIM diode structure of platinum/zinc oxide/ titanium. Finally, RF characterization reveals that input impedances in the range of 300 Ω to 25 Ω can be achieved in the low GHz frequencies (from 0.5-10 GHz). From the rectification measurements at zero bias, a DC voltage of 4.7 mV has been obtained from an incoming RF signal of 0.4 W at 2.45 GHz, which indicates the suitability of these diodes for RF rectenna devices without providing any bias. These preliminary results indicate that with further optimization, MIM diodes are attractive candidates for RF energy harvesting applications.

3:00pm **EM+AS+SS-MoA3 Diode Structure Based on Carbon Materials for Ultra high Frequency Driving**, ***JaeEun Jang***, Daegu Gyeongbuk Institute of Science and Technology (DGIST), Republic of Korea

If the antenna can be designed to absorb wavelengths in the range of a few hundred THz with multi-antenna array design, it results in high conversion efficiency due to power production from various light sources between ultraviolet (UV) and infrared (IR) radiation that is often thought of as heat and exists beyond the visible range for humans. One of the problems in this idea, however, is the nature of visible or IR light to oscillate at ultra-high frequencies. Therefore, a rectifier working at such an ultra-high frequency should be developed with a highly efficient coupling between antenna and light. Because Schottky diode is limited to frequencies less than ~ THz level, nanometer size MIM diode structure has been suggested as alternative design. Two different metals have used normally to make an asymmetric characteristic of current-voltage. However the work function difference between the metals cannot produce a high asymmetry, which causes a poor rectifier performance, even though the structure can be driven in THz range. To solve this issue, we used a structural asymmetric MIM design. The planar asymmetric design using various metals or grapheme showed better asymmetric I-V characteristics than that of simple MIM structure. In addition, for the vertical aligned design, single multi-wall carbon nanotube was formed as one electrode to get high tunneling current caused by the structural effect of sharp tip. The structural asymmetry can make a different field density states to the metals, which induces a high rectify characteristics. The contrast ratio between the forward and the reverse bias is $\sim 10^4$ level. The estimated cut-off frequency is about 4.74THz. The electrical characteristics are stable up to 423K.

3:20pm **EM+AS+SS-MoA4 Optical Rectenna Arrays using Vertically Aligned Carbon Nanotubes**, ***Baratunde Cola***, Georgia Institute of Technology

The response of a multiwall carbon nanotube to visible light has been reported to be consistent with conventional radio antenna theory. Researchers have proposed that this result might be exploited to realize an optical rectification device – that is, a device that converts free-propagating electromagnetic waves at optical frequencies to localized d.c. electricity. However, an experimental demonstration of this concept requires that the multiwall carbon nanotube antenna be coupled to a diode that operates on the order of 1 petahertz (switching speed on the order of a femtosecond). Ultralow capacitance, on the order of a few attofarads, could allow a diode to operate at these frequencies; and the development of metal-insulator-metal tunnel junctions with nanoscale dimensions has emerged as a potential path to diodes with ultralow capacitance, but these structures remain extremely difficult to fabricate and couple to a nanoscale antenna reliably. Here we demonstrate optical rectification by engineering metal-insulator-metal tunnel diodes at the tips of multiwall carbon nanotubes, which act as the antenna and metallic electron emitter in the diode. This performance is achieved using diode areas based on the diameter of a single carbon nanotube (about 10 nanometers), geometric field enhancement at the carbon nanotube tips, and a low work function semi-transparent top metal contact. Using vertically-aligned arrays of the diodes, we measure d.c. open-circuit voltage and short-circuit current at visible and infrared electromagnetic frequencies that is due to a rectification process, and quantify minor contributions from thermal effects. Our devices show evidence of photon-assisted tunneling, and exhibit zero-bias diode responsivity on the order of 0.1 amps per Watt and zero-bias differential resistance as low as 100 ohms-centimeter squared under illumination. Additionally, power rectification is observed under simulated solar illumination. Numerous

current-voltage scans on different devices, and between 5-77 degrees Celsius, show no detectable change in diode performance, indicating a potential for robust operation.

3:40pm **EM+AS+SS-MoA5 World Record Tunable Microwave Dielectrics**, *C.H. Lee,* Cornell University, *N.D. Orloff,* National Institute of Standards and Technology (NIST), *T. Birol, Y. Zhu, Y. Nie,* Cornell University, *V. Goian,* Institute of Physics ASCR, *R. Haislmaier,* Pennsylvania State University, *J.A. Mundy,* Cornell University, *J. Junquera,* Universidad de Cantabria, *P. Ghosez,* Université de Liège, *R. Uecker,* Leibniz Institute for Crystal Growth, *V. Gopalan,* Pennsylvania State University, *S. Kamba,* Institute of Physics ASCR, *L.F. Kourkoutis, K.M. Shen, D.A. Muller,* Cornell University, *I. Takeuchi,* University of Maryland, College Park, *J.C. Booth,* National Institute of Standards and Technology (NIST), *C.J. Fennie,* ***Darrell Schlom***, Cornell University **INVITED**

The miniaturization and integration of frequency-agile microwave circuits—relevant to electronically tunable filters, antennas, resonators, phase shifters and more—with microelectronics offers tantalizing device possibilities, yet requires thin films whose dielectric constant at GHz frequencies can be tuned by applying a quasi-static electric field. Appropriate systems, e.g., $Ba_xSr_{1-x}TiO_3$, have a paraelectric-to-ferroelectric transition just below ambient temperature, providing high tunability. Unfortunately such films suffer significant losses arising from defects. Recognizing that progress is stymied by dielectric loss, we start with a system with exceptionally low loss—$Sr_{n+1}Ti_nO_{3n+1}$ phases—where $(SrO)_2$ crystallographic shear planes provide an alternative to point defect formation for accommodating non-stoichiometry. Guided by theoretical predictions, we biaxially strain a $Sr_{n+1}Ti_nO_{3n+1}$ phase with $n = 6$ to introduce a ferroelectric instability and create a new type of tunable microwave dielectric. This tunable dielectric exhibits a world record figure of merit at room temperature and frequencies up to 125 GHz. Our studies also reveal details about the microscopic growth mechanism of these phases, which are relevant to preparing atomically precise oxide interfaces to these and other Ruddlesden-Popper phases.

4:20pm **EM+AS+SS-MoA7 Bandgap Engineering and Application of SiZnSnO Amorphous Oxide Semiconductor**, ***Sang-Yeol Lee***, Cheongju University, Republic of Korea **INVITED**

The band gap of the amorphous SiZnSnO (SZTO) semiconductor has been controlled by bandgap engineering using Si ratio. The addition of small amount of Si in SZTO channel layer can change the position of Fermi level in band gap. By investigating the ultraviolet photoelectron spectroscopy (UPS) characteristics, it is verified that Si atoms can modify the Fermi energy level of SZTO thin films. Carrier generation originated from the oxygen vacancy could modify the Fermi level in the band gap of oxide thin films since Si could be an oxygen vacancy suppressor. This is also related with the origin of defect state which was observed to be involved with the creation of oxygen vacancies. Since it is not so easy to derive directly the change of the Fermi energy level in the energy band gap of amorphous oxide semiconductor, no report of the relation between the Fermi energy level in the energy band gap of oxide semiconductor and the device stability of oxide thin film transistors has been reported. We derive directly band gap and Fermi energy level by using the ultraviolet photoelectron spectroscopy (UPS) characteristics, Kelvin probe (KP) and electron energy loss spectroscopy (EELS). The instability mechanism of amorphous oxide thin film transistors based on the band parameter of oxide semiconductor will be discussed and applied to display applications.

5:00pm **EM+AS+SS-MoA9 Self-aligned Vertical ZnO-based Circuits by Spatial ALD**, ***Shelby Nelson***, *C.R. Ellinger, L.W. Tutt*, Eastman Kodak Company

Metal oxide thin-film transistors (TFTs) are becoming the mainstream for display backplanes. These TFTs are fabricated with traditional photolithographic techniques, typically on rigid substrates. In our lab, we explore approaches that are more "print-compatible", with broad alignment tolerance and no small-gap mask features. We deposit zinc oxide (ZnO) semiconductors, aluminum oxide (Al_2O_3) dielectrics, and aluminum-doped zinc oxide conductors by the fast, atmospheric pressure, large-area-compatible, spatial atomic layer deposition (SALD) process. In addition to depositing good-quality thin-film transistor layers at temperatures at and below 200 °C, this process can work with a wide variety of rough and deformable substrates.

Here we describe vertical TFT and circuit architectures that unite process simplicity with high performance. The liberal design rules result from vertical transistors with self-aligned source and drain contacts that define the sub-micron channel length. Using 10-micron design rules for both the minimum line/space dimensions and for alignment tolerances, we have fabricated 9-stage ring oscillators with greater than 1 MHz oscillation frequency, at supply voltage below 6 V. Starting with a gate layer with a re-entrant profile on the edge, these devices use spatial ALD to conformally coat the Al_2O_3 gate dielectric and ZnO semiconductor, and a line-of-sight deposition process such as evaporation for the aluminum electrodes. Individual device characteristics as well as circuit performance will be discussed.

5:20pm **EM+AS+SS-MoA10 Geometrically Asymmetric Tunneling Nanostructures by Atomic Layer Deposition**, ***Jie Qi***, *X. Jiang, B.G. Willis*, University of Connecticut

Geometrically asymmetric tunneling nanostructures are of interest to make ultra-high frequency diodes for applications in detection and solar energy harvesting. Atomic layer deposition (ALD) is one of the most promising techniques for fabrication of tunneling nanostructures. In previous work, it has been demonstrated that individual metal-vacuum-metal (MVM) tunnel junctions with a gap distance of 1-2 nm can be fabricated by selective-area ALD of Cu onto Pd templates. However, optimizing nonlinearity and scaling up to large arrays of tunneling devices both introduce new challenges that include achieving precise control of nucleation and good quality conformal growth on sharply defined asymmetric nanostructures.

In this study, the fabrication of large arrays of MVM tunnel junctions is investigated using selective-area ALD. Nano-patterned Pd nanostructures with sharp asymmetric features are prepared as seed layers for planar, geometrically-asymmetric junctions on SiO_2 / silicon substrates by high-resolution electron beam lithography. Selective-area ALD applied to patterned Pd nanostructures allows tuning the size of junctions to nanometer dimensions. Microscopy and chemical analysis are used to evaluate nanostructure morphology, tunnel junction uniformity, and selective area growth characteristics. In-situ electrical measurements are used to measure DC current-voltage curves and nonlinearity. It was found that film nucleation and growth selectivity can be greatly affected by different pre-deposition sample treatments. UV/Ozone (UVO) cleaning and hydrogen annealing before ALD both enhance the nucleation of Cu thin films on Pd seed layers. In addition, UVO treatment promotes selective growth on Pd vs. SiO_2 areas while boiling samples in water to hydroxylate SiO_2 surface area contributes to a loss of selectivity. In-situ measured electrical data during ALD growth demonstrate a gradual convergence to tunneling with sub-nm control provided by the ALD method. However, control of tunneling non-linearity and geometric asymmetry is complicated by an incomplete understanding of the growth mechanism and the morphology evolution of nanostructures. There is a compromise between conditions that promote good ALD growth and those that maintain geometric asymmetry. We conclude with suggestions to promote growth, maintain sharp asymmetric features, and achieve non-linear tunneling characteristics.

Electronic Materials and Processing
Room: 210E - Session EM+NS+PS-MoA

More Moore! II
Moderator: Christopher Hinkle, University of Texas at Dallas, Andrew C. Kummel, University of California at San Diego

2:20pm **EM+NS+PS-MoA1 Effect of *Ex Situ* and *In Situ* Surface Cleaning on the Quality of Al_2O_3-SiGe(001) Interfaces**, *K. Sardashti,* ***Kai-Ting Hu***, UC San Diego, *S. Madisetti,* College of Nanoscale Science and Engineering, Albany-SUNY, *K. Tang,* Stanford University, *S. Oktyabrsky,* College of Nanoscale Science and Engineering, Albany-SUNY, *P.C. McIntyre,* Stanford University, *S. Siddiqui, B. Sahu,* Globalfoundries, *N. Yoshida, J. Kachian,* Applied Materials Inc., *A.C. Kummel*, UC San Diego

Silicon-Germanium has shown a great promise for future CMOS technology by combining the high hole and electron mobility of Ge with the ability to have both tensile and compressive strain by fabrication of alloys of higher and lower Ge content. In contrast to Si, SiGe native oxide is a combination of SiO_2 and GeO_2, SiGeOx, which has low interface quality and stability in comparison with SiO_2 due to the presence of the GeOx. Therefore, instead of thermal oxide growth, it is necessary to employ atomic layer deposition (ALD) for gate oxide deposition in SiGe MOS devices. The effects of the ex-situ wet chemical clean (such as HF and $(NH_4)_2S$ dip) and in-situ NH_3 plasma clean prior to ALD, were determined on Al_2O_3/SiGe; interface quality quantified by oxide leakage, interfacial trap density, and near-interface trap density. MOS capacitors fabricated by Al_2O_3 ALD at 120°C. Compared to HF clean, both ex-situ $(NH_4)_2S$ clean and in-situ NH_3 plasma resulted in smaller density of interface and smaller leakage current in accumulation. Furthermore, both methods resulted in high surface stability in air; queue times up to an hour could be tolerated.

Angle-resolved X-ray photoelectron spectroscopy (AR-XPS) measurements on SiGe(001) with 0.8nm thick Al_2O_3 showed that $(NH_4)_2S$ clean significantly reduces the amount of GeOx at the in Al_2O_3/SiGe(001) interface, compared to HF clean.

2:40pm **EM+NS+PS-MoA2 Surface Passivation for ALD-Al_2O_3/SiGe MOS Devices**, ***Liangliang Zhang***, Stanford University, *V. Hassan, C. Lo, C. Olsen, M.A. Foad,* Applied Materials Inc., *P.C. McIntyre*, Stanford University

We report a study of passivation of the SiGe surface, a critical challenge for future SiGe MOSFET technology. Epitaxially grown p-type SiGe films on lightly doped Si substrates are investigated. The layered surface structures of native oxide coated, as-received SiGe samples are characterized using soft x-ray synchrotron photoemission electron spectroscopy (PES). It is observed that the surface of as- received SiGe wafers have a mixed SiO_x/GeO_x oxide layer. Angle-resolved PES shows that this layer is SiO_x-rich at the top surface and GeO_x-rich below. Lab source x-ray photoelectron spectroscopy (XPS), hard x-ray PES and x-ray reflectivity (XRR) are used to characterize the interface region between atomic layer deposited (ALD) Al_2O_3 gate dielectrics and SiGe. Prior to ALD, 2% HF(aq) solution is used to remove the surface oxides, and a high quality Al_2O_3 layer on the SiGe substrate is deposited with the help of efficient sites for $Al(CH_3)_3$ (TMA) precursor adsorption produced by H_2O oxidant pre-dosing of the SiGe surface immediately prior to the TMA/H_2O ALD process. It is observed from XPS and PES that there is an increase of the SiO_x peak intensity after Al_2O_3 deposition, while there is little or no detectable Ge core level feature associated with GeO_x. The thermodynamic preference of Si (compared to Ge) atoms bonding to oxygen agrees well with the identity of the layered oxide structures extracted by fitting measured XRR data from the processed samples.

Both Pt, a metal that is a known catalyst for H_2 dissociation, and Al are investigated as gate metals for ALD-Al_2O_3/SiGe MOS capacitors (MOSCAPs) subjected to post metal forming gas (5% H_2/95% N_2) anneal (FGA). The effects of the identity of the gate metal on post-FGA interfacial oxide composition and interface trap response is studied. Capacitance-voltage analysis of Al/Al_2O_3/p-SiGe MOSCAPs detects minimal frequency dispersion in depletion and accumulation. The extracted density of interface traps is peaked near the valence band, with a maximum value of ~ $3x10^{11}$ ($eV^{-1}cm^{-2}$).

3:00pm **EM+NS+PS-MoA3 Harnessing Chemistry to deliver Materials and Process for theNext 10 Years of CMOS Evolution**, ***Robert Clark***, TEL Technology Center, America, LLC **INVITED**

Harnessing Chemistry to Deliver Materials and Processes for the Next 10 Years of CMOS Evolution

Robert Clark

TEL Technology Center, America, LLC

Albany, NY 12203

Robert.clark@us.tel.com

The continued scaling of the Integrated Circuits (ICs) according to Moore's law has led to a doubling of the number of devices per unit area in semiconductor microchips approximately every 2 years since 1962. Over the past decade traditional scaling by simple linear shrinking has effectively ceased as IC makers have adopted new 3-dimensional device structures, complex integration schemes and new processes and materials for an expanding number of applications in order to overcome fundamental physical limits. In order to continue Moore's law in the coming decade this trend will not only continue, but intensify as devices are scaled to a level approaching atomic dimensions. Broadly speaking, two major trends are influencing the development of future IC manufacturing processes: the need to harness the third dimension to extend Moore's law; and the need for "self-something" processes. "Self-something" processes refers to processes or schemes that are directed chemically to attain a desired result and includes processes that are self-limited (e.g. ALD or ALE), self-directed (e.g. directed self-assembly or selective deposition), or self-aligned (e.g. self-aligned contacts) in some way that enables device density scaling. "Self-something" processes are required in order to harness the third dimension and make use of new non-planar device architectures (e.g. FinFETs and DRAM capacitors), device arrays/stacking (e.g. 3D NAND and cross-point memory), and 3D integration (e.g. monolithic 3D, and chip stacking). Highly tailored ALD processes are being investigated to fabricate functional material layers. Interspersed treatments and doping may be used to modify the physical and electrical properties of ALD films further in order to optimize the resulting physical or electrical properties. To improve device contacts, ultra-thin dielectric and metal layers may be deposited inside of high aspect ratio contact structures in order to provide lower contact resistivity. Selective deposition processes can be used to deposit functional materials only where they are needed, thus reducing the patterning burden during IC manufacturing. Depositing dopant layers by ALD for thermal solid source doping can be used to conformally dope 3-D device structures without the damage caused by implantation. Examples of these and similar processes will be described and discussed along with the chemical processes and transformations governing film deposition, composition, structure, and interface control.

3:40pm **EM+NS+PS-MoA5 Materials Selection for Oxide-based Resistive Random Access Memory (RRAM)**, ***John Robertson***, *Y. Guo*, Cambridge University, United Kingdom of Great Britain and Northern Ireland **INVITED**

Resistive random access memory (RRAM) is a main challenger non-volatile memory technology to Flash memory. The favored materials are based on the formation of a conductive filament of oxygen vacancies across a film of a wide gap oxide. However, a wide range of material systems are presently being studied, which use various different switching mechanisms. Materials selection requires us to understand which material properties control each aspect of device performance, such as switching speed, resistance window, retention time and endurance. Here, the energies of various atomic processes in resistive random access memories (RRAM) are calculated for four typical oxides, HfO_2, TiO_2, Ta_2O_5 and Al_2O_3, to define a materials selection process. Oxygen vacancies have the lowest defect formation energy in the O-poor limit, and to dominate the processes. A band diagram defines the operating ranges of Fermi energy and O chemical potential. It is shown how scavenger metals can be used to vary the O chemical potential and thus vary the O vacancy formation energy. The high stability of amorphous phase of Ta_2O_5 is relevant to the high endurance of its RRAM.

4:20pm **EM+NS+PS-MoA7 Lower Temperature Silicon Nitride ALD on $Si_{0.5}Ge_{0.5}$(110) with No Solid By-product Formation**, ***Steven Wolf***, *M. Edmonds, T. Kent,* University of California at San Diego, *D. Alvarez,* RASIRC, *R. Droopad,* Texas State University, *A.C. Kummel*, University of California at San Diego

A silicon nitride passivation layer on semiconductor surfaces can serve several practical uses, such as acting as a diffusion barrier or channel passivation layer prior to dielectric deposition in FinFets or MOSFETs. When employed as a channel passivation layer, further reaction with an oxidant, such as anhydrous peroxide, can leave Si-N-OH termination, which is reactive with all metal ALD precursors thereby providing high nucleation density. Previous studies show stoichiometric ALD Si_3N_4 growth on Si(100) by hydrazine and Si_2Cl_6 at temperatures in excess of 350°C with solid ammonium chloride by-product formation[1]. The first half reaction of N_2H_4 leaves N-H_x surface termination, and the second reaction with Si_2Cl_6 adds silicon to the surface and creates a gaseous HCl by-product. An ammonium chloride by-product is usually caused by wall reactions of unreacted precursors. This study focuses on developing a low temperature silicon nitride ALD process with no unwanted solid by-product formation. STM/STS and XPS are employed to characterize SiN_x film growth on $Si_{0.5}Ge_{0.5}$(110).

A test chamber consisting of a reactor chamber, dosing lines, and a dry pump was created and heated to 125°C for 12 hours to allow for sufficient heating of all stainless steel components. In excess of 100 ALD cycles were ran in the test chamber with no visible evidence of powder formation on any walls, and it was concluded that this lengthy heating process prior to SiN_x ALD is necessary to eliminate the unwanted powder by-product formation. Next, at a substrate temperature of 275°C and wall temperature of 20°C, the silicon nitride ALD procedure was performed on a p-type $Si_{0.5}Ge_{0.5}$(110) surface that underwent an ex-situ wet organic clean followed by a dip into a 2% HF/water solution with a toluene layer on top. The sample was pulled through toluene and loaded into UHV as quickly as possible to minimize native oxide formation. After a 315 MegaLangmuir anhydrous hydrazine dose, XPS shows N-H_x surface termination, and removal of half of the initial carbon contamination. A subsequent 21 MegaLangmuir Si_2Cl_6 dose followed by 17 cycles of 3 MegaLangmuir hydrazine and 3 MegaLangmuir Si_2Cl_6 leads to increased silicon nitride growth as shown by a large increase in XPS Si 2p and N 1s peaks, as well as a decrease in the Ge 3d substrate peak. After the ALD cycling with room temperature walls, a white powder, presumed to be ammonium chloride, was seen in the reactor, but will now be avoided using the 125°C wall temperature.

1. S. Morishita *et. al*., Appl. Surf. Sci., **112**, p:198-204 (1997).

4:40pm **EM+NS+PS-MoA8 Novel Delivery of Unstable Precursors for Atomic Layer Deposition**, ***Daniel Alvarez***, *J. Spiegelman, E. Heinlein, R. Holmes, C. Ramos, S. Webb, K. Johnson*, RASIRC

A considerable amount of effort has gone into the development of novel metal precursors for Atomic Layer Deposition (ALD). This is primarily

driven by the need for new high *K* materials and metals films. Largely ignored has been the need for novel oxidants and sources of nitrogen. This paper focuses on the delivery of anhydrous hydrogen peroxide and anhydrous hydrazine for ALD applications.

Hydrogen Peroxide (H_2O_2) in aqueous form is commonly used in semiconductor manufacturing for cleaning and surface preparation operations. Thirty percent and fifty percent two-component mixtures have been investigated in a few ALD studies with moderate success. Especially noteworthy are Kummel's findings that the use of hydrogen peroxide leads to a 3x increase in nucleation density on Ge versus water. However, H_2O_2 has limited general utility in aqueous form due to the volatility of water. At 30C, Raoult's law predicts a headspace concentration of 294ppm H_2O_2 and 32373ppm for water, where the H_2O/H_2O_2 ratio is over 100. Clearly these are not optimal conditions for hydrogen peroxide ALD. However, in its pure state, hydrogen peroxide is highly unstable and has a propensity to decompose, forming water and oxygen. Our approach entails the use of a membrane delivery system where 99.6% hydrogen peroxide is dissolved in an organic solvent. Hydrogen peroxide permeates the membrane and is delivered to the ALD chamber, while the solvent does not permeate and remains in the liquid state. In this way, concentrations much higher than predicted by Raoult's law for aqueous mixtures are delivered to the process chamber in the absence of water.

Next generation devices have low thermal budgets and high aspect ratio structures that create new challenges for ALD grown nitride films. The use of ammonia is limited due to temperature constraints. Known Plasma methods cannot uniformly coat the side walls of the device structures and create surface damage. Hydrazine (H_2NNH_2) has been proposed as a thermal ALD low temperature nitride source.Hydrazine is highly flammable and its flash point decreases with reduced water content. In an analogous approach, we have developed a new method and formulation for the delivery of anhydrous Hydrazine by the use of an inert organic solvent and membrane delivery system. Precursor vapor pressure is maintained at levels viable for ALD. Moreover, the addition of a high boiling solvent lowers the risk of explosion by raising the solution flash point.

Preliminary ALD data will be presented showing unique properties of these new precursors along with theoretical data on precursor delivery under variable ALD conditions.

5:00pm **EM+NS+PS-MoA9 Passivation and Functionalization of SiGe(001) and (110) for ALD Nucleation in FinFET Structure***, **SangWook Park***, *H. Kim,* University of California at San Diego*, B. Sahu, S. Siddiqui,* GLOBALFOUNDRIES U.S. Inc.*, N. Yoshida, A. Brandt,* Applied Materials, Inc.*, E. Chagarov, A.C. Kummel*, University of California at San Diego

Silicon Germanium (SiGe) is a promising candidate for FinFET channels, sources, and drains due to its high mobility and utility in strain engineering. Since FinFETs are composed of three-dimensional structures utilizing multiple crystalline planes, the cleaning and passivation must provide uniform and clean surfaces in each plane to combine high mobility with low interface trap density (Dit). In this study, passivation and functionalization of SiGe(001) and (110) surfaces are discussed, using scanning tunneling microscopy (STM), scanning tunneling spectroscopy (STS), and x-ray photoelectron spectroscopy (XPS).

The SiGe(001) is dimer terminated while the SiGe(110) is dimer-free leading to differences in surface stoichiometry and order. STM and XPS measurements indicate that clean (001) is mostly terminated with Ge atoms with a uniform and well-ordered structure while (110) is terminated with adatoms of both Si and Ge atoms and lower surface order. STS measurements indicate the clean (001) surface is unpinned while the clean (110) surface is pinned mid gap between the valence and conduction band edge due to adatom dangling bonds. The sputter cleaned SiGe(110) surface was dosed at 300°C with 3,600L dose of atomic H to passivate the dangling bonds of the adatoms. STS measurements demonstrate the atomic H dosed (110) surface is unpinned with a Fermi level near the valence band due to Si-H and Ge-H bonds on adatoms. The unpinned SiGe (001) and (110) surfaces were dosed at room temperature with a saturation dose of $H_2O_2(g)$ leaving the SiGe surface terminated with an ordered monolayer of only Ge-OH sites on (001) and both of Ge-OH and Si-OH sites on (110). STS shows that on the HOOH dosed SiGe(001) and (110), the Fermi level is shifted to near the valence band edge due to the large surface dipole from the hydroxyl bonds. TMA was subsequently dosed on the HOOH/SiGe(001) and HOOH/atomic H/SiGe(110) surfaces forming an ordered monolayer of Al-O-Si bonds. In order to understand the thermal stability of the TMA dosed SiGe surfaces, the surface was annealed to 300°C and XPS measurements verify that Al-O bonds are totally transferred from Ge atoms to Si atoms forming Al-O-Si bonds on both (001) and (110) indicating that the strong affinity between Si and oxygen is pulling Si atoms toward the surface to bond with oxygen or hydroxyls while pushing Ge atoms into the subsurface during the annealing. STS indicates this unpins the Fermi level on both surfaces, leaving an electrically passive ordered layer which serves as an ideal template for further high-k ALD.

5:20pm **EM+NS+PS-MoA10 Band Structure and Critical Points of Pseudomorphic $Ge_{1-y}Sn_y$ Alloys on Ge***, **Nalin Fernando***, *T.N. Nunley, S. Zollner,* New Mexico State University*, D. Zhang, R. Hickey, J. Kolodzey*, University of Delaware

We calculate the dependence on composition and strain of the band structure of $Ge_{1-y}Sn_y$ alloys grown pseudomorphically on Ge and compare with spectroscopic ellipsometry measurements. Germanium is an indirect band gap material with limited optoelectronic applications. Because the band structure of Ge is a strong function of strain, a transition from an indirect to a direct band gap has been found for Ge under a tensile strain, which constrains the layer thickness and the composition of the substrate for heterostructure growth. Indirect to direct band gap crossover of unstrained $Ge_{1-y}Sn_y$ has been reported for y~6-10% indicating the possibility of widespread applications of Ge-based photonic devices and paving the way for the design of $Ge_{1-y}Sn_y$ lasers. Hence it is important to study the compositional dependence of the $Ge_{1-y}Sn_y$ band structure through measurements of the optical properties of $Ge_{1-y}Sn_y$ alloys. The complex pseudodielectric functions of pseudomorphic $Ge_{1-y}Sn_y$ alloys grown on Ge by MBE were measured using spectroscopic ellipsometry at 300 K in the 0.76-6.6 eV energy range for Sn contents up to 11%. Dielectric functions of $Ge_{1-y}Sn_y$ alloys were obtained to investigate the compositional dependence of the E_1 and $E_1+\Delta_1$ critical point (CP) energies. CP energies and related parameters were obtained by analyzing the second-derivative of the dielectric function. Our experimental results are in good agreement with the theoretically predicted E_1 and $E_1+\Delta_1$ CP energies of compressively strained $Ge_{1-y}Sn_y$ on Ge based on deformation potential theory. We will discuss the compositional and strain dependence of the direct and indirect band gaps as well as E_1 and $E_1+\Delta_1$ CP energies and related parameters of $Ge_{1-y}Sn_y$ alloys. We will present the nature of the band gap of pseudomorphic $Ge_{1-y}Sn_y$ on Ge and will discuss the effects of strain which critically depend on the bowing parameter of the lattice constant.

Energy Frontiers Focus Topic
Room: 211B - Session EN+AS+EM+NS+SE+SS+TF-MoA

Solar Cells II
Moderator: Adrie Mackus, Stanford University

2:20pm **EN+AS+EM+NS+SE+SS+TF-MoA1 Influence of Annealing Temperature in the Bulk Defect Formation in Perovskite Thin Films***, **Weina Peng***, *B.X. Anand, L.-H. Liu, S.C. Sampat, B.E. Bearden, A.V. Malko, Y.J. Chabal*, University of Texas at Dallas

Perovskites are emerging as front-runners for solar cell applications because of their superior optoelectronic properties. Over the past few years the grain size of perovskites has been continuously improved from several hundred of nanometers to a few millimeters which resulted in better solar conversion efficiencies. In addition to surface and grain boundary related defects, perovskites are prone to the formation of bulk defects as well. However the role of bulk defects in the determination of photovoltaic performance of perovskites is rarely explored. To this end we investigate the impact of annealing temperature on the defect density in polycrystalline $CH_3NH_3PbI_3$ thin films of ~1 micron average grain size prepared using vapor assisted solution process (VASP). The photoluminescence (PL) intensity and lifetime show systematic reduction when the annealing temperature is increased from 150°C to 200°C. A rough estimate of the defect state density obtained using fluence dependent PL measurements reveal a 5 fold increase in defect density for a 25°C increase in annealing temperature although the average grains size stays unchanged. Furthermore, surface passivation of perovskite films using Al_2O_3 via atomic layer deposition leads to an improvement in PL intensity and lifetime. But the PL quantum efficiency, as well as the lifetime, of the surface passivated 200°C annealed sample remains significantly lower than that of the un-passivated 150°C annealed sample indicating that the majority of the defects states we observe in the high temperature annealed samples originate from bulk defects. Thus the present study shows that minimizing the number of bulk defects, in addition to surface defects, is very important in the realization of highly efficient perovskite solar cells.

3:00pm **EN+AS+EM+NS+SE+SS+TF-MoA3 Tandem Solar Cells Using Perovskites, Silicon and CIGS**, *M.D. McGehee*, ***Tomas Leijtens***, Stanford University **INVITED**

The efficiency of perovskite solar cells has soared from a few percent to over 20% in the last 3 years. They are very attractive for multijunction solar

cell applications because the bandgap of perovskite semiconductors can be easily tuned in the range of 1.55 to 2.2 eV and the open circuit voltage of the cells is large. We have made highly efficient semitransparent perovskite solar cells using silver nanowire meshes as the top electrode. These cells can be used in combination with either silicon or copper indium gallium diselenide solar cells to make four-terminal and two-terminal tandems. We will also present detailed characterization of perovskite semiconductors made with different processing conditions to show what needs to be done to minimize recombination and make the solar cells stable.

3:40pm **EN+AS+EM+NS+SE+SS+TF-MoA5 Lifetime, Mobility, and Diffusion of Photoexcited Carriers in Ligand-Exchanged Lead Selenide Nanocrystal Films Measured by Time-Resolved Terahertz Spectroscopy**, *G.W. Guglietta,* Drexel University*, B.T. Diroll, E.A. Gaulding, J.L. Fordham,* University of Pennsylvania*, S. Li,* Drexel University*, C.B. Murray,* University of Pennsylvania*, **Jason Baxter***, Drexel University

Colloidal semiconductor nanocrystals have been used as building blocks for electronic and optoelectronic devices ranging from field effect transistors to solar cells. Properties of the nanocrystal films depend sensitively on the choice of capping ligand to replace the insulating synthesis ligands. Thus far, ligands leading to the best performance in transistors result in poor solar cell performance, and vice versa. To gain insight into the nature of this dichotomy, we used time-resolved terahertz spectroscopy measurements to study the mobility and lifetime of PbSe nanocrystal films prepared with five common ligand-exchange reagents. Non-contact terahertz spectroscopy measurements of conductivity were corroborated by contacted van der Pauw measurements of the same samples. The films treated with different displacing ligands show more than an order of magnitude difference in the peak conductivities and a bifurcation of time-dynamics. Inorganic chalcogenide ligand-exchanges with sodium sulfide (Na_2S) or ammonium thiocyanate (NH_4SCN) show high THz mobilities above 25 $cm^2V^{-1}s^{-1}$, which is desirable for transistors, but nearly complete decay of transient photocurrent within 1.4 ns. The high mobility with NH_4SCN and Na_2S exchanges is more than offset by their short lifetimes and results in diffusion lengths of only ~200 nm. In contrast, ligand exchanges with 1,2-ethylenediamine (EDA), 1,2-ethanedithiol (EDT), and tetrabutylammonium iodide (TBAI) show ~5x lower mobilities but much longer carrier lifetimes, with ~30% of photoexcited carriers remaining for >10 ns. The long lifetimes with EDA, EDT, and TBAI yield diffusion lengths of at least 500 nm, which is approaching the film thickness desired for strong light absorption in solar cells. This bifurcated behavior may explain the divergent performance of field-effect transistors and photovoltaics constructed from nanocrystal building blocks with different ligand exchanges.

4:00pm **EN+AS+EM+NS+SE+SS+TF-MoA6 iCVD Synthesis and Integration of Poly(vinylpyrrolidone) and Poly(4-vinylpyridine) as Polymer Electrolytes in Dye Sensitized Solar Cells***, **Yuriy Y. Smolin**, S. Janakiraman, A.J. Sauter, M. Soroush, K.K.S. Lau*, Drexel University

Initiated chemical vapor deposition (iCVD) is used to synthesize and integrate poly(4-vinylpyridine) (P4VP) and polyvinylpyrrolidone (PVP) as polymer electrolytes within the mesoporous TiO_2 photoanode of dye sensitized solar cells (DSSCs). DSSCs with conventional liquid electrolytes are prone to leakage and evaporation, which hinders DSSC durability and field implementation. In addition, liquid electrolytes lead to significant electron recombination within the cells that limit DSSC performance. In contrast, polymer electrolytes do not suffer from the practical disadvantages and could potentially enhance the cell's I-V behavior.

However, in order to enable good contact between the TiO_2 electrode and the polymer electrolyte, a major obstacle is the difficulty in achieving good pore filling of the polymer into the mesoporous TiO_2 layer. Mesoscale pore diameter, high aspect ratio, and tortuous pore structure of the photoanode along with liquid surface tension, poor wettability, and solute steric hindrance make pore filling extremely limited when using liquid techniques. This leads to poor electrical contact and lower efficiency. To overcome the challenges of pore filling, we directly synthesized polymer electrolytes inside the pore volume of the photoanode using the solvent-free technique of iCVD. iCVD relies on the vapor delivery of monomer and initiator, which facilitates infiltration into the porous TiO_2 substrate, and by controlling the relative rates of diffusion and surface polymerization through iCVD process parameters, uniform and conformal growth of polymer is achieved. The pore filling of the polymer electrolyte into 5–10 µm photoanodes using iCVD is typically 90–100% which is significantly better than that achievable with liquid techniques like spin coating.[1]

In this work, we will show that iCVD P4VP and PVP polymer electrolytes can be effectively integrated within TiO_2 mesoporous photoanodes to produce enhanced DSSCs. By varying the polymer electrolyte chemistry including the use of a crosslinking agent during iCVD to stabilize the resulting polymer structure, DSSC I-V characteristics, such as open-circuit voltage, short-circuit current density and fill factor, are tuned.[2] To gain a better understanding on the effect of the polymer electrolyte, experimental techniques such as linear sweep voltammetry, intensity modulated spectroscopy, and impedance spectroscopy are used. Mathematical modeling of DSSC behavior is also performed to relate these experimental observations with the dynamics of the operation of the cell.

1. S. Nejati and K. K. S. Lau, *Nano Lett.*, 2010, 11, 419-423.

2. Y. Y. Smolin et al., *J. Power Sources*, 2015, 274, 156-164.

4:20pm **EN+AS+EM+NS+SE+SS+TF-MoA7 Interfacial Effects on Device Performance in Organic Solar Cells***, **Huanxin Ju**, J.F. Zhu,* University of Science and Technology of China*, D.S. Ginger*, University of Washington

The better understanding of the underlying mechanisms is essential for the further development of highly efficient organic photovoltaics (OPVs) devices. In this paper, the transient photovoltage (TPV) and charge extraction (CE) measurements in combination with the synchrotron radiation photoemission spectroscopy (SRPES) were used to gain insights intothe correlation between the microscopic interfacial properties and macroscopic device performance. The OPV devices based on PCDTBT: $PC_{70}BM$ with Ca interlayer were studied as a reference system to investigate the interfacial effects on device performance. The charge carrier decay dynamics demonstrated that the device with the Ca interlayer exhibited a lower recombination constant (k_{rec}) than that only with the Al cathode at a given charge carrier density (n). In addition, the interfacial energy band structures indicated that the strong dipole moment produced by the Ca interlayer can facilitate electron extraction as well as drive hole away at the cathode/polymer interface, resulting in retarding interfacial recombination losses. Finally, we examined the device performance with the Ca interlayer to find that the efficiency is improved by 28% as compared to that without the Ca interlayer, which shows good correlation with the observed interfacial properties.

4:40pm **EN+AS+EM+NS+SE+SS+TF-MoA8 Tungsten-Titanium Mixed Oxide Thin Films for Improved Structural and Optical Properties for Solar Driven Applications***, **Mirella Vargas**,* The University of Texas at El Paso*, N.R. Murphy,* Air Force Research Laboratory*, R.V. Chintalapalle*, The University of Texas at El Paso

Tungsten oxide (WO_3) is a well-established n-type semiconductor possessing unique optical and electronic properties. WO_3 has become the most interesting inorganic material for electrochromic applications due to the reversible spectral absorption properties associated with WO_3. WO_3 thin films and nanostructures exhibit an optical band gap that permits efficient use of the solar spectrum including absorption in the blue part of the visible region and the ultraviolet region, as well as a high transmission region that extends from the near-infrared (IR) to the visible spectrum. Coupled with good electronic transport properties, photosensitivity, and chemical integrity, WO_3-based materials are attractive for applications related to sustainable energy production including energy efficient windows and architecture, photoelectrochemical (PEC) water-splitting, photocatalysis and solar cells. Anion or cation doping into WO_3 has been extensively studied as this offers the opportunity to tailor the transport properties that may influence the efficiency of solar driven devices. Titanium doping into WO_3 has proven to enhance the electrochromic response and the cyclic lifetime by a factor of five in PEC devices. In the present case a systematic investigation of progressively increasing the Ti content in the W-Ti target for reactive sputtering has been employed to tune the structure, chemistry, and properties of the films. Tungsten-titanium (W-Ti) mixed oxide thin films were fabricated using reactive sputtering of W-Ti alloy targets with Ti content ranging from 0 to 30 wt.%. X-ray photoelectron spectroscopy confirms the existence of W and Ti in their highest oxidation states of +6 and +4, respectively. Quantification of binding energy shifts for W and Ti core-level transitions confirms the formation of WO_3-TiO_2 composite oxide films. Optical analyses made from spectrophotometry measurements indicate a decrease in band gap with a discrete amount of Ti incorporation. The band gap decreases with increasing Ti from 3.0 eV to 2.5 eV. Such films are expected to have the possibility for tuning the electrical conductivity while retaining the optical transparency to make them efficient for photoelectrochemical cells and photovoltaics.

5:00pm **EN+AS+EM+NS+SE+SS+TF-MoA9 Potential Resolution to the "Doping Puzzle" in Pyrite FeS_2**, *X. Zhang, M. Li, L. O'Brien, J. Walter, M. Manno, F. Mork, J. Kakalios, **Eray Aydil**, C. Leighton*, University of Minnesota

In principle, pyrite FeS_2 is one of the most suitable photovoltaic materials for sustainable low-cost, large-scale solar cell manufacturing because it has high absorbance in the visible and comprises earth-abundant inexpensive elements. However, current efficiencies of solar cells based on pyrite FeS_2 have not exceeded 2.8%. Early research on this material concluded that unintentionally doped FeS_2 thin films are *p*-type and subsequent solar cell

work evolved based on this presumption. In fact, it is now widely accepted that FeS_2 thin films almost always exhibit *p*-type conduction even though single crystals are typically found to be *n*-type. This discrepancy between single crystals and thin films is perplexing and to date this puzzle remains unexplained. In this talk we reexamine the conclusion that undoped FeS_2 films are predominantly *p*-type and provide an explanation for this "doping puzzle" in pyrite. Using a combination of Hall effect, thermopower, and temperature-dependent resistivity measurements on a large set of well characterized single crystals and thin films, we show that the widely accepted predominant *p*-type behavior in pyrite films may, in fact, be an artifact of hopping conduction and should be revisited. Specifically, both Hall effect and thermopower measurements establish that all of our high-mobility (>1 $cm^2V^{-1}s^{-1}$) films and single crystals are *n*-type. Temperature-dependent resistivity measurements on these high mobility films and crystals establish diffusive electronic transport. We find that films with lower mobility ($4x10^{-3}$-1 $cm^2V^{-1}s^{-1}$) also show *n*-type Hall effect but exhibit a *p*-type Seebeck coefficient, leading to a discrepancy in the measured carrier type. Temperature-dependent resistivity measurements on these intermediate mobility films show a transition from diffusive to hopping transport. Finally, both Hall and Seebeck coefficients are strongly suppressed and invert in the lowest mobility thin films (<$4x10^{-3}$ $cm^2V^{-1}s^{-1}$) indicating apparent *p*-type conduction. Temperature-dependent resistivity measurements establish unambiguous hopping behavior in these lowest mobility films. Based on this evolution of Hall and Seebeck coefficients with carrier mobility, and the well-known suppression of the Hall and Seebeck effects in conductors with hopping electronic transport, we conclude that the apparent crossover from *n*-type to *p*-type with decreasing mobility is, in fact, an artifact of hopping conduction.

Work supported by the NSF under DMR-1309642, in addition to the University of Minnesota NSF MRSEC under DMR-1420013.

5:20pm **EN+AS+EM+NS+SE+SS+TF-MoA10 Interparticle Contact Radius and Electron Transport in Thin Films Comprised of Nanocrystals**, ***Elijah Thimsen***, *D. Lanigan*, Washington University, St. Louis

Thin films comprised of nanocrystals are being explored for a variety of applications that involve electron transport. For traditional applications such as photovoltaic solar cells, the goal is often to utilize solution processing to make an inexpensive thin film that essentially behaves as a bulk material with diffusive transport. For other applications, such as neuromorphic computing, variable range hopping (VRH) transport is more desirable because it enables a given nanocrystal to have orders of magnitude more nearest neighbors than it physically touches. It is of paramount importance that the structure-property relationships that control electron transport mechanism be elucidated. Previous work has demonstrated that interparticle separation distance affects charge carrier mobility. However, for films comprised of nanocrystals that are physically touching, what is the effect of contact radius? In this work, we present a systematic experimental study of the effect of interparticle contact radius on the electron transport mechanism in thin films comprised of heavily-doped ZnO nanocrystals embedded in Al_2O_3. As the contact radius increased, the electron transport mechanism crossed over from VRH to diffusive conduction. For large contact radius between nanocrystals, the room-temperature electron mobility in the film approached the local mobility within a nanocrystal, approximately 10 cm^2 V^{-1} s^{-1}. The conclusion is that for nanocrystals that are physically touching, the interparticle contact radius determines the transport mechanism. With the ability to control the electron transport mechanism in films comprised of ZnO nanocrystals, we performed an exploratory study of the Hall effect in these materials. Hall effect measurements are of great utility and are routine for determining charge carrier mobility and type, but the interpretation of data for materials that exhibit VRH has been difficult in the past. For well-connected ZnO nanocrystals that exhibit diffusive conduction, the Hall coefficient was independent of temperature, as expected for the high doping level. Alternatively, for films with small contact radius between nanocrystals, which exhibited a VRH transport mechanism, we observed an anomalous behavior of the Hall coefficient at low temperature (100 to 200 K). Surprisingly, for films that exhibited VRH, the magnitude of the Hall coefficient increased exponentially with decreasing temperature, in stark contrast to the conventional wisdom that the Hall effect is suppressed for VRH.

Plasma Science and Technology
Room: 210B - Session PS+EM-MoA

Directed Self Assembly and Plasma Synthesis of Novel Materials
Moderator: Eric Joseph, IBM T.J. Watson Research Center

2:20pm **PS+EM-MoA1 Forward and Inverse Computational Tools for Directed Self-Assembly**, *G.H. Fredrickson*, ***Sean Paradiso***, University of California at Santa Barbara **INVITED**

This presentation will provide a tutorial on the physics of bulk block copolymer self-assembly, explaining how molecular parameters such as polymer architecture, composition, and molecular weight influence the size and symmetry of nanoscale domains. In thin films, additional variables such as surface and substrate interactions and substrate topology are important in "directing" the self-assembly and thereby achieving morphologies and features useful for pattern transfer in lithography. A powerful computational framework based on polymer field theory will be described that enables simulations to be conducted for a wide range of block copolymer formulations subject to arbitrary topological confinement ("grapho-epitaxy") or substrate chemical modulation ("chemo-epitaxy"). Our recent work at UCSB has involved computational studies of block copolymer directed self-assembly (DSA) in a variety of confining templates that can be produced using conventional lithography tools and targeting both line/space patterns and vertical interconnects (VIAs). The research aims to identify polymer architectures and compositions along with template geometries and surface treatments that lead to robust DSA structures. Beyond process windows for perfect structures, we have studied defect states and the free energy landscape connecting them to perfect states, thereby providing estimates of equilibrium defect populations and kinetic barriers for defect annealing. I will finish the presentation with an example of an "inverse design" calculation, namely the identification of a template and polymer composition that optimally produces a desired self-assembled pattern. Further developments in this area will be necessary for DSA to become a practical tool in next generation lithography.

3:00pm **PS+EM-MoA3 Improvement of Block Copolymer Masked Silicon Etch Profile using Neutral Beam**, ***Deokhyun Yun***, *J.W. Park, H.S. Kim, G.Y. Yeom*, Sungkyunkwan University, Republic of Korea

These days, bottom-up block copolymer (BCP) lithography is widely investigated as alternative patterning method for deep nanoscale device replacing conventional top-down photolithography. The most widely used BCP material is polystyrene (PS)/polymethyl methacrylate (PMMA) and, nanoscale PS mask features formed on the substrates after the direct self-assembly are easily damaged by the plasma processing. Previously, neutral beam etching has been used to etch semiconducting materials without surface charging and damaging by using a highly directional radical beam instead of conventional plasma assisted ion beam. In this study, the nano-structured silicon was fabricated for nano-devices such as optical devices and transistor devices using BCP as the mask and the effect of Cl_2/Ar neutral beam instead of Cl_2/Ar ion beam on the etch characteristics of BCP and silicon was investigated. The use of neutral beam instead of ion beam decreased the degradation of BCP during the etching, therefore, more anisotropic silicon etch profile in addition to the improved etch selectivity of silicon over BCP could be observed. Also, by using the neutral beam instead of ion beam, the improvement of line edge roughness could be obtained.

3:20pm **PS+EM-MoA4 Plasma Etching of Directed Self Assembly based Patterns for Aggressively Scaled CMOS Applications**, ***Hiroyuki Miyazoe***, *H. Tsai, R.L. Bruce, S.U. Engelmann, M. Brink, A. Pyzyna,* IBM T.J. Watson Research Center, *C. Liu,* IBM Albany Nanotech Center, *A. Vora, D. Sanders,* IBM Almaden Research Center, *M. Maher, W. Durand, C. Ellison, G. Willson,* The University of Texas at Austin, *M. Guillorn, E.A. Joseph*, IBM T.J. Watson Research Center

As the feature size in CMOS technology continues to shrink, patterning below 30 nm pitch faces many challenges. Directed self-assembly (DSA) [1] and sidewall image transfer (SIT) [2] patterning techniques can augment conventional lithographic patterning by providing sublithographic multiplication of feature pitch. Recently, our group successfully demonstrated the electrical characterization of FinFET devices comprising fins formed by DSA of poly (styrene-block-methyl methacrylate) (PS-b-PMMA) block copolymers (BCPs) at 28nm fin pitch [3]. In addition, we demonstrated copper lines with dielectric patterns formed by DSA at 28nm pitch followed by metallization [4]. Patterning of Si, SiNx and SiOx at a ~24 nm feature pitch using PS-b-PMMA BCP was also shown [3]. In this work, we discuss a parametric study of factors impacting fine feature patterning to further optimize DSA line-space patterning using PS-PMMA

BCPs at 28 and 24nm pitch, and high chi BCP at 20nm and 18.7nm pitch. The use of templated DSA to generate line-space structures in the aforementioned materials was used to investigate the control of critical dimension (CD), line edge roughness (LER) and line width roughness throughout the patterning process. The line roughness of the hardmask becomes smaller at the lower substrate temperature during etch. The CD of lines was controlled well between 11nm and 15nm at 28nm pitch by controlling the etching time while keeping the LER constant (at ~3nm). We also confirmed that O_2-free plasma gas chemistry is more advantageous for BCP patterning in case of organic-organic polymer. These initial patterning studies may play an important role in understanding feature formation and density limiting ground rules.

[1] J. Cheng et al., SPIE 2010, [2] H. Yaegashi. SPIE 2012, [3] Tsai, IEDM 2014, [4] Pyzyna VLSI 2015

4:00pm **PS+EM-MoA6 Microplasma Based Synthesis of Nanomaterials**, ***Michael Gordon***, University of California at Santa Barbara **INVITED**

We present a hybrid plasma spray deposition technique, based on geometrically-confined, supersonic microplasma jets, which can create a wide range of metal, metal oxide/sulfide, and semiconductor nanoparticles and nanostructured thin film materials (e.g., CuO/CuS, ZnO, SnO_2, NiO/$NiFe_2O_4$) on virtually any surface. Organometallic or aerosolized precursors are broken down in a hollow cathode microplasma jet under different reducing/oxidizing atmospheres at high pressure (10-100 torr), creating a directed flux of active metal and oxide species for the subsequent growth of nanostructured films. Interaction of the jet afterglow with the background gas can create additional species (e.g., excited neutrals, radicals, etc.) which participate in film growth. By adjusting supersonic flow characteristics and plasma operating conditions, deposits ranging from isolated nanoparticles to films of fibers, aggregates, nanowires, and dense columns can be realized. The talk will highlight our recent efforts in nanomaterial synthesis via microplasmas with emphasis on the physics of the jet source, dynamics of the growth process, and applications such as solar cell electrodes, photo(electro)catalysis, and nanogranular films for magnetic exchange bias applications.

4:40pm **PS+EM-MoA8 Nucleation of Silicon Nanocrystals in a Remote Plasma without Subsequent Coaguation**, ***Ilker Dogan***, Eindhoven University of Technology, Netherlands, *S.L. Weeks, S. Agarwal,* Colorado School of Mines, *M.C.M. van de Sanden*, Dutch Institute for Fundamental Energy Research (DIFFER), Netherlands

We report on the growth mechanism of spherical silicon nanocrystals (Si-NCs) in a remote expanding Ar plasma using a time-modulated SiH_4 gas injection in the microsecond time range. Under identical time-modulation parameters, we varied the local density of the SiH_4 gas by changing its stagnation pressure on the injection line over the range 0.1-2.0 bar. We observed that nanocrystals were synthesized in a size range from 2 nm to 50 nm with monocrystalline morphology. Smaller nanocrystals (2-6 nm) with narrower size distributions and with higher number densities were synthesized with an increase of the SiH_4 gas-phase density. We related this observation to the rapid depletion of the number density of the molecules, ions and radicals in the plasma during nanocrystal growth, which can primarily occur via nucleation with no significant subsequent coagulation. In addition, in our remote plasma environment, rapid cooling of the gas in the particle growth zone from 1500 K to 400 K significantly reduces the coalescence rate of the nanoparticles, which makes the coagulation process highly unlikely. Our observations on nanocrystal formation via nucleation indicated that subsequent coagulation for further growth is not always an essential step on nanoparticle formation.

5:00pm **PS+EM-MoA9 Atmospheric Plasma Synthesis of Metallic Platinum Nanoparticles for PEMFC Technology using an Organometallic-Carbon Solution Nebulized in the Post-Discharge of an RF Torch**, ***Joffrey Baneton***, *D. Merche,* ULB, Belgium, *M. Raes,* VUB, Belgium, *V. Debaille,* ULB, Belgium, *G. Caldarella, V. Stergiopoulos,* ULg, Belgium, *H. Terryn,* VUB, Belgium, *N. Job,* ULg, Belgium, *F.A.B. Reniers*, ULB, Belgium

Catalytic layers are one of the most important components of proton exchange membrane fuel cells (PEMFC) because they directly influence the transport of matter and the reactivity of the electrodes [1]. In many cases, platinum associated with carbon black forms the most interesting material because of its very high catalytic activity [2]. Unfortunately, some limitations remain due to the cost of platinum and the difficulty to control the structure of the carbon support.

In this study, we propose a new promising technique using platinum (II) acetylacetonate [$Pt(acac)_2$] powder mixed with porous carbon and nebulized in a RF atmospheric plasma torch directly on commercial gas diffusion layer (GDL). This fast and "one-pot" methodology leads to the formation of homogeneous and reproducible samples with a variable and controlled content of metallic platinum on the surface, as analyzed by X-ray Photoelectron Spectroscopy (XPS) and Scanning Electron Microscopy (SEM). The catalytic activity per mass unit can be studied by a combination of Inductively Coupled Plasma Mass Spectrometry (ICP-MS) and electrochemical measurements.

We demonstrate that the plasma treatment and mostly the reactive oxygen species play a critical role in the activation of the support surface and the binding of the platinum nanoparticles on it, reinforcing previous observations [3,4]. In the case of an argon-oxygen plasma pretreatment of the GDL, a significant increase of the platinum content on the surface can be observed.

The influence of different process parameters on the synthesis of the platinum nanoparticles was studied. We show that the carrier gas flow rate, the power injected in the discharge and the treatment time do not have a significant impact on the surface composition. On the other hand, some nebulizer parameters such as the number of pulses or the loading of Pt-C allow the tuning of the amount of Pt grafted on the surface without altering its metallic nature.

Finally, the influence of the type of carbon powder (e.g. CB, CX or CNTs) was investigated. It appears that it can modify the surface organization and consequently also the intrinsic characteristics of the material. It reveals that the distribution of platinum nanoparticles and the access to the catalytic sites can be optimized depending of the porosity and the active surface of the carbon support.

[1] Gasteiger et al. Handbook of Fuel Cells – Fundamentals, Technology and Applications. **2003**, 3, 593

[2] Chatenet et al. New and Future Developments in Catalysis. **2013**, 401-423

[3] Pireaux et al. Method for Depositing Nanoparticles on Substrates, **2002** (Patent)

[4] Claessens et al. *Nanotechnology*, **2010**, 21, 38, 385603

5:20pm **PS+EM-MoA10 Low Energy Helium Ion Irradiation Induced Surface Modification of Metals**, ***Irem Tanyeli****, FOM Institute DIFFER, Netherlands, *L. Marot, D. Mathys,* University of Basel, Switzerland, *M.C.M. van de Sanden,* FOM Institute DIFFER, Netherlands, *G. De Temmerman*, ITER Organization

Many applications, such as energy harvesting, energy storage, optoelectronics, demand nanomaterials and/or nanostructured surfaces for an enhanced activity. Various techniques, which can be grouped under top-down and bottom-up approaches, exist and are worked on by many researchers in order to fulfill the demands of these applications. There are some critical requirements that needs to be satisfied by nanostructures before being implemented in any application, such as high porosity, good contact between different crystallites and good electrical conductivity. Standard nanostructuring approaches, such as wet-chemical processing, can give very homogeneous particle sizes, but the contact between the particles is often poor and a necking treatment is needed to alleviate this limitation. In this study, Helium ion induced nanostructuring is proposed as an efficient technique. This top-down approach provides a good control over morphology, high porosity, good conductivity and it enables post processing, such as oxidation and nitridation.

Metal surfaces are exposed to pure Helium plasma under extreme ion flux (in the range of 10^{23} $m^{-2}s^{-1}$) and low ion energy (< 100 eV) conditions at Pilot-PSI, linear plasma generator. Different surface modifications on various metals, such as iron, titanium, copper and aluminum, are observed.[1] Pillar like structures are formed on copper and aluminum surfaces, whereas fiber like nanostructures are observed on iron surface. Controlled nanostructure formation on tungsten and molybdenum surfaces has been reported.[2] Consistently, nanostructure formation on iron surface has been controlled with surface temperature and ion fluence in this study.[3] It has been known that metal oxides are good candidates to be used as photoelectrodes in photoelectrochemical cells. WO_3 and α-Fe_2O_3 are two of the most widely studied photoanodes. Hence, Helium ion induced tungsten and iron nanostructured surfaces are oxidized to the desired phases to be tested in photoelectrochemical cells. 1mA/cm^2 of photocurrent density for WO_3 has been achieved.[4]

[1] **I. Tanyeli**, L. Marot, D. Mathys, M. C. M. van de Sanden, G. De Temmerman, Sci. Rep. 5:9779-8, 2015.

[2] G. De Temmerman et al., J. Vac. Sci. Technol. A, 30, 041306-6, 2012.

[3] **I. Tanyeli**, L. Marot, M. C. M. van de Sanden, G. De Temmerman, ACS Applied Materials & Interfaces 6 (5), pp 3462-3468, 2014.

*** Coburn & Winters Student Award Finalist**

[4] M. de Respinis, G. De Temmerman, **I. Tanyeli**, M. C. M. van de Sanden, R. P. Doerner, M. J. Baldwin, R. van de Krol , ACS Applied Materials & Interfaces 5 (15), pp 7621-7625, 2013.

Advanced Surface Engineering
Room: 212A - Session SE+EM+EN-MoA

Thin Film Technologies for Energy Storage, Conversion and Harvesting

Moderator: Michael Stueber, Karlsruhe Institute of Technology, Andrey Voevodin, Air Force Research Laboratory

2:20pm **SE+EM+EN-MoA1 Properties of Zinc Oxide Thin Films Grown on Silicon Wafers by Pulsed Laser Deposition**, ***Yilu Li***, *J.W. Wrobel, M.K. Michael*, University of Missouri-Kansas City

Pulsed ultraviolet light from a XeF excimer laser was used to grow thin films of zinc oxide on (111) p-type silicon wafers within a versatile high vacuum laser deposition system. Pressure, target temperature and distance from the target to the substrate can be adjusted in the system. Scanning electron microscopy, energy dispersive X-ray spectroscopy, X-ray diffraction spectroscopy and ellipsometry had been used to analyze the structures and properties of ZnO thin film products.

3:00pm **SE+EM+EN-MoA3 Synthesis of Crystallized and Nanostructured TiO_2 Thin Films by Reactive Magnetron Sputtering for Application as Photoanode in Dye Sensitive Solar Cells**, *J. Dervaux, P.-A. Cormier, S. Konstantinidis,* Université de Mons, Belgium*, P. Moskovkin, S. Lucas,* University of Namur, Belgium*, **Rony Snyders***, Université de Mons, Belgium

Nowadays, the efficient use of renewable energies, and more specifically of solar energy, represents a major economic and environmental issue. Among the potential solutions, the Dye Sensitive Solar Cells (DSSC) present many advantages. In order to improve the efficiency of DSSC, TiO_2 nanoparticles, which are usually used as photo-anode, could be replaced by nanostructured TiO_2 thin films. Indeed, a photo-anode of ordered porous nano-columnar TiO_2 would provide large surface area for dye absorption, fast electron transfer path, enhanced light trapping, and tight interfaces to conducting electrodes and contributes to a high fill factor and an overall higher cell efficiency. In view of this application, the anatase phase of TiO_2 is usually the preferred polymorph as electron acceptors in DSSCs even if a synergistic effect exists between anatase and rutile with an optimal rutile content of around 13 wt%.

In this work, nanostructured and crystallized TiO_2 thin films are synthesized by reactive magnetron sputtering combined with Glancing Angle Deposition (GLAD). The substrate temperature, the substrate bias voltage and the rotation speed were varied in order to determine the best experimental conditions leading to (nano-)porous films with anatase TiO_2 columns. The chemical composition, the crystalline structure and the microstructure of the films were analyzed by XPS, XRD, SEM and TEM, respectively while the surface area is evaluated by the BET method.

It is demonstrated that many type of microstructures (tilted columns, straight pillars, chevrons,…) are obtained by combining the GLAD parameters and the sputtering conditions. On the other hand, depending on these growth conditions, the phase constitution can be tuned from amorphous to pure rutile or anatase phases including mixtures of both polymorphs. The surface area of the synthesized layer strongly depends on the experimental conditions and on the associated microstructure. The highest obtained value is of ~ 140 m^2/g for a tilted columnar amorphous/anatase sample which is significantly better than the values reported for TiO_2 nanoparticules systems (~ 60 m^2/g). On the other hand, a clear correlation between the surface area and the dye absorption is demonstrated revealing a good impregnation of the layer. It is also demonstrated that this impregnation behaviour is depending on the size of the dye molecule revealing different populations of pores as a function of their size. This is supported by TEM and modelling data using NASCAM, a 2D-3D Kinetic Monte Carlo code for the simulation of deposition, diffusion, nucleation and growth of films on a surface.

3:20pm **SE+EM+EN-MoA4 Silver-Carbon-Nanotube Metal Matrix Composites for Metal Contacts on Space Photovoltaic Cells**, ***Omar K. Abudayyeh***, *C. Nelson, S.M. Han,* University of New Mexico*, N. Gapp, D.M. Wilt*, Air Force Research Laboratory

The advanced solar cells used in space vehicles today are rapidly moving towards thin-film-based inverted metamorphic multijunction (IMM) solar cells mounted on flexible substrates. However, the IMM cells are more prone to cracking than state-of-the-art triple junction cells. The cell cracking can lead to metal contact failure on IMM cells, compromising the power generation. To mitigate the power loss and increase the lifetime of IMM cells, silver metal films imbedded with carbon nanotubes (CNTs), otherwise known as metal matrix composites, have been developed and investigated for the reinforced mechanical strength against stress-induced cracking. We have primarily focused on (1) surface functionalization of CNTs to make their surface more hydrophilic and wetting to metals, (2) optimization of a cyanide-free electrochemical deposition of silver, (3) electrochemical deposition, drop casting and nanospreader technique to control the composite microstructure, and (4) mechanical and electrical characterization of the composite films. We observe that carboxylation of CNTs produces a stable, homogeneous suspension of negatively charged CNTs at pH > 6. Lustrous-mirror-finish silver films are also successfully deposited, using a commercial cyanide-free silver-plating solution with precise control of current density. Currently, one of the microstructures being explored is a silver-carbon-nanotube layer-by-layer structure, where the surface coverage of CNTs is an important parameter that directly affects the CNT packing fraction and metal intercalation through the CNT network. We quantify the CNT surface coverage as a function of different deposition variables by digitally analyzing scanning electron microscopy images. In this presentation, we will further discuss how this surface coverage correlates to the mechanical and electrical properties of the MMC films. We characterize the mechanical properties, using nanoindentation and strain failure tests. The initial nanoindentation analysis reveals that the composite film has a lower elastic modulus (10 GPa) than pure silver (73 GPa) or CNT (1000 GPa). The lower elastic modulus is attributed to the electroplating process of silver, in which hydrogen is incorporated and trapped within the composite. Our finite element analysis also corroborates this speculation, where the elastic modulus near 10 GPa is predicted with approximately 4% void fraction. While the composite elastic modulus is lower than that of pure silver, the strain failure tests show that carbon nanotubes can bridge 20 to 50-mm-wide microcracks, maintaining electrical conductivity of the composite.

3:40pm **SE+EM+EN-MoA5 Laser Liftoff of Single Crystal GaAs Thin Films and Energy Conversion Devices**, ***Bruce Clemens***, *G. Hayes, V. Parameshwaran, A. Jan, J.B. Reeves*, Stanford University **INVITED**

GaAs and related III-V sphalerite materials offer a wide array of tunable characteristics that lend themselves to many advanced device technologies. However, the cost of GaAs substrates limits their use, specially for photovoltaics. Separating epitaxially-grown layers from a growth substrate can reduce costs, however the current approach, which uses an acid to laterally etch an epitaxial sacrificial layer, is slow and can damage other device layers. Here, we demonstrate laser lift-off as a new approach that is orders of magnitude faster, and that enables more freedom in the selection of other device layers. We grow a structure with a spatially-tuned optical absorption coefficient by growing a small-band-gap, pseudomorphic layer between the GaAs substrate and a GaAs film and device structure. By using InGaAsN with a band gap of 0.9 eV for this layer, we achieve high absorption of 1064 nm (1.17 eV) light from a Nd:YAG nanosecond laser pulse, while GaAs is essentially transparent for this wavelength. Illumination through the back of the GaAs substrate with laser fluences of about 0.7 J/cm^2 achieves transfer of the GaAs layer to a flexible polymer substrate. Transmission electron microscopy and x-ray diffraction show that the initial InGaAsN layer is coherently strained to match the GaAs substrate, and that the GaAs film is strain-free and free of dislocations, both before and after lift-off. Thermal modeling shows only modest heating outside of the InGaAsN layer, so that the film or device above the InGaAsN layer experiences minimum thermal exposure. Examination of the lift-off interfaces shows evidence of melting and re-solidification. We demonstrate a process using additional InGaP etch layers that allow for quick and easy clean-up of this melted region, resulting in restoration of the original GaAs wafer surface to a condition suitable for re-use. Thus our process can transform the GaAs substrate from a consumable to a manufacturing tool. Device performance and material properties of lifted-off devices will be reported.

4:20pm **SE+EM+EN-MoA7 Optical and Structural Properties of Metal-dielectric Composite Films**, ***Lirong Sun***, *N.R. Murphy, J.G. Jones, J.T. Grant*, Air Force Research Laboratory

In this work, the metal - metal oxide composite films were prepared in multilayer stacks. A medium layer of silver or a mixture of silver and oxide (SiO_2, Al_2O_3, ZnO and ITO) was embedded between the host (SiO_2, Al_2O_3, ZnO and ITO) materials. The mixture of silver and oxide was deposited by co-sputtering the silver target and one oxide target in pure argon simultaneously using DC and pulse DC magnetron sputtering techniques. The optical constant of composite films was tailored by varying deposition time of the medium layer, deposition conditions and host material. The

absorbing spectral peaks were influenced by silver content, silver particle sizes and oxide matrix. The *in situ* spectroscopic ellipsometry data was performed in real time during film growth to derive film thickness and optical constants. The dispersion results were further correlated with absorption spectra, film density, grain sizes and surface morphology by UV-Vis-NIR spectra, X-ray diffraction, X-ray reflectivity and scanning electron microscope measurements.

5:00pm **SE+EM+EN-MoA9 Atomic Layer Deposition of Alumina and Titania Passivation Layers in Microchannel Reactors for Coke Suppression***, **Hao Feng***, Xi'an Modern Chemistry Research Institute, China

Alumina and titania thin films are deposited inside the channels of stainless steel tubes by atomic layer deposition to deactivate the metal surface for the purpose of coke suppression. The ALD equipment is modified to incorporate the high-aspect-ratio metal tubes into the flow path. Experiment parameters are adjusted to ensure complete and uniform coverage of the internal surface areas of the metal tubes. The thicknesses of the passivation layers are precisely controlled by adjusting the number of ALD cycles. In coking experiments the passivated metal tubes are used as reactors for thermal cracking of a hydrocarbon fuel composed of C_{12}-C_{16} paraffins. The lifetime of the experiment system passivated by ALD alumina films can be up to 5 times longer compared to the system using bare metal tubes as the reactor. By analyzing the tested metal tube samples it is discovered that the ALD alumina film remains intact after the coking experiment so that the metal catalyzed filament coke formation can be completely inhibited by the alumina passivation layer. The anti-coking performances of ALD titainia passivation layers are also noticeable but not as stable. The formation of filament cokes can also be suppressed by titania passivation layers. However, the ALD titania films tend to crack during the coking experiments. This could lead to failures of the passivation layers and acceleration of coke formation.

2D Materials Focus Topic
Room: 212C - Session 2D+EM+NS+SS+TF-TuM

Optical and Optoelectronic Properties of 2D Materials
Moderator: Andrea Young, University of California at Santa Barbara

8:00am **2D+EM+NS+SS+TF-TuM1 The Tri-Angular Lattice Exciton (3ALE) Model: Exciton Physics at the Atomic Scale**, *F. Tseng,* NRC Research Associate*, E. Simsek,* George Washington University*, **Daniel Gunlycke***, Naval Research Laboratory

Descriptions of excitons in pristine semiconducting crystals usually rely on the hydrogen model adopted for excitons. Owing to the weak screening in monolayer transition-metal dichalcogenides, however, the electron and hole separation in the strongest bound excitons is on the atomic scale, necessitating atomistic treatment. In this presentation, we present a minimalistic exciton model that accounts for the lattice and the spin-orbit and exchange interactions, thus making this model appropriate across the spectrum from Wannier to Frenkel excitons. Using this model, we show that the exciton lifetimes could be extended by transitioning the excitons into excitonic dark states. Longer exciton lifetimes could make these materials candidates for applications in energy management and quantum information processing.

This work has been funded by the Office of Naval Research (ONR), directly and through the Naval Research Laboratory (NRL). E.S. and F.T. acknowledge support from NRL through the ONR Summer Faculty Program and the NRC Research Associateship Program, respectively.

8:20am **2D+EM+NS+SS+TF-TuM2 Opposite Dependence of Microwave-Induced vs. Field-Induced Imaging Contrast in NV⁻ based Fluorescence Microscopy as Function of Optical Excitation**, ***Etienne Goovaerts****, S.K.R. Singam,* University of Antwerp, Belgium*, M. Nesladek,* Hasselt University, Belgium*, M. Giugliano*, University of Antwerp, Belgium

The charged nitrogen-vacancy (NV^-) center is a remarkable defect in diamond which allows interrogation of spin state through its fluorescence. Among the proposed applications, background-free imaging based on fluorescent nanodiamond (FND) was demonstrated [1-3]. The FNDs emission can be discriminated from spurious fluorescence by switching on resonant microwaves (MW) and/or a static magnetic field [1-3], as demonstrated in cells [1] and potentially in small animals [2]. It is now important to understand the origin of the contrast in either of these approaches, and the optimal experimental parameters.

NV^- defects in single-crystal diamond as well as in FNDs were excited by a 532nm laser through the microscope objective. A compact spectrometer combined with appropriate filters allowed to measure the NV^- and NV^0 emission. MW-induced contrast is achieved using a broadband circular antenna (i.d. 1mm) on a printed plate, and for field-induced contrast we use a small-sized permanent magnet (~300mT). They are placed closely behind the sample with in each case the magnetic field component along the optical axis of the objective.

For shallow implanted NV in (100) diamond as well as for FNDs the fluorescence is quenched by application of either resonant MWs or static field, with contrast levels systematically higher in the single crystal case than for deposited nanoparticles. The contrast values were measured for laser powers covering 6 orders of magnitude. After an initial rise at very low excitation (max. 13% in crystal, 7% in FND), the MW-induced contrast significantly decreases at higher laser powers. In parallel, field-induced contrast increases from about 12% to values of 38% and 20% for the single crystal and FNDs. This is described under steady state conditions using a 5-level model that includes radiative and nonradiative decay and ground state spin relaxation. The MW-contrast results from induced spin transitions in the triplet ground state while the field effect relies on state mixing within the ground and the excited triplets which change the decay rates. The analysis also shows that the applied excitation rates runs through 3 regimes from below the spontaneous relaxation rate, via an intermediate regime, to above the decay rate of the intermediate singlet.

This work demonstrates the advantages of field-induced contrast microscopy over the MW-induced approach. These become particularly important at high excitation rates which are more often applied in confocal microscopy.

[1] R. Igarashi, et al, Nano Lett. 2012, **12**, 5726

[2] A. Hegyi, E. Yablonovitch, Nano Lett. 2013,**13**, 1173

[3] R. Chapman, T. Plakkhoitnik, Opt. Lett. 2013, **38**, 1847

8:40am **2D+EM+NS+SS+TF-TuM3 2D Materials and Heterostructures for Applications in Optoelectronics**, ***Thomas Mueller***, Vienna University of Technology, Austria **INVITED**

Two-dimensional (2D) atomic crystals are currently receiving a lot of attention for applications in (opto-)electronics. In this talk I will review our research activities on photovoltaic energy conversion and photodetection in 2D semiconductors. In particular, I will present monolayer p-n junctions, formed by electrostatic doping using a pair of split gate electrodes, and MoS2/WSe2 van der Waals type-II heterojunctions. Upon optical illumination, conversion of light into electrical energy occurs in both types of devices. I will present measurements of the electrical characteristics, the photovoltaic properties, and the gate voltage dependence of the photoresponse. In the second part of my talk, I will discuss photoconductivity studies of MoS2 field-effect transistors. We identify photovoltaic and photoconductive effects, which both show strong photoconductive gain. We envision that the efficient photon conversion, combined with the advantages of 2D semiconductors, such as flexibility, high mechanical stability and low costs of production, could lead to new optoelectronic technologies.

9:20am **2D+EM+NS+SS+TF-TuM5 Excitations and Ultrafast Charge Response in Bilayer Transition-Metal Dichalcogenides**, ***Volodymyr Turkowski****, T.S. Rahman*, University of Central Florida

We analyze the absorption spectrum and ultrafast charge dynamics in bi-layer 2L-MoS2 , 2L- MoSe2 and MoS2-WS2 systems by using time-dependent density functional theory in the density-matrix representation. In particular, we calculate the values of the binding energies of excitons in these structures for both intra- and inter-layer electron-hole excitations and demonstrate that, similar to the case of a single layer, these energies can be as large as hundred(s) of meVs. We also analyze the ultrafast dynamics of the electrons, holes and excitons in the photoexcited bilayers. We pay special attention to the ultrafast hole transfer in these systems and find transfer times of the order 100fs, in agreement with the experimental finding for the MoS2-WS2 system. We perform a detailed *ab initio* study of the spatially- and time-resolved charge density in the systems during the hole transfer and conclude that sulfur and selenium orbitals play an important role in the process. Finally, we discuss possible applications of the results in light harvesting technologies.

Work supported in part by DOE Grant No. DOE-DE-FG02-07ER46354

9:40am **2D+EM+NS+SS+TF-TuM6 Automatic Localization and Identification of 2D-Material Flakes by Spectroscopic Imaging Ellipsometry**, ***Sebastian Funke****, P.H. Thiesen,* Accurion GmbH, Germany*, G. Greg Hearn*, Accurion Inc.

With the rising of 2D materials in surface sciences, the localization of mono- to few-layers of 2D materials, such as graphene, Molybdenum disulfide, hexagonal boron nitride is a time consumptive task. With the help of imaging spectroscopic ellipsometry flakes of 2D materials can be found and its layer numbers can be differentiated.

Therefore a spectroscopical mapping of the sample is done. At selected wavelengths nulling ellipsometry for each pixel in the field of view is done to measure Δ/Ψ. The measurement of all pixels is done simultaneously. To cover larger areas than the field of view a XY-patterning is done automatically. For each XY-position spectroscopic Δ/Ψ maps are obtained. Every pixel of a Δ/Ψ map represents the spectroscopic angle Δ/Ψ respectively. By comparing the spectral Δ/Ψ values for each pixel with the ellipsometric model of e.g. graphene monolayer, flakes of graphene monolayers on the sample can be found. To ensure, that only flakes are found, a grid with a threshold is used. The threshold indicates the number of pixels in the grid that need to fit to the model.

In the talk we present the capability of imaging ellipsometry to localize and identify monolayer to few-layers of 2D Materials. Flakes of MoS_2 with a size smaller than 10 µm can be localized. Monolayer of graphene can be distinguished from bilayers of graphene. To improve the time factor, the use of a Scheimpflug corrected objective is presented. Further investigations on different 2D materials, e.g. h-BN and the implementation of a Raman System is in progress.

11:00am **2D+EM+NS+SS+TF-TuM10 Systematic Hydrogen Intercalation of Epitaxial Graphene for THz Plasmonics**, ***Kevin Daniels***, National Research Council postdoc working at NRL, *A. Boyd,* American Society for Engineering Education postdoc working at NRL, *R.L. Myers-Ward, D.K. Gaskill*, Naval Research Laboratory

Epitaxial growth of graphene via sublimation of silicon and graphitization of carbon atoms from silicon carbide (SiC) is ideal for large scale manufacturing of plasmonic devices but due to partially covalent bonding between the SiC (0001) substrate and the first carbon layer (6√3 buffer layer), the high room temperature mobility necessary for THz plasmonics is reduced significantly compared to exfoliated graphene. The objective of this work is to improve THz response of EG by increasing the mobility and carrier concentration of graphene through hydrogen intercalation where the Si atoms covalently bound to the buffer layer are satisfied by hydrogen atoms and create quasi free standing graphene.

Epitaxial graphene was grown from 6H-SiC (0001) in an Aixtron/Epigress VP508 horizontal hot-wall reactor, etching in H_2 during temperature ramp to 1570°C and growing graphene in Ar ambient at 1580°C. H-intercalation of EG was carried out in the same reactor at 1050°C with a flow of 80slm of H_2 and chamber pressure of 900mbar for 15-75 minutes. Morphology of the quasi-free standing graphene was observed by AFM and SEM. Raman spectroscopy using a 532nm laser (9.6mW) and spot size of 0.3µm were used to take 80x10µm maps of each sample where release of the buffer layer is observed, with broadening of the 2D peak full-width-half-max (FWHM) before and after H-intercalation is observed on the graphene terraces and step edges. Number of monolayers before and after H-intercalation was determined by XPS.

From SEM, AFM, Raman and Hall we observe changes in degree of hydrogen intercalation with respect to time. Large areas of partially intercalated EG is observed at 15 minutes which confirmed by a mix of charge carriers and reduced carrier mobility at ~250cm^2/Vs. At 30 minutes some graphene terraces remain coupled to the SiC substrate with carrier mobility ~2250cm^2/Vs. From 45, 60 and 75 minutes the buffer layer becomes mostly quasi free standing with small spots possibly coupled to the substrate as observed in the SEM with mobilities of ~3900, ~4000 and ~3700cm^2/Vs respectively. Measurements of the resulting THz transmission spectra are currently underway to determine if the increase in mobility and carrier concentration results in narrower THz response.

11:20am **2D+EM+NS+SS+TF-TuM11 Determining the Optical Properties of Exfoliated 2D Molybdenum Disulfide on Various Substrates with Imaging Spectroscopic Ellipsometry**, ***Peter H. Thiesen***, Accurion GmbH, Germany, *S. Funke,* HAWK, Germany*, B. Miller, E. Parzinger,* TU München, Germany*, G. Hearn,* Accurion Inc.*, A.W. Holleitner, U. Wurstbauer*, TU München, Germany

Ellipsometry is a non-destructive optical method for determining film thickness and optical properties. It measures the change in the state of polarization of the light reflected from the film interfaces. Imaging ellipsometry, which combines the power of ellipsometry with microscopy, has overcome the limitation of poor sample lateral resolution found in conventional non-imaging ellipsometers. The enhanced spatial resolution of imaging ellipsometers potentially expands ellipsometry into new areas of microanalysis, microelectronics, and bio analytics.

Molybdenum disulfide is a layered transition metal dichalcogenide. From the point of current research, 2D-nano materials based on MoS_2 are very promising because of the special semiconducting properties. The bulk material has an indirect 1.2 eV electronic bandgap, but single layer MoS_2 has a direct 1.8 eV bandgap. The monolayer can be used in prospective electronic devices like transistors (MOSFETs) or photo detectors.

Wavelength spectra of ellipsometric parameters Delta and Psi of the MoS_2 monolayers and multilayers were recorded as well as microscopic maps. In case of Sapphire, The psi maps at wavelength of higher energies than the bandgap show a clear contrast between the monolayer and the substrate and at lower energies there is no contrast between the monolayer and the substrate, but the multilayer areas still show a clear contrast-making the unique properties of MoS_2 monolayers directly visible. The advantage of imaging ellipsometry is the visualisation of the shape of the monolayer and the opportunity to classify the homogenity of the optical properties of the microcrystallite. To quantify the optical properties, different approaches of optical modelling will be discussed.

11:40am **2D+EM+NS+SS+TF-TuM12 Nonlinear Optical Spectroscopy of 2D Semiconductor Monolayers**, ***Xiaobo Yin***, University of Colorado Boulder **INVITED**

Transition metal dichalcogenide (TMDC) monolayers have recently emerged as an important class of two-dimensional semiconductors with potential for electronic and optoelectronic devices. Unlike semi-metallic graphene, layered TMDCs have a sizeable bandgap. More interestingly, when thinned down to a monolayer, TMDCs transform from indirect-bandgap to direct-bandgap semiconductors, exhibiting a number of intriguing optical phenomena such as valley-selective circular dichroism, doping-dependent charged excitons and strong photocurrent responses. Using nonlinear optical spectroscopy, we probe experimentally the evidence of a series of excitonic dark states as well as structural symmetry in single-layer WS2 and MoS2.

Electronic Materials and Processing
Room: 210E - Session EM-TuM

Beyond CMOS: Materials and Devices for a Post CMOS Era
Moderator: Christopher Hinkle, University of Texas at Dallas, Suzanne Mohney, Penn State University

8:00am **EM-TuM1 Secret Ingredients in Thin-TFET: A 2D Material-based Transistor**, ***Grace Huili Xing***, Cornell University **INVITED**

Thin-TFET stands for Two-dimensional Heterojunction INterlayer Tunnel Field Effect Transistor [1]. This name was coined by my student, Mingda Oscar Li, based on one of the device concepts we submitted in the LEAST center proposal. The rationale behind this device concept was derived from our earlier work on III-V based TFETs, in particular, TFETs with tunneling aligned with the gate field [2] and our investigations on the impact of band alignment (straddling [3], staggered and broken-gap [4]) on TFET. In the recent benchmarking exercise [5,6], a few more intriguing features were discovered in this 2D embodiment of the TFET with tunneling aligned with the gate field, in additional to being the ultimate scaled TFET down to the atomic thickness. [1] M. Li et al, JAP, 074508 (2014). [2] Y. Lu et al. EDL, 655 (2012). [3] G. Zhou et al. EDL, 782 (2012); G. Zhou et al. EDL, 1516 (2011). [4] G. Zhou et al. DRC (2011); G. Zhou et al. IEDM (2012). [5] M. Li et al. J-EDS, 200 (2015); [6] D. Nikonov et al., J. Exploratory Solid-State Computational Devices and Circuits, 10.1109/JXCDC.2015.2418033 (2015).

8:40am **EM-TuM3 Application of Thermodynamics to Processing Transition Metal Dichalcogenides**, ***Suzanne Mohney****, A.C. Domask, T.N. Walter, R.L. Gurunathan, Y. Zeng*, Penn State University

We have applied thermodynamics to guide us in processing transition metal dichalcogenides for ohmic contact formation, oxidation, and etching. Annealing has been reported by a number of researchers to reduce the resistance of electrical contacts to transition metal dichalcogenides. To better understand the effect of annealing and guide our ongoing experiments, we have surveyed the condensed phase equilibria in the transition metal-Mo-S systems. The phase diagrams we have calculated or found in the literature fall into three categories: the metal is in thermodynamic equilibrium with MoS2, there is a driving force for the metal to reduce MoS2, or there is a stable solid solution or ternary phase that dominates the phase diagram. We have performed a similar analysis of the metal-W-Se systems, although there is less thermodynamic data available for the transition metal selenides than the transition metal sulfides. In this presentation, we will first compare materials characterization of annealed contacts to MoS_2 and WSe_2 to our predictions. Then, we will turn our attention to oxidation and etching. Introducing transition metal dichalcogenides to an oxidizing environment can have different effects on the material, depending on the temperature and partial pressure of the oxidizing agent. Using O_2, we find from our thermodynamic calculations that a solid product of oxidation forms on MoS_2 and WSe_2 at mildly elevated temperatures, whereas at higher temperatures we can use O_2 as a vapor phase etchant due to the volatility of the oxygen-bearing reaction products. We have found good agreement between our predictions and characterization of processed samples using light microscopy, atomic force microscopy, scanning electron microscopy, and scanning Auger microscopy.

9:00am **EM-TuM4 Stress-Directed Compositional Patterning of SiGe Substrates for Lateral Quantum Barrier Manipulation**, *S. Ghosh,* University of New Mexico*, D. Kaiser,* University of Pennsylvania*, J. Bonilla,* University of New Mexico*, T. Sinno,* University of Pennsylvania*,* ***Sang M. Han***, University of New Mexico

For large-scale manufacturing of single-electron transistors, the capability to form an addressable 2D array of quantum dots would prove useful. While vertical stacking of quantum well and dot structures is well established in heteroepitaxial semiconductor materials, however, manipulation of quantum

barriers in the lateral direction in a uniform array poses a significant engineering challenge. Here, we demonstrate lateral quantum barrier manipulation in a crystalline SiGe alloy, using structured mechanical fields to drive compositional redistribution. To apply stress, we make use of a nano-indenter array that is pressed against a $Si_{0.8}Ge_{0.2}$ wafer in a custom-made mechanical press. The entire assembly is then annealed at high temperatures, during which the larger Ge atoms are selectively driven away from areas of compressive stress. Compositional analysis of the SiGe substrates reveals that this approach leads to a transfer of the indenter array pattern to the near-surface elemental composition, resulting in near 100% Si regions underneath each indenter and a natural pathway to quantum barrier modulation. The process is studied in detail using multiscale computer simulations that demonstrate its robustness across a wide range of applied stresses and annealing temperatures. We computationally explore a carefully chosen set of indenter arrangements to show that Ge atoms can be focused into dots. We expect that this "stress transfer" method can be applied to other crystalline alloys in a scalable way.

9:20am **EM-TuM5 Interlayer Tunnel FETs**, ***Sanjay Banerjee***, Microelectronics Research Center, University of Texas at Austin **INVITED**

The scaling limits of conventional silicon based Complementary Metal Oxide Semiconductor (CMOS) devices has triggered a wide range of research in search of potential candidates for beyond CMOS logic devices. We will discuss the operation of vertical interlayer tunnel field effect transistors (ITFETs) using a stacked double bilayer graphene (BLG) and hexagonal boron nitride (hBN) heterostructure as one such potential candidate. The device is fabricated with a sequential pickup transfer method with the edges of the top and bottom BLG flakes being rotationally aligned to roughly 60° for alignment of the K points in the Brillouin zone of the two graphene layers, and using the hBN as the top, interlayer and substrate dielectric. The device shows multiple negative differential resistance (NDR) peaks which can be adjusted through the gate bias. Temperature dependent measurements show that the peak width of the differential conductance slightly broadens and the height somewhat lowered when the temperature is increased, but overall the temperature dependence is weak enough to be indicative of resonant tunneling being the primary mechanism. Through electrostatic calculations, it is shown that the multiple peaks occur when the two conduction bands at the K-point of the top and bottom bilayer graphene become aligned at certain bias conditions. It is also shown that by adjusting the rotational alignment of the bands of the top and bottom BLG through an in-plane magnetic field, the conductance peaks can be broadened or sharpened. As an example of a potential application, by utilizing the NDR characteristic of the device, a one-transistor latch or SRAM operation is demonstrated which operation margin can be adjusted through the gate bias.

11:00am **EM-TuM10 Graphene and TMD for Electronic Devices**, ***Seongjun Park**, J. Lee, J. Heo, K. Lee, E. Lee, S. Lee, S. Jung*, Samsung Advanced Institute of Technology, Republic of Korea **INVITED**

Two dimensional (2D) materials including Graphene and Transition Metal Dichalcogenide (TMD) have been considered as potential materials for post Si technology. They are atomically thin and have exceptional electronic and optoelectronic properties, such as high electron mobility and high reponsivity. In addition, they have unique mechanical properties as inorganic semiconductors, such as flexibility and even some stretchabilities due to their atomic thin nature.

TMS's have band gaps and TMD based device can have high on/off ratio. Thus, they have been considered as channel materials for atomically thin nano devices. There are various TMD materials with various band gaps and this is somewhat advantages for TMD's since they can be considered many different applications depending on their band gaps.

Unlike TMD, graphene has no band gap and it is difficult to achieve high on/off ratio. We propsed and demonstrated a new device structure, Barristor, based on one of the unique properties of graphene, work function tunability. The key feature of the device is the modulation of Schottky barrier height between graphene and semiconductor through the gate voltage modulation. This new device shows high on/off ratio of 1,000,000 or higher can be achieved. In addition, Barristor is fully compatible with curent Si technology and we were able to fabricate the devices with 6" wafer scale with CVD (Chemical Vapor Deposition) grown graphene.

In this presentation, we will cover some of our recent developments of TMD based devices. We investigated various TMD's and we will present the summary of their performances. Also we will discuss about the details od Barristor including vertical tunneling devices. In addition, we will dIscuss the issues on wafer scale developments and some of the process related issues of TMD devices and Graphene Barristor and their potential applications.

11:40am **EM-TuM12 On Smart Textiles and Vacuum: The Joys of Innovation and Discovery on Quality of Life**, ***Sundaresan Jayaraman***, Georgia Institute of Technology **INVITED**

The discovery of vacuum has had a transformational impact on the quality of life of individuals. Until recently, the term "wearable" referred to a garment that is worn by individuals. However, the invention of the wearable motherboard or smart textiles has given new meaning to the term "wearables" and it goes beyond the traditional definition of clothing. Rather, it refers to an accessory that enables *personalized mobile information processing.*

We present the the concept of the wearable motherboard integrating electronics and textiles. We discuss the role of textiles as a "meta-wearable," and how it has transformed a multitude of disciplines ranging from sports to healthcare. Finally, we the discuss the future of smart textiles as a key enabler in the context of "big data," and its impact on the quality of life of individuals.

Energy Frontiers Focus Topic
Room: 211B - Session EN+AS+EM+SE+SS-TuM

Photocatalysis
Moderator: Jason Baxter, Drexel University, Manjula Nandasiri, Pacific Northwest National Laboratory

8:00am **EN+AS+EM+SE+SS-TuM1 Ultra-dense Hydrogen and Low Energy Nuclear Reactions**, ***Sveinn Olafsson***, Science Institute, Physics department University of Iceland, *L. Holmlid*, University of Gothenburg, Sweden

For over the last 25 years the science of cold fusion/LENR has been researched around the world with slow pace of progress. Modest quantity of excess heat and signatures of nuclear transmutation and helium production have been confirmed in experiments and theoretical work has resulted in a flora of possible theoretical scenarios. [1-2]

Here we present energy production in several stages of surface processes that result first in the formation of Rydberg matter of Hydrogen [3] that can later condense in a new ultra-dense Hydrogen phase with 2.3 pm short bond distances. This phase is nuclear active showing break-even fusion reaction [7] under 100mW laser pulsing and slow spontaneous fusion occurring without laser pulsing[4,5,6]. The experimental work in around 30 publications is briefly reviewed and latest experimental results presented and discussed.

In that work high-energy particles are detected from the spontaneous processes using scintillation and other similar detectors. Both spontaneous line-spectra and a spontaneous broad energy distribution similar to a beta-decay distribution are observed indicating detection of particles such as muons. The broad distribution is concluded to be due to nuclear particles, giving straight-line Kurie-like plots. They are observed even at a distance of 3 m in air and have a total rate of 10^{7}-10^{10} s^{-1}. In the talk the link of these observation to Low energy nuclear reactions (LENR) or so called cold fusion will be discussed experimentally and theoretically.

1. The science of low energy nuclear reaction.

Storms E. World Scientific Publishing Company; **2007**.

2. The explanation of low energy nuclear reaction.

Storms E. Ienergy Press; **2014**.

3. Review paper: Experimental Studies and Observations of Clusters of Rydberg Matter and Its Extreme Forms Leif Holmlid. J Clust Sci (**2012**) 23:5–34

4. Spontaneous ejection of high-energy particles from ultra-dense deuterium D(0)

Leif Holmlid and Sveinn Ólafsson

Volume 40, Issue 33, 7 September **2015**, Pages 10559–10567)

5. Charged particle energy spectra from laser-induced processes: nuclear fusion in ultra-dense deuterium D(0) Leif Holmlid and Sveinn Ólafsson submitted **2015**.

6. Muon detection studied by pulse-height energy analysis: Novel converter arrangements

Leif Holmlid and Sveinn Ólafsson. Rev. Sci. Instrum. 86, 083306 (**2015**);

7. Heat generation above break-even from laser-induced fusion in ultra-dense deuterium

Leif Holmlid. AIP Advances 5, 087129 (**2015**);

8:20am **EN+AS+EM+SE+SS-TuM2 Optical and Surface Properties of Semiconductor Nanowires for Solar Fuels**, ***Eleonora Frau***, *J. Vukajlovic, A. Dalmau-Mallorqui, A. Fonctuberta i Morral, E. Alarcon Llado*, Ecole Polytechnique Fédérale de Lausanne (EPFL), Switzerland

Semiconductor nanowires (NWs) are filamentary crystals with new properties from their bulk counterparts. Their large versatility makes them excellent candidates as building blocks for contributing to solving the energy problem in the near future. In this work, we will assess two main properties of semiconductor NWs that have an impact to solar energy conversion.

First, it is known that light is strongly absorbed by NW arrays since light resonances give rise to effective absorption cross-sections that are much larger than the geometrical ones. Optical resonances depend on NW geometry and dielectric environment, and can result into absorption effective diameters up to 25 times larger than the geometrical for certain wavelengths. We have used finite-difference time-domain (FDTD) electromagnetic simulations to understand and design NW-based sunlight scavengers. For instance, a GaAs NW array that is only covering 3% of the surface can generate more photocurrent than a planar film, considering a 30% reflectivity (see figure1). Also that thanks to optical resonances, an indirect-bandgap material such as Si is capable of absorbing most of the light within a 2um long NW array that only covers 7% of the device surface.

On the other hand, it is also known that surface states and traps detriment device performances. However, in case where solar energy is directly converted into fuel (such as hydrogen) in a photoelectrochemical (PEC) cell, the large surface-to-volume ratio of NW forests is an important asset. Since the electrochemical reactions happen at the semiconductor surface, NWs enable the use of low-cost catalysts (e.g. MoSx) even though they exhibit lower performances than noble metals (e.g. Pt). In order to assess the effects of nanostructuring photo-electrodes for solar fuel generation, we have studied photo-cathodes based on Silicon nanopillar structures. The photo-cathodes were fabricated by using a top-down approach and their diameters range from ~200 to 900nm and lengths ~2um. We observe that reducing the size of the nanostructure, increases the overpotential, and thus the overall efficiency (see figure 2). By coating the surface with thin TiO_2 layers, the performance is improved in terms of overpotential and fill factor. We explain these findings by using an electrico-kinetic model of the semiconductor-water junction. We find that the TiO_2 layers actually act as a hole blocking layer, preventing recombination.

8:40am **EN+AS+EM+SE+SS-TuM3 Engineering Surfaces and Interfaces for Photoelectochemical (PEC) Water-Splitting**, ***Thomas Jaramillo***, *J.D. Benck,* Stanford University, *J. Kibsgaard,* SLAC National Accelerator Laboratory, *T.R. Hellstern, C.J. Hahn, P. Chakthranont, R. Britto, K.D. Fong*, Stanford University **INVITED**

The talk will focus on engineering surfaces and interfaces for solar photoelectrochemical (PEC) water-splitting for the direct, renewable production of H_2. In particular, this talk begin by describing research efforts to develop H_2 evolution catalysts that are active, stable, and comprised of only earth-abundant elements, including transition metal sulphides, phosphides, and phosphosulfides.[1-3] Next, we will describe recent efforts to integrate these catalysts onto semiconductor surfaces to provide corrosion protection as well as enhanced interfacial catalysis for PEC water-splitting.[4] This talk will focus on the need for high turnover frequency (TOF) catalysts, which ultimately enable the greatest flexibility in designing optimum interfaces for high performance devices.

[1] J. Kibsgaard, T.F. Jaramillo, F. Besenbacher, "Building an appropriate active site motif into a hydrogen evolution catalyst with thiomolybdate $[Mo_3S_{13}]^{2-}$ clusters," *Nature Chemistry*, **6** (2014) 248.

[2] J.D. Benck, T.R. Hellstern, J. Kibsgaard, P. Chakthranont, T.F. Jaramillo, "Catalyzing the Hydrogen Evolution Reaction (HER) with Molybdenum Sulfide Nanomaterials," *ACS Catalysis*, **4** (2014) 3957.

[3] J. Kibsgaard and T.F. Jaramillo, "Molybdenum Phosphosulfide: An Active, Acid-Stable Earth-Abundant Catalyst for the Hydrogen Evolution Reaction," *Angewandte Chemie*, **53** (2014) 14433.

[4] J.D. Benck, S.C. Lee, K.D. Fong, J. Kibsgaard, R. Sinclair, T.F. Jaramillo, "Designing active and stable silicon photocathodes for solar hydrogen production using molybdenum sulfide nanomaterials," *Advanced Energy Materials*, **4** (2014) 1400739.

9:20am **EN+AS+EM+SE+SS-TuM5 Bulk and Surface Effects of Incorporating Titanium Into Hematite Thin Films to Improve Photoelectrochemical Water Splitting**, ***Anthony Abel***, *A.M. Patel,* Drexel University, *I.G. Torregrosa,* Utrecht University, Netherlands, *B. Opasanont, J.B. Baxter*, Drexel University

Hematite (α-Fe_2O_3) has emerged as a promising photoanode material for photoelectrochemical (PEC) water splitting due to its chemical stability, earth-abundance, low cost, and suitable band gap for both water splitting and visible light absorption. However, poor charge separation due to low hole mobility and high recombination rate, and sluggish oxygen evolution reaction kinetics have limited its potential as an economical water-splitting catalyst. Here, we investigate titanium incorporation into hematite photoanodes and provide insight into the role of Ti^{4+} in improving PEC performance. Planar hematite thin films (~45 nm thick) were deposited by successive ionic layer adsorption and reaction (SILAR) of FeOOH on an FTO/glass substrate and subsequent annealing to induce phase transition to α-Fe_2O_3, and titanium was incorporated up to 10% Ti/(Ti+Fe) by either modification of the SILAR solution (SM:α-Fe_2O_3) or solid-state diffusion (SSD:α-Fe_2O_3) during the annealing process. PEC measurements revealed substantial improvements in both charge separation efficiency and hole injection into the electrolyte, increasing photocurrent from nearly zero to ~0.6 $mAcm^{-2}$ under 1-sun irradiation at 1.23 V_{RHE}. Mott-Schottky analysis indicated a 100 mV cathodic shift in the flat band potential upon doping with Ti^{4+} regardless of fabrication method, but a 100-fold increase in carrier density only in SM:α-Fe_2O_3 films, resulting in a high 20 % separation efficiency at 1.23 V_{RHE} with optimized 5 % Ti/(Ti+Fe) in the modified SILAR solution. Electrochemical impedance spectroscopy showed a 4x increase in the surface state capacitance peak near the water oxidation onset potential, possibly due to reduced Fermi level pinning as a result of more efficient hole injection into the electrolyte . More importantly, doping with titanium resulted in a 100-fold decrease in the charge transfer resistance from surface states to the electrolyte, revealing the strong influence of Ti^{4+} on interfacial kinetics . Further surface modification with an ultrathin FeOOH surface passivation layer raised the plateau photocurrent to ~0.8 $mAcm^{-2}$ at 1.23 V_{RHE}, representing a 3x improvement over previous reports of SILAR-deposited hematite films and comparable with record performance for planar hematite deposited using high vacuum synthesis techniques.

9:40am **EN+AS+EM+SE+SS-TuM6 Iron Oxide Nanoparticle Growth on Highly Oriented Pyrolytic Graphite (HOPG) and Photocatalytic Properties of Pt on Iron Oxide**, ***Jayde Kwon***, *J.C. Hemminger*, University of California, Irvine

Highly oriented pyrolytic graphite (HOPG) is an ideal substrate to study the fundamental growth mechanism of iron oxide independent from substrate effects. Platinum on iron oxide is a model heterogeneous catalyst with importance to biotechnology and solar cell applications. Selective growth of iron oxide nanoparticle (NP) either on step edges of HOPG or oxygen plasma treated HOPG by physical vapor deposition (PVD) will be presented. The successful selective iron oxide NP growth was validated by scanning electron microscopy (SEM), transmission electron microscopy (TEM), and X-ray photoelectron spectroscopy (XPS). The development of the NP array system is highly significant in that it can provide an ideal template for theoretical calculations for fundamental metal growth studies. Pt nanoparticles was subsequently deposited on the iron oxide nanoparticles using a selective photodeposition technique. The application of these nano-systems (Pt nanoparticles on iron oxide nanoparticles) towards photocatalysis of methylene blue will be presented. Although iron oxide is a promising semiconductor photocatalyst, it suffers from a short hole diffusion length, low electrical conductivity and a high rate of electron hole recombination. However, this bimetallic system using platinum deposited on iron oxide overcomes these barriers. A novel method was developed using small quantities of Pt on iron oxide to significantly enhance methylene blue decomposition. This system is also being explored as a catalytic model for water-gas shift reactions.

11:00am **EN+AS+EM+SE+SS-TuM10 Interface Design for Efficient and Stable Photoelectrochemical Water Splitting**, ***Joel Ager***, Lawrence Berkeley National Laboratory **INVITED**

Solar photoelectrochemical (PEC) water splitting is potential future carbon-neutral energy source which could dramatically change the landscape of global energy generation and storage. The half reactions for water splitting are as follows:

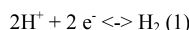

$2H^+ + 2e^- <-> H_2$ (1)

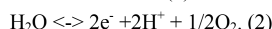

$H_2O <-> 2e^- + 2H^+ + 1/2O_2$. (2)

The free energy change for the overall reaction, $H_2O <-> H_2 + 1/2O_2$ corresponds to 1.23 eV per electron transferred; however, typically >1.5 V is required to overcome kinetic limitations, particularly for the O_2 evolution reaction. The most commonly used approach for integrated solar water splitting employs photocathodes (H_2 or hydrocarbon producing) and photoanodes (O_2 producing) linked in a tandem geometry [1].

The interface challenges required to demonstrate a practical system which is both efficient and stable under operation are substantial and severe. In addition to constructing interfaces, either solid-solid or solid liquid, which achieve the desired photovoltaic charge separation, the surfaces of these photoelectrodes can be a failure point under sustained operation due to

corrosion. We have found that the use of nanoscale conformal oxide layers can greatly reduce corrosion rates. Moreover, it is possible to achieve both high performance and lifetime by the use of protection layers which are also tuned for selective carrier contact.

Examples of such a strategy will be shown for photocathodes [2-5] and for photoanodes [5]. Recent work on p-type transparent oxides (p-TCOs) used as selective hole contacts for photoanodes will be emphasized. For example, it will be shown that using $NiCo_2O_4$ as the p-TCO and n-type Si as a prototypical light absorber, a rectifying heterojunction capable of light driven water oxidation can be created. By placing the charge separating junction in the Si using a np^+ structure and by incorporating a highly active Ni-Fe oxygen evolution catalyst, efficient light-driven water oxidation can be achieved. The generality of the p-TCO protection approach is demonstrated by multi-hour, stable, water oxidation with n-InP/p-$NiCo_2O_4$ heterojunction photoanodes.

Acknowledgements. This material is based upon work performed by the Joint Center for Artificial Photosynthesis, a DOE Energy Innovation Hub, supported through the Office of Science of the U.S. Department of Energy under Award Number DE-SC0004993.

References.

1. J. W. Ager *et al.*, Energy Environ. Sci. (2015). DOI:10.1039/C5EE00457H

2. M. H. Lee *et al*., *Ang. Chemie Int. Edition***51** 10760 (2012).

2. Y. Lin *et al*., *Nano Letters***13** 5615 11 (2013)

3. Y. Lin *et al.*, *J. Phys. Chem*. C **119**, 2308 (2015).

4. J. Yang *et al*., *J. Amer. Chem. Soc.***136** 6191 (2014).

11:40am **EN+AS+EM+SE+SS-TuM12 Buried, Hetero, and p-i-electrolyte III-V Photoelectrochemical Junctions with Significantly Enhanced Photocurrent Onset Potentials**, ***James Young***, *H. Doscher, J. Turner, T. Deutsch*, National Renewable Energy Laboratory

To approach the maximum achievable solar-to-hydrogen (STH) conversion efficiencies with photoelectrochemical (PEC) devices, it is necessary to employ the lowest possible band gap (E_g) absorbers that can still provide sufficient voltage to drive water splitting at high rates (1.7-1.8 V for 25% STH). The record 12.4% STH was achieved by a $GaInP_2$/GaAs PEC/photovoltaic (PV) tandem device while an all solid state $GaInP_2$/GaAs PV/PV tandem produces an open-circuit voltage that approaches 2.4 V. Since GaAs (E_g = 1.4 eV) is the current-limiting junction in these devices, it can be substituted by InGaAs with E_g = 1.0 eV to reach 25% STH. The current-for-voltage tradeoff of using lower-E_g absorbers moves toward the constraint of insufficient voltage for spontaneous water splitting. To address this approaching constraint, we investigate several alternative device structures at the III-V/electrolyte interface that show photocurrent onset potential enhancements of a few hundred mV. We will present band diagram calculations and electrochemical measurements to discuss the voltage performance of these structures.

12:00pm **EN+AS+EM+SE+SS-TuM13 X-ray Absorption Studies on the Li-S Battery Cathode Side**, ***Yifan Ye***, University of Science and Technology of China, *A. Kawase*, Lawrence Berkeley National Laboratory, *H.X. Ju*, University of Science and Technology of China, *E. Cairns*, Lawrence Berkeley National Laboratory, *J.-H. Guo*, Lawrence Berkeley Lab, University of California, Berkeley, *J.F. Zhu*, University of Science and Technology of China

As increasing global energy consumption in the coming days, sustainable, clean energy technologies are highly desirable. The high theoretical specific capacity of 1675 mA·h/g for elemental S has prompted intense effort to study the Lithium-Sulfur batteries. With the application of cetyltrimethyl ammonium bromide (CTAB), modified sulfur-graphene oxide (S-GO) nano-composite based Li/S batteries exhibited a very high initial discharge capacity of 1440 mA·h/g of sulfur at 0.2C with excellent rate capability of up to 6C for discharge and 3C for charge while still maintaining high specific capacity. And the batteries demonstrated cycling performance up to 1500 cycles with extremely low decay rate of 0.039% per cycle. With the introduction of CTAB, the performance of the GO-S based Li-S battery has been improved significantly, thus it is important to figure out the role of CTAB played in the system. During the synthesis process of the cathode materials, S and Na_2S were used as the precursors, the ratio of S/Na_2S is crucial to the components of the precursors. Moreover, the sequence of mixing GO/CTAB solution with precursor solution is a key point to effective cathode synthesis procedure. Understanding these information helps to optimize the methodology for the controllable synthesis of desired cathode material that can be used to fabricate an efficiency and well-performed Li/S battery. S K-edge X-ray absorption spectroscopy (XAS) is applied to study the chemical species evolution during the GO-S-CTAB cathode material synthesis. The influences on the cathode materials related to the battery performance are monitored by S K-edge XAS. The research revealed the interaction between CTAB and GO, S, Na_2S and Na_2S_x. It indicated that CTAB can physical absorbed on Na_2S_x molecules by bonding with the terminal S atoms of Na_2S_x chains, and this kind of bonding can convert to chemical C-S bonding with heating treatment. Thus the interaction of CTAB with GO, formed C-S between CTAB and S and interaction of GO and S provided a tight tri-layer structure which can immobilize the S particles on GO sheet and finally enhanced the battery performance. The information from this work proved the importance of Na_2S:S ratio, CTAB/GO adding procedure in the fabrication process, and we can easily apply XAS to optimize these recipe. And moreover, this work proved strong evidence that XAS tools can be used to do the initial characterization on the battery performance before real cycling procedure.

Thin Film
Room: 111 - Session TF+EM+MI+MS-TuM

ALD for Alternative Devices
Moderator: Paul Poodt, Solliance/TNO, Richard Vanfleet, Brigham Young University

8:00am **TF+EM+MI+MS-TuM1 FAST-ALD™ with Close Proximity (CP) Plasma for Low Temperature Applications: Nano-Composite Layer (NCL) Stacks for Flexible Substrates**, ***SangIn Lee***, Veeco **INVITED**

The stress of the film is an important factor in mechanical stability and reliability of the devices, especially flexible electronic applications and microelectro-mechanical systems (MEMS), because it causes mechanical cracks, delamination and degradation in reliability of the device. Moreover, mechanical integrity of nano-scaled devices requires not only the physical properties of the individual films such as thermal expansion coefficient and elastic modulus, but also integral structural properties such as interface adhesion, and therefore residual stress of the film need to be managed.

Veeco's proprietary ALD technology, Fast Array Scanning Technology (FAST-ALD™) with Close-Proximity (CP) Plasma, has unique characteristics that are differentiated from other spatial ALD technologies. CP-plasma in FAST-ALD™ provides very uniform radical streams onto the substrate without plasma-induced damages and substrate heating enabling FAST-ALD™ to provide plasma-ALD films and stable polymeric MLD films from CP Plasma which cannot be obtained from conventional plasma process, for high-quality films at extremely low temperature for use in stress-sensitive device applications such as low-k films on Si wafers or flexible functional films on plastic substrates.

Stresses in inorganic ALD layers can be offset by either carbon-incorporated dielectric (CID) interlayers or polymeric MLD interlayers. The relative percentage of the inorganic ALD film to CID interlayer can be changed to tailor the stress of the stacked film to the device requirements. In this experiment, the combinations of an inorganic dielectric layer (Al_2O_3) with CID interlayers as part of nano-laminates, obviously in the same philosophy with polymeric MLD interlayers, nano-composite layer (NCL) stacks were deposited at 80°C to control the stress of the stacks from tensile to compressive state and vice versa, by changing the thickness and atomic content of Al_2O_3 layer and materials. By changing the ratio of the thickness in NCL stacks, 4:2 stacked film (4 Al_2O_3 layers and 2 CID layers as a sub-stack) and 1:1 stacked film (1 Al_2O_3 layer and 1 CID layer as a sub-stack) with total 30nm thickness show very low tensile stress and compressive stress of +58MPa and -89MPa, respectively, indicating the potential application of these free standing film stacks to nano-scaled devices and/or environmentally sensitive devices. NCL stack shows higher immunity to cracks and competitive barrier properties than that of the single ALD layer. NCL concept approaches can be applied to semiconductor in low-k pore sealing and oxidation barrier in the backend-of-line (BEOL) and cutting-edge devices with flexible substrates.

8:40am **TF+EM+MI+MS-TuM3 Atmospheric Roll-to-Roll Spatial Molecular Layer Deposition for flexible barriers**, ***Fieke van den Bruele***, *F. Grob, P. Poodt*, Holst Centre / TNO, Netherlands

Proper encapsulation of devices such as OLEDs and thin-film photovoltaics is critical, as exposure to moisture from the ambient will degrade these devices, reducing their efficiency, lifetime, or even lead to failure altogether. Especially for OLEDs, the barrier requirements are very challenging, with a Water Vapor Transmission Rate < 10^{-6} g/m^2/day. To achieve these very low WVRTs, very high quality barrier layers are required, being pinhole free over the entire device area. Encapsulation of flexible devices is even more challenging as the encapsulation should not affect the device flexibility too much.

The recent development of roll-to-roll and large-area Spatial ALD technology has spurred the interest in ALD for encapsulation and barriers. Thin layers of inorganic material (10-20 nm) made with (spatial) ALD have sufficiently low intrinsic WVTR but often do not meet the requirements for barriers because they are very sensitive to particles and roughness that lead to defects. Thick inorganic films are less sensitive to particles, but suffer from stress and can have a limited flexibility. Various flexible thin film encapsulation techniques have been recently developed, often combining one or more thin inorganic diffusion barrier layers (e.g. SiN_x, Al_2O_3) with an organic layer that acts as stress relief layer but has no additional barrier functionality. One of those proposed interlayers for stress relief and flexibility are organic materials deposited through Molecular Layer Deposition (MLD). A well-studied example are the Alucones, prepared by reacting trimethyl aluminum with an alcohol. There are several reports on the barrier properties of Al_2O_3 – Alucone multilayer stacks, but the results seem to be inconclusive.

Assessing the flexibility these MLD layers are is not straightforward as measuring the mechanical properties of these very thin layers is difficult. We use a simple, qualitative method to test the flexibility of these MLD layers, by combining bending test with a polymer etch test to visualize cracks and other defects in the MLD film caused by bending. Preliminary results show that the flexibility of MLD layers, like their organic counterparts, largely depend on film thickness and can suffer from instability.

The next step in making MLD barriers is upscaling towards large-area and roll-to-roll production. We will present the results of our atmospheric roll-to-roll spatial MLD of alucones on polymer foils. Furthermore, an outlook to full-industrial scale R2R ALD/MLD production of barriers will be discussed.

9:00am **TF+EM+MI+MS-TuM4 Low Temperature, Temporal and Spatial Atomic Layer Deposition of TiO_2 using Titanium Tetra-Isopropoxide as Precursor**, ***Morteza Aghaee,*** Eindhoven University of Technology, Netherlands, *P.S. Maydannik,* Lappeenranta University of Technology, Finland, *P. Johansson,* Tampere University of Technology, Finland, *M. Creatore,* Eindhoven University of Technology, Netherlands, *T. Homola, D.C. Cameron,* Masaryk University, Czech Republic, *J. Kuusipalo*, Tampere University of Technology, Finland

Spatial atomic layer deposition (S-ALD) is a technique which has been shown to lead to high quality moisture barrier films (e.g. Al_2O_3) in a roll-to-roll process[1]. However, TiO_2 is expected to outperform Al_2O_3 because of its higher stability against long-term degradation than Al_2O_3. For high throughput S-ALD at low temperature, highly reactive precursors with high vapour pressure are necessary. Titanium chloride is typically used but has the disadvantages of residual chlorine incorporation in the film and generation of corrosive by-products. Titanium tetra-isopropoxide (TTIP) is a valid alternative because of its high vapour pressure at room temperature compared to other titanium organometallic compounds[2]. TTIP has not previously been used as a precursor for S-ALD.

In this work, a preliminary investigation has been carried out on the temporal ALD approach consisting of alternating exposure of a polyethylene naphthalate (PEN) substrate to the precursors TTIP and water, ozone or oxygen-fed plasma. The deposition was carried out at a substrate temperature of 80-120ºC. The highest growth rate (0.056 nm/cycle) and refractive index (2.33) values have been obtained by using an O_2- fed plasma. The water vapour transmission rates have been found to be lower than 5×10^{-4} $g.m^{-2}.day^{-1}$ at 38°C, 90% RH conditions for a film thickness of 20 nm. For the water process, WVTR values were found to be in the range of 10^{-3} for a 40 nm film.

Based on these results, a low pressure S-ALD process was developed using a Beneq TFS200R system. Titanium dioxide films were successfully deposited by TTIP and water as S-ALD precursors in the same temperature range as temporal, and their properties were characterised in terms of growth per cycle, refractive index and chemical composition. The growth rate saturated at precursor exposure time of 230 ms at every deposition temperature, which was slightly higher than the growth rate in temporal ALD mode at the same temperature range. Similar properties (refractive index and chemical composition) to temporal ALD have been obtained by adopting S-ALD.

---

[1] P. S. Maydannik, T. O. Kääriäinen, K. Lahtinen, D. C. Cameron, M. Soderlund, P. Soininen, P. Johansson, J. Kuusipalo, L. Moro, and X. Zeng, J. Vac. Sci. Technol. A **32**, 051603 (2014).

[2] M. Aghaee, P. S. Maydannik, P. Johansson, J. Kuusipalo, T. Homola, M. Creatore, D. C. Cameron, Submitted to J. Vac. Sci. Technol. (2015)

9:20am **TF+EM+MI+MS-TuM5 Spatial Atomic Layer Deposition into Flexible Porous Substrates**, ***Kashish Sharma,*** University of Colorado at Boulder, *D. Routkevitic, N. Varaksa,* In Redox, *S.M. George*, University of Colorado at Boulder

Spatial atomic layer deposition (S-ALD) is important for ALD commercialization. S-ALD has been successfully demonstrated on flat substrates. In this work, S-ALD was examined on flexible porous substrates using anodic aluminum oxide (AAO) membranes and Li ion battery electrodes. The AAO membranes were coated with ZnO ALD using diethylzinc and ozone as the reactants. The Li ion battery electrodes were coated with Al O ALD using trimethylaluminum and ozone as the reactants. These experiments utilized a rotating cylinder reactor for S-ALD that is scalable to roll-to-roll operation [K. Sharma et al., , 01A132 (2015)].

ZnO S-ALD into the pores of AAO membranes depends on gas transport that is determined by the pore diameter, pore aspect ratio and reactant pulse duration. The reactant pulse duration is defined by the substrate speed in S-ALD. Different reaction conditions and AAO membrane characteristics were explored using energy dispersive spectroscopy (EDS) to measure the Zn coverage profiles. Substrate speeds were defined by rotating cylinder rates of 10, 100 and 200 revolutions per minute (RPM). The AAO pore diameters were 50, 100 and 150 nm.

For AAO pore lengths of 10 microns, the EDS analysis revealed that uniform Zn coverage profiles were obtained at 10 RPM. The Zn coverage profiles were less uniform at higher RPM values and smaller pore diameters. These results indicate that S-ALD into porous substrates is feasible. However, the uniformity of the ALD coverage will depend on reaction parameters and the characteristics of the porous substrate. In addition, $LiNi_{1/3}Mn_{1/3}Co_{1/3}O_2$ Li ion battery electrodes on flexible metal foil were coated with Al_2O_3 ALD using the S-ALD reactor at 10-100 RPM. Initial coin-cell testing has demonstrated that enhanced capacity stability of these cathode electrodes is obtained after 2-5 Al_2O_3 ALD cycles.

9:40am **TF+EM+MI+MS-TuM6 Accurate Precursor and Reactant Delivery for Quantitative Atomic Layer Deposition**, ***Masafumi Kitano,*** Stanford University, *M. Nagase, N. Ikeda,* Fujikin Incorporated, Japan, *P.C. McIntyre*, Stanford University

Atomic layer deposition (ALD) has been widely discussed in the literature from various points of view. Typically, the amount of the precursor and reactant supplied into the ALD chamber is dictated only by controlling valve operation time, and is not quantitatively defined. To achieve a more quantitative ALD process, we have developed new flow rate control system (FCS) which can accurately dose precursor and reactant into an ALD reactor. This FCS consists of an orifice plate, pressure sensor, thermal sensor, and piezo control valve. It can be heated to 250˚C to achieve sufficient vapor pressure for most precursors used in ALD of various inorganic compounds and elements. The FCS controls the flow rate under critical expansion conditions (or choked flow conditions); the flow rate through the orifice is proportional only to the upstream pressure of the orifice.[1,2] The piezo control valve accurately controls the upstream pressure and, thus, the flow rate. This mode of operation makes it possible to control the dosing of precursor and reactant by simply operating an endpoint valve placed close to the ALD reactor, because the upstream pressure is controllable whether the gas flow is running or not.

We have demonstrated an ALD process with trimethylaluminum (TMA) and water vapor (H_2O) reaction for Al_2O_3 deposition using the FCS to accurately control dosing into the ALD reactor. Excellent uniformity and reproducibility of deposition, and high quality dielectric properties of the resulting Al_2O_3 films have been achieved. The critical doses of TMA and H_2O into the chamber have been found to achieve surface saturating ALD of Al_2O_3 on a silicon substrate.

[1] A. Guthrie, R. K. Wakerling, "Vacuum Equipment and Techniques" McGraw-Hill book company, Inc., pp17, (1949)

[2] R. H. Perry, D. Green, "Perry's Chemical Engineers' Handbook, Sixth Edition" McGraw-Hill Co., pp5-14, (1984)

11:00am **TF+EM+MI+MS-TuM10 ALD for Capacitor Technologies**, ***Ramakrishnan Rajagopalan***, *C. Randall*, The Pennsylvania State University **INVITED**

Atomic layer deposition (ALD) is a powerful processing technique that can be used to modify interfacial processes occuring in electrochemical capacitors. Charge storage mechanism in electrochemical capacitors is either due to electrostatic double layer formation or pseudocapacitive faradaic interactions at electrode/electrolyte interfaces. The talk will present an overview of our efforts in developing pseudocapacitive vanadium oxide thin films using ALD approach on high surface area carbon electrodes. The deposition process is dependent upon the carbon properties such as surface functionalization and porosity. We will report our investigation of deposition of ALD films on nanostructured carbon electrodes with

controlled porosity in mesopores (<20 nm) to ultramicropore (0.8 nm to 2 nm) ranges. ALD also facilitates the possibility of combining electrochemical effects with dielectric effects. ALD of dielectrics such as Al_2O_3 on electrodes used in aqueous, organic and lithium based electrolytes can mitigate the issues relating to electrochemical stability due to solvent decomposition reactions and leakage performance with limited effect on the ESR performance of the capacitor. There is also possibility of designing novel solid state capacitor structures that synergistically integrates the electrical double layer interactions due to ions with dielectric energy storage.

11:40am **TF+EM+MI+MS-TuM12 Compositionally and Functionally Graded Hybrid Layer for High-Performance Adhesion**, ***Yichuan Ding***, *R.H. Dauskardt*, Stanford University

Reliable bonding of organic/inorganic interfaces continues to be one of the most important challenges in multilayer devices including microelectronic, photovoltaic and display technologies. Hybrid molecular materials which contains both organic and inorganic components has been shown to be well suited for bonding organic/inorganic (metals, metal-oxides, nitrides, …) interface, mitigating moisture degradation and even stress migration. The hybrid films (less than 100nm) made of two primary precursors, an epoxysilane and a zirconium alkoxide, have been deposited via solution based synthesis, with low cost and high throughput. By optimizing sol-gel chemistry and processing conditions, we achieved an impressive tenfold improvement in interfacial adhesion at the epoxy/Si substrate interface, and have proven the suppression of moisture degradation at the interface.

In this work, we emphasized on our newly developed spray deposition technique with more versatility and better suited to large-scale manufacturing. We utilized both bilayer coating and dual-sources spray strategies to create highly compositionally and functionally graded hybrid film compared with films achieved via traditional dip-coating. XPS depth profiling shows highly graded hybrid films with independent compositional control within 80nm can be achieved via spray coating in the dry regime. We took advantage of the compositional control brought by spray coating to unravel the structure-property relationships in the multi-functional hybrid films by varying components/parameters to fine tune the molecular structure of the resulting film and relate that to its properties obtained from our advanced thin-film mechanical testing techniques together with other chemical characterization techniques (XPS, FTIR, NMR and GCMS). The evolution of the hybrid molecular network during film process and how molecular level details of the hybrid film has a large effect on its mechanical properties were better understood.

2D Materials Focus Topic
Room: 212C - Session 2D+EM+MC+MI+NS+SP+SS+TF-TuA

Electronic and Magnetic Properties of 2D Materials
Moderator: Thomas Mueller, Vienna University of Technology, Austria, Xiaobo Yin, University of Colorado Boulder

2:20pm **2D+EM+MC+MI+NS+SP+SS+TF-TuA1 Direct Capacitive Probe of Isospin Order in Graphene Bilayers**, ***Andrea Young***, University of California at Santa Barbara **INVITED**

Bilayer graphene is a highly tunable electronic system in which electric fields can be used to control both the carrier density as well as the electronic structure. Like its monolayer cousin, the bilayer graphene Landau levels are characterized by approximate spin and valley degeneracy; unlike monolayer, however, the three dimensional structure of the bilayer allows control of the sublattice splitting with a perpendicular electric field. This feature has been used extensively to probe the phase diagram of interacting electrons, particularly within the zero energy Landau level, revealing a number of interacting states characterized by spin and/or valley order. Typically, however, the spin or valley order is inferred indirectly by varying conjugate fields and inferring the order from the resulting changes in conductivity. Here I will describe a technique capable of resolving layer-polarization directly through high sensitivity capacitance measurements. The measurements confirm the known features of the bilayer graphene phase diagram, while revealing several new phases and a series of sharp features associated with phase transitions between states of different layer polarization. These features suggest a new mechanism for inversion symmetry breaking in Bernal stacked bilayer graphene.

3:00pm **2D+EM+MC+MI+NS+SP+SS+TF-TuA3 Patterning Hydrogenated Graphene via Electron Beam Irradiation**, ***Woo-Kyung Lee***, *K.E. Whitener, J.T. Robinson, P.E. Sheehan*, Naval Research Laboratory

We demonstrate that electron-beam irradiation selectively removes hydrogen atoms from hydrogenated graphene (HG) prepared by the Birch reduction.[1] Hydrogen removal can pattern the surface with two different functionalities. First, we show that partially-hydrogenated graphene (Phg) on a SiO_2 substrate is ferromagnetic, and that the local magnetic strength can be tuned using e-beam irradiation. An e-beam lithography system enables us to modulate or eliminate the permanent magnetization over a large area to produce a patterned magnetic array. Secondly, since removal of the hydrogens converts the highly electrically insulating HG back into conductive graphene, we can write chemically isolated, dehydrogenated graphene nanoribbons (GNR) as narrow as 100 nm. These GNRs have a low sheet resistance (≥ 31.5 Kω/□), only 10x that of the pristine graphene, and their Dirac points before and after e-beam irradiation appear at comparable gate voltages.

1. *W.K. Lee et al., Advanced Materials, 27, 1774 (2015).*

3:20pm **2D+EM+MC+MI+NS+SP+SS+TF-TuA4 Large-Area Low-Pressure Synthesis of Single-Layer MoS_2 Films and Schottky-Barrier Formation upon Metal Deposition**, ***Michael Gomez***, *J. Martinez, M. Valentin, L. Bartels*, UC Riverside

Using a high vacuum CVD process we are able to synthesize large are monolayer MoS_2 films. Organic chalcogen precursors are released into the growth chamber and react with a Mo filament creating films up to $2cm^2$ in size that are uniform and free of oxides. The films have pronounced photoluminescence intensity and are in Raman spectroscopy indistinguishable from exfoliated material. Metal contact formation to these films was investigated under UHV conditions utilizing X-Ray Photoelectron Spectroscopy . These measurements permit us to follow the formation of a Schottky Barrier with increasing metal film thickness on the Angstrom scale. We utilize core level spectroscopy to indicate the evolution of the MoS_2 valence band under metal deposition.

4:20pm **2D+EM+MC+MI+NS+SP+SS+TF-TuA7 Accelerating the Discovery of Alternative Fuel Catalysts through Intelligent Computational Framework**, ***Altaf Karim***, COMSATS Institute of Information Technology, Pakistan **INVITED**

In today's modern world of high performance computing, properties of materials can be predicted with high accuracy before these materials are ever made. In this scenario my focus has been on the development of state of the art computational framework based on intelligent/ smart self-learning algorithms for the design and discovery of catalytic materials. By giving some examples, I will describe how this enterprise of the predictive multi-scale modeling/simulation has been passing through the stages of its evolution and how these complex algorithmic species integrated themselves into an intelligent python, which is helping scientists design & discover new materials for alternative fuel catalysis. In practice, our computational framework develops databases of candidate catalysts. Further this framework enables a set of algorithms to screen across a broad range of multi metallic catalytic materials with variable reactivity, selectivity, and stability while searching for materials with desired combination of properties required for the optimal catalytic performance for alternative fuel production. I would also explain that how our computational tools in catalyst design deal with the multi-component microstructures of catalysts composed of multi-element nano chunks. In order to tune up the rate limiting processes we can take advantage of the multi-element nano chunks. For example, on many catalytic surfaces the diffusion is rate limiting process for larger organic molecules. To enhance the diffusion such molecules on such surfaces, nano chunks of other materials (on which the diffusion of the organic molecules is comparatively higher) can be integrated in the catalyst's surface, which improves the overall performance of the catalyst in terms of overall reactivity and also selectivity. In addition to that our tools also help us to filter out, from the databases, stable multi-component microstructures of artificially engineered catalysts.

5:00pm **2D+EM+MC+MI+NS+SP+SS+TF-TuA9 Probing Massive Dirac Electrons in Bilayer Graphene**, ***Feng Wang***, University of California at Berkeley **INVITED**

Electrons in monolayer graphene are described by massless Dirac electrons, which exhibit unique quantum phenomena due to the pseudospin and Berry phase of the massless electrons. In this talk, I will discuss our effort in probing massive Dirac electrons in gapped bilayer graphene. In particular, I will discuss the topologically protected 1D conducting channel at the domain boundary of AB-BA bilayers, which can be attributed to the quantum valley Hall edge states in gapped bilayer graphene.

5:40pm **2D+EM+MC+MI+NS+SP+SS+TF-TuA11 Combining Photoemission and Photoluminescence Microscopy to Study Substrate Transfer Process Effects in Chemical Vapor Deposited MoS_2 Monolayers**, ***Olivier Renault***, *M. Frégnaux,* Univ. Grenoble Alpes/ CEA, LETI, MINATEC Campus, France, *J. Bleuse,* Univ. Grenoble-Alpes & CEA-INAC, France, *H. Kim,* Univ. Grenoble Alpes/ CEA, LETI, MINATEC Campus, France, *D. Voiry, M. Chhowalla*, Rutgers University

Within the perspective of integrating two-dimensional transition metal dichalcogenides (2D TMDs) such as molybdenum disulfide (MoS_2), into devices, it becomes of utmost importance to assess the influence of each step of the device fabrication process on the optical and transport properties of the MoS_2 single layer (1L) domains. Particularly at the deposition stage the properties may be influenced by substrate effects [1], and later, transfer processes may further alter the desired properties of TMDs. This requires effective microscopic characterization techniques.

We present a characterization method combining photoemission microscopy (XPEEM and Kpeem) and photoluminescence microscopy to compare the structural, optical and electronic properties of both as-deposited and transferred MoS_2 1L domains onto different substrates. XPEEM is used with laboratory sources in both direct space imaging for work function and core-level mapping [2] and particularly in the momentum microscopy mode (k-PEEM) to perform parallel angular imaging and retrieve the band structure in a one shot experiment [3]. Micro-photoluminescence spectroscopy at low (5K) and room temperature is used to detect the specific radiative recombination that occurs in MoS_2 1L (direct band gap semiconductor behavior) and to evidence the eventual presence of midgap states caused by process-induced defects. The results of both characterization techniques will be presented for MoS_2 1L domains transferred onto silica and gold substrates highlighting the roles of substrate nature (metal or insulant), surface roughness, and the presence of structural defects whether induced by the preparation process or intrinsic such as grain boundaries.

[1] Jin et al. Phys. Rev. Lett. 111 (2013), 106801.

[2] Kim, Renault, et al. Appl. Phys. Lett. 105 (2014) 011605.

[3] Mathieu et al., PRB 83 (2011) 235436.

Electronic Materials and Processing
Room: 210E - Session EM+MN+PS-TuA

More than Moore: Novel Approaches for Increasing Integrated Functionality

Moderator: Andy Antonelli, Nanometrics, Sean King, Intel Corporation

2:20pm **EM+MN+PS-TuA1 Maintaining the Pace of Progress as we Approach the end of Moore's Law: *Heterogeneous Integration, New Materials, New Processes, New Architectures*, *Bill Bottoms***, 3MTS **INVITED**

The environment is rapidly changing as we approach the end of Moore's Law scaling. Scaling continues but benefits in performance, power and cost are reduced. At the same time drivers for the electronics industry are impacted by the emerging Internet of Things and Migration to the Cloud. Satisfying the requirements of these emerging drivers cannot be accomplished with the current technology. It will require innovative heterogeneous integration approaches to satisfy demands for power, latency, bandwidth, reliability and cost in an environment where transistors will wear out.

Overcoming the limitations of the current technology will require heterogeneous integration using different materials, different device types (logic, memory, sensors, RF, analog, etc.) and different components incorporating multiple technologies including electronics, photonics, and MEMS in new, 3D, system-in-package (SiP) architectures. New materials, manufacturing equipment and processes will be required to accomplish this and meet the market demand for continuous reduction in cost per function.

The requirements, difficult challenges and potential solutions will be discussed.

3:00pm **EM+MN+PS-TuA3 More than Moore - Wafer Scale Integration of Dissimilar Materials on a Si Platform**, ***Thomas Kazior***, *J. LaRoche*, Raytheon Company **INVITED**

Advances in silicon technology continue to revolutionize microelectronics. However, Si cannot do everything, particularly for high performance, high frequency RF and mixed signal applications. As a result circuits based on other materials systems, such as III-V semiconductors, are required. However, these other device technologies do not enjoy the integration density, cost benefit and manufacturing infrastructure of Si. So how can we get the 'best of both worlds'? What is the best way to integrate these dissimilar materials with Si? In this paper, we review different heterogeneous integration approaches and summarize our results on the successful wafer-scale, 3D heterogeneous integration (3DHI) of GaN HEMTs and Si CMOS.

Our Au-free GaN HEMTs have been successfully fabricated entirely in a Si foundry on semi-standard, 200 mm diameter Si wafers using Cu damascene interconnects. RF performance compares favorably with GaN on SiC devices fabricated in a III-V foundry with Au-based contact and interconnect metallurgy. Oxide bonding is being used to integrate these GaN on Si wafers with Si CMOS wafers. Through-dielectric-vias (TDVs) are used to interconnect the high performance GaN RF devices/circuits with high density CMOS control and logic circuits, resulting in ultra-short, wide-bandwidth interconnects enabling circuit optimization through intimate and arbitrary placement of CMOS logic and control circuitry relative to III-V devices. Through-substrate-vias (TSVs) are used for thermal management. This 'flexible' wafer-scale, integration platform is compatible with other III-V devices, other (non-Si) device/component technologies and any node of Si CMOS or SiGe BiCMOS. The 3DHI process is being used to fabricate cost effective, high performance, digitally enhanced, RF and mixed signal ICs such as 'intelligent' and adaptive/reconfigurable transceivers.

Energy Frontiers Focus Topic
Room: 211B - Session EN+EM+NS+SE+SS+TF-TuA

Batteries and Supercapacitors

Moderator: Elijah Thimsen, Washington University, St. Louis, Andrew C. Kummel, University of California at San Diego

2:20pm **EN+EM+NS+SE+SS+TF-TuA1 Behavior of Layered Cathode Materials: A Route to Higher Energy Density for Li-Ion Batteries**, ***Marca Doeff***, *F. Lin,* Lawrence Berkeley National Laboratory, *I. Markus*, Lawrence Berkeley Lab, University of California, Berkeley **INVITED**

The most promising cathode materials for Li-ion batteries geared towards vehicular applications are the so-called NMCs ($LiNi_xMn_yCo_zO_2$), based on cost and performance considerations. NMCs exhibit a slightly sloping voltage profile in lithium half-cells, with typical utilizations significantly lower than the theoretical capacity of about 280 mAh/g. An attractive strategy for increasing the energy densities of devices meant for traction applications would be to cycle NMCs to a higher potential than is currently used (usually about 4.3V vs. Li^+/Li) so that more lithium can be extracted and cycled. For this approach to be viable, the cathodes must exhibit excellent structural stability and good reversibility over a wide composition range. Our recent work has been directed towards understanding the high-potential behavior of NMCs, using an array of synchrotron x-ray techniques as well as transmission electron microscopy. These techniques show that surface reconstruction to rock salt and spinel phases occur during high voltage cycling, and result in impedance rises and apparent capacity losses. The degree to which this occurs is a function of how the material is made and its electrochemical history. Partial substitution of Ti for Co in NMCs not only increases the capacities obtained during cycling to 4.7V in lithium half-cells compared to baseline materials, but appears to improve the cycling behavior as well. First principles calculations show that the aliovalent substitution lowers the voltage profile slightly. This allows a greater amount of lithium to be extracted and cycled below 4.7V, resulting in higher practical capacities. The Ti-substitution also delays the formation of rock salt during charging, resulting in better capacity retention. These observations suggest that optimizing the synthesis and judicious substitution can mitigate deleterious structural changes of the NMCs due to high potential operation in Li-ion cells. These strategies should be combined with those designed to prevent side reactions with electrolytic solutions during high potential operation, such as new electrolytic solutions with improved oxidative stability, or atomic layer deposition coatings on electrode surfaces, to further ensure stable cycling.

3:00pm **EN+EM+NS+SE+SS+TF-TuA3 Next-Generation Electrolytes for Lithium-Ion Batteries**, ***Sarah Guillot,*** University of Wisconsin - Madison, *M. Usrey, A. Pena-Hueso,* Silatronix, Inc., *R.J. Hamers*, University of Wisconsin-Madison and Silatronix, Inc.

Current-generation electrolytes for lithium-ion batteries are limited in electrochemical stability and thermal stability. Over the last several years, researchers at University of Wisconsin and at Silatronix, inc. have developed several new generations of electrolytes based upon incorporation of organosilane groups into the molecular structure. A recently developed class of compounds shows unprecedented enhancements in performance, including the ability to cycle full cells over 400 times at 70 degrees C, and the ability to reduce or eliminate "gassing" at cathode surfaces. In this talk we will discuss the molecular structure of these organosilane-based compounds, quantitative measurements of the decomposition pathways, and the resulting mechanistic insights into the molecular properties that gives rise to their outstanding performance characteristics.

3:20pm **EN+EM+NS+SE+SS+TF-TuA4 Physico-Chemical Properties of Polyamidoamine Dendrimer-Based Binders for Carbon Cathodes in Lithium-Sulfur Batteries**, ***Manjula Nandasiri***, *P. Bhattacharya, A. Schwarz, D. Lu,* Pacific Northwest National Laboratory, *D.A. Tomalia,* NanoSynthons LLC, *W.A. Henderson, J. Xiao*, Pacific Northwest National Laboratory

Lithium-sulfur (Li-S) batteries are one of the most promising energy storage systems, offering up to five-fold increase in energy density as compared with state-of-the-art lithium-ion batteries to meet the growing demand for environmentally benign energy storage devices with high energy density, low cost, and long life time. For practical applications, high sulfur (active material) loading (> 2 mg/cm^2) within the carbon cathode in Li-S batteries is essential. Most reports on engineered cathode materials for Li-S batteries are based upon low sulfur loadings (typically ~1 mg/cm^2), which are impractical and often give misleading results. It is unknown how these novel engineered cathodes behave under high sulfur loading conditions. The

binder is perhaps the most critical material in achieving a high sulfur loading in carbon cathodes. We have recently used dendrimers with various surface chemistries as functional binders in Li-S cells with SuperP-carbon/S as the cathode material. Even without engineering the cathode, very favorable cycling stability and electrolyte wetting were obtained with these binders. It was attributed to the high density of surface functional groups on the dendrimers, high curvature of the binder and its porosity, and the interactions between the large number of basic nitrogen and oxygen atoms on the dendrimers and lithium polysulfides.

Here, we will discuss the fundamental properties of dendrimers as aqueous binders for Li-S battery cathodes and compare their performance with other aqueous, commonly used linear polymeric binders such as styrene butadiene rubber (SBR) and sodium carboxyl methyl cellulose (CMC). Specifically, generation 4 polyamidoamine (PAMAM) dendrimers with hydroxyl (OH), 3-carbomethoxypyrrolidinone (CMP), and sodium carboxylate (COONa) surface functional groups served as good, electrochemically stable binders at high S loadings (~3-5 mg/cm^2) with high initial capacities (> 1000 mAh/g). In comparison to CMC-SBR binder-based electrodes which failed at high C-rates (0.2C) after 40 cycles**,** dendrimer-based binders showed a capacity retention of >85% for more than 100 cycles. It was also observed that acidic groups and all-NH_2 surface groups are poor binders, whereas binders with COO^- and neutral surface groups (OH, CH_3) show better performance. X-ray photoelectron spectroscopy was used to identify different surface functional groups in these dendrimers and understand their interactions with SuperP-carbon/S cathode. In addition, a detailed physico-chemical characterization using IR spectroscopy and XANES/EXAFS will be presented to substantiate the superior dendrimer-carbon/S interactions.

4:20pm **EN+EM+NS+SE+SS+TF-TuA7 The Road beyond Lithium Batteries is Paved — In Three Dimensions — With Rechargeable, Dendrite-Free Zinc**, ***Debra Rolison***, *J.F. Parker, C.N. Chervin, I.R. Pala, M.D. Wattendorf, J.W. Long*, U.S. Naval Research Laboratory **INVITED**

Lithium-ion batteries dominate the energy-storage landscape, but do so with the ever-present threat of thermal runaway and conflagration courtesy of flammable electrolytes and oxygen-releasing electrode materials. Fortunately, Zn-based batteries offer a compelling alternative grounded in the innate safety and cost advantages of aqueous electrolytes augmented by the high earth-abundance of Zn and the high energy density of Zn-based batteries (comparable to Li-ion). Traditional Zn-based batteries provide suboptimal utilization of the zinc (typically <60% of theoretical capacity) and poor rechargeability—thanks to the complex dissolution/precipitation processes that accompany Zn/Zn^{2+} cycling of conventional powder-bed Zn electrode structures in alkaline electrolyte. We address these limitations by redesigning the zinc anode as a porous, 3D-wired “sponge” architecture. Zinc sponge electrodes achieve >90% Zn utilization when discharged in primary Zn–air cells, retaining both the 3D framework of the Zn sponge and an impedance characteristic of the metal thanks to an inner metallic core of 3D zinc. When cycled in Ag–Zn and Ni–Zn cells, the Zn sponges retain monolithicity and reveal uniform deposition of charge/discharge products at the external and internal surfaces, even to deep depth-of-discharge of the zinc. These results show that all Zn-based chemistries can now be reformulated for next-generation rechargeable, Li-free batteries

5:00pm **EN+EM+NS+SE+SS+TF-TuA9 Porous Silicon Electrochemical Capacitor Devices for Integrated On-Chip Energy Storage**, ***Donald Gardner***, *C.W. Holzwarth III, Y. Liu, S. Clendenning, W. Jin, B.K. Moon, Z. Chen, E.C. Hannah, T.V. Aldridge,* Intel Corp*, C.P. Wang, C. Chen,* Florida International University*, J.L. Gustafson*, Intel Corp

Integrated on-chip energy storage is increasingly important in the fields of internet of things (IoT), energy harvesting, and sensing. Silicon is already the materials of choice for the integrated circuits found in every IoT device; however, the efforts to integrate electrochemical (EC) capacitors on a silicon die have been limited. Unlike batteries, EC capacitors are electrostatic devices and do not rely on chemical reactions enabling cycle lifetimes of >1M. This is especially important for off-power-grid IoT devices where difficulty associated with regularly replacing the batteries of billions of devices is prohibitive. This work demonstrates electrochemical capacitors fabricated using porous Si nanostructures with extremely high surface-to-volume ratios and an electrolyte. Devices were fabricated with tapered channels sized from 100 nm at the top to 20 nm and with aspect ratios greater than 100:1. Surface coatings were necessary for long-term stability because unpassivated silicon structures react with the electrolytes. To obtain uniform coatings using stop-flow atomic layer deposition (ALD), efficient surface reactions are needed between high volatility, low molecular weight, small molecular diameter precursors without chemical vapor deposition side reactions. $TiCl_4$ and NH_3 precursors were found to coat porous Si with TiN uniformly. Measurements of coated P-Si capacitors reveal that an areal capacitance of up to 6 mF/cm^2 can be achieved using 2 µm deep pores, and scales linearly with depth with 28 mF/cm^2 measured for 12 µm deep pores. Three-terminal CV measurements with EMI-BF_4 ionic electrolyte were used to examine the stability of different pore sizes and TiN coating thicknesses. Pores with an average 50 nm width and 100:1 aspect ratio were stable to ±1.2 V when cycled at 10 mV/s and stable to ±1.0 V when cycled at 1 mV/s. Different ionic liquids were studied to determine the ionic liquid best suited to TiN coated porous Si including TEA-BF_4/AN, EMI-BF_4, EMI-Tf, and a 3M EMI-BF_4/propylene carbonate (PC) mixture. Using impedance spectroscopy, the time constant for a 2 µm deep porous Si EC capacitor with a high conductivity TiN coating was found to be 17.6 ms which is fast enough that this can be used for applications involving AC filtering for AC-DC conversion. Measurements of volumetric energy density versus power density of porous Si devices versus other devices show several orders of magnitude higher energy density than electrolytic capacitors with a similar voltage range. These results are also between one to two orders of magnitude higher than other studies utilizing porous silicon and are comparable to commercial carbon-based EC capacitors.

5:20pm **EN+EM+NS+SE+SS+TF-TuA10 Investigations of Magnesium Stripping and Deposition using *Operando* Ambient Pressure X-ray Photoelectron Spectroscopy**, ***Yi Yu***, Lawrence Berkeley National Laboratory*, Q. Liu,* Shanghai Tech University, China*, B. Eichhorn,* University of Maryland, College Park*, E.J. Crumlin*, Lawrence Berkeley National Laboratory

Since the first demonstration of rechargeable magnesium battery, magnesium metal has been considered as an attractive battery anode due to its high volumetric energy density, high negative reduction potential, natural abundance in the earth crust, and relatively good safety features due to its dendrite-free formation. Although it is well accepted that the dissolution and plating of metal plays an important role in the electrochemical properties related to the discharge and charge of the battery, the nature of metal-electrolyte chemical and electrochemical interaction is still not fully established. In an effort to elucidate the interfacial electrochemical mechanisms, we present the studies of magnesium deposition and stripping using *operando* ambient pressure X-ray photoelectron spectroscopy (AP-XPS). Synchrotron X-rays at the Advanced Light Source, Lawrence Berkeley National Laboratory and our ‘tender’ X-ray AP-XPS endstation allow for probing the liquid-solid interface at pressures up to 20 Torr. Cyclic voltammetry is employed to examine the reversibility of electrochemical magnesium deposition. This talk will provide details on how *operando* AP-XPS coupled with electrochemistry allows for studying electrochemical processes of magnesium deposition and stripping at the liquid-solid interface and yields chemical information relevant to real-world applications.

5:40pm **EN+EM+NS+SE+SS+TF-TuA11 Atomic Layer Deposition of Solid Electrolytes for Beyond Lithium-Ion Batteries**, ***Alexander Kozen***, *G.W. Rubloff*, University of Maryland, College Park **INVITED**

Solid Li-based inorganic electrolytes offer profound advantages for energy storage in 3-D solid state batteries: (1) enhanced safety, since they are not flammable like organic liquid electrolytes; and (2) high power and energy density since use of the 3D geometry can maximize the volume of active material per unit area, while keeping the active layer thickness sufficiently small to allow for fast Li diffusion. The quality of thin solid electrolytes is currently a major obstacle to developing these solid state batteries, restricting electrolyte thickness to >100 nm to control electronic leakage, consequently slowing ion transport across the electrolyte and impeding 3-D nanostructure designs that offer high power and energy.

Furthermore, the ion-conducting, electron-insulating properties of solid electrolytes are promising for their use as protection layers on metal anodes (e.g., Li, Na, Mg) and on cathodes in proposed “beyond-Li-ion” battery configurations such as Li-NMC, Li-O_2, and Li-S to prevent electrolyte breakdown.

Atomic layer deposition (ALD) is well suited to the challenge of solid electrolytes, providing ultrathin, high quality films with exceptional 3-D conformality on the nanoscale. We have developed a quaternary ALD processes for the solid electrolyte LiPON, exploiting *in-operando* spectroscopic ellipsometry and *in-situ* XPS surface analysis for process development. ALD LiPON has tunable morphology, and a nitrogen-dependent tunable ionic conductivity as high as 3.5×10^{-7} s/cm.

We explore the potential of ALD solid electrolytes for the fabrication of solid, 3D microbatteries, as we as the use of thin ALD solid electrolyte coatings on metal anodes to improve interfacial stability against organic electrolytes and thus prevent SEI formation. We demonstrate and quantify protection of lithium metal anodes with low ionic conductivity ALD Al_2O_3 coatings to prevent degradation reactions, and probe the surface chemistry and morphology of these anodes. Finally, we demonstrate that protection of Li metal anodes using ALD protection layers can improve the capacity of

Li-S batteries by 60% by preventing anode corrosion by dissolved sulfur species in the electrolyte.

This work has implications beyond the passivation of lithium metal besides its focus and greatest impact on the Li-S battery system, as ALD protection layers could also be applied to other promising metal anode battery systems such as Mg and Na, and other beyond Li-ion technologies such as Li-NMC or- Li-Air where similar reactivity issues prevent adoption.

Electronic Materials and Processing
Room: Hall 3 - Session EM-TuP

Electronic Materials and Processing Poster Session

EM-TuP1 Ionic Liquid Gated Electric Double Layer Transistors based on a-IGZO Thin Films, ***PushpaRaj Pudasaini**, J.H. Noh, A. Wong, A.V. Haglund,* The University of Tennessee Knoxville*, S. Dai, T.Z. Ward,* Oak Ridge National Laboratory*, D. Mandrus,* University of Tennessee, Knoxville and Oak Ridge National Laboratory*, P.D. Rack*, The University of Tennessee Knoxville

The electric filed effect with the field effect transistor configuration is a powerful approach for externally tuning the carrier density of a material and investigating associated changes in the electronic properties of the material. To this end, ionic liquid gated field effect transistors have been extensively studied due to their low operation voltage, ease of processing and the realization of high electric fields at low bias voltages. Herein, we report ionic liquid (IL) gated field effect transistor based on amorphous Indium Gallium Zinc Oxide (IGZO) thin film active layers. The transport measurement of the IL revealed the intrinsic n-channel property of the IGZO thin film with high ON/OFF ratio ~10^5 and a large field effect electron mobility of 5.38 $cm^2V^{-1}S^{-1}$ at 300K and a threshold voltage of 0.1V. Comparable measurements on the bottom SiO_2 gate insulator revealed an ON/OFF ratio ~10^9 and field effect electron mobility of 12.53 $cm^2V^{-1}S^{-1}$ and a threshold voltage of 2.5V. Furthermore, we found that the ionic liquid gating of a-IGZO thin film leads to not only an electrostatically induced carrier accumulation but also the field induced creation of O_2 vacancy, with constituent migration of oxygen in and out of the film depending on the polarity of the bias used. This could leads to the bias induced control of carrier density in an amorphous oxide semiconductors.

EM-TuP2 Resistor Thermal Noise Rectification for Energy Harvesting, ***Amina Belkadi**, S. Joshi,* University of Colorado at Boulder*, G. Moddel*, University of Colorado at Boulder and Redwave Energy

Resistor noise produces real power and can, in principle, be rectified for thermal energy harvesting. For ambient temperatures and above, the peak frequency in the noise spectrum is at least 30 THz, which requires an ultra-high-speed diode for rectification and a quantum-based theory to describe the rectification process. In this study, we analyze harvesting energy through the rectification of resistor thermal noise. The electrical noise spectrum generated by a warm resistor is similar to that from one-dimensional blackbody radiation channeled through an antenna. This allows the use of optical rectenna circuitry and concepts, in the presence of a temperature gradient between the resistor and the diode, by merely replacing the antenna with a resistor. We use the semi-classical theory of photon-assisted tunneling to explain the diode rectification behavior. In contrast to an antenna-coupled diode, using a resistor modifies and may help resolve some optical rectenna challenges such as the RC time constant and optical coherence limitations, impedance matching to the diode, and undesired heating of the diode. However, a key challenge remains: the very low power produced by the hot resistor. This limits the diode rectification efficiency. If challenges of low power and low rectification efficiency are overcome, the concept can be used for applications such as (i) efficient harvesting of energy from waste heat sources and even from the earth, when a suitable heat sink is provided, and (ii) conversion of solar energy either directly or via an intermediate thermal transducer. The fact that conventional photovoltaic devices use only the high energy part of the solar spectrum to produce power places a limit on their conversion efficiency. Therefore, integration of solar cells with a resistor-based thermal noise energy harvesting device could potentially increase the overall efficiency of solar cells.

EM-TuP5 Electrical and Optical Properties of the Porous Nickel Oxide Thin Film as Counter Electrode for the Application to Electrochromic Devices, ***WonChang Lee**, J.U. Wie, E.C. Choi, B.Y. Hong*, Sungkyunkwan University, Republic of Korea

Electrochromic materials are able to change the optical properties persistently and reversibly by an external voltage. Applications of electrochromic materials include rearview mirrors, smart windows, display panels, etc. A large number of transition metal oxides such as the well-known tungsten trioxide (WO_3) cathodic material, which reversibly switches from transparent to blue upon lithium or proton insertion.

In contrast, nickel oxide (NiO) is an anodically coloring material but despite promising features such as high coloration efficiency, good optical memory and cost effectiveness. NiO is often used as a secondary electrochromic material to complement cathodically coloring WO_3 in prototype electrochromic devises. Because NiO have for a long time attracted attention as counter electrode regarding their brownish color in the oxidized state that, together with the blue color of the reduced WO_3, yields a neutral gray color device in the colored state. The electrochromism in NiO films is rather complicated although it is generally accepted that the reversible transition between colored and bleached states is related to redox process between the NiOOH and NiO. Moreover, owing to their rapid degradation on cycling, difficulties in using nickel oxide films have been encountered. However, the problems of NiO thin films that limit their commercialization and poor durability are still debated. When NiO film is formed as porous structure, the surface area to the volume ratio is large and the same probably lead to an increase in the ion intercalation and deintercalation. The large-area surface of the porous film structure can be helpful for the augmenting the optical modulation.

In our study, the porous NiO thin film was deposited using sol gel-method and dip-coating technique on the Indium Tin Oxide (ITO) glass. The NiO thin film was formed by annealing process at different temperatures after the dip-coating technique. Studies on the effect of annealing temperature to improve the crystallinity and the electrochromic properties of the NiO thin films have been carried out. So, we confirmed that the electrochromic efficiency was improved by optimizing of the annealing condition.

EM-TuP6 Tunable Optical Extinction of E-Beam Fabricated Nano-Rectennas Modified by Atomic-Layer Deposition, ***Raymond Wambold**,* The Pennsylvania State University*, G.J. Weisel, D.T. Zimmerman,* The Pennsylvania State University, Altoona*, J. Qi, B.G. Willis*, University of Connecticut

We present a systematic study of plasmon extinction characteristics of arrays of tunable nanoscale rectennas, which have possible application as solar-energy harvesting devices and optical-IR sensors. Each nanorectenna is composed of a triangular prism and a flat counter-electrode, both made of palladium. We fabricate arrays of rectennas on silica using standard electron-beam lithography. We then use atomic-layer deposition (ALD) of copper to control the gap distance between the two electrodes. To measure optical extinction we employ a broadband (Quartz-tungsten-halogen) light source in a confocal, transmission arrangement. Our measurements demonstrate that the plasmon extinction resonance can be tailored by varying the e-beam dose and the cycles of ALD. The most important feature of our work is the ability to reduce the gap spacing between the two electrodes, which serves to systematically redshift the extinction peak and ultimately bring the two electrodes into the tunneling regime. We also investigate the effects of overall size, morphology, and material properties on the extinction resonance. We employ Finite-Difference Time-Domain simulations to support our device design and to corroborate our experimental measurements. In addition, we use scanning electron microscopy to correlate the device-dimension and morphology changes to the plasmon extinction characteristics.

EM-TuP7 The Study of Light Control using Nanoantenna, ***JeongHee Shin**, S. Kim, J.E. Jang*, Daegu Gyeongbuk Institute of Science and Technology (DGIST), Republic of Korea

Recently, the antenna has been scaled down to nanometer to absorb higher electric-magnetic wave. Traditionally in communication area, high frequency is required to transmit or receive much more information. Nanometer antenna is different from general antenna in communication area due to properties and applications. Nanoantenna can cover the visible to near-infrared (NIR) wavelength regions; thus, it has a lots of applications in communication, optics, bioelectronics and so forth. Especially in optics area, not only the light control but also structure-depended absorption, reflection, and transmission using nanoantenna have been studied. The light absorption using nanoantenna can be useful to harvest electrical energy instead of solar cells expected to be much higher efficiency as well. The optical properties of nanoantenna can be affected by geometry factors such as structure, shape, and pitch. It cannot correspond traditional antenna theory due to surface plasmons (SPs) which are coherent delocalized electron. This penomenons exist at the interface between two materials, strong couplings between electrons on metal and incident light. Designing nanoantenna is much more complicate than that of general antenna so that it does not simply follow conventional antenna theory. To apply the nanoantenna to various applications, the study of parameters to define optical properties in nanoantenna should be necessary. We focused on control of color via nanoantenna depending on various geometries. First of all, we investigated the relation between parameters and color change. We can design the target peak wavelength in visible region. Then, we will report optical transistor to control colors. It can be applied to various

applications such as color filter, next-generation display, energy harvesting system with higher efficiency, and so on.

EM-TuP8 MIM: Role of Design and Fabrication, ***Aparajita Singh**, S. Bhansali*, Florida International University

The early assumptions have been that thin-film development and contact area the two major issues in defining characteristics of the MIM tunnel diode. Based on this the focus has rigorously been on patterning and various thin-film deposition techniques for MIM formation. Several designs with varied fabrication methods have been considered for fabrication of MIM devices till date for applications like energy-harvesting devices, terahertz electronics, macro electronics, etc. Here we elaborate upon each design and associated fabrication challenges for Ni-NiO based MIM and MIIM diodes. The goal is to optimize the MIM device design for: (1) ease of integration with other circuit devices, and (2) simpler fabrication steps for minimizing alteration in oxide property and inherent device impedance. Fabrication issues such as material selection, metal deposition, oxide growth/deposition, and patterning are discussed. Since ALD is currently the leading way to provide uniform, pinhole free and ultra-thin oxide layers, we present a comparison of oxide properties deposited by sputtering and ALD (the leading techniques) along with their impact on I-V characteristics. Influence of surface preparation on oxide and growth/deposition temperature are also discussed.

EM-TuP9 Comparison of Hafnium Oxide and Zirconium Oxide Thin Films for Fabricating Electronic Devices, ***Jouantrey Spence**, F. Cunningham, R. Moten, Z. Xiao*, Alabama A&M University

Thin films of hafnium dioxide (HfO_2) and zirconium oxide (ZrO_2) are used widely as the gate oxide in fabricating integrated circuits (ICs) because of their high dielectric constants. In this research, we report the growth of hafnium dioxide (HfO_2) and zirconium oxide (ZrO_2) thin films using e-beam evaporation, and the fabrication of complementary metal-oxide semiconductor (CMOS) integrated circuits using the HfO_2 and ZrO_2 thin films as the gate oxide. MOSFETs, CMOS inverters, and CMOS ring oscillator were fabricated, and the electrical properties of the fabricated devices were measured. The measurement results on the devices fabricated with the two films were compared, and will be reported in the Conference.

EM-TuP10 Non-Equilibrium First-Principles Study on Electron Scattering Processes in Magnetic Tunnel Junction, ***Masaaki Araidai,*** Nagoya University, Japan*, T. Yamamoto,* Tokyo University of Science, Japan*, K. Shiraishi*, Nagoya University, Japan

Investigation of magnetic tunnel junction (MTJ) is a key issue for the development of advanced magnetoresistive random access memories (MRAMs). MTJs consist of two metal ferromagnets, thick magnetization-fixed and thin magnetization-free layers, separated by a thin insulator, and they exhibit two resistances, low or high, depending on the relative direction of the magnetizations of fixed and free layers, parallel (P) or antiparallel (AP) configuration. The simplest way to reverse the magnetization of free layer is switching by external magnetic fields. However, absolute currents required for the magnetic-field switching do not scale with reducing the junction size. At present, current-induced magnetization switching (CIMS) proposed by Slonczewski [1] and Berger [2] is drawing attention as the most promising candidate for a mechanism of magnetization reversal of free layer, owing to the scalability of CIMS [3]. Although CIMS has been successfully applied to the operation of MRAM, it has not been sufficiently understood yet.

In this work, we investigated electron scattering processes in CIMS of a MTJ by the non-equilibrium Green's function technique coupled with the density-functional theory [4]. We employed a Fe/MgO/Fe MTJ sandwiched between ferromagnetic Fe and paramagnetic Ta electrodes, as a typical MTJ model. The current-voltage characteristics indicated high tunnel magnetoresistance of the MTJ (about 600% at zero bias) and was highly antisymmetric with respect to the bias voltage, originating from the antisymmetric structure and the magnetization configuration. We found from the current density dependence of magnetization of the free layer that the switching from AP to P configuration could be realized by lower electrical power than P-to-AP case. From detailed analyses of the density of states subject to a finite bias voltage, we clarified that the asymmetric behavior originates from the difference in the electron scattering processes between switching directions.

[1] J. C. Slonczewski, J. Magn. Magn. Mater. **159**, L1 (1996).

[2] L. Berger, Phys. Rev. B **54**, 9353 (1996).

[3] Ikeda et al., IEEE TRANSACTIONS ON ELECTRON DEVICES, VOL. **54**, 991 (2007).

[4] M. Araidai, T. Yamamoto, and K. Shiraishi, Appl. Phys. Express **7**, 045202 (2014).

EM-TuP11 First Principles Study on Switching Mechanism of Superlattice $(GeTe)_2/Sb_2Te_3$ Phase Change Memory, ***Masayuki Takato**, H. Shirakawa, M. Araidai, K. Shiraishi*, Graduate School of Engineering, Nagoya University, Japan

Superlattice phase change memory (superlattice PCM) consisting of $(GeTe)_2/Sb_2Te_3$ stacked structure is one of the most promising candidates for next-generation non-volatile memories and has received considerable attention in recent years [1,2]. The memory operations are attributed to small structural change between two atomic configurations before and after switching. Therefore, the energy required for switching between higher and lower resistive states is much lower than that of conventional PCMs utilizing phase transition between crystal and amorphous phases [3]. However, the reaction pathway in switching of superlattice PCM has not yet been clarified and the detailed analyses of the structural transition between high-resistive and low-resistive states are prerequisites for fully understanding the switching mechanism.

In this work, we investigated the switching process of the superlattice $(GeTe)_2/Sb_2Te_3$ PCM using the first-principles electronic states calculations. The atomic structures and the electronic states were calculated by VASP code [4], which is based on density functional theory with the plane-wave basis sets, a PBE-type exchange-correlation functional and the projector augmented-wave method. For the calculations, $\boldsymbol{k}$ points of 8 x 8 x 4 Monkhorst-Pack grid were used and the cutoff energy was 500eV.

We found that atomic configurations of high-resistive and low-resistive states are not stable but metastable [5]. Therefore, the superlattice $(GeTe)_2/Sb_2Te_3$ PCM can do cyclic operations due to the metastability. In addition, we clarified the structural transition process between high-resistive and low-resistive states. I will show the detail process in the announcement. Furthermore, the validity of our proposal will be shown from the detailed analyses of the potential energy surface and electron-density distribution.

[1] J. Tominaga, et al., Jpn. J. Appl. Phys. **48**, 03A053 (2009).

[2] N. Takaura, et al., IEDM Tech. Dig., p.685 (2014).

[3] R. E. Simpson, et al., Nat. Nanotech. **6**, 501 (2011).

[4] G. Kresse and J. Hafner, Phys. Rev. B **47**, 558 (1993).

[5] R. Ohyanagi, et al., Appl. Phys. Lett. **104**, 252106 (2014).

EM-TuP12 First Principles Study on Atomic-scale Behavior of N, H Atoms and O Vacancy Related Defects in SiO_2 Layer of MONOS Memories, ***Hiroki Shirakawa,*** Graduate School of Engineering Nagoya University, Japan*, M. Araidai,* Graduate School of Basic Engineering, Nagoya University, Japan*, K. Kamiya,* Center for Basic Education and Integrated Learning, Kanagawa Institute of Technology, Japan*, K. Shiraishi*, Graduate School of Engineering, Nagoya University, Japan

Metal-Oxide-Nitride-Oxide-Semiconductor (MONOS) memories have attracted a great attention as one of the next generation NAND flash memories. MONOS memories can trap charges inside defect sites in charge trap layers (SiN) that are spatially separated each other, leading to great merits for integration techniques such as 3D-structure and multi-level-cell operation. On the charge trapping layer in MONOS memories, it has been reported that large amounts of O and N atoms are incorporated into SiO_2/SiN interfaces, leading to the formation of electron occupied defects near the interfaces [1]. In addition, Vianello et al. have found that a lot of H atoms distribute in SiO_2, SiN and interface [2]. Yamaguchi et al. have also reported atomic-scale behavior of such defects in MONOS SiN layers during program/erase (P/E) cycles [3]. However, for SiO_2 layer of MONOS memories, the decisive atomic-scale information has not been clarified yet.

In this work, we investigate the behavior of N, H atom and O vacancy in SiO_2 during P/E cycles using VASP code [4], which is based on the density functional theory with GGA of Perdew-Wang-91. Core valence interactions were described by the ultrasoft pseudo potential. To simulate N related defects in SiO_2 layer near SiN/SiO_2 interface, we employed the 72 atoms super-cell of α-quartz including the defects. The defects formed by substituting two N atoms for two O atoms in SiO_2. The P/E operations correspond to the electron and hole injections into the defects in our calculation.

We found that O vacancies are induced by the two N-substituted defects, forming the complex defect (VoN2) that consists of one O vacancy and two N atoms. Then, VoN2 defect cannot traps charges when the Fermi energy of MONOS is within the ranges of SiN band gap. We also found that the diffusing H atoms in SiO_2 change the characteristics of VoN2 defect. VoN2 defect is transformed to another defect including H atoms (VoN2-H) by adsorbing hydrogen atoms. While VoN2-H defect is energetically unstable compared with VoN2 in the neutral charge state, VoN2-H defect becomes very stable in the negative charge state. This indicates that VoN2-H defect is able to trap electrons.

These results suggest that the amount of trapped charges on MONOS memories strongly depends on the dynamics of H atoms in SiO_2 during P/E

cycles; namely, the thermal diffusion of H atoms would bring about the threshold voltage shift of MONOS memories.

[1] M. Miura, *et al*., IEICE Tech. Rep. SDM, pp.17, (2007).

[2] E. Vianello *et at*., IEDM Tech. Dig., pp.75, (2009).

[3] K. Yamaguchi, *et al*., IEDM Tech. Dig., p.122, (2010).

[4] G. Kresse and J. Hafner, Phys. Rev. B **47**, 558 (1993).

EM-TuP14 Hybridization and Characterization of Reduced Graphene Oxide with Copper Nanoparticles, *J.D. Lee, L.R. Hubbard,* ***Anthony Muscat***, University of Arizona

An in-situ crystallization technique was used to prepare a hybrid containing Cu nanoparticles (NPs) bound to reduced graphene oxide (rGO) sheets. The hybrid material was investigated with scanning electron microscopy (SEM), Raman spectroscopy, ultraviolet visible spectroscopy (UV/vis), X-ray photoelectron spectroscopy (XPS), and Fourier transform infrared spectroscopy (FTIR). SEM results show that spherical Cu nanoparticles ranging from 1.6 to 7.4 nm in diameter and agglomerates were randomly dispersed on rGO sheets. SEM images show that Cu NPs were intercalated between rGO sheets to form a hybrid material. UV/vis of the rGO:Cu hybrid contained peaks associated with GO and Cu NPs with a blue shift in the peak resulting from n→pi* transitions of C=O bonds to 283 nm and a red shift in the peak indicative of the Cu surface plasmon resonance to 585 to 630 nm. XPS confirmed the presence of CuO and $Cu(OH)_2$ with peaks at 933.4 and 934.5 eV respectively. The presence of imidazole, from the ionic liquid [Bmim][BF_4] used to synthesize the Cu NPs, was confirmed by the XPS peak found at 400.4 eV and the contributions to fingerprint regions in the FTIR. The as synthesized rGO:Cu hybrid had an electrical conductivity of $3.5*10^6$ S/m. This value is intermediate between GO with a baseline of 0.04 S/m and Cu NP thin film conductivity of $2.0*10^7$ S/m.

EM-TuP15 Hybrid Transparent Conductive Electrodes Embedded with Pt Nanoclusters for Reliable and Efficient GaN-based Light-Emitting Diodes, *K. Kim,* ***Hyunsoo Kim***, Chonbuk National University, Republic of Korea

A key technology to fabricate highly efficient and reliable GaN-based light-emitting diodes (LEDs) is transparent conductive electrodes (TCEs), which are used as the Ohmic contact to *p*-GaN and the current spreader. Indeed, a lot of attempts have been made to fabricate better TCEs with high optical transmittance, low sheet resistance, and low contact resistance by employing Pt, oxidized Ni/Au, indium tin oxide (ITO), zinc oxide (ZnO), carbon nanotubes, graphene, et c. Among these TCEs, ITOs are the best in terms of their high optical transmittance in the visible wavelength range, low sheet resistances, feasible Ohmic contact to *p*-GaN, and guaranteed robustness, enabling them to be practically used in commercial products. Unfortunately, however, the sputtering process, which can produce the best quality of ITO films, cannot be used for the deposition of ITO film to p-GaN, associated with the sputtering damage of *p*-GaN surface. As an alternative, therefore, the *e*-beam evaporation technique, which is a representative physical vapor deposition technique free of ion damage, has been used for the ITO deposition. However, the evaporated ITO films were relatively poorer than the sputtered films due to the lack of stoichiometry and insufficient crystallinity of the ITO.

Metallic Pt thin film was shown to act as efficient current spreader in the GaN-based LEDs due to its low R_{sh} value and feasible Ohmic contact associated with its large work function (5.65 eV). More interestingly, Pt thin film has a distinctive feature of agglomeration upon thermal annealing, a so-called Ostwald ripening, leading to the formation of Pt islands or nanoclusters. This feasibility suggests that the combination of sputtered ITO or ZnO films and Pt nanoclusters, namely, hybrid TCEs, may be successful for fabricating novel TCEs for GaN-based LEDs since Pt nanoclusters are expected to act as the preventer of ion damage or an Ohmic patch. In this regard, hybrid TCEs were investigated by combining Pt nanoclusters and sputtered films. Notably, hybrid ITO TCEs fabricated by combining interfacial Pt nanoclusters with a coverage ratio of 23.7 % (acting as an Ohmic patch) and a 100-nm thick sputtered ITO film yielded a low specific contact resistance of ~$1.3x10^{-2}$ Ωcm^2, a sheet resistance of 24 Ω/sq, and a high optical transmittance of 90 % at 450 nm. LEDs fabricated with the hybrid ITO TCEs showed a 17.2 % brighter light output power compared to reference LEDs. This indicates that the high-quality sputtered ITO film can be practically used in LEDs by embedding Pt nanoclusters.

EM-TuP16 Selective Area Growth of InN on Patterned Substrate by Plasma-Assisted Metal-Organic Molecular Beam Epitaxy, ***Wei-Chun Chen***, National Applied Research Laboratories, Taiwan, Republic of China, *S.Y. Kuo,* Chang Gung University, Taiwan, Republic of China, *F.I. Lai,* Yuan-Ze University, Taiwan, Republic of China, *Y.C. Lee,* Chung Yuan Christian University, Taiwan, Republic of China, *C.N. Hsiao*, National Applied Research Laboratories, Taiwan, Republic of China

In this article, we investigated selective area growth of InN materials on sapphire substrate using molybdenum mask patterned with various growth temperature. The surface morphology, structural and optical properties of InN materials were analyses by field emission scanning electron microscopy (FE-SEM), transmission electron microscopy (TEM), X-ray diffractiometer and photoluminescence, respectively. XRD results indicated that the InN materials exhibited preferred orientation along the <0001> direction at 550 ºC. Surface morphology shows that the InN crystals were grown on Mo-patterned substrate with *hexagonal* micro-rods *array* surface texturing. TEM images show these InN films are single phase wurtzite crystals with preferred orientation along the *c* axis. Optical properties showed the peaks of near band-edge emission at energies between 0.72 - 0.9 eV.

EM-TuP17 N+-InGaP or N+-GaAs NanoWires for JunctionLess Transistors Fabricated by Focused Ion Beam (FIB) System, ***Cássio Almeida***, *L.P.B. Lima,* UNICAMP, Brazil, *H.T. Obata, M. Cotta,* University of Campinas, Brazil, *J.A. Diniz*, UNICAMP, Brazil

N+-InGaP and N+-GaAs layers were grown by Chemical Beam Epitaxy (CBE) on GaAs substrates with (001) orientation. Two group of samples with N+-InGaP (350 nm)/GaAs-buffer layer (300 nm)/GaAs S.I. (Semi-Insulating) and N+-GaAs (300 nm)/GaAs-buffer layer (300 nm)/GaAs S.I. were obtained. X-Ray diffraction (XRD) analysis was used in order to determine the InGaP lattice mismatch on GaAs. N+-InGaP lattice-matched layers on GaAs were obtained using a growing temperature of 550ºC during the process in CBE reactor, while, for N+-GaAs on GaAs samples, the temperature was 550ºC. By Hall measurements, a silicon doping of 10^{+18} cm^{-3} was extracted for both group of samples, indicating the formation of N+-type layers. These samples are being used for MOS Junctionless (JL) Transistors applications, because III-V semiconductors present higher electron mobility values than silicon. These JL transistors (with three terminals: gate, source and drain) are being fabricated using Focused Ion Beam (FIB) System, based on similar process steps of the JL devices, which were fabricated on Silicon-on-Insulator (SOI) substrate[1]. Thus, Gallium (Ga^+) Focused Ion Beam (FIB) is used to define the III-V (InGaP or GaAs) nanowires (III-VNW), which are the electron conduction channel between source and drain, and for depositions of SiO_2 (as gate dielectric) and Pt (as gate, drain and source electrodes) layers[2]. Finally, drain-source current (I_{DS}) versus drain-source voltage (V_{DS}) and drain-source current (I_{DS}) versus gate-source voltage (V_{GS}) measurements of Junctionless devices will be extracted and will be able to indicate if these InGaP or GaAs nanowires are suitable for Junctionless transistors applications.

References:

[1] Lima, L. P. B., *et al*. "Junctionless Fabrication on SOI Wafers Using Focused Ion Beam Milling and Al Diffusion."*ECS Transactions* 49.1 (2012): 367-374.

[2] dos Santos, Marcos V. Puydinger, *et al*. "Fabrication of p-type silicon nanowires for 3D FETs using focused ion beam."*Journal of Vacuum Science & Technology B* 31.6 (2013): 06FA01.

EM-TuP18 Thermoelectric Figure of Merit of E-Beam-Grown Nanoscale Multilayered Bi_2Te_3/Sb_2Te_3 Thin Films, ***Zhigang Xiao***, *S. Budak*, Alabama A&M University

Nanoscale multilayered Bi_2Te_3/Sb_2Te_3 thin films were grown using the e-beam evaporation. The in-plane and cross-plane micro thermoelectric devices were fabricated using the clean room-based microfabrication techniques such as UV lithography. The e-beam-grown multilayered thin films and the fabricated thermoelectric devices were measured and characterized. The nanoscale multilayered Bi_2Te_3/Sb_2Te_3 thin films can have much higher thermoelectric figure of merit than their bulk materials. The measurement results on the electrical and thermal properties of the nanoscale multilayered thin films will be reported in the conference.

EM-TuP21 Band-Gap Measurements of Low-K Porous Organosilicate Dielectrics using Vacuum Ultraviolet Irradiation, *H. Zheng,* ***Joshua Blatz***, University of Wisconsin-Madison, *S.W. King,* Intel Corporation, *E. Ryan,* GLOBALFOUNDRIES, *Y. Nishi,* Stanford University, *J.L. Shohet*, University of Wisconsin-Madison

Porous low-k organosilicate dielectrics are of great interest in semiconductor fabrication due to their low-k properties and understanding their behavior during vacuum ultraviolet irradiation is important for their utilization in industry. Experimental measurements of the band-gap of low-

k organosilicate dielectrics are presented in this work. Specifically, vacuum ultraviolet (VUV) synchrotron photoemission spectroscopy was used to investigate the effect of VUV radiation on porous organosilicate (SiCOH) dielectrics during processing. By comparing photoemission spectroscopic data before and after VUV exposure, VUV irradiation with photon energies less than 9.0 eV was found to be beneficial in depleting accumulated charge in SiCOH films while VUV photons with higher energies did not have this effect. Moreover, VUV irradiation with 8.9 eV photons depletes the most charge. This energy serves as a reference point from which other properties of the materials such as the location and presence of defect states could be detected and band-gap energy of SiCOH could be achieved finally. [1] In addition, a comparison of band-gap measurements of low-k dielectrics made with other techniques, such as X-ray photoelectron spectroscopy (XPS) [2] is presented.

This work was supported by the Semiconductor Research Corporation under Contract 2012-KJ-2359 and by the National Science Foundation under Grant CBET-1066231.

[1] H. Zheng, S. W. King, V. Ryan, Y. Nishi and J. L. Shohet, "Bandgap measurements of low-k porous organosilicate dielectrics using vacuum ultraviolet irradiation", *Appl. Phys*. **104**, 062904 (2014).

[2] M. T. Nichols, W. Li, D. Pei, G. A. Antonelli, Q. Lin, S. Banna, Y. Nishi and J. L. Shohet, "Measurement of Bandgap Energies in low-k organosilicates", *J. Appl. Phys*. **115**, 094105 (2014).

EM-TuP22 VUV Curing Process for Low-k Organosilicate Dielectrics, ***Huifeng Zheng****, X. Guo,* University of Wisconsin-Madison*, S.W. King,* Intel Corporation*, E. Ryan,* GLOBALFOUNDRIES*, Y. Nishi,* Stanford University*, J.L. Shohet*, University of Wisconsin-Madison

Porous SiCOH films are of great interest in semiconductor fabrication due to their low-k properties. Post-deposition treatments of SiCOH thin films are required to decompose the labile pore generator (porogen) and ensure optimum network formation to improve the electrical and mechanical properties of low-k dielectrics. The currently used UV curing method has some weaknesses such as the required high curing temperature (400-425ºC) and the time for curing (several minutes). Vacuum ultraviolet (VUV) irradiation over specific energy ranges was found to overcome some of these drawbacks by efficiently decreasing the dielectric constant and increasing the hardness and elastic modulus of low k dielectrics at room temperature. Specifically, photon energies equal to or larger than 6.0 eV were found to decrease the k value of SiCOH films while lower energies did not have this effect. 6.2 eV photons were found to be most effective. [1] In addition, photons with energies equal to or larger than 8.3 eV enhanced the mechanical properties of SiCOH films significantly. Fourier Transform Infra-red Spectroscopy (FTIR) shows that the breaking of $C-H_x$ stretching bonds (3050-2850 cm^{-1}) in organic porogens and transitioning of Si-O-Si stretching bonds (1250-1000 cm^{-1}) from cage-like to network-like structures contribute to the decrease of dielectric constant and increase of hardness and elastic modulus of SiCOH films. [2] [#_edn2] These investigations show that the optimum photon energies for post-deposition treatment of SiCOH might exist in the VUV range and a VUV-involved curing process could be utilized as a post treatment method in low-k material deposition technologies.

This work was supported by the Semiconductor Research Corporation under Contract 2012-KJ-2359 and by the National Science Foundation under Grant CBET-1066231.

[1] H. Zheng, E.T.Ryan, Y. Nishi and J.L. Shohet, "Effect of vacuum-ultraviolet irradiation on the dielectric constant of low-k organosilicate dielectrics,"*Appl. Phys. Lett.* **105,** 202902 (2014).

[2] [X. Guo, J. E. Jakes, S. Banna, Y. Nishi and J. L. Shohet, "Effects of plasma and vacuum- ultraviolet irradiation on the mechanical properties of low-k porous organosilicate glass", *J. Appl. Phys.* **116**, 044103 (2014).

EM-TuP26 Identification of Topological Surface States in $(Bi_{1-x}Sb_x)_2Te_3$ Thin Films, ***Jenna Walrath****, A.S. Chang, V.A. Stoica, Y.H. Lin, W. Liu, L. Endicott, C. Uher, R. Clarke,* University of Michigan*, R.S. Goldman*, University of Michigan, Ann Arbor

Bi_2Te_3 and Sb_2Te_3 are well-known materials for thermoelectric applications, which have also recently been identified as topological insulators (Tis) with surface states consisting of a single Dirac cone. Spin-momentum locking in Tis make them desirable for spintronics and other applications. However, to be useful for such devices, these materials must be bulk insulating and have accessible surface states, requiring both the Fermi level and the Dirac point to be located within the bulk bandgap. Furthermore, it is desirable to possess these properties at room temperature in ambient conditions. Robust surface states in ambient conditions have been demonstrated for Bi_2Se_3, [1] but to our knowledge direct detection of topological surface states has yet to be demonstrated in BiSbTe systems. Here we use scanning tunneling microscopy and spectroscopy to characterize the band structure of 30nm MBE-grown $(Bi_{.42}Sb_{.58})_2Te_3$ thin films, revealing the presence of topological surface states within the bulk band gap. Both the Fermi level and the Dirac point are located inside the bulk bandgap, indicating bulk insulating behavior with accessible surface states. Furthermore, the surface states are robust to room temperature and limited air exposure.

[1] C. Chen, S. He, H. Weng, W. Zhang, L. Zhao, H. Liu, X. Jia, D. Mou, S. Liu, J. He, Y. Peng, Y. Feng, Z. Xie, G. Liu, X. Dong, J. Zhang, X. Wang, Q. Peng, Z. Wang, S. Zhang, F. Yang, C. Chen, Z. Xu, X. Dai, Z. Fang, and X.J. Zhou, Proc. Natl. Acad. Sci. U.S.A.**109**, 3694 (2012).

EM-TuP27 Quantitative Potential Profiling Across Metal-Oxide-Semiconductor Stacks, ***Sylvie Rangan****, M. Kalyanikar, J. Duan, G. Liu, R.A. Bartynski, E. Andrei, L. Feldman, E. Garfunkel*, Rutgers, the State University of New Jersey

Band alignment between materials and potential changes across thin films is of great importance for understanding electronic properties of multilayer structures and their resulting properties in devices. Although energy alignment and band bending has been studied for decades, an accurate profile of the potential across an ultrathin insulating layer (<10nm) has yet to be determined. In this work, we have developed a new approach to precisely measure the potential profile across Metal/Oxide/Semiconductor (MOS) stacks under in-situ gate-biasing conditions, using x-ray photoemission spectroscopy (XPS). Previous attempts of potential profile measurements have been limited to qualitative assertions due to the absence of controlled biasing. Here, interface dipoles and band bending at the oxide/semiconductor interface, as well as the effective potential across the oxide have been directly measured as a function of the bias applied between the semiconductor and the gate. This technique opens a large field of research, as it allows simultaneously a chemical mapping and a quantitative characterization of potential profiles in novel structures.

Additive Manufacturing/3D Printing Focus Topic
Room: 211B - Session AM+EM+MS+TF-WeM

Materials, Designs, and Applications of Additive Manufacturing
Moderator: Erik B. Svedberg, The National Academies

8:00am **AM+EM+MS+TF-WeM1 An Overview of Additive Manufacturing**, ***Ed Morris***, *R. Gorham*, NCDMM **INVITED**

"An Overview of Additive Manufacturing" - Additive manufacturing, also called 3D printing, has captured worldwide attention. Many believe that it is introducing the next industrial revolution because of its impact on product innovation and its unique manufacturing capabilities. America Makes – National Additive Manufacturing Innovation Institute is the first Manufacturing Innovation Institute established as part of a National Network for Manufacturing Innovation. Mr. Ed Morris, Director of America Makes and Vice President, National Center for Defense Manufacturing and Machining, will give an overview of additive manufacturing, and will discuss America Makes' actions to accelerate the use of additive manufacturing technologies in the United States and increase our nation's global manufacturing competitiveness.

8:40am **AM+EM+MS+TF-WeM3 Material Considerations and Opportunities for Laser Powder Bed Additive Manufacturing**, ***Michael W. Peretti***, *D.H. Abbott*, General Electric Aviation **INVITED**

Additive Manufacturing (AM) has the potential to be a significant supply chain disruptor over traditional means for manufacturing a broad range of components for aerospace and other demanding applications. The ability to unlock complex, high-performance designs while reducing part count and number of manufacturing steps is beginning to revolutionize the way we think about making things. One of the key areas of development to further expansion of opportunities for AM is the production and supply of high-quality raw materials. This presentation discusses the critical issues for AM input raw materials, with particular emphasis on metal powder input stock for laser powder bed AM processes. Some background and experience from GE Aviation's development of the LEAP fuel nozzle will be shared, along with comments on the direction that the AM industry could take and the role of and potential for AM-specific metal powder alloys.

9:20am **AM+EM+MS+TF-WeM5 High Quality and High Speed EBM 3D Printing by the Integration of High Performance Electron Sources**, ***Colin Ribton,*** TWI Ltd., UK, *S. del Pozo*, TWI Ltd. and Brunel University, UK

Production of high integrity components must use smart manufacturing methods to be efficient in use of scarce materials and other resources, and must ensure its environmental impact is minimized. Advanced manufacturing techniques, such as metal powder bed 3D printing , can be carried out by selective laser melting (SLM) or electron beam melting (EBM). In both cases the component is built layer by layer, with a beam as an intense energy source drawing each layer by melting powder. EBM is significantly faster than SLM and has been used to create metal parts in large quantities over the past 5 years. EBM machines have produced many tens of thousands of orthopedic implants. There are a number of key benefits in employing this manufacturing technology – including 'complexity for free', efficient use of material and flexibility of design. Increasingly, the aerospace industry is investigating the use of EBM for the manufacture of aircraft components and aero engine parts. However, the size of many of these components presents challenges to the EBM process in production rate and quality consistency over long build times (i.e. 150 hours).

The aim of this work is to overcome key obstacles concerning future requirements for EBM 3D printing for production of aerospace parts through the integration of two enabling technologies. The work will develop and integrate a novel plasma cathode electron source with an EBM machine focusing on realizing the enhanced capabilities of low maintenance, consistent manufacturing performance and higher productivity. Also, development and integration of an array probe device will provide quantified quality assurance of machine manufacturing readiness. The key research challenges will be the design of the electron source and optics and the development of new build procedures making best use of the new source.

The equipment will enable the wider adoption of EBM leading to efficient use of materials – particularly strategic titanium alloys and nickel based super alloys at first.

9:40am **AM+EM+MS+TF-WeM6 Laser Induced Forward Transfer of High-Viscosity, Polymer-Based VO_2 Inks**, ***Eric Breckenfeld***, *H. Kim, T. Sutto, N. Charipar, A. Piqué*, Naval Research Laboratory

Additive manufacturing direct-write processes such as direct-write assembly, micropen, inkjet, and laser-induced forward transfer (LIFT) have become increasingly popular as interest in printable electronics and maskless patterning has grown. Compared to conventional lithography, these additive manufacturing processes are inexpensive, environmentally friendly, and well suited for rapid prototyping and large-area applications. At the same time, researchers have pursued various chemical solution deposition processes for combining additive manufacturing technology with functional electronic materials. Among a multitude of transition-metal oxides, vanadium dioxide (VO_2) has emerged as a material of particular interest due to its sharp semiconductor-to-metal phase transition near room temperature. A set of distinct optical and electronic properties which arise as a result of this transition have made VO_2 popular for thermochromic coatings, resistive switching, optical storage, light modulators, and other applications. Here, we demonstrate the development of a polymer-based solution for the deposition of VO_2 thin films. By exploring a variety of sintering and annealing conditions as well as exploring different polar solvents, we have optimized the growth of these films on glass and crystalline substrates. We go on to explore printing of VO_2 devices via the LIFT technique, which is notable for its ability to print high-viscosity inks and pastes. Finally, we will discuss our efforts toward the development of low temperature laser sintering in order to realize VO_2 films on substrates incompatible with high furnace temperatures.

11:40am **AM+EM+MS+TF-WeM12 Printing Multi-Functionality using Additive Manufacturing**, ***Ryan Wicker***, University of Texas at El Paso **INVITED**

Since the commercial introduction of Additive Manufacturing (AM) technologies more than two decades ago, considerable advancements in processing speed, accuracy, resolution and capacity have been achieved and the available AM materials have expanded considerably, enabling customized end-use products to be directly manufactured for a wide range of applications. Many AM technologies have been released that use different processes for fabricating the individual layers from a variety of liquid, solid, and powder-based materials ranging from photoreactive polymers to metals. In 2000, the University of Texas at El Paso identified AM as an emerging technology and invested strategically in establishing the W.M. Keck Center for 3D Innovation (Keck Center). The Keck Center has grown to occupy over 13,000 sq. feet with more than 50 commercial and experimental AM machines, representing 10 system manufacturers, nine distinct layer processing methods, and several custom AM-based patented and patent-pending systems. One particular focus of Keck Center research is on developing the methods and systems required to have automated control over material placement and structure creation, leading to, for example, the realization of complex 3D devices that integrate electronics and thus intelligence within mechanical structures as well as 3D spatially complex bioactive, implantable, tissue engineered constructs. There are myriad issues associated with combining multiple materials to create functional products – from the deposition and processing of different materials to the combined performance of the materials in the resulting product. Despite these issues, the opportunities for AM in aerospace, defense, biomedical, energy and enumerable other applications continue to expand as the achievable length scales in AM decrease, the number of materials available for use in AM increases, the performance of these materials are characterized and controlled in the final product, and new strategies for integrating AM with other manufacturing technologies are successfully demonstrated.

Electronic Materials and Processing
Room: 210E - Session EM-WeM

Beyond CMOS: Resistive Switching Devices
Moderator: Christopher Hinkle, University of Texas at Dallas

8:00am **EM-WeM1 Tantalum Oxide Resistive Memory Devices by IAD**, ***Ronald Goeke***, *M. Marinella, D.R. Hughart*, Sandia National Laboratories

Resistive random access memory (ReRAM), or memristors, may be capable of significantly improving the efficiency of neuromorphic computing, when

used as a central component of an analog hardware accelerator. However, the current fabrication methods for these nano-ionic resistive memory devices suffer from significant electrical variation within a single device and between devices. This variation degrades the maximum efficiency and accuracy, which can be achieved by a ReRAM-based neuromorphic accelerator.

The switchable resistive thin film at the heart of these memristor devices has been fabricated from sub-stoichiometric tantalum pentoxide using Ion Assisted Deposition (IAD). These devices fabricated with IAD have shown a significant improvement in yield and a big reduction in device performance variability. This success has been repeated many times now. The devices are fabricated from a sub-stoichiometric tantalum pentoxide using IAD to control the oxygen to tantalum ratio. The IAD deposition approach involves e-beam evaporation of tantalum metal with a reactive beam of oxygen and argon ions impinging upon the growing film. Using this technique, the oxide formation occurs at the substrate resulting in good control over film stoichiometry. IAD is a popular technique for the deposition of oxide thin films in the optical coating industry, but has now been demonstrated as a valuable method for growth of oxide electronics. The electrical and optical characterization of these films will be presented.

Sandia National Laboratories is a multi-program laboratory managed and operated by Sandia Corporation, a wholly owned subsidiary of Lockheed Martin Corporation, for the U.S. Department of Energy's National Nuclear Security Administration under contract DE-AC04-94AL85000.

8:20am **EM-WeM2 Capacitance and Resistance Switching in HfO_2 RRAM**, ***Christophe Vallee***, *P. Gonon, C. Mannequin, T. Wakrim, M. Saadi,* LTM, Univ. Grenoble Alpes, CEA-LETI, France, *A. Sylvestre*, G2elab, Univ. Grenoble Alpes, France

This work addresses a new class of electrical devices that could be named “memory impedance”, or “MEM-Z” devices. These structures are based on the capability of HfO_2 MIM (Metal – Insulator –Metal) to switch both their resistance and capacitance with a memory effect. Recently, during works led on HfO_2 OxRAM [1], we found that for a specific design, upon voltage biasing, not only does the resistance changes but the capacitance also varies from positive to negative values. In other words, *both the real and imaginary part of the impedance can be controlled by the voltage bias*. If the impedance state can be non-volatile (memory function), then a new class of devices (MEM-Z) can be defined. MEM-Z devices (mem-capacitors and mem-inductors) were recently theorized and their potential applications reviewed [2]: like memristors, they can be used as non-volatile memories, for fuzzy logic (non-binary computing based on continuous variables), and as self-learning devices (neuro-inspired systems, adaptive filters…). They can also be used in tunable electronic circuits such as reconfigurable impedance matching network, reconfigurable amplifiers, programmable filters and oscillators.

In the present work we investigate both resistance and capacitance switching of HfO_2-based MIM device. By comparison to HfO_2 OxRAM, the device has been modified in order to avoid any breakdown during the capacitance switch. Therefore a bi-layer structure is used to obtain a self-compliance MEM-Z device. With this structure a bipolar capacitance cycle has been obtained with decreasing values of capacitance in the ON state. Negative values of capacitance near SET and RESET voltages are also observed. Memory effect for both positive and negative values of capacitance is also demonstrated. At present, the physical origin of capacitance variation is an open question. One hypothesis is that conduction paths, which lead to resistance switching, are the same which lead to capacitance decrease (through the inductive behavior of conduction paths, hopping conduction). This will be discussed in this presentation from the frequency dependence study of the capacitance switch.

[1] P. Gonon, M. Mougenot, C. Vallée, C. Jorel, V. Jousseaume, H. Grampeix, F. El Kamel, "Resistance switching in HfO_2 metal-insulator-metal devices", *Journal of Applied Physics*, vol.107, p.074507 (2010)

[2] Y.V. Pershin, M. Di Ventra, "Memory effects in complex materials and nanoscale systems", *Advances in Physics*, vol. 60, p.145 (2011)

8:40am **EM-WeM3 Density Functional Theory Molecular Dynamics Simulations and Experimental Characterization of high-k/SiGe(110) and SiGe(001) Interfaces**, *A.C. Kummel, E. Chagarov,* University of California at San Diego, *B. Sahu,* Globalfoundries, *S. Oktyabrsky, S. Madisetti,* College of Nanoscale Science and Engineering, Albany-SUNY, ***Tobin Kaufman-Osborn***, University of California at San Diego

Density-Functional Theory (DFT) Molecular Dynamics (MD) simulations were employed to investigate formation at finite temperature of direct interfaces between a-Al_2O_3 oxide and $Si_{0.50}Ge_{0.50}$ substrate with Si- and Ge-terminations. The simulated interfaces revealed mixed bonding between the semiconductor substrate atoms and both O and Al oxide atoms. The oxide/SiGe band gaps were unpinned and close to the SiGe bulk band gap value. The interfaces had SiGe dangling bonds but they were nearly filled and therefore did not produce mid-gap states and could not be passivated by atomic H. The Si terminated surface had a better electronic structure after bonding to oxide compared to the Ge terminated surface since the dangling bonds on the Si atoms tend to be more filled since the Si terminated interface is a better charge acceptor. C-V spectroscopy combined with angle-resolved X-ray photoelectron spectroscopy (AR-XPS) experimentally confirmed formation of interfaces with low interface trap density via direct bonding between a-Al_2O_3 and SiGe.

9:00am **EM-WeM4 Density-Functional Theory Molecular Dynamics Simulations of a-HfO_2/Ge(100)(2x1) and a-ZrO_2/Ge(100)(2x1) Interface Passivation**, ***Evgueni Chagarov***, University of California at San Diego, *L.M. Porter,* Carnegie Mellon University, *A.C. Kummel*, University of California at San Diego

: The structural properties of a-HfO_2/Ge(2x1)-(001) and a-ZrO_2/Ge(2x1)-(001) interfaces were investigated with and without a GeOx interface interlayer using density-functional theory (DFT) molecular dynamics (MD) simulations. Realistic amorphous a-HfO_2 and a-ZrO_2 samples were generated using a hybrid classical-DFT MD “melt-and-quench” approach and tested against experimental properties. The oxide/Ge stacks were annealed at 800K, cooled to 0K, and relaxed providing system with enough freedom to form realistic interfaces. For each high-K/Ge stack type, two systems with single and double interfaces were investigated. All stacks were free of midgap states; however, stacks with an GeOx interlayer had band-edge states which decreased the band gaps by 0-30 %. These band-edge states were mainly produced by under-coordinated Ge atoms in GeOx layer or its vicinity due to deformation, intermixing, and bond-breaking. The DFT-MD simulations show that electronically passive interfaces can be formed either directly between high-K dielectrics and Ge or with a monolayer of GeO_2 if the processing does not create or properly passivates under-coordinated Ge atoms and Ge’s with significantly distorted bonding angles. Comparison to the charge states of the interfacial atoms from DFT to experimental XPS results show that while most studies of gate oxide on Ge(001) have a GeO_x interfacial layer, it is possible to form a oxide/Ge interface without a GeO_x interfacial layer. Comparison to experiments is consistent with the dangling bonds in the suboxide being responsible for midgap state formation.

9:20am **EM-WeM5 Role of Active and Inert Electrodes in Filament Formation in Resistive Switching Devices (RRAM)**, ***Gargi Ghosh***, Virginia Tech, *S.W. King,* Intel Corporation, *M.K. Orlowski*, Virginia Tech

Reliable filamentary resistive switching (RS) depends largely on the electrochemical properties of the active and inert electrodes. A resistive switching memory cell in a RRAM is generally built as a capacitor-like MIM Cu/TaOx/Pt structure, comprised of an insulating or resistive material sandwiched between two electron conductors. Cu electrode produces via a redox reaction (Cu -> Cu^++e^-) highly mobile Cu^+ cations that drift in TaO_x and discharge at the inert Pt electrode forming a conductive filament (CF) of the ON state. To assess the role of active and inert electrodes, we report manufacturing and characterization of 4 derivative devices: Cu/TaO_x/Ta, Cu/TaO_x/Ti, Ta/TaO_x/Pt, Ti/TaO_x/Pt. For a possible integration of RRAM in CMOS back-end, two new metals Ta and Ti used in CMOS metalization are selected. In all four derivative cells a CF formation could be observed at voltages 2V-5V, comparable with Cu/TaO_x/Pt. However, Cu/TaO_x/Ti could not be reset, being permanently damaged. Cu/TaO_x/Ta could be reset but only a few times displaying noisy reset behavior. Ta/TaO_x/Pt device shows resistive switching with a low forming voltage of 2V. The best resistive switching behavior was shown by Ti/Ta_2O_5/Pt device. Main conclusions of the study: 1) In Cu/TaO_x/Ti Cu CFs are formed with a weak base at the Ti electrode due to Cu dissolution in Ti. Cu CF has low resistance and cylindrical shape being difficult to rupture. 2) Cu/TaO_x/Ta device shows better switching properties than Cu/TaOx/Ti, because Ta is better diffusion barrier for Cu than Ti. 3) Ta/TaO_x/Pt is a potential candidate for RS but suffers from: i) the redox reaction Ta -> Ta^++e^- is much weaker than for Cu, ii) the diffusion of Ta in TaO_x is faster than of Cu in TaO_x. The result of these two competing mechanisms are fragile CFs with no resistive constrictions. Hence, the RS is observed but its operation is unreliable. 4) Ti/TaO_x/Pt displays if noisy RS. This is due to Ti being known as a getter for oxygen. The Ti CF is therefore fragile as Ti is easily and permanently incorporated in the oxide matrix forming a $Ta_xTi_yO_z$ compounds. The overall conclusion from this comparative study is a better understanding of conditions for reliable RS: a metallic filament has to be formed with a resistive constriction, e.g. in the form of truncated cone with a sharp apex. Cylindrical CFs are hard to rupture and hence undesirable for RS. Cone-like CFs for reliable RS require: a) copious supply of metal ions, b) high metal ion diffusivity in the dielectric, c) high ion stopping power of the counter electrode, and d) moderate compliance currents to be applied during the set operation to assure cone-like shape of the CFs.

9:40am **EM-WeM6 Neutron Induced Effects on HfO_x-Based Resistive Random Access Memory**, ***Karen Hsu**, T. Chang,* University of Wisconsin-Madison*, L. Zhao,* Stanford University*, R. Agasie,* University of Wisconsin-Madison*, Y. Nishi,* Stanford University*, Z. Ma, J.L. Shohet*, University of Wisconsin-Madison

As the size of devices decreases and the complexity of electronic chips increases, cosmic-ray-induced crashes are becoming a severe threat to electronic circuits and devices. Resistive Random Access Memory (RRAM) [1], which is considered as a very promising memory technology for embedded systems, has undergone intense research in both industry and academia in the last ten years. As RRAM technology matures and electronic devices using RRAM are likely to be built soon, malfunctions of RRAM will become an important problem in industry since the size of these devices will continue to decrease. Neutrons that come from earth bound or from cosmic ray sources are likely one to produce significant effects on the RRAM [2] based on their fluxes at terrestrial altitudes and their interaction cross sections. In this work, neutrons from the University of Wisconsin Max Carbon Radiation Science Center were used as the radiation source The neutron-induced effects on HfO_X RRAM include single-event-upset (SEU), modification to forming voltage, resistance of both the high-resistance (HRS) and low-resistance states (LRS) and shifts in set/reset voltage.

Some RRAM cells can actually be formed during neutron irradiation and then switch from the HRS to the LRS after additional neutron irradiation. The SEU rate increases linearly as neutron fluence increases. For those neutron-irradiated RRAM cells that did not switch from the HRS to the LRS under irradiation, a smaller forming voltage was required after irradiation. In addition, an increase in the HRS resistance and better switching behavior was observed in those RRAM cells formed entirely by neutron irradiation.

Shifts in the set/reset voltage were also observed after neutron radiation. X-ray diffraction was used on HfO_2 films to investigate the physical mechanism, which is attributed to atomic-structure changes in HfOx caused by neutron irradiation.

This work was supported by the Semiconductor Research Corporation under Contract No. 2012-KJ-2359, by the National Science Foundation under Grant No. CBET-1066231.

References:

1. H.-S. Philip Wong, H-Y Lee, S. Yu, Y. S. Chen, Y. Wu, P-S Chen, B. Lee, F. T. Chen, and M-J Tsai, "Metal–oxide RRAM," *Proceedings of the IEEE***100** 1951 (2012).

11:00am **EM-WeM10 Relation of Low-k Interconnect Si-based Dielectric Breakdown to Resistive Switching Behavior**, ***Marius Orlowski**, G. Ghosh, P. Kassalen, R. Gupta,* Virginia Tech*, S.W. King*, Intel Corporation

The relation between resistive switching (RS) and breakdown and reliability mechanisms are studied for metal-insulator-metal (MIM) structures with low-k dielectrics (SiOC:H, SiCOH, SiNC:H, SiCN:H, SiC:H, SiON:H, SiN:H) all 25 nm thick, with Ti, and Cu as electrode materials that are commonly used in the CMOS back-end process. The TDDB time is correlated with defect generation and related to mechanisms responsible for RS. Defect generation depends exponentially on E_a-bxE_{el}, where E_a is the activation energy, b is the bond polarization factor being proportional to the molecular dipole moment p_o, b=(2+k)/3p_o, and E_{el} is the electric field across the dielectric. The breakdown field E_{bd} is determined by E_a-bxE_{bd}=0, i.e. at high enough electric fields there is effectively no barrier impeding creation of defects. From this condition, the breakdown field E_{bd}=E_a/b is determined. We obtain, for SiC:H E_a=0.28 eV and p_o=10e-A, for SiCN:H E_a=0.26 eV and b=4e-A, for SiN:H, E_a=0.17 eV and p_o=1.2eA, for SiON:H p_o=1.5e-A. for SiOC:H we obtain E_a=1.67eV and p_o=15e-A. We find that E_a values of low-k dielectrics are very low compared with those for high-k dielectrics, e.g. E_a=4.4 eV for HfO_2 with k=21. On the other hand, the strength of the molecular dipole for low-k dielectrics is comparable to that for high-k dielectrics (e.g. p_o=11e-A for HfO_2). In terms of RS properties under a linear voltage sweep the low-k materials display varied behavior: SiNC:H does not exhibit resistive switching, i.e. under linear voltage stress it shows gradual decrease of resistance but the on-state is volatile, i.e. it evanesces when the cell is unpowered. A similar behavior is observed for SiCN:H, i.e. soft volatile breakdown with a volatile on-state. SiOC:H shows a sharp resistive switching that cannot be reversed - the cell is on permanently. The set voltage is high V_{set}=11.8V and it decreases significantly with increasing temperature. SiON:H shows comparable behavior as SiOC:H with slightly lower set voltages. SiC:H shows sharp resistive switching behavior at a moderate set voltage V_{set}=6.5V @ 300K. SiN:H displays also a sharp resistive switching but at much higher voltage, V_{set}=11.5V @300K. The high set voltages for SiC:H and SiN:H correlate well with high densities of those dielectrics, both at 2.5 g/cm^3 and similar dielectric constant of k=7.2 and 6.5, respectively. The on-state is attributed to the formation of a Cu conductive filaments. The conductive filaments are cylindrical and difficult to rupture. The paper discusses correlation, differences, and commonalities between data obtained for dielectric breakdown and resistive switching mechanisms in terms of the film properties.

11:20am **EM-WeM11 Thin Film Carbon Nanofuses for Permanent Data Storage**, ***Kevin Laughlin**, S. Jamieson, H. Wang, J. Bagley, T. Pearson, R.C. Davis, M.R. Linford, B.M. Lunt*, Brigham Young University

As memory elements shrink, the reliable life span of digital data is decreasing. Today we all have more data, in less stable formats. For hard drives, DVDs, and flash memory, the reliable life of the data is less than 10 years. Rewriting data extends life, but at high maintenance costs. A potential solution to this challenge is write once read many storage media where writing the data results in a permanent, irreversible change. We have been developing thin film carbon nanofuses for use as a permanent data storage medium. Carbon shows particular promise as an electronic storage medium due to its high localized bond strength resulting in high surface stability and reasonable electrical conductivity. I will present the fabrication and characterization of nanoscale fuses with feature sizes down to ~50nm. The low resistance sp^2 carbon is arc deposited and then patterned using electron beam lithography and plasma etching. The electron beam resist used, HSQ, results in a glass etch mask for pattern transfer into the carbon film with an O_2 plasma. The fuses were written and detected electrically, and excellent stability was observed.

11:40am **EM-WeM12 Low-k/Cu Resistive 2-Level PROM Memory Collocated with CMOS Back-End Metallization**, ***Anshuman Verma**, G. Ghosh,* Virginia Tech*, S.W. King,* Intel Corporation*, M.K. Orlowski*, Virginia Tech

Building nonvolatile memory directly into a CMOS low-k/Cu interconnects would reduce latency in connectivity constrained computational devices and reduce chip's footprint by stacking memory on top of logic. NVM memory includes two flavors: i) random-access memory, and ii) programmable read-only memory (PROM). The paper investigates suitable choice of materials for an integration of PROM compatible with manufacturing of CMOS back-end. Three capacitor-like MIM structures Al/Ti/I/Cu, with dielectrics I=SiOC:H, SiC:H, SiCN:H, all 25 nm thick, have been selected among samples manufactured by Intel Inc and investigated for resistive switching properties. The samples have been subjected to set and reset operations applied customarily to resistive switching devices with TiAl electrode being grounded and a positive bias applied to Cu electrode. For SiOC:H devices, a sharp transition from R_{OFF}=200MΩ to $R_{ON}(1)$=120kΩ at threshold $V_{set}(1)$= 0.9V - 1.2 V is observed. When the set device is subsequently subjected to a linear voltage ramp, a secondary sharp set transition from $R_{ON}(1)$=120kOhm to $R_{ON}(2)$=2-10Ω is observed at $|V_{set}(2)|$=1.0-1.3V and high compliance currents I_{cc}≈100mA, independent of the bias polarity. $R_{ON}(2)$ can be controlled by the level of I_{cc} (@I_{cc}≈10mA $R_{ON}(2)$=34Ω). Both transitions are irreversible and the low resistance states are stable. The 1st transition is likely to be caused by formation of a Cu conductive filament (CF). Because of the weak diffusion/migration stopping power of Ti for Cu, the resulting Cu CF is of a cylindrical form instead of a conical with the former being very difficult to rupture. The 2nd set transition leads to a dramatic decrease of R_{ON} by a factor 10^5. To ascertain the nature of the CF, we have measured the temperature coefficient of resistance α of the CF and obtain unusually high values, typically α=0.04K^{-1}, which is 10X larger than a for bulk Cu, α=0.0039K^{-1}, or for Cu CF in Cu/TaO_x/Pt, α=0.0033K^{-1}) and 40X higher than a for oxygen vacancy defects CF, α=0.001K^{-1}. The secondary set from $R_{ON}(1)$ to $R_{ON}(2)$ is attributed to some, presently unknown, dramatic phase transformation. Structures with SiC:H (same metal electrodes) show different behavior, but result in the same low resistivity state $R_{ON}(2)$. They require high V_{set}= 3-4V and display volatile behavior at low I_{cc} values. At higher I_{cc} they set into a stable and very low R_{ON}≈5Ω, constituting thus only 1-level PROM. Similarly, devices with SiCN:H are setting permanently only at high I_{cc} currents (50-100mA) and display also very low final resistance of about 10Ω. The paper discusses the properties of the highly conductive, metallic CFs with the uncharacteristically high α.

12:00pm **EM-WeM13 Novel Contact Materials for Reliable Nanoelectromechanical Switches**, ***Frank Streller**, G. Wabiszewski, D. Durham, R.W. Carpick*, University of Pennsylvania

Nanoelectromechanical (NEM) switches were identified by the roadmap of the semiconductor industry as a low-power "beyond CMOS" technology. However, the reliability of the contact interface currently limits the commercialization of NEM switches, as the electrical contact has to be able to physically open and close up to a quadrillion times without failing, which typically occurs due to adhesion (sticking shut) or contamination (reducing switch conductivity). These failure mechanisms are not well understood, and materials that exhibit the needed performance have not been demonstrated. Thus, commercially viable NEM switches demand the scientific development and characterization of novel contact materials,

along with efficient methods to evaluate the interfacial performance of these materials.

We have developed novel contact material candidates that are highly conductive, minimally adhesive, chemically inert, mechanically robust, and amenable to CMOS fabrication processes.[1,2] One promising candidate is platinum silicide (Pt_xSi). The controlled diffusion of sequentially-deposited thin films of amorphous silicon and Pt allowed us to tune the chemical composition of Pt_xSi over a wide range ($1<x<3$). We measured the mechanical and electrical contact properties of Pt_xSi of multiple stoichiometries in comparison with pure Pt. These experiments showed that the Pt-rich silicide phase (Pt_3Si) may be an ideal contact material for NEM switches due to its desirable combination of mechanical robustness with metal-like conductivity. We also demonstrate that Pt_xSi can be used to release NEM switches with a self-formed gap caused by interfacial separation driven by shrinkage-induced tensile stress.

To assess contact material candidates under NEM switch-like conditions, we developed a novel, high-throughput electrical contact screening method based on atomic force microscopy that enables billions of contact cycles to be tested in laboratory timeframes. We compared the performance of self-mated and dissimilar single asperity Pt and Pt_xSi contacts under forces and environments representative of NEM switch operation, and cycled them up to two billion times. The contact resistance increased by up to six decades due to cycling-induced growth of insulating tribopolymer in the case of Pt-Pt contacts, while Pt_xSi exhibited better stability. Additionally, we found that the original conductivity can be largely recovered by sliding of the contact, which essentially leads to the displacement of the tribopolymer. This suggests a route for mitigating contamination-induced failure.

[1] Streller *et al.*, *Adv. Mater. Interfaces*, 1 (2014).

[2] Streller *et al.*, *IEEE Nanotech. Mag.*, 1 (2015).

2D Materials Focus Topic
Room: 212C - Session 2D+EM+IS+MC+NS+SP+SS-WeA

Dopants and Defects in 2D Materials
Moderator: Daniel Gunlycke, Naval Research Laboratory, Zenghui Wang, Case Western Reserve University

2:20pm **2D+EM+IS+MC+NS+SP+SS-WeA1 The Effect of Defect Density on the Mechanical Properties of Graphene**, ***Jonathan Willman***, *J.M. Gonzales,* University of South Florida, *R. Perriot,* Los Alamos National Laboratory, *I.I. Oleynik*, University of South Florida

Recent experiments involving nanoindentation of graphene have demonstrated counterintuitive weakening of Young's modulus with increasing concentrations of point defects in graphene in contradiction to previous investigations. To fully resolve these inconsistencies we perform large-scale molecular dynamics simulations of nanoindentation under conditions of Atomic Force Microscopy (AFM) nanoindentation experiments. The reliable description of interatomic interactions is achieved by using recently developed screened environment-dependent bond order (SED-REBO) potential. The elastic properties of the defective graphene, the breaking strength and the mechanisms of fracture under indenter are investigated as a function of type of point defects as well as their concentration.

2:40pm **2D+EM+IS+MC+NS+SP+SS-WeA2 Investigation of Grain Boundaries in CVD Grown MoS_2**, ***Kolyo Marinov***, *D. Ovchinnikov, D. Dumcenco, A. Kis*, Ecole Polytechnique Fédérale de Lausanne (EPFL), Switzerland

We present the characterization of grain boundaries in polycrystalline CVD-grown MoS_2 films. Epitaxial growth on sapphire substrates is achieved leading to preferred orientation of the domains, which is confirmed by transmission electron microscopy experiments. Using Scanning Kelvin probe microscopy the local potential drop across the three predominant types of grain boundaries in field effect transistors is investigated. These measurements demonstrate that the interfaces between single grains do not degrade the electrical conductivity, which is due to the well aligned growth of the single domains. Furthermore, the relatively high mobility of electrons in the polycrystalline material stays constant even in devices with channels of 80 μm containing multiple grains, separated by grain boundaries. Our approach is a step forward to fabrication of large-area, uniform and high quality single-layer CVD MoS_2.

3:00pm **2D+EM+IS+MC+NS+SP+SS-WeA3 Polycrystalline 2D Materials: Atomic Structure and Electronic Transport Properties**, ***Oleg Yazyev***, Ecole Polytechnique Fédérale de Lausanne (EPFL), Switzerland **INVITED**

Grain boundaries and dislocations are intrinsic topological defects of polycrystalline materials, which inevitably affect their physical properties. In my talk, I will discuss the structure of topological defects in two-dimensional (2D) materials such as graphene and monolayer transition metal dichalcogenides (TMDCs) [1].

I will first introduce a general approach for constructing dislocations in graphene characterized by arbitrary Burgers vectors and grain boundaries covering the complete range of possible misorientation angles. By means of first-principles calculations we address the thermodynamic properties of grain boundaries revealing energetically favorable large-angle configurations as well as dramatic stabilization of small-angle configurations via the out-of-plane deformation, a remarkable feature of graphene as a two-dimensional material [2]. Both the presence of stable large-angle grain-boundary motifs and the out-of-plane deformation of small-angle configurations have recently been observed by scanning tunneling microscopy [3].

In the rest of my talk, I will focus on the electronic transport properties of polycrystalline 2D materials. Ballistic charge-carrier transmission across periodic grain boundaries is governed primarily by momentum conservation. Two distinct transport behaviors of such grain boundaries in graphene are predicted − either perfect reflection or high transparency with respect to low-energy charge carriers depending on the grain boundary periodicity [4]. It is also shown that certain periodic line defect structures can be engineered and offer opportunities for generating valley polarized charge carriers [5]. Beyond the momentum conservation picture we find that the transmission of low-energy charge carriers can be dramatically suppressed in the small-angle limit [6]. Unlike graphene, TMDCs combine a two-valley electronic band structure with strong spin-orbit effects. The latter can be employed for creating spin-polarized currents and adds yet another conservation law in the electronic transport across regular defects such as the frequently observed inversion domain boundaries [7,8].

* This work has been supported by the Swiss NSF, ERC and Graphene Flagship.

[1] O. V. Yazyev and Y. P. Chen, Nature Nanotechnology **9**, 755 (2014).

[2] O. V. Yazyev and S. G. Louie, Phys. Rev. B **81**, 195420 (2010).

[3] Y. Tison *et al.,* Nano Lett. **14**, 6382 (2014).

[4] O. V. Yazyev and S. G. Louie, Nature Materials **9**, 806 (2010).

[5] J. H. Chen *et al.,* Phys. Rev. B **89**, 121407(R) (2014).

[6] F. Gargiulo and O. V. Yazyev, Nano Lett. **14**, 250 (2014).

[7] A. Pulkin and O. V. Yazyev, *submitted.*

[8] O. Lehtinen *et al.,* ACS Nano **9**, 3274 (2015).

4:20pm **2D+EM+IS+MC+NS+SP+SS-WeA7 Defects Compensation and Refining Optical Luminescence in Organic/Transition Metal Dichalcogenide Heterostructure**, *J.H. Park,* UC San Diego, *A.M. Sanne, H.C.P. Movva,* UT-Austin, *S. Vishwanath,* Cornell University, ***Il Jo Kwak***, UC San Diego, *H. Xing,* Cornell University, *J. Robertson,* University of Cambridge, UK, *S.K. Banerjee,* UT-Austin, *A.C. Kummel*, UC San Diego

Since layered transition-metal dichalcogenides(TMD) have demonstrated novel electronic and optoelectronic property, intense research has focused synthesis and integration into future electronic devices. Unlike graphene, TMD materials have band gaps, and these band structures can be tuned by thickness. However, in many cases, unintentional defects can be observed on TMD giving rise to the degradation of performance in the devices. Even for mechanical exfoliated TMD, there is a high density of defects, such as vacancies. For successful integration of TMD into devices, proper passivation of defects on TMD requires high stability in ambient conditions. In this study, a TiOPc monolayer was employed for passivation of defects to improve electrical and optical properties in TMD devices. Multilayer MoS_2 flakes were cleaved in ambient condition and transferred into the UHV chamber; afterwards. TiOPc monolayers were deposited on the MoS_2 surfaces by organic molecular beam epitaxy. After deposition, TiOPc forms a monolayer with only few defects, and the TiOPc monolayer structure has square lattice in a 1.5x1.5 nm grid. This crystal structure indicates that each TiOPc in the monolayer is directed outward to vacuum. The deposited TiOPc layer has very high thermal stability on MoS_2; the TiOPc layer on MoS_2 requires annealing above of 673K for desorption. This high thermal stability indicates there are strong interaction between TiOPc and MoS_2 surface. STS shows the band gap of the monolayer is 1.8 eV, while bulk MoS_2 has a 1.3eV band gap. Moreover, the Fermi level of TiOPc/bulk MoS_2 is shifted to the valence band, consistent with a P type shift. However, bulk MoS_2 surface, where less than monolayer of TiOPc was deposited, has Fermi level shifted towards the conduction band, consistent with N type doping. In the single layer MoS_2 deposited TiOPc monolayer, threshold bias is shifted from -30 V to near O V, indicating P-doping of MoS_2. It can be hypothesized that the work function transition of MoS2 is changed as a function of thickness. Before deposition of the TiOPc monolayer, the defects peak corresponded to S vacancy is displayed at 1.7 eV in photoluminescence. Conversely, the deposition of TiOPc monolayer almost completely suppresses S vacancy peak located 1.7 eV. Moreover, in the single layer MoS_2 FET, the on/off ratio is enhanced more than 2 orders magnitude. The similar charge transfer behavior also can be observed in TiOPc/WSe_2; on the bilayer WSe_2/HOPG, the TiOPc monolayer deposited on the first layer of WSe_2 shows the a conduction band shifted Fermi level, while a TiOPc monolayer deposited on the second layer of WSe_2 shows a valence band shifted Fermi level.

4:40pm **2D+EM+IS+MC+NS+SP+SS-WeA8 Reactivity and Wettability of PVD Metals on 2D Transition Metal Dichalcogenides**, ***Christopher Smyth***, *S. McDonnell, R. Addou, H. Zhu, C.L. Hinkle, R.M. Wallace*, University of Texas at Dallas

Transition metal dichalcogenides (TMDs) have been studied for years due to their tribological properties, but recent discoveries have illuminated unique opportunities for the use of single or few layer TMDs in electronics, specifically tunnel field effect transistors (TFETs). The properties of FETs fabricated with single and few layer TMDs have been investigated with some degree of success, but it has been shown via in-situ chemical analysis that interface interactions between certain contact metals and the underlying TMD are not fully understood[1,2].

In this study, the wettability and reactivity of various metals with a number of bulk TMDs (MoS_2, $HfSe_2$, $SnSe_2$, etc.) were investigated. Multiple samples were processed in parallel to ensure that all sample sets saw

identical metal depositions. The metal-TMD interface was monitored in-situ using X-ray photoelectron spectroscopy (XPS) and metal film topography was imaged using atomic force microscopy (AFM). For some low work function metals, noticeable differences in interface chemistry were found between samples that saw high vacuum rather than UHV metal e-beam depositions.

Significant variations in compatibility between contact metal and TMD were discovered. These variations were dependent upon the metal-TMD pair and the base pressure of the chamber prior to metal deposition. Au exhibits far superior wettability on $MoSe_2$, where uniform thin films were achieved, compared to $ReSe_2$, on which Au grows as clusters. Au wettability varies between that of thin films and clusters for the other TMDs studied. An Au thin film deposited on $SnSe_2$ results in the formation of reaction products such as Sn metal, as evidenced by the evolution of different chemical states in the Sn 3*d* spectrum after deposition. Reactions between MoS_2 and Sc producing Mo metal occur when Sc is deposited in UHV instead of HV. These results provide further understanding for the critical interface between Sc and TMD in high performance TFETs.

This work was supported in part by NSF Award No. 1407765, the Center for Low Energy Systems Technology (LEAST), one of six centers supported by the STARnet phase of the Focus Center Research Program (FCRP), a Semiconductor Research Corporation program sponsored by MARCO and DARPA, and by the Southwest Academy on Nanoelectronics (SWAN) sponsored by the Nanoelectronic Research Initiative and NIST.

[1] McDonnell, S.; Addou, R.; Buie, C.; Wallace, R. M.; Hinkle, C. L. Defect Dominated Doping and Contact Resistance in MoS_2. *ACS Nano* **2014**, *8,* 2880-2888.

[2] Das, S.; Chen, H.Y.; Penumatcha, A. V.; Appenzeller, J. High Performance Multi-Layer MoS_2 Transistors with Scandium Contacts. *Nano Lett.* **2012**, *12,* 100-105.

5:00pm **2D+EM+IS+MC+NS+SP+SS-WeA9 Defects and Boundaries in 2D Materials: Correlating Electronic Properties to Atomic Structures**, ***An-Ping Li***, Oak Ridge National Laboratory **INVITED**

The quest for novel two-dimensional (2D) materials has led to the discovery of hybrid heterostructures of graphene and other 2D atomic films, which provide us fascinating playground for exploring defects and boundaries in a variety of atomic layers. Even in graphene itself, there usually exist large amount of extended topological defects, such as grain boundaries and changes in layer thickness, which divide graphene into grains and domains. These interfaces and boundaries can break the lattice symmetry and are believed to have a major impact on the electronic properties, especially the transport, in 2D materials.

Here, we report on the electronic and transport properties of two types of defects studied by STM and multi-probe scanning tunneling potentiometry with a focus on the correlations to their atomic structures. The first type of defect is the monolayer-bilayer (ML-BL) boundaries in epitaxial graphene on SiC. By measuring the transport spectroscopy across individual ML-BL graphene boundaries, a greater voltage drop is observed when the current flows from monolayer to bilayer graphene than in the reverse direction, displaying an asymmetric electron transport upon bias polarity reversal [1, 2]. Interestingly, this asymmetry is not from a typical nonlinear conductance due to electron transmission through an asymmetric potential. Rather, it indicates the opening of an energy gap at the Fermi energy. Another type of defect is 1D interface in hexagonal boron nitride (hBN) and graphene planar heterostructures, where a polar-on-nonpolar 1D boundary is expected to possess peculiar electronic states associated with edge states of graphene and the polarity of hBN [2]. By implementing the concept of epitaxy to 2D space, we grow monolayer hBN from fresh edges of monolayer graphene with lattice coherence, forming a 1D boundary [3]. STM/STS measurements reveal an abrupt 1D zigzag oriented boundary, with boundary states about 0.6 eV below or above the Fermi level depending on the termination of the hBN at the boundary [4]. The boundary states are extended along the boundary, and exponentially decay into the bulk of graphene and hBN. The origin of boundary states and the effect of the polarity discontinuity at the interface will be discussed.

This research was conducted at the Center for Nanophase Materials Sciences, which is DOE Office of Science User Facility.

1 K. W. Clark, et al., *ACS Nano***7**, 7956 (2013).

2 K. W. Clark, et al., *Phys. Rev. X***4**, 011021 (2014).

3 L. Liu, et al., *Science***343**, 163 (2014).

4 J. Park et al., *Nature Commun*. **5**, 5403 (2014).

5:40pm **2D+EM+IS+MC+NS+SP+SS-WeA11 Metal Ion Intercalated 2D Materials as Transparent Electrodes**, ***Jiayu Wan****, *W. Bao, F. Gu,* University of Maryland, College Park, *M. Fuhrer,* Monash University, Malaysia, *L. Hu*, University of Maryland, College Park

Transparent electrode materials are critical for optoelectronic devices such as touch screen and solar cells. Graphene has been widely studied as transparent electrodes for its unique physical properties. To further boost the performance of graphene based transparent electrodes, we novelized Li-ion intercalation in graphene, and achieved highest performance of carbon based transparent electrodes.[1] Transmission as high as 91.7% with a sheet resistance of 3.0 ohm/sq is achieved for 19-layer LiC_6, which corresponds to a figure of merit ($Sigma_{dc}/Sigma_{opt}$) at 1,400, significantly higher than any other continuous transparent electrodes. The unconventional modification of ultrathin graphite optoelectronic properties is explained by the suppression of interband optical transitions and a small intraband Drude conductivity near the interband edge. To achieve low cost, large scale graphene-based transparent electrodes, we further developed Na-ion intercalated printed reduced graphene oxide (RGO) film[2]. Unlike pristine graphene that inhibits Na-ion intercalation, the larger layer-layer distance of RGO allows Na-ion intercalation, leading to simultaneously much higher DC conductivity and higher optical transmittance. The typical increase of transmittance from 36% to 79% and decrease of sheet resistance from 83 kohms/sq to 311 ohms/sq in the printed network was observed after Na-ion intercalation. Compared with Li-intercalated graphene, Na-ion intercalated RGO shows much better environmental stability, which is likely due to the self-terminating oxidation of Na ions on the RGO edges. This study demonstrated the great potential of metal-ion intercalation to improve the performance of graphene-based materials for transparent conductor applications.

Reference

1. Jiayu Wan[a], Wenzhong Bao[a], et al., Nature communications, 2014,5, 4224. ([a] equally contribution)

2. Jiayu Wan, Feng Gu, Wenzhong Bao, et al. Nano Letters, 2015, DOI: 10.1021/acs.nanolett.5b00300.

6:00pm **2D+EM+IS+MC+NS+SP+SS-WeA12 Oxygen Reduction Reaction on Nitrogen-doped Graphene**, ***Jun Nakamura,*** The University of Electro-Communications (UEC-Tokyo), Japan, *A. Ichikawa, H. Matsuyama, A. Akaishi*, The University of Electro-Communications (UEC-Tokyo)

Recently, several groups have reported high oxygen reduction reaction (ORR) activities in nitrogen-doped carbon nanomaterials which are candidates of metal-free catalysts for ORR [1]. Lee et al. have successfully fabricated nitrogen-doped graphene with the high ORR activity in acid media [2]. It has been confirmed that local atomic configurations of dopants in nitrogen-doped graphene are classified into three functional groups (pyrrole-like, pyridine-like, and graphite-like configurations) [3,4]. However, the mechanism of the ORR on the nitrogen-doped graphene has not fully understood.

In this work, we examine the ORR on the nitrogen-doped graphene containing the graphite-like N in a basal plane using first-principles calculations. In general, the ORR occurs mainly two pathways: The two-electron pathway (2e-) that is reduced to hydrogen peroxide (H2O2), and the direct four-electron pathway (4e-) that reduces to water (H2O). Thermodynamic electrode potentials of each process at standard conditions are about 0.68V (2e-) and 1.23V (4e-), respectively. In case of the associative mechanism for the two- and four- electron reduction pathways, the electrocatalytic activity is governed by the stability of reaction intermediates like OOH*, OH*, and O* (where "*" refers to a surface site). Free energies of the reaction intermediates have been calculated based on the computational hydrogen electrode model suggested by Nørskov et al. [5]. We have taken account of effects of electrode potential, Ph of a solution, a local electric field in double layer, and water environment.

We have constructed energy diagrams at several electrode potentials on the basis of the first-principles calculations. It has been shown that the 2e- and 4e- reduction processes proceed at potentials up to about 0.5V and 0.8V, respectively. This means that we can control the reduction pathway for the nitrogen-doped graphene with the graphite-like N. Proton-electron transfer to OOH* (the 2e- pathway), and the formation of OOH* (the 4e- pathway) are confirmed to be the rate-limiting steps, respectively. Density dependence of N on the ORR activity will also be discussed in the presentation.

References

[1] J. Ozaki, N. Kimura, T. Anahara, and A. Oya, Carbon **45**, 1847 (2007).

[2] K. R. Lee et al., Electrochem. Commun. **12**, 1052 (2010).

*** NSTD Student Award Finalist**

[3] H. Niwa et al., J. Power Sources **187**, 93 (2009).

[4] T. Umeki, A. Akaishi, A. Ichikawa, and J. Nakamura, J. Phys. Chem. C **119**, 6288 (2015).

[5] J. K. Nørskov et al., J. Phys. Chem. B **108**, 17886 (2004).

Electronic Materials and Processing
Room: 211C - Session EM+AS+MS+SS-WeA

Surface and Interface Challenges in Wide Bandgap Materials

Moderator: Aubrey Hanbicki, U.S. Naval Research Laboratory, Rachael Myers-Ward, U.S. Naval Research Laboratory

2:20pm **EM+AS+MS+SS-WeA1 Effects of Nitrogen and Antimony Impurities at SiO_2/SiC Interfaces**, ***Patricia Mooney***, Simon Fraser University, Canada **INVITED**

4H-SiC is an attractive material for devices operating at high power and high temperatures because of the large bandgap energy, 3.23 eV, the high critical breakdown field, 2.0 $MVcm^{-1}$, and high electron mobility,

850 $cm^2V^{-1}s^{-1}$. Commercialization of 4H-SiC MOSFET technology was long delayed due to the high density of defects near the SiO_2/SiC interface. Post oxidation annealing in NO ambient, the process that enabled the commercialization of SiC Power ICs in 2011, significantly reduces the density of near-interface traps and results in typical effective MOSFET channel electron mobility (μ_{FE}) values of ~20 $cm^2V^{-1}s^{-1}$ [1]. The relatively high density of near-interface traps having energy levels within 0.5 eV of the SiC conduction band was investigated using constant capacitance transient spectroscopy (CCDLTS). These measurements showed that NO annealing reduced the density of the two near-interface oxide trap distributions, attributed to Si interstitials and substitutional C pairs in SiO_2, by as much as a factor of 10 [1,2].

It has also been shown that introducing impurities such as Na, P, or Sb near the SiO_2/SiC interface further increases μ_{FE} , to peak values of 104 $cm^2V^{-1}s^{-1}$ and to 50 $cm^2V^{-1}s^{-1}$ at high electric field for Sb [3]. The much higher value of μ_{FE} in Sb-implanted MOSFETs was attributed to counter-doping by Sb in SiC near the interface. To investigate the effects of Sb at SiO_2/SiC interfaces, Sb ions were implanted near the surface of the 4H-SiC epitaxial layer and the wafer was annealed at 1550℃ in Ar to activate the Sb donors. Dry thermal oxidation was done at 1150℃ and the sample was then NO-annealed at 1175℃ for 30 or 120 min. CCDLTS results of Sb-implanted MOS capacitors were compared with those having no Sb implant but with similar dry oxidation and NO-annealing processes. The density of near-interface oxide traps was similar in samples with and without Sb, indicating that Sb has little effect on those defects. However, CCDLTS spectra taken at bias and filling pulse conditions that reveal defects in the SiC depletion region, show both the deeper of the two N donor levels at E_C - (0.10±0.01) eV and a second energy level only in Sb-implanted samples at E_C - (0.12±0.01) eV. To our knowledge this is the first measurement of Sb donors in SiC and it confirms counter doping of SiC by Sb near the SiO_2/SiC interface.

[1] P.M. Mooney and A.F. Basile, in *Micro and Nano-Electronics: Emerging Device Challenges and Solutions*, Ed. T. Brozek (CRC Press, Taylor and Francis, 2014) p. 51.

[2] A.F. Basile, et al., J. Appl. Phys. **109**, 064514 (2011).

[3] A. Modic, et al., IEEE Electron Device Lett. **35**, 894 (2014).

3:00pm **EM+AS+MS+SS-WeA3 Hydrogen Desorption from 6H-SiC (0001) Surfaces**, ***Sean King***, Intel Corporation, *R. Nemanich, R. Davis*, North Carolina State University

Due to the extreme chemical inertness of silicon carbide (SiC), *in-situ* thermal desorption is commonly utilized as a means to remove surface contamination prior to initiating critical semiconductor processing steps such as epitaxy, gate dielectric formation, and contact metallization. *In-situ* thermal desorption and silicon sublimation has also recently become a popular method for epitaxial growth of mono and few layer graphene. Accordingly, numerous thermal desorption experiments of various processed silicon carbide surfaces have been performed, but have ignored the presence of hydrogen which is ubiquitous throughout semiconductor processing. In this regard, we have performed a combined temperature programmed desorption (TPD) and x-ray photoelectron spectroscopy (XPS) investigation of the desorption of molecular hydrogen (H_2) and various other oxygen, carbon, and fluorine related species from *ex-situ* aqueous hydrogen fluoride (HF) and *in-situ* thermal and remote hydrogen plasma cleaned 6H-SiC (0001) surfaces. Using XPS, we observed that temperatures on the order of 700 - 1000°C are needed to fully desorb C-H, C-O and Si-O species from these surfaces. However, using TPD, we observed H_2 desorption at both lower temperatures (200 – 550°C) as well as higher temperatures (> 700°C). The low temperature H_2 desorption was deconvoluted into multiple desorption states that, based on similarities to H_2 desorption from Si (111), were attributed to silicon mono, di, and trihydride surface species as well as hydrogen trapped by sub-surface defects, steps or dopants. The higher temperature H_2 desorption was similarly attributed to H_2 evolved from surface O-H groups at ~ 750°C as well as the liberation of H_2 during Si-O desorption at temperatures > 800°C. These results indicate that while *ex-situ* aqueous HF processed 6H-SiC (0001) surfaces annealed at < 700°C remain terminated by some surface C-O and Si-O bonding, they may still exhibit significant chemical reactivity due to the creation of surface dangling bonds resulting from H_2 desorption due from previously undetected silicon hydride and surface hydroxide species.

3:20pm **EM+AS+MS+SS-WeA4 Chemical and Microstructural Characterization of Interfaces between Metal Contacts and *β*-Ga_2O_3**, ***Lisa M. Porter***, *Y. Yao, J.A. Rokholt, R.F. Davis*, Carnegie Mellon University, *G.S. Tompa, N.M. Sbrockey, T. Salagaj*, Structured Materials Industries, Inc.

β-Ga_2O_3 is a promising alternative to traditional wide bandgap semiconductors, as it has a wider bandgap (~4.9 eV) and a superior figure-of-merit for power electronics and other devices; moreover, *β*-Ga_2O_3 bulk single crystals have recently been grown commercially using melt-growth methods. While several groups have demonstrated Ga_2O_3-based devices such as Schottky diodes and MOSFETs, understanding of contacts to this material is limited. In this study, we investigated a variety of metal contacts (Ti, In, Mo, W, Ag, Au, and Sn) to both (-201) *β*-Ga_2O_3 single crystal substrates (from Tamura Corp.) and *β*-Ga_2O_3 epitaxial layers grown by MOCVD on various substrates (sapphire and single crystal *β*-Ga_2O_3) by co-authors at Structured Materials Industries. We have characterized these substrates and epilayers using techniques such as X-ray diffraction and transmission electron microscopy (TEM), which show that the epitaxial layers are oriented (-201) with respect to the substrates. We found that the electrical characteristics of the metal contacts to the Ga_2O_3 epilayers and substrates are highly dependent on the nature of the starting surface and the resulting interface, and less dependent on the work function of the metal than expected. For example, both Ti and bulk In readily form ohmic contacts to Ga_2O_3, whereas other low-workfunction metals, such as Sn, did not form ohmic contacts even after annealing to 800 °C. For Ti ohmic contacts on Sn-doped Ga_2O_3 substrates the optimal annealing temperature was ~400 °C: the electrical characteristics continually degraded for annealing temperatures above ~500 °C. Thermodynamics predicts that Ti will reduce Ga_2O_3 to produce Ti oxide, therefore indicating that the Ti/Ga_2O_3 interface is unstable. In correspondence with this prediction, high-resolution cross-sectional TEM images of 400 °C-annealed samples show the formation of an ultra-thin (~2 nm) interfacial amorphous layer. TEM samples at higher annealing temperature have also been prepared for analysis; electron energy loss spectroscopy will be used to characterize the interfacial composition profiles in these samples to determine the relationship between composition and thickness of the interfacial layer and the electrical degradation of the contacts. Schottky diodes with Au, Mo, W and Sn as the Schottky metal were also fabricated. The Schottky barrier heights (SBHs) showed a weak dependence on the metal workfunction. An overview of the electrical behavior of different metals as ohmic or Schottky contacts to Ga_2O_3 and the interfacial chemistry and microstructure will be presented.

4:20pm **EM+AS+MS+SS-WeA7 Regrown InN Ohmic Contacts by Atomic Layer Epitaxy**, ***Charles Eddy, Jr.***, U.S. Naval Research Laboratory, *N. Nepal*, Sotera Defense Solutions, *M.J. Tadjer, T.J. Anderson, A.D. Koehler, J.K. Hite, K.D. Hobart*, U.S. Naval Research Laboratory

For the past 25 years, compound semiconductors comprised of elements from group III-B of the periodic table and nitrogen have attracted a sustained, high-level of research focus. More recently they have found growing application to rf and power electronics in the form of advanced transistor structures such as the high electron mobility transistor (HEMT) with and without insulated gates. Key performance parameters for such devices (cut-off frequency for rf transistors and on-resistance for power transistors) are often dominated by the contact resistance. The current best approach to contact resistance minimization involves aggressive processing requirements that challenge device fabrication, especially when insulated gates are required. A potential solution is the regrowth of highly conducting semiconductor contact layers where ohmic contacts are needed.

Here we report on initial efforts to employ regrown indium nitride (InN) contact layers by atomic layer epitaxy (ALE) as a low temperature solution to the ohmic contact challenge for III-N transistors. Recently, we have

reported that good crystalline quality InN can be grown at less than 250°C by ALE [1]. Here we employ such conditions to grow very thin layers and assess them morphologically and electrically.

InN regrown contact layers of 5nm thickness grown on sapphire are very smooth (rms roughness < 0.17nm) and possess sheet resistances as low at 3.6 kΩ/sq, corresponding to electron sheet carrier densities of 2-3 $x10^{13}$ cm^{-2} and mobilities of 50 cm^2/V-s. These electron mobilities are higher than previously reported (30 cm^2/V-s) for much thicker films (1.3 µm) [2]. Similarly grown 22.5 nm thick InN layers on highly resistive silicon were processed with mesa isolation regions and 20/200 nm thick titanium/gold contact metals. Without any contact annealing, an ohmic contact resistance of $9.7x10^{-7}$ Ω-cm^2 (1.2 Ω-mm) was measured, comparable to the best high temperature alloyed contact to an AlGaN/GaN HEMT.

In our initial non-alloyed ohmic contact process, contact regions were recessed down to the GaN buffer layer to establish physical contact between the highly-conductive InN layer and electrons in the HEMT channel. A 25 nm thick InN layer was then grown by ALE, and the InN-filled ohmic regions were then capped with a Ti/Al/Ti/Au layers. Using the metals as an etch mask, the InN outside of the ohmic regions was etched away. We will report on initial results of application of ALE InN regrown contact layers and the modified fabrication approaches to AlGaN/GaN HEMTs.

1. N. Nepal, et al., *J Cryst. Growth and Design*, **13**, 1485-1490 (2013).

2. Kuo et al., *Diamond & Related Materials***20**, 1188 (2011).

4:40pm **EM+AS+MS+SS-WeA8 High-Temperature Characteristics of Ti/Al/Pt/Au Contacts to GaN at 600°C in Air**, ***Minmin Hou***, *D.G. Senesky*, Stanford University

The high-temperature characteristics (at 600°C) of Ti/Al/Pt/Au contacts to gallium nitride (GaN) in air are reported. GaN is a wide bandgap semiconductor material being developed for high-temperature electronics and micro-scale sensors. Ti/Al/Pt/Au metallization is frequently used for forming ohmic contacts to GaN. However, few studies have been devoted to studying the electrical characteristics of the Ti/Al/Pt/Au metallization at elevated temperatures and even fewer in oxidizing environments. It is not practical to obtain a hermetic sealing at elevated temperatures and a number of sensing applications may require non-hermetic packages. Therefore, the electrical characteristics of Ti/Al/Pt/Au contacts in a hot oxidizing ambient instead of an inert ambient or vacuum can provide new insights. In this work, the electrical and microstructural properties of Ti/Al/Pt/Au contacts to GaN upon exposure to 600°C in air are presented.

In this work, microfabricated circular-transfer-line-method (CTLM) patterns were used as the primary test structure. Ti/Al/Pt/Au were patterned through a standard lift-off process on unintentionally-doped GaN epitaxial layer grown by metal organic chemical vapor deposition (MOCVD) on sapphire. After lift-off, the samples were subject to a rapid thermal annealing (RTA) process at 850°C for 35 seconds in a nitrogen ambient.

To observe the impact of thermal exposure on the electrical and microstructural properties, the test structures were subject to a 10-hour thermal storage test in a furnace (air ambient), during which time the test structures were taken out of the furnace every two hours and their I-V characteristics were measured at room temperature. After the initial 2-hour “burn-in” period, the contact resistance remained stable over the entire reminder thermal storage test, with the variance within less than 3% and the specific contact resistivity remained on the order of 10^-5 Ω-cm^2.

In addition, the samples were subject to in-situ high-temperature I-V tests at 600°C in air both before and after the thermal storage using a high-temperature probe station. The linear I-V response confirms that the contacts remained ohmic after the thermal storage. The contact resistance at 600°C showed minimal change (approximately 9%) for a 20-µm-wide gap CTLM test structure, before and after thermal storage.

The microstructural analysis with atomic force microscopy (AFM) showed minimal changes (less than 0.1%) in surface roughness after thermal storage. The results support the use of Ti/Al/Pt/Au metallization for GaN-based sensors and electronic devices that will operate within a high-temperature and oxidizing ambient.

5:00pm **EM+AS+MS+SS-WeA9 Schottky Contacts and Dielectrics in GaN HEMTs for Millimeter-Wavelength Power Amplifiers**, ***Brian Downey***, Naval Research Laboratory **INVITED**

Although GaN RF transistor technology has begun to enter commercial markets, there are still several active research efforts aimed at extending the operating frequency of GaN devices to the millimeter-wavelength (MMW) frequency range of 30 – 300 GHz. In order to facilitate power gain at MMW frequencies, both geometric device scaling and novel heterostructure/device design are required, which present interesting materials and processing challenges. In this talk, an overview of NRL’s approaches to MMW GaN high-electron-mobility transistor (HEMT) technology will be presented. In one approach, N-polar GaN inverted HEMT structures are employed, which places the GaN channel at the surface of the device. In this case, Schottky gate contacts are made directly to the N-polar GaN channel. The effect of GaN crystal polarity on Schottky barrier height will discussed along with strategies to increase the Schottky barrier height of metals to N-polar GaN. In a second approach, Ga-polar GaN HEMTs with vertically-scaled barrier layers are utilized to reduce the surface-to-channel distance in order to maintain electrostatic control of the channel in short gate length devices. The high electric fields in these vertically-scaled barrier devices can create large tunneling-related gate leakage currents, leading to high off-state power dissipation and soft breakdown characteristics. The use of gate dielectrics in these scaled structures will be discussed including their effect on device electrical performance.

5:40pm **EM+AS+MS+SS-WeA11 Nitrogen as a Source of Negative Fixed Charge for Enhancement Mode Al2O3/GaN Device Operation**, ***MuhammadAdi Negara***, *R. Long, D. Zhernokletov, P.C. McIntyre*, Stanford University

In recent years, significant research efforts have focused on developing enhancement mode (E-mode) GaN-based devices fueled by many potential applications. Simpler power amplifier circuits using a single polarity voltage supply and increased safety using a normally-off device can be achieved using E-mode devices leading to lower cost and an improvement of system reliability. Using the combination of E-mode and depletion mode (D-mode) devices in direct coupled logic open up also new applications for nitride semiconductors. To realize normally-off operation of GaN transistors, several approaches have been reported in the past including recessed gate structures [1], p-type gate injection [2], fluorine plasma treatment [3], surface channel GaN [4], thermally oxidized gate insulator [5] and oxide charge engineering [6]. In this report, nitrogen impurities introduced during atomic layer deposition of an Al_2O_3 gate dielectric are investigated as a means of modifying the threshold voltage (V_{th})/flat band voltage (V_{fb}) of GaN MOS devices. As reported in reference [7], nitrogen may incorporate on either cation or anion substitutional sites or on interstitial sites in Al_2O_3 and become a source of negative fixed charge within Al_2O_3. The effectiveness of this approach for fixed charge modification of ALD-grown Al_2O_3 compared to several alternative approaches will be presented.

References:

[1] W. B. Lanford, et al., Electron. Lett. 41, no. 7, 449 (2005).

[2] Y. Uemoto, et al., IEEE Trans. Elect. Dev. 54, no. 12, 3393 (2007).

[3] Zhang et al., Appl. Phys. Lett. 103, 033524 (2013).

[4] W. Huang, et al., IEEE Elect. Dev. Lett. 27, no. 10, 796 (2006).

[5] K. Inoue et al., Elect. Dev. Meet., IEDM Technical Digest. International, pp. 25.2.1 (2001).

[6] B. Lu, et al., in Proc. Int. Workshop Nitride Semicond. Abstr.,536 (2008)..

[7] Choi et al., Appl. Phys. Lett. 102, 142902 (2013).

6:00pm **EM+AS+MS+SS-WeA12 Activation of Mg-Implanted GaN Facilitated by an Optimized Capping Structure**, ***Jordan Greenlee***, *B.N. Feigelson, T.J. Anderson, K.D. Hobart, F.J. Kub*, Naval Research Laboratory

For a broad range of devices, the activation of p and n-type implanted dopants in GaN is needed. The activation of implanted ions by annealing requires post-implantation damage removal and the arrangement of implanted ions in their proper lattice sites. Post-implantation activation of Mg via annealing requires high temperatures (>1300 ˚C). At these high annealing temperatures, GaN decomposes, leaving behind a roughened surface morphology and a defective crystalline lattice, both of which are detrimental for GaN device applications. To combat decomposition, either a high pressure environment, which is prohibitively expensive and not easily scalable, or a capping structure combined with short exposure to T >1300˚C is required to preserve the GaN. In this work, we explore the effects of different capping structures and their ability to protect the GaN surface during a high temperature pulse, similar to those used in the Multicycle Rapid Thermal Annealing (MRTA) process.

It was determined that the sputtered cap provides sufficient protection for the underlying GaN during a rapid heat pulse. The in situ MOCVD-grown AlN cap, although it should have a better interface and thus provide more protection for the GaN layer, is inferior to the sputtered cap as determined by Nomarski images. After etching the surface with AZ400k developer, it was determined that the GaN underneath the MOCVD-grown cap has pits as-grown. Since both GaN layers were grown with the same recipe, we attribute these pits to the HT MOCVD AlN growth process. Atomic force microscopy was used to determine the as-grown and post annealing surface morphologies of the samples. The as-grown sample covered with MOCVD AlN does not exhibit the same smooth step flow growth as the as-grown

sample without the MOCVD AlN cap. After annealing and etching off the AlN caps, the surface that was capped with MOCVD AlN shows evidence of pitting while the sample that was protected with only sputtered AlN no longer exhibits step flow growth like the as-grown sample. Since we are above 2/3 of the melting point of GaN, we expect that bulk diffusion is occurring and causing this rearrangement at the surface. This implies that sputtered AlN can provide sufficient protection of the underlying GaN surface, which will facilitate mid-process implantation and activation of Mg in GaN.

Electronic Materials and Processing
Room: 210E - Session EM-WeA

Interconnects: Methods and Materials for Removing Connectivity Constraints
Moderator: Andy Antonelli, Nanometrics, Michelle Paquette, University of Missouri-Kansas City

2:20pm **EM-WeA1 Interdiffusion Characterization of Selective Chemical Vapor Deposition Cobalt Cap and Copper**, ***Jeff Shu***, *Z. Sun, S. Choi, B. Yatzor, Z. Bayindir, G. Zhang, Y. Lee, H. Liu, J. Lansford*, GLOBALFOUNDRIES U.S. Inc.

Electromigration (EM) failure is always one of the key challenges of BEOL Cu interconnects. The continuous shrink of Cu feature size leads to higher current densities, which lower EM lifetimes. The interface between Copper and dielectric cap has been identified as the key diffusion path for copper atoms, and the adhesion of the interface is critical to EM performance. Different methods developed to improve the adhesion between copper and dielectric cap interface. One method of improving the adhesion has been the use of alloy seed, CuMn or CuAl. Mn (Al) will segregate and bond chemically to the copper and dielectric cap interface during dielectric cap deposition which can improve the adhesion of the interface and suppress Cu atoms migration along the interface under current stress. An alternate method of improving the adhesion is to have a self-aligned CoWP Cap or Selective CVD Co Cap on top of Cu which was developed for more stringent EM requirement of advanced nodes, such as 32nm, 20nm and beyond. Compare to self-aligned CoWP plating process, selective CVD Co Cap has higher selectivity and more compatible with porous ultra low k film. In this paper, we focus on interdiffusion characterization of selective CVD Co cap and copper. Co/Cu interdiffusion of cobalt films with different precursors are thoroughly evaluated and compared. Nitrogen content in Co film which enriches the grain boundaries due to low solubility in Co was identified as the key knob to control Co/Cu interdiffusion. Less nitrogen in Co film results in more copper diffusion. Better EM results on 20nm groundrule test structures demonstrated with higher nitrogen in Co film. Thermal anneal with H2 gas was found to be able to reduce nitrogen content in Co film which result in more Cu diffusion. Secondary Ion Mass Spectrometry (SIMS), X-ray photoelectron spectroscopy (XPS) and Electron Energy Loss Spectroscopy (EELS)/ Energy Dispersive X-ray Analysis (EDX) line scan were used for Cu diffusion characterization which clearly show Cu signal on top of Co film. A novel analytical technique of SIMS has been developed to characterize nitrogen content in Co film that CoN was selected as nitrogen detection molecular since nitrogen has some interaction with Co within the film.

2:40pm **EM-WeA2 Contact Engineering on Carbon Nanotube Interconnect Vias**, ***Yusuke Abe***, *A. Vyas, R. Senegor, C. Yang*, Santa Clara University

Nanocarbons such as carbon nanotubes (CNTs) and graphene are candidate materials for next-generation integrated circuit technologies due to their high current-carrying capacities and excellent electrical, thermal, and mechanical properties [1,2]. The key performance-limiting factor continues to be the high contact resistance at the interface with metal electrodes [3]. Metal depositions are frequently used during post-fabrication contact engineering for these nanocarbons to mitigate the high resistances between these materials and metal electrodes, with various degrees of success in achieving stable low-resistance contacts [4]. We have fabricated test devices for CNT vias, and measured their current-voltage (I-V) characteristics [5]. In this study, post-fabrication contact engineering is performed using electron-beam induced deposition of tungsten (EBID-W) [6] to improve the electrode contacts and hence reduce the total device resistance.

Fabrication of these via test structures without top contact metallization was described elsewhere [5]. In the present study, EBID-W is used to form the via top contacts (Fig. 1). From I-V and resistance measurements on 500 nm x 500 nm CNT vias with and without EBID-W top contact metallization, the effect of EBID-W contact on resistance reduction is clearly demonstrated (Fig. 2). While similar improvement can be obtained by current stressing without contact metallization [5], such technique would introduce an additional thermal cycle to the chip fabrication process and hence undesirable. On the other hand, the resistance of a via with W top contact is shown to have reached its minimum which is unaffected by further annealing (Fig. 3). Thus the contact resistance of the CNT via is indeed improved by top contact metallization with W, and that the resistance is stable. Without increasing the thermal budget from current stressing in chip fabrication, the use of EBID-W for via top contact metallization could facilitate the eventual functionalization of CNT via interconnects.

REFERENCES

[1] T. Saito, T. Yamada, D. Fabris, H. Kitsuki, P. Wilhite, M. Suzuki, and C.Y. Yang, Appl. Phys. Lett. 93, 102108 (1-3), 2008.

[2] M. S. Dresselhaus, G. Dresselhaus, and P. Avouris, Berlin, New York, Springer, 2001.

[3] F. Wakaya, K. Katayama, and K. Gamo, Microel. Eng. 67–68, 853–857, 2003.

[4] P. Wilhite, A.A. Vyas, J. Tan, J. Tan, T. Yamada, P. Wang, J. Park, and C.Y. Yang, Semicond. Sci. Technol. 29, 054006 (16pp), 2014.

[5] C. Zhou, A.A. Vyas, P. Wilhite, P. Wang, M. Chan, and C.Y. Yang, Electron Device Lett. 36, 71-73, 2015.

[6] S.J. Randolph, J.D. Fowlkes, and P.D. Rack, Crit. Rev. Solid State Mater. Sci. 31, 55-89, 2006.

3:00pm **EM-WeA3 Innovative Technological Solutions for Low-k Integration Beyond 10 nm**, ***Mikhail Baklanov***, IMEC **INVITED**

The general issue of porous low-k materials is degradation of their properties with the increasing porosity. The porous materials are soft, mechanically weak, and do not adhere well to silicon or metal wires. The large pore size also make them more sensitive to plasma damage (because of easy penetration of plasma species into the pores). All these challenges are becoming critical in advanced technology nodes when the distance between the metal wires has reduced to tens nm. This is the reason why the present efforts of researches and engineers are oriented to development and evaluation of new types of low-k materials. The materials need to have good mechanical properties, to have sufficient chemical and plasma resistance and small pore size. At the same time the research efforts are also oriented to development of new technological approaches reducing degradation of low-k materials during the integration. The invited talk will include 2 parts. 1. The first part of presentation includes the results of evaluation of new materials with low dielectric constant that are considered as potential candidates for future generations of nanoelectronic devices. These dielectric materials includes new generations of organosilicate glasses (Periodic Mesoporous Organosilicates (PMO), Zeolites and Metal-Organic Frameworks (MOFs). Fabrication of PMO materials is based on self-assembling chemistry and therefore it allows better control of critical properties of low-k materials. MOFs and Zeolites have very small pore size and unique mechanical properties. These materials have been developed in collaboration with several Universities. Their evaluation at imec includes measurement of their porosity and pore size (ellipsometric porosimetry – a technique patented by author), mechanical properties using Nanoidentation, chemical composition (FTIR, XPS, SIMS and some other techniques). Dielectric constant of these materials are measured my using metal-insulator-semiconductor (MIS) structures with Pt electrode. 2. The second part of the presentation is related to development of innovative technological approaches that are considered as key solutions for successful integration of porous low-k materials. Particularly, detailed analysis of recently patented cryogenic plasma etching of low-k materials will be reported. In this technology, the initial chemistries and reaction products are condensed in pores, makes the material dense and prevent penetration of plasma active into the bulk of low-k materials and reduce the plasma "damage". The results of evaluation have already been published in several papers. By using this technique the lowest integrated k-value of ultralow-k material has been achieved. Completely different integration scenario is considered for 5 nm technology nodes. The damascene technology can't work in this case because of plasma damage of low-k and the technology can return back to the subtractive approach with metal patterning. Although some industrial Companies are trying to develop technology of plasma etching of Cu, we are developing an alternative approach with metal patterning by using patterned sacrificial polymers. After metal deposition and planarization by chemical mechanical polishing , the sacrificial polymer is removed by using hydrogen plasma, then the trenches and vias are filled by ultralow-k dielectrics. The deposited low-k films is not exposed to plasma. The first results have been generated, the dielectric constants were achieved close to ones obtained cryogenic etch technology. However, some challenges still remain and they also will be highlighted.

4:20pm **EM-WeA7 Challenges and Directions for Dielectric Interconnect Materials for the 10nm node and Beyond**, ***Jeffery Bielefeld***, *J. Blackwell, S. Bojarski, M. Chandhok, J. Clarke, C. Jezewski, N. Kabir, S.W. King, M. Krysak, D.J. Michalak, M. Moinpour, A. Myers, J. Plombon, M. Reshotko, K. Singh, J. Torres, R. Turkot, H. Yoo*, Intel Corporation **INVITED**

To enable the continued scaling of interconnect layers for the 10nm node and beyond an increased number of materials and integration challenges will need to be addressed. Historically, interconnect dielectric materials have been broken down into Interlayer Dielectrics (ILDs) and Etch Stop (ES) / Hard Mask (HM) materials. The ILD layer is the major driver in capacitance improvement, while the ES layer enables patterning and acts as a diffusion barrier. In this paper, we will discuss two major challenges: (1) Pathways for the integration of porous low-k ILDs, and (2) Development needs for ES materials to enable improved patterning options.

The industry continues to work on the integration of low-k ILDs, but the momentum to implement these films has slowed in recent years due to the challenges of working with porous thin films. Low-k ILDs (k~2.0) exhibit 40-50% porosity with an interconnected pore network. The increased porosity can lead to damage and increased roughness during patterning, and can allow precursor penetration during the metal barrier deposition. To mitigate the problems of integrating a porous ILD, we have utilized the approach of pore stuffing. In this process, a sacrificial material is infiltrated into the pores of a fully cured ILD. The resultant film is non-porous with increased mechanical properties.

In this paper, we will discuss the challenges of finding a pore stuffing material that can fill the pores of the ILD, remain in place during dual damascene processing and can then be removed from the low-k ILD post metallization and CMP. In addition, we will show how pore stuffing improves trench profiles, and how it prevents metal penetration during barrier deposition. Finally the successful implementation of this process will be demonstrated and integrated capacitance improvement will be presented.

In a classic dual damascene flow, the ES layer is used as a diffusion barrier and as a patterning stop between ILD layers. To enable more advanced patterning and integration schemes, the role of these materials needs to be expanded. Specifically, there may be situations where multiple ES/HM materials are needed and with high etch selectivity to each other (>20:1). Etch selectivity values for typical materials (e.g. nitrides, carbides, amorphous silicon, metal hard masks and carbon hardmasks) are not currently sufficient. Development of new material options, deposition techniques and etch processes are needed. In this paper, we will discuss the current needs for new ES\HM materials and novel etch technology, along with our current progress toward this challenge.

5:00pm **EM-WeA9 Pore Sealing of Low-k Films by UV Assisted CVD Processes**, ***Priyanka Dash***, *D. Padhi*, Applied Materials

Porous ultra-low k (ULK) dielectric films with high porosity and larger pore size (k<2.4 and beyond) pose a serious challenge for their integration into next-generation microchips. In this paper, we report the formation of a thin layer of SiCxNy based pore sealing film deposited by UV assisted CVD. This film when deposited on damaged ULK surface assists in sealing the interconnected pores to prevent diffusion of metal liner and barrier metal precursors during the subsequent metallization steps. In addition pore sealing also enables an efficient sidewall protection to ULK thereby reducing its degradation by radical penetration during subsequent wet clean processes. A side benefit of this method is replenishment of depleted methyl species in damaged subsurface sites thereby improving hydrophobicity and recovery of k damage. A very thin pore seal film ~15 Ang is found to be sufficient to prevent metal precursor diffusion into a porous ULK k2.4 material. Porosimetry and backside SIMS were used to assess sealing behavior on surface pores of damaged ULK. On pattern wafers pore sealing treatment has been shown to significantly improve VBD and TDDB of k2.4 ULK to a level comparable to that observed for industry standard ULK k2.55 material. No structural change is observed in pattern CD for up to 15A of pore-seal deposition. Although this deposition is highly selective to surface sites available on damaged ULK, a thin layer (i.e. < 5A) of pore seal residue formed on Cu via bottom has been shown to be completely removed by typical CuOx wet clean solutions. Kelvin via measurements on structure wafers show that pore-seal with wet clean yields comparable via resistance as compared to wafers without pore-seal.

5:20pm **EM-WeA10 Copper Deposition and *In Situ* Chamber Cleaning using Pulsed-CVD Technique**, ***Fabien Piallat***, *J. Vitiello*, Altatech, France

Due to the conformity required for deposition of metals in high aspect ratio vias, Physical Vapor Deposition is replaced by techniques from the Chemical Vapor Deposition (CVD) family. Conformity wise, the Atomic Layer Deposition (ALD) appears to be the best of the CVD techniques, but the low throughput is dissuasive for layers thicker than 10nm. At the edge between CVD and ALD, the Fast Atomic Sequential Technique (FAST) developed and patented by Altatech, enables deposition of layers with conformity close to the ALD at a higher throughput.

Through Silicon Vias are extensively used for interconnections and necessitate highly conductive materials in holes of aspect ratio higher than 10. Of all low-resistivity metals, namely Ag, Al, Au, Cu and W, studies showed that Cu is the best for filling trenches. Therefore, both the metal and the technique used are imposed, i.e. Cu deposition by CVD is the most suitable solution.

The main obstacle for a complete adoption of Cu as an interconnection metal is the difficulty to clean the chamber after process, since Cu cannot be etched by the usual fluorinated in-situ dry etching processes.

Successful deposition of conformal Cu layer was performed in vias with an aspect ratio of 10, using Altatech AltaCVD deposition chamber and a commercially available Cu precursor. Optimised deposition parameters resulted in low resistivity Cu, down to few µΩ.cm, with deposition rates higher than 100 $nm.min^{-1}$. Plotting the deposition rate depending on the substrate temperature highlighted an Arrhenius law behaviour, which in turn provided the optimal deposition temperature. Complementary SEM observation showed Cu layer with low roughness.

Futhermore, taking advantage of the Altatech pulsed solution, FAST, an in-situ dry cleaning process was developed using hexafluoroacetylacetone (hfacH) solvent. The main scheme for Cu etching comprise one step of Cu surface oxidisation and a second step where CuO_x compounds react with hfacH solvent to form volatile species. Several approaches were assessed; the following one will be presented and discussed:

O_2 and hfacH introduced simultaneously in the chamber

Alternation of O_2 plasma and hfacH fill

Pulsed alternation of O_2 and hfacH fill

O_2 plasma and pulses of hfacH

Optimising and understanding the influence of each process parameter was made possible by the use of a Residual Gaz Analyzer (RGA) and an Optical Emissions Spectrometer (OES). Cleaning efficiency at the particle generation level of all the approaches are compared, after few microns of Cu deposition and a chamber clean.

Finally, the efficiency of the most promising approach will be investigated on different chamber coatings.

5:40pm **EM-WeA11 Study of UV Impact on PECVD Non-Porogen ULK (Ultra low κ) SiCOH Film Nano-Structures, Film Mechanical and Electrical Properties**, ***Zhiguo Sun***, *J. Shu, S. Srivathanakul, H. Liu*, GLOBALFOUNDRIES U.S. Inc.

With the continuous shrinkage of back end of line (BEOL) metal pitches of sub-10nm technology node, integration with ultra-low κ (ULK) film becomes even more challenging. In comparison to traditional PECVD ULK films introduces pore through deposition with porogen precursor followed by UV or E-beam exposure to generate porosity , a new single precursor based ULK (ultra low κ) film has been formed without porogen and show promising on the sub 10nm technology road map . In this paper, we will use transmission Fourier Transform-Infrared (FTIR) spectroscopy, X-ray photoelectron spectroscopy (XPS) and Ellipsometric Porosimetry (EP) etc. to investigate the impact how different UV conditions will modify chemical bondings, film composition, pore structure and porosities. The role of UV in this new type of ULK film formation will be studied while difference UV conditions include UV bulbs and UV curing vacuum ambient etc. Film mechanical properties as well as electrical properties will be thoroughly compared. The interaction with downstream integration process steps, such as plasma induced damage and selectivity to MOCVD cobalt capping will be examined.

6:00pm **EM-WeA12 Bandgap Narrowing in Low-K Dielectrics**, ***Xiangyu Guo***, University of Wisconsin-Madison, *S.W. King*, Intel Corporation, *P. Xue*, University of Wisconsin-Madison, *J.-F. de Marneffe, M. Baklanov*, IMEC, Belgium, *V. Afanas'ev*, Catholic University of Leuven, Belgium, *Y. Nishi*, Stanford University, *J.L. Shohet*, University of Wisconsin-Madison

Electrical reliability in Cu interconnect structures has become a vital concern as the nano-electronics industry moves to sub-16 nm technology nodes and strives to implement insulating dielectric materials with increasingly lower dielectric constants (i.e., low-k). Studies have shown a direct correlation between trap/defect densities and electrical leakage of low-k materials,[1,2] , while the knowledge of the fundamental mechanism producing the damage is still limited. The bandgap energy, often serving as a reference point from which the presence and location of defect states in the bulk or at the interface can be understood, is of fundamental importance for understanding the electrical degradation in these dielectrics. In this work, core-level X-ray photoelectron spectroscopy (XPS) was utilized to

determine the surface bandgap for various non-porous and porous low-k a-SiCOH dielectrics before and after ion sputtering by examining the onset of inelastic energy loss in core-level atomic spectra. Bandgap narrowing was observed in Ar+ ion sputtered low-k dielectrics. The reduction of bandgap energies ranges from 1.3 Ev to 2.2 Ev depending on the film composition. By examining the valence-band spectra measured with high-resolution XPS, we show that the bandgap narrowing in the low-k dielectrics is contributed to the arising and uplifting of the valence-band tail as evidenced by the presence of additional electronic states above the valence-band maximum (VBM). Electron spin resonance (ESR) measurements were also performed on the a-SiCOH films and the localization of each type of defect within the dielectric band gap is analyzed and compared. A combination of these results with the band gap measurements suggests the additional electron states contributing to the narrowed bandgap originate from carbon-related defects in the material. This work was supported by the National Science Foundation under Grant CBET-1066-231 and by the Semiconductor Research Corporation under Contract 2012-KJ-2359.

1. J. Atkin, D. Song, T. Shaw, E. Cartier, R. Laibowitz, and T. Heinz, J. Appl. Phys. 103, 94104 (2008).

2. B. Bittel, P. Lenahan, and S.W. King, Appl. Phys. Lett. 97, 63506 (2010).

Thin Film
Room: 111 - Session TF+AS+EM+EN+MN-WeA

CV Infiltration Methods and Energetic and Thermal Properties of Thin Films

Moderator: Richard Vanfleet, Brigham Young University, David Allred, Brigham Young University

2:20pm **TF+AS+EM+EN+MN-WeA1 The Many Avatars of PVD**, ***Murali Narasimhan***, Applied Materials, Inc. **INVITED**

Physical Vapor Deposition has been used for many years for depositing thin film coatings for diverse uses ranging from jewelry to industrial cutting tools. PVD has found usage in the manufacture of advanced semiconductor manufacturing for depositing various metals and some specialty dielectrics as well. The majority of high purity metal deposition for semiconductor use has been done using PVD although the use of CVD and ALD has increased over the years because of requirements of conformality and gap fill where conventional planar PVD has not been adequate. However, breakthroughs in PVD technology have been successful in extending the use of PVD to advanced semiconductor manufacturing nodes by changing the geometry of PVD sources and reactors and the nature of the plasma involved. Collimated and long-throw sources developed by the semiconductor equipment industry in the early '90s enabled the deposition of high-purity Ti to lower contact resistance for transistors. Reactive sputtering of TiN enabled a robust barrier for CVD W plugs used at the 0.5um node. Further, use of electromagnetic fields to ionize and then guide the plasma and sputtered ionized atoms has been successful in improving the conformality of PVD Ti films. Ionized Metal Plasma (IMP), Hollow-Cathode Magnetron (HCM) and Self-Ionized Plasma (SIP) were innovations in ionized PVD reactor design that led to widespread adoption of PVD TaN and PVD Cu for Cu interconnect barrier and seed layer production from the 90nm node to the present. The application of thermal energy on the substrate during PVD Al and Cu has been useful in improving the flow of deposited material and subsequent gap-fill of sub-micron features. The use of Radio Frequency (RF) energy to power the target has allowed for more efficient ionization at lower power levels. The application of a capacitive tuner to modulate the ion bombardment on the wafer and tailor the film properties of TiN for hard mask applications has enabled the realization of etched features at the 22nm node. Pulsed DC magnetrons enable sputtering of dielectric materials, thus opening up the controlled deposition of thin films of insulating films for various applications such as improving the brightness of high-efficiency LEDs. Multi-cathode off-axis PVD magnetrons have enabled the deposition of multi-layers of ultra-thin films for magnetic devices such as advanced in-plane and out-of plane MRAM and the manufacture of EUV mask blanks for sub 10nm manufacturing. This talk will present the above listed progression of PVD technology over the years and its use for many applications in semiconductor manufacturing.

3:00pm **TF+AS+EM+EN+MN-WeA3 Reactive Foil Ignition by Laser Irradiation: Experimental and Modeling Results**, ***Ryan Murphy***, *C.D. Yarrington*, Sandia National Laboratories, *R.V. Reeves*, Lawrence Livermore National Laboratory, *D.P. Adams*, Sandia National Laboratories

It has been shown that forced mixing of reactive layers (foils) leads to an exothermic release of energy after initiation by pulsed laser irradiation. In order to understand the ignition of foils initiated by laser irradiation, we study the interaction of laser pulses with Al/Pt multilayer reactive foils prepared by sputter deposition. It will be shown that the single-pulse ignition threshold and dynamics are dependent on the length of the laser pulse as the pulse length is varied from 150 fs to 100 ms. The dependence of the ignition threshold on pulse length is a combination of laser-material interactions such as the size of the heat affected zone and the onset of ablation for ultrafast irradiation. Simulations of single-pulse laser heating were performed with Aria, the thermal package of the SIERRA finite element computational framework. Three-dimensional geometries were subjected to laser flux boundary conditions equal to those measured from the experimental conditions. Modeling and experimental results are correlated to show the effects of the heat affected zone size and shape on ignition thresholds and onset times.

Sandia National Laboratories is a multi-program laboratory managed and operated by Sandia Corporation, a wholly owned subsidiary of Lockheed Martin Company, for the United States Department of Energy's National Nuclear Security Administration under Contract DE-AC04-94AL85000.

3:20pm **TF+AS+EM+EN+MN-WeA4 The Effects of a Heat Sink on Self-Sustained Propagating Reactions in Sputter-Deposited Bimetallic Multilayers**, ***David Adams***, *R.V. Reeves*, *M. Hobbs*, Sandia National Laboratories

Reactive multilayers grown by sputter deposition have recently attracted interest for applications including material joining (soldering, brazing) and energy sources. For these applications, a metal-metal multilayer is typically designed to have many discrete reactant layers and a composition that corresponds to the peak enthalpy for a given material system. A thickness of reactive multilayers as small as 1.6 microns has recently been demonstrated for microelectronics joining (Braeuer et al. ECS Transactions, 2012). However, little is known about the minimal multilayer thickness required for ensuring a self-sustained, high temperature synthesis (SHS) reaction.

With this presentation, we describe the behavior of thin reactive Al/Pt multilayers tested as freestanding foils and as adhered films. For multilayers having a total thickness of 1.6 microns, self-sustained, high temperature reactions readily occur when the multilayer is tested as a freestanding foil. When coupled to a semi-infinite substrate, the likelihood of reaction is reduced depending on the multilayer design.

Sandia National Laboratories is a multi-program laboratory managed and operated by Sandia Corporation, a wholly owned subsidiary of Lockheed Martin Corporation, for the U.S. Department of Energy's National Nuclear Security Administration undercontract DE-AC04-94AL85000.

5:00pm **TF+AS+EM+EN+MN-WeA9 Beyond Deep Silicon Etching – Generating High Aspect Ratio Microstructures by Infiltration of Carbon Nanotube Frameworks**, ***Robert Davis***, Brigham Young University **INVITED**

In addition to being the anchor material for microelectronics, silicon is widely used as the basis of high aspect ratio microfabrication for MEMS with applications ranging from inertial sensors to neural probe arrays. Carbon nanotube templated microfabrication (CNT-M), extends the palate of materials and structures for high aspect ratio microfabrication beyond those achievable with vertically etched bulk silicon. In CNT-M, 3-D forests of patterned vertically-aligned carbon nanotubes are grown as a high aspect ratio framework and then the "forests" are infiltrated with a secondary material by chemical vapor deposition. Precision structures (including nanoporous structures) with very high aspect ratios (greater than 400:1) can be generated with CNT-M. The infiltration materials range from ceramics to metals and include silicon dioxide, silicon nitride, carbon, nickel, and yes silicon. We are using CNT-M to fabricate functional structures for applications including mechanical actuation, chemical separations and detection, and electrochemical energy storage.

5:40pm **TF+AS+EM+EN+MN-WeA11 The Influence of Thin Binder Films on Reaction Behavior in Reactive Powder Complexes**, ***Robert Reeves***, *K.T. Sullivan, A.E. Gash*, Lawrence Livermore National Laboratory

With the recently renewed interest in additive manufacturing (AM), there has been a recent upswell in the number of AM processes available. One such process that could be useful for reactive materials utilizes a curable liquid binder to adhere loose powders into coherent solid forms. In this process, tap-density powders are nearly saturated with binder, so the resulting film of binder present on each particle can represent a significant contaminant to the reaction system. In this work, the effect of the binder on reaction behavior in the Ni-Al system is explored. First, the distribution of binder and its elemental constituents are studied by electron microscopy and energy dispersive spectroscopy for powders with varying levels of binder saturation. Then, the effect of binder on the reaction kinetics and overall behavior is investigated. The change in overall heat release and apparent activation energy are quantified through differential scanning calorimetry, and the bulk reaction propagation rate is measured by high speed

photography as a function of the weight fraction of binder in the compact. Finally, the reaction products are identified through x-ray diffraction. In all tests, comparisons are made to the neat Ni-Al system.

This work performed under the auspices of the U.S. Department of Energy by Lawrence Livermore National Laboratory under Contract DE-AC52-07NA27344.

6:00pm **TF+AS+EM+EN+MN-WeA12 Carbon Nanotube Sheets from Horizontally Aligned Carbon Nanotubes**, ***Nathan Boyer***, *D.B. Syme, J.T. Rowley,* Brigham Young University*, M. Harker, R. Creighton, S. Cornaby,* Moxtek Inc.*, R. Vanfleet, B.D. Iverson,* Brigham Young University*, L. Pei,* Johns Hopkins University*, R.C. Davis*, Brigham Young University

Carbon sheets comprised of horizontally aligned carbon nanotubes (CNT) were prepared by rolling vertically aligned CNTs into a thin-film. A subsequent infiltration step to coat the rolled CNTs with amorphous carbon or polymer has also been performed to improve adhesion of neighboring CNTs. Amorphous carbon infiltration was achieved using chemical vapor deposition and polymer infiltration was performed by dipping the sheet into a solvent-mediated, polymer solution. The typical failure mode of the CNT thin-films is to tear parallel to the alignment of the CNTs. Infiltration of the aligned CNT film with additional materials strengthens the film against tearing and increases burst pressure. Non-infiltrated CNT thin-films have sustained a differential pressure of 1.4 atm over a circular area of 7 mm2 on a bulge test apparatus. Both carbon and polymer infiltrated sheets could be used in many applications including micromechanical sensing and actuation.

2D Materials Focus Topic
Room: 212C - Session 2D+EM+MG+NS+SE+SM+SS+TF-ThM

Emergent 2D Materials
Moderator: Paul Sheehan, Naval Research Laboratory

8:00am **2D+EM+MG+NS+SE+SM+SS+TF-ThM1 CVD Growth and Characterization of 2D MoS_2, $MoSe_2$, $MoTe_2$, WS_2, WSe_2, and $MoS_{2(1-x)}Se_{2x}$ Alloys**, ***David Barroso***, *T. Empante, A. Nguyen, V. Klee, I. Lu, E. Preciado, C. Lee, C. Huang, W. Coley, S. Naghibi, G. von Son, A. Brooks, J. Kim, L. Bartels*, University of California, Riverside

Transition Metal Dichalcogenides (TMDs) have been of increasing interest over the past years due to their exciting semiconducting properties. In the bulk, TMDs possess a native indirect bandgap and transition to a direct bandgap as they approach the monolayer limit. The bandgaps range from 1.15 eV to 1.95 eV depending on composition. Using organic liquids and/or inorganic powders as precursors, CVD growth techniques have been realized for MX_2 TMDs (M = Mo, W; X = S, Se, Te) and their alloys at tunable compositions. We achieved consistent synthesis of these TMDs materials. The films can either be made homogeneous in bandgap or exhibiting a linear bandgap gradient. Characterization of the films include Raman and photoluminescence spectroscopy, as well as AFM. Device fabrication allows for transport measurements. Depending on the composition, the materials show n- or p-doping in a consistent fashion.

8:20am **2D+EM+MG+NS+SE+SM+SS+TF-ThM2 Investigation of Manganese Dioxide Nanosheets by STM and AFM**, ***Loranne Vernisse***, *S. Afsari, S.L. Shumlas, A.C. Thenuwara, D.R. Strongin, E. Borguet*, Temple University

Interest in ultrathin two-dimensional nanosheets has grown exponentially thanks to their unique and diverse electronic properties. As they possess atomic or molecular thickness and infinite planar dimension, they are expected to have different properties than the bulk of the material from which they originate. This offers opportunities for the development of devices in various areas, ranging from catalysis to electronics. Using the exfoliation approach, it is possible to investigate 2D nanosheets of different materials in search of new phenomena and applications. Bearing this mind, we focused on manganese dioxide (MnO_2), and more specifically δ-MnO_2 (Birnessite). This mineral has the advantage to present a low surface enthalpy[1], which results in weak water binding. Moreover, the presence of defects, e.g., oxygen vacancies has a dopant effect on water oxidation. These properties make MnO_2 a perfect candidate as a catalytic surface for water splitting and pave the way to the design of clean and renewable energy system. Furthermore, MnO_2 can be easily exfoliated into ultrathin nanosheets owing to the layered structure of the manganese oxide precursors.

Our goal is to investigate the catalytic activity of ultrathin MnO_2 nanosheets using scanning probe microscopy techniques, especially atomic force microscopy (tapping mode) and scanning tunneling microscopy (ambient and electrochemical conditions). In this perspective, we have first improved the deposition processes and find the imaging conditions to observe MnO_2 nanosheets with an average thickness of one or two layers. We have also showed that MnO_2 single layer nanosheets exhibit an expected hexagonal atomic pattern and present some defects. We will now resolve and identify the different defects and investigate the evolution of the conductivity as a function of the defect concentration and the number of layers.

This work was supported as part of the Center for the Computational Design of Functional Layered Materials, an Energy Frontier Research Center funded by the U.S. Department of Energy, Office of Science, Basic Energy Sciences under Award #DE-SC0012575.

[1] M. M. Najafpour, E. Amini, M. Khatamian, R. Carpentier, S. I. Allakhverdiev, Journal of Photochemistry and Photobiology B: Biology (2014), 133, 124.

8:40am **2D+EM+MG+NS+SE+SM+SS+TF-ThM3 Two-Dimensional Early Transition Metal Carbides and Carbonitrides "MXenes": Synthesis, Properties and Applications**, ***Michael Naguib***, Oak Ridge National Laboratory **INVITED**

Ternary layered carbides and nitrides with formula of $M_{n+1}AX_n$ (M stands for early transition metal, A for group A element, X is carbon or nitrogen, and n=1, 2, or 3), so called MAX phases, are known for their unique combinations properties of ceramics and metals. It was found recently that etching atomically thin layers of aluminum from the MAX phases results in forming weakly bonded stacks of two-dimensional (2D) layers of early transition, coined as *MXenes*. The etching was carried out in fluoride contained aqueous systems. Thus MXenes surfaces are terminated with a mixture of groups including OH, O, and F. Sonicating MXenes in water results in delaminating few layers of MXenes from each other. However, to achieve a large-scale delamination, intercalation of a large compound between the layers prior to delamination is needed. MXenes were found to be a very interesting family of 2D materials since they are electrically conductors and hydrophilic. They also showed an excellent performance as electrodes for electrochemical super capacitors and Li-ion batteries. Here the recent progress in MXenes research from the synthesis to properties and applications will be covered, and in more details, large-scale delamination of MXenes will be discussed. Also, light will be shed on the performance of MXenes as electrode materials for electrochemical energy storage systems.

9:20am **2D+EM+MG+NS+SE+SM+SS+TF-ThM5 Molecular Beam Epitaxy of Large area HfSe2($ZrSe_2$)/$MoSe_2$ van der Waals Heterostructures on AlN(0001)/Si substrates**, ***Athanasios Dimoulas***, *P. Tsipas, E. Xenogiannopoulou, D. Tsoutsou, K.E. Aretouli, J. Marquez-Velasco, S.A. Giamini, N. Kelaidis*, NCSR DEMOKRITOS, Greece

Two dimensional (2D) semiconductor van der Waals heterostructures (HS) made of group IVB (Zr, Hf) and group VIB (Mo, W) metal dichalcogenides are predicted [1] to have type II or type III band alignments mainly because of a large difference in their workfunctions and band gaps, which makes them candidates for novel 2D staggered, or broken gap tunneling field effect transistors (TFET). We use molecular beam epitaxy (MBE) to grow high quality large area $HfSe_2$ [2,3], $ZrSe_2$ [4] and $MoSe_2$ [5] films directly on AlN(0001)/Si(111) substrates. We confirm by RHEED and HRTEM that atomically thin layers (1-6 ML) are grown in single crystal form with a well-defined in-plane orientation on AlN. The films are continuous with smooth surface morphology (0.6 nm RMS roughness) and abrupt interfaces with no detectable reaction as verified by in-situ XPS and HRTEM. Micro Raman mapping for all layers confirms their structural integrity down to one monolayer and reveals very good uniformity on a cm-scale wafer and excellent stability of MoSe2 over a period of at least two weeks in air. Strong room temperature PL signal of 1 ML $MoSe_2$ indicate high quality direct gap semiconductor in agreement with valence band structure details imaged by our in-situ ARPES [3, 5]. In a second step, MoSe2/$HfSe_2$ [3] and $MoSe_2$/$ZrSe_2$ [4] HS were grown. Despite the large lattice mismatch, all layers are grown epitaxially as evidenced by RHEED with no detectable defects at the interfaces as confirmed by HRTEM suggesting good quality VdW epitaxy [6]. Using UPS the workfunctions (WF) were estimated to be 5.2, 5.5 and 5.4 eV for $MoSe_2$, $HfSe_2$ and $ZrSe_2$ respectively [3,4]. The last two differ substantially from theoretical values (~ 6 eV). Based on our STM and DFT calculations [3], we conclude that this difference is due to an ordered Se adlayer which lowers the $HfSe_2$ and $ZrSe_2$ WF bridging the WF gap between them and MoSe2. As a result, small valence band offsets of 0.13 and 0.58 eV were found for the $HfSe_2$/$MoSe_2$ and $ZrSe_2$/$MoSe_2$ HS, respectively leading to type II band alignments. The availability of low cost wide-gap-AlN/Si wafers in 300 mm wafer sizes defines a manufacturable route for single crystal 2D semiconductor technology.

We acknowledge financial support from ERC Advanced Grant SMARTGATE-291260. We thank IMEC for providing the AlN/Si substrates.

[1] C. Gong et al., *APL*. **103**, 053513 (2013)

[2] R. Yue et al., *ACS Nano***9**, 474 (2014)

[3] K. E. Aretouli et al., *APL***106**, 143105 (2015)

[4] P. Tsipas et al., *Microelectron. Eng*. (2015), http://dx.doi.org/10.1016/j.mee.2015.04.113

[5] E. Xenogiannopoulou et al, *Nanoscale* **7**, 7896 (2015)

[6] F.S. Ohuchi et al., *JAP***68**, 2168 (1990)

9:40am **2D+EM+MG+NS+SE+SM+SS+TF-ThM6 Surface Investigation of WSe_2 Atomically Thin Film and Bulk Crystal Surfaces**, ***Rafik Addou***, *H. Zhu,* University of Texas at Dallas, *Y.-C. Lin, S.M. Eichfeld, J.A. Robinson,* Penn State University, *R.M. Wallace*, University of Texas at Dallas

Heterogeneous fabrication of semiconducting two-dimensional layered materials presents a promising opportunity to develop highly tunable electronic and optoelectronic materials.(1-2) An example of crystalline monolayer of WSe_2 grown by chemical vapor deposition on epitaxial graphene (EG) grown from silicon carbide had been investigated at nanoscale level. The WSe_2 surface was characterized using atomic force microscopy (AFM) scanning tunneling microscopy/spectroscopy (STM/STS) and X-ray photoelectron spectroscopy (XPS).(3,4) AFM and

large STM images show high-quality WSe_2 monolayers. The sharpness of the W *4f* and Se *3d* core levels confirms the absence of any measurable reaction at the interface and oxide formation. The photoemission measurements of WSe_2-Graphene interface suggest p-type doping due to charge transfer (EG withdraws electrons from WSe_2) at the interface and formation of Schottky-type contact,(5) suggesting possible applications of such heterostructures as diodes and photodetectors. High-resolution STM images reveal atomic-size imperfections induced by Se vacancies and impurities. Additionally, the investigation of bulk $WSe_2(0001)$ surface shows spatial variation attributed to the presence of two components in W $4f_{7/2}$ core level attributed to the presence of both n- and p-type behavior. STM images exhibit also various types of defect induced by vacancies and dopants. The STS spectra reveal two main characteristics i) expected p-type conductivity where the Fermi level located at the valence band edge, and ii) zero conductivity at negative bias explained by defect-induced band bending as reported on geological MoS_2 crystal surfaces.(4) In conclusion, the spatial variation (topography and electronic structure) is more noticeable in bulk WSe_2 grown by chemical vapor transport than in CVD thin films.

This work was supported in part by the Southwest Academy on Nanoelectronics sponsored by the Nanoelectronic Research Initiative and NIST and the Center for Low Energy Systems Technology, one of six centers supported by the STARnet phase of the Focus Center Research Program, a Semiconductor Research Corporation program sponsored by MARCO and DARPA.

(1) Yu-Chuan Lin et al., Nano Lett., **14** (2014) 6936-6941.

(2) Yu-Chuan Lin et al., Nature Comm. arXiv:1503.05592v1.

(3) Robert M. Wallace, *ECS Trans*. **64** (2014) 109-116.

(4) Rafik Addou, Luigi Colombo, and Robert M. Wallace, ACS Appl. Mater. Interfaces (Accepted, 2015).

(5) Horacio Coy Diaz, Rafik Addou, and Matthias Batzill, Nanosclae **6** (2014) 1071-1078.

11:00am **2D+EM+MG+NS+SE+SM+SS+TF-ThM10 A Kinetic Study on the Adsorption of Polar (Water) and Non-Polar (Benzene) Molecules on CVD Graphene**, ***Nilushni Sivapragasam****, U. Burghaus*, North Dakota State University

The adsorption kinetics of water and benzene at ultrahigh vacuum conditions were studied. Two different chemical vapor deposited graphene samples (graphene/SiO_2 and graphene/Cu) were utilized. Different surface analytical techniques (Auger electron spectroscopy, X-ray photoelectron spectroscopy, and Raman spectroscopy) were used to characterize the surface. Subsequently, a kinetics study - to understand the adsorption of water and benzene- using thermal desorption spectroscopy (TDS) was conducted. The TDS results revealed the hydrophobicity of water on graphene. However, the adsorption kinetics of water on graphene did not mimic the bare substrate, i.e., graphene is non-transparent for water adsorption. In contrast, graphene was transparent for benzene adsorption. Furthermore, the adsorption kinetics of both, water and benzene were substrate dependent.

11:20am **2D+EM+MG+NS+SE+SM+SS+TF-ThM11 Epitaxial Ultrathin $MoSe_2$ Layers Grown by Molecular Beam Epitaxy**, ***Ming-Wei Chen****, M.B. Whitwick, O. Lopez-Sanchez, D. Dumcenco, A. Kis*, Ecole Polytechnique Fédérale de Lausanne (EPFL), Switzerland

Two-dimensional transition metal dichalcogenides (TMDs) have attracted widespread attention recently, and the focus is specifically on ultrathin layers due to the strong spin-orbit coupling and direct band-gap transition of single-layers. The unique properties of various TMDs also enable the possibilities for future optoelectronic applications. However, the synthesis of TMDs with uniform large-area and high-quality still remains challenging. While chemical vapour deposition has been demonstrated as a promising technique, the complexity of chemical precursors and the lacking of *in-situ* observation technique strongly hinder the progress.

Here, We propose to use ultra-high vacuum molecular beam epitaxy (MBE) to grow $MoSe_2$ ultrathin layers, down to single-layer in a controllable way. Epitaxial $MoSe_2$ layers were successfully grown on different crystalline substrates via van der Waals epitaxy mechanism, benefited from the weak interlayer interaction and the lacking of dangling bonds. Reflection high energy electron diffraction (RHEED) was used to *in-situ* monitor the initial growth stage and revealed a clear transition of the streaks, demonstrating the formation of $MoSe_2$ layer. Sharp streaks were obtained in the growth end, with the streak spacing corresponding to $MoSe_2$ lattice constant, and no significant strain effect was observed. In order to demonstrate the validity of van der Waals epitaxy, different crystalline substrates with lattice mismatch up to 30 % have been tested. The epitaxial layers showed a smooth and uniform surface in atomic force microscopy, and the quality was further confirmed in Raman spectrum and transmission electron microscopy. Furthermore, photoluminescence of the single-layer $MoSe_2$ showing a sharp peak of ~1.58 eV at room temperature demonstrates the direct band-gap feature and indicates the potentials of photovoltaic applications. In the end, the growth of two-dimensional van der Waals heterostructures has also been addressed and the results pave way for heterostructure studies.

In summary, molecular beam epitaxy has been proved to be a reliable route to grow large-area and high-crystalline transition metal chalcogenides, and is promising to facilitate the integration of other two-dimensional materials in the future.

11:40am **2D+EM+MG+NS+SE+SM+SS+TF-ThM12 A Two-Dimensional Oxide Quasicrystal**, ***Stefan Förster****,* Institute of Physics, Martin-Luther-Universität Halle-Wittenberg, Germany*, J.I. Flege,* Institute of Physics, Univerisity of Bremen, Germany*, K. Meinel, R. Hammer, M. Trautmann,* Institute of Physics, Martin-Luther-Universität Halle-Wittenberg, Germany*, J. Falta,* Institute of Solid State Physics, University of Bremen, Germany*, T. Greber,* Physik-Institut, University of Zürich, Switzerland*, W. Widdra*, Institute of Physics, Martin-Luther-Universität Halle-Wittenberg, Germany **INVITED**

With the recent discovery of the first oxide quasicrystal (QC) aperiodicity is entering the field of two-dimensional materials [1]. Aperiodicity means that the system exhibits long-range order as expressed by sharp diffraction spots but since the ordering follows an aperiodic function the system is lacking translational symmetry. We report here on the complex growth process of the oxide QC involving a high-temperature wetting process and periodic approximant structures.

The QC is derived from $BaTiO_3$ thin films on a hexagonal Pt(111) substrate and exhibits a sharp twelve-fold diffraction pattern [1]. Based on scanning tunneling microscopy the aperiodic atomic structure had been resolved [1]. It is formed by surface atoms arranged in forms of squares, triangles, and rhombi with a next-neighbour distance of 0.69 nm. In addition to this dodecagonal atomic arrangement, building blocks of squares, triangles, and rhombi are also found on $(2+\sqrt{3})$ and $(2+\sqrt{3})^2$ larger scales indicating the characteristic self-similarity of an ordered QC [1]. The high-resolution STM measurements allow furthermore to identify atomic flips in the structure indicating lattice excitations in the quasicrystal called phasons. Using low-energy electron microscopy (LEEM) the preparation and the growth of the QC films on top of the hexagonal Pt(111) is monitored in all details from room temperature up to about 1200 K. LEEM shows that upon high-temperature annealing large 3D$BaTiO_3$ islands are formed with bare Pt(111)-(1x1) in between. At temperatures above 1020 K a wetting layer spreads on the free Pt area. This wetting process can be reversed by annealing in an oxygen atmosphere. In-situ LEEM measurements show that under these conditions the QC decays into small $BaTiO_3$ islands. The observed interface-driven formation of a 2D QC from a perovskite oxide in contact with a hexagonal substrate is expected to be a general phenomenon.

1. S. Förster, K. Meinel, R. Hammer, M. Trautmann, and W. Widdra, *Nature* **502**, (2013) 215.

Additive Manufacturing/3D Printing Focus Topic
Room: 211A - Session AM+EM+MS+TF-ThM

Technologies Enabled by Additive Manufacturing/Future of Additive Manufacturing
Moderator: Vincent Smentkowski, General Electric Global Research Center

8:40am **AM+EM+MS+TF-ThM3 Additive Manufacturing Enabling Advanced Technologies**, ***Teresa Clement***, Raytheon Company **INVITED**

The aerospace and defense industry for the last decade has taken note and contributed to significant advances in materials and process capabilities enabled by the field of additive manufacturing (AM) to fabricate beyond state-of-the-art advanced technologies. Conventional and non-conventional industry partners continue to push the boundaries of next-generation materials and multi-materials for additive manufacturing in order to further extend product capabilities. As these material developments continue evolving, our industrial base begins to realize the many benefits of AM: reducing lifecycle costs, engineering resilience and capability surprise by rapidly reconfigurable responses to adaptive adversarial threats, and the enabling of truly agile manufacturing via AM integration with the model based enterprise (aka marrying AM to the ‘digital thread’). Some specific examples of advanced technologies are discussed herein, with examples of design iteration cycle-time reduction and use of material/process controls to verify by inspection and full characterization demonstrations of improved or

unprecedented material performance and multi-functionality (electrical, thermal, structural, etc) made possible by additive manufacturing.

9:20am **AM+EM+MS+TF-ThM5 4D Printing: Three Dimensional Printing with Material Composition as the Fourth Dimension**, ***Douglas C. Hofmann***, NASA Jet Propulsion Laboratory, California Institute of Technology **INVITED**

Much of the current research in additive manufacturing in the aerospace community is focused on qualifying materials for service, which is a critical requirement for using additive materials. However, additive manufacturing is a powerful tool for creating materials and applications that cannot be replicated using traditional means. In the past, this has meant 3D printing complex geometries that cannot be easily machined. In the current talk, we will discuss what we call 4D printing; 3D printing where the fourth dimension is the material composition. By using multiple materials strategically in additive manufacturing, a whole new frontier of materials science becomes possible. The science behind these alloys and their applications will be discussed.

11:00am **AM+EM+MS+TF-ThM10 The Future of Additive Manufacturing and Multifunctional Parts**, ***Phill Dickens***, University of Nottingham, UK, United Kingdom of Great Britain and Northern Ireland **INVITED**

Additive Manufacturing has many advantages for producing complex components and systems and this has already started to be exploited for parts made of a single material. There is now much interest in the possibility of building parts with multiple materials so that electrical circuits and electronic items can be included within the structure. This paper will highlight some of the research that is taking place at the University of Nottingham and some recent examples of simple products that could exploit this technology.

Some of the issues will be covered where the layer manufacturing process provides some limitations.

Spectroscopic Ellipsometry Focus Topic
Room: 112 - Session EL+EM+EN-ThM

Spectroscopic Ellipsometry: Novel Applications and Theoretical Approaches
Moderator: Tino Hofmann, University of Nebraska - Lincoln, Vimal Kamineni, Globalfoundries, Ny, Usa

8:00am **EL+EM+EN-ThM1 Multi-Spectral Polarimetric Imaging and Biomedical Applications**, ***Bernard Drevillon***, *A. Pierangelo*, LPICM-CNRS, Ecole Polytechnique, France **INVITED**

In the last years Polarimetric Imaging has received considerable attention in the literature thanks to its tremendous potential for the assessment of biological tissues in biomedical diagnostics. Light Polarization allows obtaining morphological information on tissues microscopic structure, potentially improving the diagnosis and treatment of several pathologies. Moreover, polarimetric imaging can be implemented using conventional light sources, like LED or halogen lamps, making it a cheap alternative to current standards. For several years the PICM Laboratory has designed and built innovative polarimetric imagers for biomedical applications. In particular, the development of the *eigenvalue calibration method* [1], led to the design of several polarimeters for macroscopic and microscopic analysis (in real and Fourier space) of *ex vivo* samples and for *in vivo* diagnoses. The development of such new instruments ranged from the simple measurement of polarization degree to the complete Mueller polarimetry. Several studies were devoted to the early detection and staging of uterine cervix cancer and to show that polarimetric imaging is effective for the visualisation and first grading of cervical dysplastic regions for patients with anomalous Pap smear [2]. Mueller matrix imaging polarimetry also provides enhanced contrast to differentiate types of cancer of colon and their stage of progress and penetration, which is currently detectable only by histological examination [3]. Moreover, this technique may also be useful to quickly verify the presence of residual cancer in the rectum after treatment with radiochemotherapy [4]. Finally, as a complementary development to experimental techniques, the set-up of Monte-Carlo detailed modelling of polarized light scattering in tissues has been carried out in the last few years and provides fundamental insight on the origin of observed polarimetric contrasts [5]. In conclusion the synergy of new experimental techniques based on polarimetry with the biomedical analysis and theoretical computer models, led to significant advances in the field of biological tissues characterization and diagnosis of related pathologies.

[1] E. Compain et al., Appl. Opt. 38, 3490-3502 (1999).

[2] A. Pierangelo et al., Opt. Express, 21, 14120 -14130 (2013).

[3] A. Pierangelo et al., Opt. Express 19, 1582 (2011).

[4] A. Pierangelo et al., J. Biomed. Opt., 18 (04), 046014 (2013).

[5] M.R. Antonelli et al., Opt. Express 18, 10201 (2010).

8:40am **EL+EM+EN-ThM3 Anisotropic Optical Properties of Rhombohedral and Tetragonal $BiFeO_3$ Phases**, ***Daniel Schmidt***, National University of Singapore, *L. You*, Nanyang Technological University, Singapore, *X. Chi*, National University of Singapore, *J. Wang*, Nanyang Technological University, Singapore, *A. Rusydi*, National University of Singapore

Single crystalline bismuth ferrite ($BiFeO_3$) is a multiferroic perovskite structure and exhibits magnetic as well as strong ferroelectric behaviour at room-temperature. Since about a decade $BiFeO_3$ is of strong research interest due to its potential applicability in ferroelectric memory devices and spintronics, for example [1].

While the lattice system of bulk $BiFeO_3$ is rhombohedral, the crystal structure of thin films can be engineered by introducing epitaxial strain. Depending on the choice of single crystalline substrate materials the thin film $BiFeO_3$ crystal structure and associated physical properties can be modified.

Here, we present the anisotropic optical properties of high-quality multiferroic $BiFeO_3$ thin films determined with Mueller matrix ellipsometry at room-temperature within the spectral range of 0.6 and 6.5 eV. The full dielectric function tensors of tetragonal-like and rhombohedral-like $BiFeO_3$ phases epitaxially grown on $LaAlO_3$ and $SrTiO_3$ single crystal substrates, respectively, are discussed. Significant birefringence and dichroism are observed as well as strain-induced differences in critical point energies between both phases.

The importance of careful optical analysis of anisotropic Mueller matrix data will be discussed, which allows for characterization of subtle sub-band gap crystal field transitions and reveals indications of an indirect band gap. Such transitions have been observed before by means of other techniques but not by ellipsometry. Additionally, the analysis of Mueller matrix data revealed that an unintentional substrate miscut can introduce an overall polarization tilt of the ferroelectric thin films. This tilt was confirmed by extensive in- and out-of-plane piezoelectric force microscopy studies.

An accurate determination of the dielectric function tensor is of high importance to verify or, if necessary, improve and correct ab-inito calculations, which are crucial for understanding the driving physical principles in such complex materials. A comparison of the experimental results with state-of-the art first-principle calculations will be presented.

[1] G. Catalan and J.F. Scott, Adv. Mater. 21, 2463 (2009).

9:00am **EL+EM+EN-ThM4 Temperature Dependent Structural and Optical Properties of SnO_2 Thin Film**, ***Junbo Gong***, *R.C. Dai, Z.P. Wang, Z.M. Zhang, Z.J. Ding*, University of Science and Technology of China

SnO_2, which is an n-type semiconducting material with a wide band gap 4 eV, is an interesting material due to its high electrical conductivity and optical transparency. SnO_2 film is attractive for many applications such as optoelectronic devices, gas sensors, thin film transistors, transparent electrodes, anti-reflecting coating, and as catalyst support.

In this work, the ellipsometric parameters of SnO_2 films on quartz glass are measured by spectra ellipsometer(J. A. Woollam M-2000U) in the wavelength range of 300 to 1000 nm at different temperature from room temperature to 600 ^oC. By using a semitransparent model, the precise thickness and optical constants of SnO_2 thin film depending on the temperature were obtained and the evolution process was studied. The film thickness significantly decreased with increased temperature from 100 ^oC to 300 ^oC and the absorption edge has an obvious blue shift which means an increased band gap. The result reveals that this process is not reversible. Combined with XRD measurement, we identified that the change of thickness and optical properties of SnO_2 film was due to a phase transition from rutile structure to columbite structure.

9:20am **EL+EM+EN-ThM5 Determining Curvature Radius of a Curved Surface by use of Mueller Matrix Ellipsometry**, ***Weiqi Li***, *H. Jiang, C.W. Zhang, X.G. Chen, S.Y. Liu*, Huazhong University of Science and Technology, China

Determining curvature radius of a curved surface by use of Mueller matrix ellipsometry

Weiqi Li, Hao Jiang, Chuanwei Zhang, Xiuguo Chen, and Shiyuan Liu*

State Key Laboratory of Digital Manufacturing Equipment and Technology, Huazhong University of Science and Technology, Wuhan 430074, China.

* Corresponding author: shyliu@hust.edu.cn

Ellipsometry is a powerful metrology tool for the characterization of surfaces and thin films. Generally, the basic principle of conventional ellipsometry is based on the assumption that the studied film or structure is on a planar surface [1], in another word, the conventional ellipsometry works the best for a flat surface. When the studied surface is tilted or curved, the measurement accuracy of the conventional ellipsometry will be significantly degraded, or even be incorrect. It is thus important to develop a method to deal with the cases when the surface for characterization is tilted or curved. Comparing with the conventional ellipsometry, the Mueller matrix ellipsometry (MME) can provide all 16 elements of a 4 by 4 Mueller matrix, and consequently can acquire much more useful information about the curved surface and thereby shows great potential in the curved surface metrology.

In this work, we propose an optical model that is able to process curved surface based on our in-house developed dual rotating-compensator MME [2] to characterize the surface layer of a single crystal silicon sphere crown with a radius of about 51 mm for demonstration. Focus probe accessory is used in the MME to achieve sufficient small spot on the curved surface so that the detected area on the spherical surface can be approximately regarded as a tilted one. We found that some of the measured off-diagonal Mueller matrix elements are very sensitive to the offset between the actual detected spot and the surface vertex, which is proportional to the deviation angle α of the surface normal across the surface vertex. An optical model of the spherical layer is proposed by considering the curved surface of the silicon sphere crown and the offset. With the proposed model, the deviation angle α as well as the surface layer thickness can be extracted from the measured Mueller matrix spectrum, and then the curvature radius of the sphere crown can be achieved. Experiments are performed on the silicon sphere crown show that not only the accuracy of measurement can be improved but also the curvature radius of the sphere crown is capable to be measured using the proposed optical model.

[1] R. M. A. Azzam and N. M. Bashara, *Ellipsometry and Polarized Light* (North-Holland, 1992).

[2] S. Y. Liu, X. G. Chen, and C. W. Zhang, *Thin Solid Films* **584**, 176-185 (2015).

9:40am **EL+EM+EN-ThM6 Cavity-Enhanced Optical Hall Effect in AlInN/GaN-based HEMT Structures Detected at Terahertz Frequencies**, ***Sean Knight***, University of Nebraska-Lincoln, *S. Schöche,* J.A. Woollam Co. Inc., *V. Darakchieva, P. Kühne,* Linköping University, Sweden, *J.-F. Carlin, N. Grandjean,* Ecole Polytechnique Fédérale de Lausanne (EPFL), Switzerland, *C.M. Herzinger,* J.A. Woollam Co. Inc., *M. Schubert, T. Hofmann*, University of Nebraska-Lincoln

The terahertz optical Hall effect (THz-OHE) has been established as a non-contact and therefore valuable tool for the investigation of free charge carrier properties in semiconductor heterostructures [1-4]. In this work, we demonstrate that the THz-OHE signal for samples grown on THz transparent substrates can be controlled and enhanced by a tunable, externally coupled Fabry-Pérot cavity mode [5]. An AlInN/GaN-based high electron mobility transistor structure (HEMT) grown on a sapphire substrate is investigated as an example, while the cavity enhancement phenomenon discussed here is generally applicable to situations when a layered sample is deposited onto a THz transparent substrate. We show that in the vicinity of an externally coupled-cavity mode, a strong enhancement of the OHE signatures of up to one order of magnitude can be achieved by optimizing the cavity geometry, which is very useful for small magnetic field strengths. This signal enhancement allows the determination of free charge carrier effective mass, mobility, and density parameters using OHE measurements in low magnetic fields. Previously, high-field electromagnets needed to be employed for THz-OHE measurement for the determination of free charge carrier parameters in semiconductor heterostructures. Tuning the external cavity allows an enhancement of the THz-OHE signatures by as much as one order of magnitude. We propose to employ this enhancement effect to reliably and accurately determine free charge carrier properties in semiconductor structures at small magnetic fields dispensing with the need for expensive high magnetic fields. Cavity-enhanced THz-OHE may therefore enable the wide spread contactless measurement of free charge carrier properties at THz frequencies and which is indispensable for the development of the next generation of group-III nitride-based high frequency devices.

11:00am **EL+EM+EN-ThM10 Biosensor based on Imaging Ellipsometry and its Biomedical Applications**, *Y. Niu, **Gang Jin***, Institute of Mechanics, Chinese Academy of Sciences, China **INVITED**

The concept of biosensor based on imaging ellipsometry (BIE) was proposed in 1995 [1, 2]. With the development in recent 20 years, it has been formed an automatic analysis technique for detecting biomolecule detection interaction with merits of rapid, label-free, quantitative, high throughput and real-time. Its principle, methodology, biosensor system and biomedical applications are reviewed in this report.

A BIE system can be divided into four parts: the microfluidic array reactor, the imaging ellipsometer, the control system, and the biosensor database. The microfluidic array reactor serves to fabricate the protein microarray and accommodate biomolecular interactions. Using the microfluidic array reactor, various ligands are immobilized to different cells to form a sensing array, and each sensing surface can be prepared homogeneously under the flow condition. The imaging ellipsometer acts as a reader for data acquisition from the microarray. Since imaging ellipsometry is sensitive to slight variations of optical thickness, it can be used to visualize ultra-thin films and the change of molecular mass surface concentration. The control system combines the reactor with the imaging ellipsometer and functions to control the hardware's mechanical motion and obtain results in images, while the biosensor database is to aid BIE users in determining optimized experimental conditions and comparing previous test data.

The sensitivity and flexibility of the biosensor is very important for practical purpose, especially in biomedical fields. The sensitivity depends not only upon the resolution of imaging ellipsometry but also upon the bio-system of ligand-receptor on the microarray that is the bioactivity and its act related to the ligand screen, ligand immobilization, unspecific blocking and interaction conditions, etc. The flexibility mainly depends on the mechanical, electrical, informatics and biological control. So far, a serviceable engineering system of the biosensor and some bio-systems is installed available for more applications, especially for high throughput protein analysis, such as antibody screening [3], disease markers serological detection [4] and joint detection of tumor markers [5] as well as virus infection identification [6-7].

References

[1] G. Jin, et al., *Anal. Biochem.* **232**, 69 (1995).

[2] G. Jin, R. Jansson, and H. Arwin, *Rev. Sci. Instrum.***67**, 2930 (1996).

[3] Y. Niu, et al., *Thin Solid Films***519** 2768 (2011).

[4] C. Qi, et al., *J. Viral Hepatitis***16**, 822 (2009).

[5] Y. Niu , et al., *Thin Solid Films***571**, 453 (2014).

[6] C. Qi, et al., *Biosensors & Bioelectronics***25**, 1530 (2010).

[7] C. Qi, et al., *Virus Res.***140**, 79 (2009).

11:40am **EL+EM+EN-ThM12 Screening Breast Cancer by Joint Detection of Tumor Marker Carbohydrate Antigen 15-3 and Carbohydrate Antigen 242 with Biosensor Based on Imaging Ellipsometry**, ***Yu Niu**, G. Jin*, Institute of Mechanics, Chinese Academy of Sciences, China

Breast cancer which develops from breast tissue is the leading type of cancer in women worldwide, accounting for more than 25% of all carcinogenesis [1]. Compared with other common cancers, the survival rate of breast cancer is remarkably positive and optimistic that between 80% and 90% of those in developed country could be alive for at least 5 years. Therefore, screening high risk population and further concluding a clinical diagnosis in the early stage act as a pivotal factor to cure breast cancer, because it can provide overwhelming contribution to carry out essential therapy in time. Carbohydrate Antigen 15-3 (CA 15-3) and Carbohydrate Antigen 242 (CA 242) are widely-used tumor markers for breast cancer in clinic and their concentrations in serum vary sensitively with breast cancer genesis. The biosensor based on imaging ellipsometry (BIE) for visualization of biomolecular interactions was reported in 1995 [2] and now it is composed of a 48 protein unit array and imaging ellipsometry reader with a field of view (20 x 30 mm) and good resolution for protein adsorption layer on a silicon substrate (lateral and vertical is 1 μm and 0.1 nm, respectively) [3]. In this investigation, joint detection of these two tumor markers simultaneously has been performed with BIE as a trial for screening breast cancer for clinical purpose.

To realize the joint detection, a series of design and optimization has been performed, including the ellipsometric setting, ligand immobilization strategy, ligand surface density, as well as the blocking and rinsing procedures. The test concentration range calibration and the detection limit for quantitative detection have been established by standard samples, which meet the standards of clinical test. By diluting sera to the detection range fitting to the calibration curves, joint quantitative detection of CA 15-3 and CA 242 can be achieved simultaneously.

149 serum samples composed of both the healthy and patients have been performed with BIE. Compared with the results obtained by standard approaches in clinic, the correlation analysis indicates the BIE are highly consistent with clinical methods. In order to estimate the BIE performance for tumor markers detection, ROC curve analysis has been introduced. Its result suggests that the single marker detection by BIE presents good capability to distinguish the normal from patients and the joint detection of

CA 15-3 and CA 242 plays a positive role in the improvement of the diagnosis specificity and accuracy.

Reference

[1] A. Jemal, et al., *CA Cancer J. Clin.***61**, 69 (2011).

[2] G. Jin, et al., *Anal. Biochem.***232**, 69 (1995).

[3] G. Jin, et al., *Thin Solid Films***519,** 2750 (2011).

12:00pm **EL+EM+EN-ThM13 Decomposition of Angle Resolved Spectroscopic Mueller Matrices from Scarabaeidae Beetles***,* ***Roger Magnusson****,* Linköping University, Sweden*, R. Ossikovski, E. Garcia-Caurel,* LPICM-CNRS, Ecole Polytechnique, France*, K. Järrendahl, H. Arwin*, Linköping University, Sweden

We use angle-dependent Mueller-matrix spectroscopic ellipsometry (MMSE) to determine Mueller matrices of Scarabaeidae beetles which show fascinating reflection properties due to structural phenomena in the exocuticle which are often depolarizing. It has been shown by Cloude [1] that a depolarizing matrix can be decomposed into a sum of up to four non-depolarizing matrices according to $\mathbf{M}= a\mathbf{M}_1+b\mathbf{M}_2+c\mathbf{M}_3+d\mathbf{M}_4$, where a, b, c and d are eigenvalues of the covariance matrix of **M**. Using the same eigenvalues the matrices $\mathbf{M}_i$ can be calculated. This method provides the full solution to the decomposition with both the non-depolarizing matrices and the weight of each of them in the sum.

An alternative to Cloude decomposition is *regression decomposition*. Here any Mueller matrix can be decomposed into a set of matrices $\mathbf{M}_i$ which are specified beforehand. Whereas in Cloude decomposition the only constraint on the matrices is that they are physically realizable non-depolarizing Mueller matrices, we can now limit the constraint and only use Mueller matrices representing pure optical devices having direct physical meaning, such as polarizers, retarders, etc. This leaves a, b, c, d as fit parameters to minimize the Frobenius norm $\mathbf{M}^{exp}$ $-\mathbf{M}^{reg}$ where $\mathbf{M}^{exp}$ is the experimentally determined Mueller matrix to be decomposed and $\mathbf{M}^{reg}$ is the sum of all $\mathbf{M}_i$. Depending on $\mathbf{M}^{exp}$ an appropriate choice of $\mathbf{M}^{reg}$ matrices has to be made and different values of a, b, c and d are obtained through regression analysis.

We have previously shown that regression decomposition can be used to show that the Mueller matrix of *Cetonia aurata* can be decomposed into a sum of a circular polarizer and a mirror [2]. Here we expand the analysis to include angle-resolved spectral Mueller matrices, and also include more species of Scarabaeidae beetles.

One effect of the decomposition is that when depolarization is caused by an inhomogeneous sample with regions of different optical properties the Mueller matrices of the different regions can be retrieved under certain conditions. Regression decomposition also has potential to be a classification tool for biological samples where a set of standard matrices are used in the decomposition and the parameters a, b, c, d are used to quantify the polarizing properties of the sample.

[1] Cloude S.R. 1989. Conditions for the physical realisability of matrix operators in polarimetry. Proc. SPIE 1166, Polarization Considerations for Optical Systems II, pp. 177-185

[2] Arwin H, Magnusson R, Garcia-Caurel E, Fallet C, Järrendahl K, De Martino A, Ossikovski R, 2015. Sum decomposition of Mueller-matrix images and spectra of beetle cuticles. Opt. Express, vol. 23, no. 3, pp. 1951–1966

Electronic Materials and Processing
Room: 210E - Session EM+MS-ThM

III-N Nitrides for Optoelectronic Applications
Moderator: Rachael Myers-Ward, U.S. Naval Research Laboratory, Aubrey Hanbicki, U.S. Naval Research Laboratory

8:00am **EM+MS-ThM1 Hollow Cathode Plasma-Assisted Atomic Layer Deposition of Wurtzite InN and $In_xGa_{1-x}N$ Thin Films with Low Impurity Content***,* ***Ali Haider****, S. Kizir, C. Ozgit-Akgun, E. Goldenberg, M. Alevli, A. Kemal Okyay, N. Biyikli*, Bilkent University, Turkey

Among the III-nitride compound semiconductor family, InN is known with its unique properties which are crucial for both electronic and optoelectronic applications such as narrow band gap, small effective mass, and high electron mobility. Since InN and its alloys are currently the backbone of LED industry for bandgap tuning and are mostly grown using high-temperature epitaxy, experimental efforts on enabling low-temperature growth are critical to widen its perspective for applications like flexible (opto)electronics. In addition, a growth method in which indium composition can be precisely controlled for $In_xGa_{1-x}N$ alloys is highly imperative for band gap engineering.

In this work, we summarize our recent progress on the development of crystalline InN and $In_xGa_{1-x}N$ thin films with low impurity content at a substrate temperature as low as 200 °C by hollow cathode plasma-assisted ALD (HCPA-ALD). Deposition of polycrystalline wurtzite InN thin films was achieved using trimethylindium ($InMe_3$) and N_2 plasma sources. Process parameters including $InMe_3$ pulse time, N_2 flow rate and duration, purge time, deposition temperature, and plasma power were investigated. Detailed structural and optical characterizations of InN and $In_xGa_{1-x}N$ were performed. N_2 plasma exposure time had a profound effect on the impurity content of the InN films. After saturating the surface of substrate with $InMe_3$ molecules, the ligands of $InMe_3$ were removed completely only after sufficient exposure dose of N_2 plasma. Insufficient exposure times of N_2 plasma resulted in InN films with higher carbon impurity contents as determined from XPS measurements, which were arising from methyl ligands of $InMe_3$. After optimizing the precursor dosages,XPS survey scan obtained from the bulk part of the InN film showed that *h*-InN films were carbon and oxygen free. On the other hand, indium composition in different $In_xGa_{1-x}N$ thin films was determined by energy-dispersive X-ray spectroscopy, X-ray photoelectron spectroscopy, and X- ray diffraction. GIXRD measurements revealed the hexagonal wurtzite crystalline structure of the grown InN and $In_xGa_{1-x}N$ thin films. Refractive index of the InN film at 750 nm was estimated to be 2.67 while refractive indices of $In_xGa_{1-x}N$ thin films increased from 2.28 to 2.42 at wavelength of 650 nm with increase in indium composition. Optical band edge studies of the $In_xGa_{1-x}N$ films confirmed the successful tunability of the optical band-edge with alloy composition. Our results show that HCPA-ALD is an alternative technique to grow crystalline InN and $In_xGa_{1-x}N$ films at low substrate temperatures.

8:20am **EM+MS-ThM2 Infrared Nanoscopy of Indium-rich InGaN Epilayers***,* ***Yohannes Abate****, D. Seidlitz, N. Dietz,* Georgia State University*, I. Ferguson*, Missouri University of Science and Technology

The unique optical and electrical properties of ternary $In_{1-x}Ga_xN$ epilayers and heterostructures therewith makes this material system attractive for various optoelectronic device applications, including but not limited to high-speed electronics, frequency agile photovoltaic solar cells, or light emitting devices. However, the presently utilized growth methods enable the indium incorporation in $In_{1-x}Ga_xN$ heterostructures to a narrow composition range, before phase instabilities are encountered. As a potential pathway to extend the stable composition range and the control of point defects in the alloys, we explored in recent years the reactor pressure dependency under superatmospheric MOCVD - also denoted high-pressure chemical vapor deposition (HPCVD) - conditions. In this contribution we will report and discuss on the growth of indium-rich ternary $In_{1-x}Ga_xN$ epilayers and the influence of the pulse separations on the phase purity and stability of indium-rich $In_{1-x}Ga_xN$ epilayer and resulting structural and optical properties. The InGaN epilayers have been characterized by x-ray diffraction, Raman spectroscopy, atomic force microscopy, and by several optical techniques such as infrared (IR) reflectance and optical absorption spectroscopy. The free carrier concentrations have been estimated by analyzing the IR-reflectance spectra and by Raman A1(LO) mode line shape analysis.

8:40am **EM+MS-ThM3 Surface Treatment and Characterization of InN (0001)***, S.P. Park, T. Kaufman-Osborn, K. Sardashti,* University of California San Diego*, S.M. Islam, D. Jena,* University of Notre Dame*,* ***Hyunwoong Kim****, A.C. Kummel*, University of California San Diego

Indium nitride (InN) is a promising material due to the its band offset to GaN. However, employing InN in practical devices is still challenging because it has an electron accumulation at the surface which is hypothesized to be due to an In-In double layer at the surface. For practical InN devices, it is critical to remove this In-In double layer and form a non-metallic surface. This work describes the transformation of the atomic order, elemental composition, and electric structure of InN (0001) surface during the removal of the metallic layer and its replacement with gate oxide using scanning tunneling microscopy (STM), x-ray photoelectron spectroscopy (XPS), and scanning tunneling spectroscopy (STS). Three cleaning methods were studied. (1) Ex -situ wet cleaning was performed by using HCl, NH OH, and (NH) S solution to remove native oxide. STM showed the surface is smooth and uniform and STS showed n-type conductivity with a band gap of 0.7 eV consistent with strong intrinsic accumulation of electrons on the surface. (2) In-situ atomic hydrogen cleaning on wet cleaned InN surface was performed. However, due to the preferential nitrogen depletion in atomic hydrogen cleaning, the ratio of indium to nitrogen was increased. STM images showed rows of indium dimers, and STS showed that there was a metallic zero band gap surface, consistent with an In-In double layer surface termination. (3) As an alternative method to eliminate the accumulation of electron at InN surface, an O passivation was performed on wet cleaned InN. The O exposed surface was atomically flat and uniform.

STM line traces showed islands were formed with step height of 3.5 angstrom consistent with formation of an O-In-O layer. The band gap of the O passivated InN surface was 0.8 eV and the Fermi level was midgap consistent with absence of In-In double layer.ALD nucleation was studied using TMA pre-dosing and an additional 10 cycles of TMA and H_2O doses on an O_2 passivated InN substrate. After the 10 cycles of ALD, the ratio of Al to O ratio was 2:3 consistent with the stoichiometric ratio of Al_2O_3, The ALD process broadened the band gap from 0.8 eV to 1 eV due to the formation of Al-O-Al bonding, In sum, an unpinned non-metallic surface without the formation of In-In layer was achieved on InN using an oxidant and cyclic dose of TMA and water.

9:00am **EM+MS-ThM4 State-Of-The-Art High Efficiency Thermoelectric Material: III-Nitrides as a Wide Bandgap Semiconductor**, *B. Kucukgok, N. Lu,* University of North Carolina at Charlotte, ***Nikolaus Dietz***, Georgia State University, *I. Ferguson*, Missouri University of Science and Technology

Thermoelectric (TE) devices have gained widespread interest as a renewable energy source in the field of energy conservation and emission reduction due to their direct conversion of heat into electricity by Seebeck effect of TE materials. Additionally, TE devices have been used in wide variety of applications, due to their reliability, stability, and low-cost, such as automotive industry, spacecraft radioisotope power supply, and photovoltaic solar cells. Since TE device performance is directly related to material efficiency, material selection becomes essential. Recently, the interest of potential applications of III-nitride semiconductors in the TE field has been initiated due to their distinguished features including high-temperature operation, high mechanical strength, and large-band gap range and their promising TE figures of merit (*ZT*), mostly for materials based on AlGaN and InGaN alloys. Here, we demonstrate the room temperature thermoelectric properties of III-nitrides such as GaN and its alloys, grown by metalorganic chemical vapor deposition (MOCVD). The structural, optical, electrical, and thermal properties of the samples were examined by X-ray diffraction, photoluminescence, van der Pauw hall-effect, and thermal gradient methods, respectively. The objectives of this paper are to understand the role of defects, carrier density n, and composition x on the TE properties of III-nitrides.

9:20am **EM+MS-ThM5 Nanofabrication of Advanced Nanophotonic Structures by Nanoimprinting**, ***Stefano Cabrini***, Lawrence Berkeley National Laboratory (LBNL) **INVITED**

To exploit the potentialities of Nanophotonics, it is important to control the properties of the material at the nanometer scale, obtaining a good agreement between the experiments and the theory. Nanofabrication can open the way for new concept of devices. In this presentation we will present the fabrication and characterization of simple photonic crystals directly pattern by nanoimprinting using a special functional resist with high refractive index.

11:00am **EM+MS-ThM10 Advanced III-Nitride Device for RF Switch Applications: A Record 2THz Fco Super-Lattice Castellated Field Effect Transistor (SLCFET) for Low Loss RF Switching**, ***Shalini Gupta***, *R. Howell, E. Stewart, J. Parke, B. Nechay, M. King, H. Cramer, J. Hartman, R. Freitag, M. Snook, I. Wathuthanthri, G. Henry, K. Renaldo*, Northrop Grumman ES **INVITED**

Northrop Grumman Electronic Systems (NGES) reports on the development of a novel field effect transistor structure, based on a super-lattice epitaxial layer combined with a three dimensional castellated gate structure to achieve a 3x improvement in RF switch figure of merit compared to current state of the art transistor technologies. RF switch components are vital for the successful implementation of a variety of system architectures, spanning applications from phased array radars to the wireless components of mobile phones and consumer electronics.

NGES used MOCVD growth techniques to grow a GaN/AlGaN based super-lattice on a 100 mm diameter semi-insulating SiC substrate which is used as the SLCFET conductive channel. This super-lattice creates multiple 2DEGs producing parallel current channels between the source and drain of the device resulting in currents several times higher than conventional FETs and a record low GaN epi sheet resistance of 60 ohm/sq. The low epi sheet resistance in turn reduces the on resistance of the FET which results in a low insertion loss RF switch. Although super-lattice structures have been employed to make optoelectronic semiconductor devices, their use in FETs have been limited due to difficulty in pinching-off the stacked paralleled current channels. This is because the top channels screen the bottom channels from the electric field of the gate thereby increasing the voltage needed to pinch off the channel and turn off the device to a value beyond the breakdown field of the semiconductor. The SLCFET overcomes this challenge by employing a side-pinching gate. This is realized by etching features in the semiconductor prior to a 0.25 um gate deposition which allows the gate metal to surround the channels on the top and sides. This feature resembles the crenellations of a castle and hence is called a castellated gate.

Electrical measurements of the SLCFET transistor reveal a high I_{MAX} of 2.7 A/mm and a pinch off voltage of -8V. The SLCFET has a low on resistance (R_{ON}) of 0.4 Ohm-mm and an off capacitance (C_{OFF}) of 0.2 pF/mm, resulting in an RF switch figure of merit ($Fco = 1/2\pi R_{ON}C_{OFF}$) of 2 THz, 3x higher than the current state of the art FET based RF switches. SLCFET MMICs have been designed and tested including Single Pole Double Throw (SPDT) switches, tunable filters, and true time delay units. State of the art electrical results have been obtained, such as a series-shunt broadband (1-18 GHz) SLCFET SPDT with a measured insertion loss of 0.25 dB at 10 GHz, with -35 dB of isolation and -23 dB of return loss. These state-of-the-art results demonstrate that SLCFET is an enabling technology for next generation RF systems.

11:40am **EM+MS-ThM12 Developing Periodically Oriented Gallium Nitride for Frequency Conversion**, ***Jennifer Hite***, *R. Goswami, J.A. Freitas, M.A. Mastro, I. Vurgaftman, J.R. Meyer,* U.S. Naval Research Laboratory, *C.G. Brown,* University Research Foundation, *F.J. Kub, S.R. Bowman, C.R. Eddy, Jr.*, U.S. Naval Research Laboratory

Gallium nitride is a semiconductor widely used in both optical and electronic devices. The polarity of GaN (+/- c-direction) influences many properties of the resultant material, including chemical reactivity and electric field in these 'spontaneously polarized' materials. By engineering inversion layers, we have demonstrated control of GaN polarity on both polar faces of GaN. By employing a selective growth method to deposit the IL, the lateral polarity of the GaN can be alternated, thus enabling structures referred to as periodically oriented (PO) GaN.

On N-polar substrates, we demonstrated that optimization of the MOCVD growth rates resulted in sharp, vertical interfaces and smooth surfaces. This work has moved the technology substantially closer to practical non-linear optic emitters by using HVPE to extend the PO GaN templates on N-polar substrates to total thicknesses of up to 500 mm, while faithfully maintaining the pattern of alternating polarity. Additionally, cross-sectional cathode-luminescence (CL) imaging of such an extension shows that the large initial dislocation densities occurring in the original inversion layers greatly decreased after about 25 μm of regrowth.

For growth on Ga-polar substrates, we have demonstrated that inversion layers can be created using atomic layer deposition (ALD) of Al_2O_3. This new capability is especially relevant because Ga-polar films are more prominent in devices, as they result in lower impurities, higher quality and smoother films. In this case, GaN grown over the inversion layer is N-polar. This inversion layer was used to form laterally-patterned stripes of alternating Ga- and N-polar films. We find that annealing the ALD films crystallizes the Al_2O_3, thereby allowing N-polar GaN to be grown over the new sapphire-like surface. Transmission electron microscopy shows that the inversion layer in a PO GaN structure is crystalline, a-plane oriented, and a-phase. TEM characterization further indicates that the GaN layers, both above and below the Al_2O_3 inversion layer, are c-oriented without any rotation between them. The optimization of this process has enhanced the surface smoothness. The latest results in demonstrating secondary harmonic generation will be presented.

These methods of GaN polarity inversion offer the promise of engineered materials with custom lateral and vertical polarity variations for applications in novel electronic and optoelectronic devices, a subset of which are expected to be suitable for non-linear optics.

12:00pm **EM+MS-ThM13 Electronic and Optical Device Applications based on III-Nitride Films Grown by Plasma-Assisted ALD**, *B. Tekcan,* ***Sami Bolat***, *C. Ozgit-Akgun, N. Biyikli, A.K. Okyay*, Bilkent University, Turkey

For many electronic and optical applications, III-nitride materials are much sought after due to their direct and high optical band-gap, high electron saturation velocity and band-gap tunability [1]. These important features enable many possible device applications, which are generally used in high power and high frequency applications [2]. However, these films are generally grown using high temperature and high vacuum processes namely, MOCVD [3], MBE [4] which limit substrate selection along with CMOS compatibility. In our work, we offer an alternative way of growth to fabricate thin film transistors (TFTs) and UV metal-semiconductor-metal (MSM) photodetectors. Hollow cathode plasma assisted Atomic Layer Deposition (HC-PA-ALD) technique make low temperature device applications possible. We have grown GaN and InGaN films and analyzed TFT and photodetector properties in detail. Electrical and optical characteristics of these devices are inspected.

The results can pave the way for ALD to be used for III-Nitride based electronic and optical devices. Thin film transistor exhibit $2x10^3$ ON/OFF ratio with threshold voltage of 11.8 V. Metal-semiconductor-metal (MSM)

photodetectors, on the other hand, showed 20 pA under -20 V voltage bias with a UV responsivity of 680 m A/W under 290 nm incident light with only a 20 nm thick film. Effect of annealing on the device performance is also studied. TFTs ON/OFF ratio increased to $2x10^4$ with a lower threshold voltage and contact resistance decreased 4000 times when annealed at 800 °C for 30 seconds. Moreover, MSM devices performance also enhanced after annealing 600 °C. The photoresponsivity as high as 950 m A/W at 290 nm incident light is recorded. The dark current reduced significantly, a current value of 50 fA is recorded under -20 V voltage bias.

Along with GaN devices, InGaN based photodetectors are fabricated and characterized. MSM devices based on InGaN devices showed responsivity and dark current levels controlled by In concentration. The resistivity of the films decreased with concentration of In in the semiconductor. Changing the In concentration, bandgap tunability is possible.

References:

[1] A. Krost and A. Dadgar, Phys. State Solidi A 194, 361 (2002).

[2] J. S. Moon, M. Micovic, P. Janke, P. Hashimoto, W. S. Wong, R. D.Widman, L. McCray, A. Kurdoghlian, and C. Nguyen, Electron. Lett. 37, 528 (2001).

[3] S. Nakamura, Y. Harada, and M. Seno, Appl. Phys. Lett. 58, 2021 (1991).

[4] E. J. Tarsa, B. Heying, X. H. Wu, P. Fini, S. P. Den Baars, and J. S. Speck, J. Appl. Phys. 82, 5472 (1997).

Electronic Materials and Processing
Room: 211C - Session EM-ThM

Interconnects II
Moderator: Andy Antonelli, Nanometrics, Sean King, Intel Corporation

8:00am **EM-ThM1 John A. Thornton Memorial Award Lecture - PECVD Low and Ultralow Dielectric Constant Materials: From Invention and Research to Products**, ***Alfred Grill***, IBM Research Division, T.J. Watson Research Center **INVITED**

In April this year we celebrated the 50th anniversary of Moore's law which has been followed by the semiconductor industry together with Dennard's scaling law, resulting in continuously improved performance and increased density of the semiconductor microprocessors. For 22 years this was accomplished using the same material composed of Si, Al, O, N, and shrinking the dimensions of the devices. At the 0.25 mm node, the interconnect became the bottleneck to the improvement of the performance of the VLSI integrated circuits and required the introduction of new materials to reduce its RC. After the replacement of Al with the more conductive Cu in 1997, it took seven more years to replace the SiO_2 insulator (k=4) of the interconnect with a low-k dielectric. While the academia and industry were aware already in the 1990s of the need for a low-k dielectric and many potential materials were developed and investigated, none could be integrated in a VLSI product requiring multiple revisions of the. The early, unsuccessful efforts were focused on polymeric or hybrid organic-inorganic films fabricated by spin-on techniques. Realizing that PECVD materials would have superior properties to those of the spin-ons, we invented, developed and characterized the carbon-doped oxide SiCOH, deposited by PECVD, obtaining a material with a dielectric constant k=3 which was successfully integrated in VLSI products starting at the 90 nm node and became the industry standard as the interconnect dielectric. This development has continued with the invention of porous pSiCOH ultralow-k (ULK) dielectrics with further reduced k values. pSiCOH with k as low as ~2 was demonstrated in research lab and a materials with k=2.4 was successfully implemented in products at the 45 nm node, to maintain a reduced capacitance for the scaled dimensions of the shrunken technology nodes.

The talk will discuss the development and optimization of the PECVD SiCOH and pSiCOH dielectrics, integration issues related to these materials of reduced mechanical and chemical properties compared to SiO_2, understanding the correlation between process parameters, dielectric characteristics and the reliability of the integrated interconnect, and the current state of the art of the interconnect dielectrics which enabled the continuation of Moore's law into nanoscale dimensions.

8:40am **EM-ThM3 Moving Across the Periodic Table: Amorphous Hydrogenated Boron Carbide for Low-*k* Dielectric Applications**, ***Michelle Paquette***, *B.J. Nordell, T.D. Nguyen, S.S. Purohit, A.N. Caruso,* University of Missouri-Kansas City*, W.A. Lanford,* University at Albany-SUNY*, P. Henry, S.W. King*, Intel Corporation

A major challenge facing the semiconductor industry is the development of new low-dielectric-constant (low-*k*) materials for metal interconnects to mitigate the issues surrounding resistance–capacitance (RC) delays as dimensionality is reduced. Such materials include not only bulk inter-/intra-layer dielectrics (ILDs), but also more specialized layers such as Cu diffusion barriers, etch stop layers, and hard masks. Traditional materials for these purposes have been derived from the Si family; however, it is becoming increasingly challenging to tailor these to meet all of the integration requirements, particularly maintaining mechanical and chemical resilience as *k* is lowered. Toward this end, amorphous hydrogenated boron carbide (a-$B_xC:H_y$) is an intriguing alternative. Amorphous $B_xC:H_y$ is a unique solid based on six-coordinate icosahedral 'molecular' units. As a semi-insulating low-density solid with one of the lowest possible average atomic numbers, Z (H = 1, B = 5, C = 6), a-$B_xC:H_y$ is expected to feature a low dielectric constant, while also inheriting the appealing properties of crystalline BC, which include extreme hardness, as well as thermal and chemical robustness. We describe novel a-$B_xC:H_y$ materials for low-*k* ILD, diffusion barrier, and etch stop applications with dielectric constant (<3.5), leakage current ($<10^{-8}$ A/cm^2 at 2 MV/cm), and mechanical properties (Young's modulus >100 GPa) that meet or surpass those of Si-based materials currently being used for these applications. We further explore some of the fundamental similarities and differences between Si- and BC-based classes of materials.

9:00am **EM-ThM4 Enhancing Mechanical and Fracture Properties of ULK Materials with Filled Pores**, *S.G. Isaacson,* Stanford University*, K. Lionti, W. Volksen, T.P. Magbitang,* IBM Almaden Research Center*, **Reinhold Dauskardt**,* Stanford University*, G. Dubois*, IBM Almaden Research Center

Pore filling has emerged as a promising strategy for the protection of ultra-low-k dielectrics (ULK) against plasma-induced damage [1-3]. In this work we use polymers with a wide range of molecular weights (10^3 – 10^6 g/mol) to create filled ULK materials, leading to uniform penetration, a high level of fill (~100%), and confinement of polymer chains to dimensions far smaller than their bulk radius of gyration. This confinement alters the conformations and inter-molecular interactions of the polymer phase, resulting in novel fracture behavior that has important implications for the reliability of pore-filled ULK materials.

Despite its promise as a processing technique, the effects of pore filling on the mechanical properties, fracture strength, and reliability of these backfilled ULK materials remain poorly understood. We show that the mechanical and fracture properties of a nanoporous ULK matrix can be considerably improved by filling the porosity with a polymeric second phase. Importantly, the degree of toughening increases significantly with the polymer molecular weight, and is also found to depend on processing conditions. We show that the mechanism for toughening is based on the pullout of individual confined polymer chains from the ULK matrix, distinct from the more common entanglement-based mechanisms seen in bulk polymers. This mechanism is quantified with a model that describes the nanomechanical processes occurring on the length scale of individual pores.

Nanoindentation measurements demonstrate that pore filling with confined polymers also improves mechanical properties such as Young's modulus and hardness. Furthermore, we present subcritical crack growth measurements that highlight the mixed effects of pore filling on the moisture-assisted cracking of ULK materials. This study provides new insight into the mechanical behavior of pore-filled ULK materials and suggests potential routes for increasing the cohesive strength of materials where the traditional bulk toughening mechanisms may be absent.

[1] T. Frot, W. Volksen, S. Purushothaman, R. Bruce, G. Dubois, Adv. Mater. 2011, 23, 2828-32.

[2] T. Frot, W. Volksen, S. Purushothaman, RL. Bruce, T. Magbitang, DC Miller, VR. Deline, G. Dubois, Adv. Funct. Mater. 2012, 22, 3043-3050.

[3] W. Volksen, K. Lionti, T. Magbitang, G. Dubois, Scripta Mater., 2014, 74, 19-24.

9:20am **EM-ThM5 Status Update on a New Class of Solution Processable Low-k Dielectric Coatings for Use as ILD with K < 2.4**, ***Hash Pakbaz****, N. Hacker,* SBA Materials*, Z. Tokei, M. Baklanov*, IMEC, KU Leuven Belgium **INVITED**

Liquid Phase Self Assembly (LPSA) is used as a unique approach to create porous carbon-doped SiOx solution processable coatings. In this approach, self assembling organic template, in a solution consisting of various silanes

and other additives, form nano-particles. These nano-particles are the basis for pore formation in the final coated film where-by to minimize the over-all energy of the system, the nano-particles tend to maximize their respective distances in solution and during the coating process. Thin films are coated using spin coating and the templates are removed by thermal curing or UV curing the coated film without pore collapse. This leads to formation of “ordered” porous coatings where pore overlap does not occur until high levels of porosity (> 60%) are introduced. As a result, low-k dielectric coatings with k values below 2.0 can be achieved with excellent mechanical properties. In this paper, fundamental properties of LPSA low-k dielectric, integration results in advanced node BEOL dual-damascene structures as well as solution storage lifetime consistent with meeting requirements for production are presented.

11:00am **EM-ThM10 The Effect of Vacuum Ultraviolet Irradiation on TDDB of Low-K Dielectrics using Synchrotron Radiation**,
Dongfei Pei, *M. Nichols,* University of Wisconsin-Madison*, S.W. King, J. Clarke,* Intel Corporation*, Y. Nishi,* Stanford University*, J.L. Shohet*, University of Wisconsin-Madison

Time-dependent dielectric breakdown (TDDB) is a major concern for low-k dielectrics. Plasma processing, which involves ion bombardment and vacuum ultraviolet (VUV) irradiation, has been shown to cause TDDB degradation of low-k dielectrics. [i] Synchrotron radiation provides high-intensity monochromatic VUV photons with continuous variable wavelength. In this work, synchrotron irradiation between 5 and 20 eV was used to simulate VUV photon irradiation from a plasma without any particle flux. In this work porous organosilicate glass (SiCOH) was irradiated. A Cu / capping layer / SiCOH / titanium stack structure was fabricated so as to analyze the TDDB lifetime of both pristine and VUV-irradiated dielectrics. The photon flux varies with the wavelength so the irradiation time was chosen to produce the same amount of photon fluence at each photon energy. VUV photon energies larger than 7eV were found to create damage to porous SiCOH and cause TDDB degradation. With a photon fluence of 10^{16} photons/cm^2, VUV photons with higher energies tend to cause more TDDB degradation.

This work was supported by the Semiconductor Research Corporation under Contract No. 2012-KJ-2359 and by the National Science Foundation under Grant CBET-1066231.

---

[i] M. T. Nichols, H. Sinha, C. A. Wiltbank, G. A. Antonelli,Y. Nishi, and J. L. Shohet, *Appl. Phys. Lett* **100**, 112905 (2012)

11:20am **EM-ThM11 Influence of Porosity on VUV Induced Damage to Low-K Dielectrics**,
Faraz Choudhury*,* University of Wisconsin-Madison*, J.-F. de Marneffe, M. Baklanov,* IMEC, Belgium*, S.W. King,* Intel Corporation*, Y. Nishi,* Stanford University*, J.L. Shohet*, University of Wisconsin-Madison

During various stages of plasma processing, low-k dielectrics are exposed to high levels of VUV radiation emitted from the plasma. Modern ultra-low-k materials have interconnected pores within the dielectric layer that make them susceptible to damage due to their low density and deep penetration of active species into the film. In this work, VUV induced degradation of low-k dielectrics as a function of porosity is investigated. Organosilicate low-k films of porosities between 15% (k=2.7) and 50% (k=1.9) were exposed to synchrotron VUV radiation with energies ranging from 6 -12eV. Both electrical and chemical properties of the films were analyzed to find the most damaging spectral region. FTIR spectra showed increased depletion of the methyl group after VUV irradiation as a function of film porosity and CV measurements showed an increase in the dielectric constant along with a flat-band voltage shift. IV characteristics of the VUV irradiated porous films indicated an increase in leakage currents and lower breakdown voltage. The degree of damage is higher for the more porous films indicating that the introduction of pores deteriorate the electrical properties of the low-k films. The higher leakage currents in the more porous films were attributed to more porogen residues within the dielectric layer. To remove the porogen residues, the films are treated with hydrogen downstream plasma at 300° C. FTIR measurements confirm removal of porogen residues and leakage currents are significantly reduced after the hydrogen-annealing process.

This work has been supported by the Semiconductor Research Corporation under Contract No. 2012-KJ-2359 and the National Science Foundation under Grant No. CBET-1066231.

References

[1] K. Maex, M.R. Baklanov, D. Shamiryan, F. Iacopi, S.H. Brongersma, and Z.S. Yanovitskaya, *J. Appl. Phys.* **93,** 8793 (2003)

11:40am **EM-ThM12 An Electron Paramagnetic Resonance Study of Processing Effects in Porous Low-κ Dielectrics**,
Michael Mutch*, P.M. Lenahan,* Pennsylvania State University*, S.W. King*, Intel Corporation

We utilize electron paramagnetic resonance (EPR) to study defects in porous, low-κ SiOC:H powders as a function of processing parameters. The powders were generated by mechanically removing the SiOC:H films from sililcon substrates. The SiOC:H powders studied have previously been investigated after remote hydrogen plasma (RP) and UV cures.[1] To better understand the role of RP and UV curing on defect chemistry, we utilize EPR measurements at each processing step.

First, EPR measurements were performed on a an SiOC:H powder before and after UV treatment. Prior to UV treatment, a spectrum with a zero-crossing *g* of 2.0027 with a line width of 4.5 Gauss is detected. The measured defect concentration prior to UV treatment is about 3x10^{15} cm^{-3}. The zero-crossing *g* suggests a carbon dangling bond defect. Post UV treatment, a carbon dangling bond spectrum is detected with a corresponding defect concentration of 2.1x10^{17} cm^{-3}.[1] The large increase in carbon dangling bond concentration post UV anneal suggests an incomplete removal of the sacrificial porogen resulting in carbon dangling bond defects.

Second, an SiOC:H powder is studied before and after remote hydrogen plasma (RP) and UV treatments. Via fast passage EPR, two overlaying signals are detected prior to RP and UV cures. The two signals are identical in line width and zero-crossing *g* to spectra which have been provisionally attributed to two carbon dangling bond centers termed Cdb1 and Cdb2 by Pomorski et al.[1] Pre RP and UV cure, the measured defect concentrations of Cdb1 and Cdb2 are 2.1x10^{17} cm^{-3} and 2x10^{15} cm^{3}, respectively. Post RP (but prior to UV treatment), the Cdb2 signature is detected and has a defect concentration of 1.8x10^{15} cm^{-3}. The Cdb1 signature, is not detected. This suggests that the hydrogenation of these films via RP is successful in removing some carbon dangling bonds. Post RP and UV cure, a defect with a line width of 11 Gauss and a zero-crossing *g* of 2.0028 is detected at a concentration of 5x10^{17} cm^{-3}.[1] The post UV processed zero-crossing *g* close to that of the free-electron *g* suggests the presence of carbon dangling bond defects. Again, we tentatively attribute these defects to an incomplete removal of sacrificial porogens from the films.

[1] T. A. Pomorski et al., J. Appl. Phys. **115**, 234508 (2014).

12:00pm **EM-ThM13 The Effects of VUV Radiation on Low-k Organosilicate Glass (SiCOH) as Measured with Electron-Spin Resonance**,
Panpan Xue*, H. Zheng, W. Li,* University of Wisconsin-Madison*, J.-F. de Marneffe,* IMEC*, M. Baklanov,* IMEC, Belgium*, V. Afanas'ev,* Catholic University of Leuven, Belgium*, Y. Nishi,* Stanford University*, J.L. Shohet*, University of Wisconsin-Madison

Here, we investigate the effects of VUV radiation on the defect concentrations in SiCOH. Electron-spin resonance (ESR) spectroscopy is a very effective tool to detect defects in dielectrics. It has been used on various high-k dielectrics, such as HfO_2[1]. In this work, in order to obtain a clear spectroscopic signal, 60nm SiCOH (k=2.4) was deposited on high-resistivity (3000 Ω-cm) wafers. There are at least two kinds of detectable defects in SiCOH: Si dangling bonds (g=2.0054) and Oxygen vacancy (g=2.002). In this work, we concentrate on the silicon dangling bond defects. In order to eliminate dangling bonds from the silicon substrate as well as its edges, CP4 [2] and HF treatments were used. The samples were treated in three ways before ESR (1) CP4 etch that removes surface and edge damage but leaves the SiCOH on the sample. (2) CP4 followed by an HF etch to remove the SiCOH. (3) same as method (2) except here the SiCOH is covered with wax so the HF only etches bare silicon including its edges. Method 3 passivates dangling bonds on the Si surface so any remaining signal should only from the SiCOH. The measurements showed that the sample with SiCOH remaining (method 3) has roughly 1.6 times the number of Si dangling bonds compared with bare Si. In addition, samples having the same edge areas but smaller surface areas were seen to have fewer defects. This shows that the defects measured with ESR are actually from the SiCOH layer but not the edges of the sample. In order to investigate the influence of VUV radiation, the samples were exposed to synchrotron radiation with photon energies of 12 eV for both 10 and 40 minutes. The ESR measurements showed that the defect concentration increased after 10 minutes of VUV exposure and kept increasing with longer VUV exposure times.This is consistent with the fact that the energy threshold for Si-H bond photolysis at the surface of H-passivated Si is ~7.9 eV[3].The ESR signals have a Lorentzian shape and the Bloch model [4] fits these well. We conclude that silicon dangling bond defects in SiCOH and its interface with silicon can be detected using ESR and that VUV exposure increases the defect concentration.

Work supported by the Semiconductor Research Corporation under Contract No. 2012-KJ-2359 and the National Science Foundation under Grant No. CBET-1066231.

[1] H. Ren, S. L. Cheng, Y. Nishi, and J. L. Shohet, *Applied Physics Letters*, **96** 192904 (2010)

[2] ANU Centre for Sustainable Energy Systems (CSES), "HNA (HF:Nitric:Acetic) Etch - Full Procedure (also known as 'CP4 Etch')" (2009)

[3] A. Pusel, U. Wetterauer, and P. Hess, *Phys. Rev. Lett.* **81**, 645 (1998)

[4] SC Agarwal, *Physical Review B*, **7** 685 (1973)

Selective Deposition as an Enabler of Self-Alignment Focus Topic
Room: 210F - Session SD+AS+EM-ThM

Fundamentals of Selective Deposition
Moderator: Scott Clendenning, Intel Corporation, Suvi Haukka, ASM Microchemistry Ltd., Finland

8:00am **SD+AS+EM-ThM1 Fundamental Examinations of Surface Chemistry-Driven Approaches to Selective Area Atomic Layer Deposition**, *W. Zhang, J.-R. Chen,* ***James Engstrom***, Cornell University

Most approaches taken to date concerning selective area growth have involved the use of masking layers consisting of photoresists or self-assembled monolayers (SAMs). While some success has been achieved with this approach there are a number of disadvantages intrinsic to these methods. First, SAMs are very difficult to form defect free, and second, and perhaps more important, these masking layers themselves must be patterned or deposited selectively. A second approach to selective area ALD relies on intrinsic reactivity differences between exposed surfaces, which, unfortunately, may be limited to a few special cases. Here we seek to develop a more general approach to achieving selective area growth. We initially focus on the first half-cycle of ALD, where demonstrating selectivity for this part of the ALD process is a necessary, but not sufficient condition for selective area growth. We are examining two specific approaches to the surface chemistry: (*i*) the use of adsorption reversal agents; and (*ii*) the use of molecular blocking agents. Here for a thin film precursor we examine transition metal complexes with the generic structure, $M(XR_m)_n$, where M is the transition metal and XR_m is the coordinating ligand. In pursuing strategy (*i*) we examine the introduction of a second species in the first half-cycle that can act as a coordinating ligand, e.g., HXR'_m, or $HXR'_{m-1}R''$, etc. In pursuing strategy (*ii*) species (Y) are selected that can effectively compete for adsorption sites, dependent on the composition of the substrate. Concerning strategy (*i*) we are currently investigating reactions between transition metal amido compounds and a series of amines ($X = N$). We have found a somewhat unexpected result for this chemistry: the partial pressure of H_2NR' produces similar effects on both a metal (Cu) and a dielectric (SiO_2) surface, where a low partial pressure attenuates the irreversible adsorption of the thin film precursor, while a high partial pressure results in no adsorption of the precursor. An investigation of the reactions between the thin film precursor and a molecular blocking agent with the structure HSR'', gave much more encouraging results. Here we found complete blockage of chemisorption of the thin film precursor on a Cu surface, whereas on SiO_2 the molecular blocking agent had no effect on the adsorption of the metal for the first half-cycle. We will conclude this presentation with a discussion of the mechanisms that are likely operative in both cases, making use of *in situ* measurements involving X-ray photoelectron spectroscopy, and also initial results concerning the effectiveness of this approach for multiple (5-20) cycles of ALD.

8:20am **SD+AS+EM-ThM2 Mechanistic Understanding of Surface-Selective Chemical Vapor Deposition of Copper Films Using a Molecular Inhibitor**, ***Elham Mohimi****, S. Babar, B. Trinh, G.S. Girolami, J.R. Abelson*, University of Illinois at Urbana Champaign

Surface-selective chemical vapor deposition of thin films can enable the fabrication of nanoscale devices by eliminating difficult patterning and etching steps. However, stray nucleation of film on the non-growth surface due to defect or impurity sites remains a challenging problem. We previously demonstrated the use of molecular growth inhibitors in copper CVD to control morphology, ranging from a smooth and continuous thin film to particles in a narrow size distribution. Here, we show that an inhibitor can also be used to afford essentially perfect selective growth. Addition of vinyltrimethylsilane (VTMS) molecules during copper CVD from the Cu(hfac)VTMS precursor reduces the growth rate of copper on copper by a factor of four, but reduces the Cu deposition on thermal SiO_2 or porous carbon doped SiO_2 to below one monolayer (area averaged). In-situ FTIR and mass spectroscopy show that the VTMS undergoes associative desorption with adsorbed Cu(hfac) intermediate on the non-growth surface, and is responsible for the surface selective deposition of copper only on the intended (metallic) substrate areas. The processing window for this method is wide in terms of VTMS pressures (> 1 mTorr), growth times (1-90 min), and substrate temperature (100-180°C).

8:40am **SD+AS+EM-ThM3 Selective Deposition of Copper-Manganese Alloy for Interconnects**, ***Roy Gordon***, Harvard University **INVITED**

As copper interconnections are made smaller, they fail more easily by electromigration. The dominant pathway for motion of Cu atoms is along the interfaces between Cu and the surrounding insulator surfaces. In current technology, a tantalum nitride diffusion barrier and a Ta or Co adhesion layer are placed between Cu and the insulators. Because these layers are more resistive than Cu, the composite interconnect line has a higher resistance than one that would consist entirely of pure Cu. Here we describe how selective placement of manganese within the insulator surface can provide the necessary stabilization, adhesion and barrier properties for Cu lines without the resistance penalty of TaN/(Ta or Co) layers. After trenches and vias are etched into the insulator, CVD is first used to deposit a thin layer of manganese nitride conformally on all exposed surfaces of the insulator as well as on the Cu exposed at the bottoms of the vias. Then less than a monolayer of iodine is chemisorbed onto the MnN_x from ethyl iodide vapor. Next, this iodine catalyzes selective, bottom-up CVD of Cu-Mn alloy so that it fills even the narrowest trenches and vias without any voids or seams at the centerlines. The iodine "floats" on the growing surface of the Cu, and is finally removed by chemical-mechanical polishing along with the Cu-Mn overburden and the MnN_x on top of the insulator. During subsequent anneals, Mn rapidly diffuses out from the MnN_x and from the Cu-Mn alloy into the near-surface regions of the insulator to form an insulating layer of $MnSi_xO_yN_z$ surrounding the Cu. The necessary Cu adhesion and barrier properties are provided by this insulating layer of $MnSi_xO_yN_z$ selectively placed just inside the surfaces of the insulators. During anneals, Mn and nitrogen originally located on the Cu surfaces at the bottoms of vias disappear as the Mn and N are re-distributed by diffusion to nearby insulator surfaces. The result is direct, low-resistance connection between Cu in vias with Cu in the metallization level below. This selective migration of Mn leaves pure, low-resistance Cu completely filling the entire volume of trenches and vias, providing the lowest possible line resistance. Thus Mn is placed selectively only where it is required to increase adhesion and lifetime before failure by electromigration, to prevent diffusion of Cu into the insulator and to avoid corrosion of Cu by water or oxygen. The same sequence of process steps can apply Cu to the walls of through-silicon-vias to conduct signals from one chip to another. This process can also form Cu seed layers for electrodeposition of Cu-filled vias for distributing power through silicon chips.

9:20am **SD+AS+EM-ThM5 Selective Growth of First Row Transition Metal Films by Atomic Layer Deposition**, ***Charles Winter***, Wayne State University **INVITED**

Our laboratory seeks to develop the growth of metallic first row transition metal thin films using atomic layer deposition (ALD). The microelectronics industry is calling for the growth of metallic first row transition metal films by the ALD method for a variety of applications, including copper metallization, seed layers for copper metallization, copper/manganese alloys for self-forming copper diffusion barriers, and magnetic alloys. The ALD growth of noble metal thin films has been explored extensively in the past ten years, due to the positive electrochemical potentials of these metal ions and relative ease of reduction to the metallic state. The low temperature ALD of high purity, low resistivity Cu films has been described, but ALD routes to the other metallic first row transition metal films remain poorly developed, largely because of the negative electrochemical potentials of most of the ions and a corresponding lack of powerful reducing co-reagents that can convert precursors in positive oxidation states to the metals. We will describe the synthesis, structure, and properties of a large series of new first row transition metal ALD precursors containing alkoxide ligands that combine high volatilities, high thermal stabilities, and high reactivities toward reducing agents. We will also report borane reducing agents that can react with the metal precursors to afford metallic films. Additionally, we will overview the thermal growth of metallic copper, nickel, cobalt, iron, manganese, and chromium thin films from these new precursors. Importantly, the growth of these metals is highly selective for noble metal substrates, such as ruthenium, palladium, and platinum. The noble metal substrates appear to activate the borane reducing agents, thus enabling selective metal growth. Chemical insights into the selective growth will be presented.

11:00am **SD+AS+EM-ThM10 Etching and Chemical Functionalization of Silicon Nitride Surfaces for Selective Deposition**, *L.-H. Liu, T. Peixoto, W. Cabrera, D. Dick, J.-F. Veyan,* University of Texas at Dallas, *D.J. Michalak, R. Hourani,* Intel Corporation, *M.D. Halls,* Schrodinger, Inc., *S.P. Pujar, H. Zuilhof,* Wageningen University, Netherlands, ***Yves J. Chabal***, University of Texas at Dallas

The ability to process silicon nitride and oxide films and chemically functionalize their surfaces by wet chemical methods is critical for selective deposition. The nature of HF-etched silicon nitride surface is complex and somewhat controversial. We have therefore performed an extensive study of HF etching of both Si_3N_4 and SiO_2 surfaces, combining spectroscopic techniques (Infrared absorption, X-ray photoemission, Low energy ion scattering), imaging (atomic force microscopy) and contact angle measurements with first principles calculations, as a function of HF concentration. We have also performed post-treatment in cold and hot water, and chemical functionalization with a range of organic molecules to help determine the chemical nature of the HF-etched surfaces.

The nature of silicon nitride surfaces is complex. We find that immediate rinsing in deionized water after HF wet-chemical etching yields smooth silicon nitride surfaces with clear evidence for Si-F surface termination. Low energy ion scattering experiments and XPS measurement as a function of gentle sputtering with Gas cluster ion beams (GCIB) confirm that the F is all located at the surface (i.e. not distributed into the bulk), and in the form of Si-F with high temperature stability (up to 600 ºC in ultra-high vacuum). Hydrolysis in water is very slow at room temperature, but can be achieved at high temperature (~90 % removal at 70 ºC for 30 min). However, water is found to etch silicon nitride, as evidence by a loss of Si_3N_4 phonon absorption, suggesting that the removal of the surface fluorine may not only be due to surface reaction through a direct exchange mechanism via pentavalent Si intermediate, but also to the hydrolyzation of Si_3N_4 itself through back-bond chemical attack by water. In addition to F, we find that there is also surface -NH_2 species, as evidenced by IR active -NH_2 bending modes at 1550 cm^{-1}, which we estimate to be only ~20 % monolayer from analysis of reaction with aldehyde molecules. However, this coverage appears sufficient to protect the Si_3N_4 surface. Finally, LEIS and XPS indicate that there is oxygen at the surface, which could either be in the form of -OH or Si-O-Si. Functionalization with alkylsiloxanes reveals that ~50 % of the surface contains Si-OH. In summary, the sum of the concentrations (50 %, 20 %, 50 % in ML), i.e. exceeding 1 ML, suggests that the etched surface may be atomically rough. Overall, these findings provide a method for selective deposition by using first aldehyde reaction for Si_3N_4 functionalization, followed by silane reaction for SiO_2 functionalization.

11:20am **SD+AS+EM-ThM11 Area Selective Deposition of Ultrathin Magnetic Cobalt Films via Atomic Layer Deposition**, ***John Ekerdt***, *H. Nallan, T. Ngo, S. Chopra, Z. Zhang*, University of Texas at Austin

Ferromagnetic thin films find applications in a variety of fields, such as electronics, spintronics, RF technology, energy, etc. With ever-decreasing device feature sizes, film conformity and crystalline structure become very important to determining magnetic properties. As such, atomic layer deposition (ALD) is a very attractive technique for magnetic film deposition as it ensures atomic level conformity. Since ALD film growth necessarily involves a film nucleation step, it is possible to engineer the surface energy of the substrate to cause preferential wetting and nucleation in only desired areas, resulting in area selective ALD (AS-ALD). Unlike conventional photolithography-based fabrication, a bottom-up patterning approach could eliminate the need for etch steps, reducing the cost of fabrication and overcoming scaling limitations in manufacturing devices. This work investigates the selective deposition of cobalt oxide via ALD that is subsequently reduced to carbon-free cobalt metal for use as the free magnetic layer within the magnetic tunnel junction of spin-transfer torque random access memory.

Alkylchlorosilanes and poly(trimethylsilylstyrene) are utilized to block water and cobalt bis(N-tert butyl, N'-ethylpropionamidinate) from an oxide substrate, such as silicon dioxide, hafnium dioxide and magnesium oxide, ensuring selective deposition of CoO films. Poly(trimethylsilylstyrene) is the half of a lamellar forming diblock copolymer that remains after self-assembly and feature development. The alkylchlorosilanes can be blanket deposited through the vapor phase or stamped onto the oxide surface using a poly(dimethylsiloxane) stamp. Cobalt oxide ALD proceeds on the exposed oxide surface. Strontium and Al are deposited atop the CoO films to scavenge oxygen during thermal annealing to yield cobalt metal films. Alternatively, reducing gases such as CO and H_2 can be employed as an oxygen sink during thermal reduction of CoO to Co metal. Finally, we demonstrate control over the tunability of the coercivity of the resultant films by controlling the reduction conditions.

11:40am **SD+AS+EM-ThM12 Area-Selective Al_2O_3 Pattern Grown by Atomic Layer Deposition**, ***Seunggi Seo***, *H. Jung, I.K. Oh, H. Kim,* Yonsei University, Republic of Korea, *J. Yoon, C. Yoo, H.-J. Kim, Y.-B. Lee*, LG Display Co., Ltd., Republic of Korea

Over many past years, area-selective atomic layer deposition (AS-ALD) has been developed for fabricating 3D nanostructures. ALD is a method to deposit thin films by self-limiting surface reactions between supplied gaseous precursors. Since ALD is a surface sensitive deposition technique, surface modification of substrate renders the deposition of films to be area-selective. Most previous studies on AS-ALD have utilized self-assembled monolayer (SAM), which inhibits the chemical reaction between substrate and precursors, so that the film cannot grow on SAM-coated area. AS-ALD has been studied on various materials, such as TiO_2, ZnO, and HfO_2. Although Al_2O_3 has been widely used for ALD, there is no experimental report on AS-ALD Al_2O_3 by using SAM. Rather, a previous report on the calculation of surface reactions between TMA and SAM by density functional theory (DFT) has been presented[1]. That paper describes that CH -terminated SAM shows no thermodynamic driving force for the reaction between them, leading to AS-ALD Al_2O_3 by using TMA.

In this work, we systematically investigated AS-ALD of Al_2O_3 on SAM in various conditions, such as SAM coating methods, the kinds of SAM and substrate, and ALD process parameters. Addressing previous calculation report, Al_2O_3 was deposited on CH_3-terminated SAM, octadecyltrichlorosilane (ODTS) and octadecylphosphonic acid (ODPA).

However, we observed Al_2O_3 layers were formed on SAM coated SiO_2 and Ti substrate, which is inconsistent with previous report. To clarify, we investigated ALD Al_2O_3 on SAM coated substrate by using various analytic techniques such as contact angle measurement, Fourier transform infrared spectroscopy, ellipsometry, X-ray photoelectron spectroscopy (XPS), X-ray-reflectometry (XRR), and α-scanning. We observed TMA was physisorbed on CH_3-terminated SAM, leading to Al_2O_3 deposition. Alternatively, we moved to our research toward the change of SAM coating methods, dipping and stamping, to lift both Al_2O_3 and underneath SAM coating off. Since stamping method is a faster process than dipping one, so that SAM by stamping might remain randomly distributed as forming weak bonding between SAMs and substrate. Moreover, we chose ODPA as a SAM due to its poor adsorption on SiO_2. We observed that both Al_2O_3 and its underneath ODPA stamped on SiO_2 were lifted-off from the substrate, resulting in area-selective Al_2O_3 pattern. This result opens a new way to patterning techniques for many areas of technology.

[1] Xu et al./ Chem. Mater. 2004, 16, 646-653

Surface Science
Room: 113 - Session SS+AS+EM+EN-ThM

Semiconductor Surfaces and Interfaces - I
Moderator: Yves J. Chabal, University of Texas at Dallas

8:00am **SS+AS+EM+EN-ThM1 Reaction of 1,2,3-Benzenetriol with the Ge(100)-2x1 Surface**, ***Tania Sandoval***, *S.F. Bent*, Stanford University

Functionalization of semiconductor surfaces can provide tunable control of interfacial properties in organic-inorganic hybrid devices. In particular, multifunctional molecules have the potential to change the surface chemistry by leaving unreacted functional groups available after adsorption. Understanding the adsorption of these complex molecules could lead to various applications as sensors, selective film deposition, and molecular electronics.

In this work, the reaction of 1,2,3-benzenetriol on Ge(100)-2x1 surface was investigated. While the reaction of hydroxyl groups has been previously studied, differences in selectivity can be expected due to the position of the functional groups along the ring. The purpose of this study is to determine the extent of these differences and the effect on product distribution.

An analysis of the adsorption energetics was carried out by density functional theory. As expected, a proton transfer reaction was shown to be the most stable adsorbate configuration. However, after the adsorbate reacts with the surface through its first OH group, the energetics of the second OH dissociation showed differences based on two factors: (i) surface configuration (cross or diagonal trench and end or cross bridge) and more interestingly (ii) which two of the OH groups (1 and 2 or 1 and 3) are reacting with Ge. The latter constraint affects the adsorption energy of the second dissociation, where adsorption regardless of the surface configuration is less stable when the OH groups are next to each other. Finally, transition states for dissociation of the third OH were found to be limited by the configuration of the second dissociation, and in some cases were not possible to find without unrealistic distortions of the molecule.

Chemisorbed and physisorbed O(1s) and C(1s) spectra were obtained by X-ray photoelectron spectra. Differences between these spectra can be used to identify the reaction products. No change in the C(1s) spectra was observed, suggesting that no carbon forms a bond directly with the Ge surface. On the other hand, clear differences between the chemisorbed and physisorbed O(1s) spectra are observed. The presence of a second peak with a lower binding energy only in the chemisorbed spectra, assigned to oxygen bonded to Ge, confirms that 1,2,3-benzenetriol reacts with the Ge surface through OH dissociation. Quantitative analysis of the chemisorbed O(1s) spectra provides information on the fraction of OH groups reacting with the surface. Interestingly, about 66% of the total hydroxyl groups in 1,2,3-benzenetriol are involved in reaction with Ge, indicating that there is a significant fraction of unreacted OH groups.

8:20am **SS+AS+EM+EN-ThM2 Ethylenediamine Grafting on Oxide-free H-, F-, and Cl- terminated Si(111) Surfaces***, **Tatiana P. Chopra****, R.C. Longo, K.J. Cho,* University of Texas at Dallas*, M.D. Halls,* Schrodinger, Inc.*, P. Thissen,* Karlsruhe Institute of Technology, Germany*, Y.J. Chabal*, University of Texas at Dallas

Amine termination of surfaces constitutes a core platform for fields as diverse as microelectronics and bioengineering, and for nanotechnology in general. Diamines are particularly attractive for surface amination because, unlike ammonia or simple amine molecules, they have a metal chelating capability useful in fabricating heterostructures. They can act as a linker molecule between inorganic electronic materials and biomolecules or photoactive quantum dots for applications in microlectronic, photonics and biosensing. Most work in the field utilizes self-assembled monolayers (SAMs) on oxidized substrates to present an amine termination of the surface. However, grafting on oxides through silanes or phosphonates is not robust. Moreover, several applications require as short a distance between the substrate and the amine group, which is hindered by the thickness of the oxide. Therefore, diamine grafting directly on oxide-free substrates is important, yet remains unexplored.

In this work, the attachment of liquid and vapor-phase ethylenediamine on three types of oxide-free (H-, F- and Cl-terminated) Si(111) surfaces is examined by infrared absorption spectroscopy and X-ray photoelectron spectroscopy in conjunction with first-principles calculations. We find that chemisorption is only possible on F- and Cl-terminated Si surfaces, with H-terminated Si surfaces yielding only physisorbed diamine molecules. On Cl-terminated Si surfaces, diamines adsorb in a mixture of monodentate and bridging configurations (chemical reaction of both amine endgroups), while on partially F-terminated Si surfaces the adsorption occurs primarily at one end of the molecule. The reaction of ethylenediamine with Cl-terminated Si surfaces is also characterized by complete removal of Cl and partial Si-H (~25% ML) formation on the surface. This unexpected result suggests that a proton-chlorine exchange may take place, with the endothermic barrier possibly reduced via a silicon lattice assisted process after an initial attachment of ethylenediamine to the surface.

8:40am **SS+AS+EM+EN-ThM3 Reaction of Phenylhydrazine with Cl-Si(111) Surface by Wet Chemistry and with Clean Silicon Surface in UHV***, A.V. Teplyakov,* ***Fei Gao***, University of Delaware

The monolayer coatings with aromatic functional groups can be used to tune mechanical, electronic, and chemical properties of semiconductor surfaces. This work focuses on obtaining well-defined surface of silicon functionalized with phenylhydrazine to produce an oxygen-free platform for further functionalization. Single crystalline Si(111) surface has been prepared using modified RCA procedure to produce well-ordered H-Si(111) surface. Next, Cl-terminated Si(111) surface is prepared from H-terminated Si(111) surface using PCl_5 in chlorobenzene solvent with trace amount of benzoyl peroxide as a reaction initiator under nitrogen atmosphere following previously established procedures. Phenylhydrazine-functionalized Si(111) sample is obtained from Cl-Si (111) surface with phenylhydrazine at 38^oC under N_2 atmosphere. To confirm the presence of Si-N bonds following this procedure, establish the structures of surface species produced and to investigate the oxidation mechanism, we followed the reaction by Fourier-transform infrared spectroscopy, X-ray photoelectron spectroscopy, and time-of-flight secondary ion mass spectrometry. To study the formation of Si-NH_x groups, this result was compared with the results of phenylhydrazine reactions on clean silicon surface under ultra-high vacuum (UHV) conditions. Density functional theory (DFT) calculations were performed to infer the mechanisms of surface reactions and further oxidation steps, and to compare the predicted vibrational spectra and core-level energies with the results of experimental studies.

9:00am **SS+AS+EM+EN-ThM4 Anomalously Low Surface Recombination Velocity for Fluorine Terminated Nanopatterned Si Surfaces***, W.N. Peng,* ***Jonghan Park****, L.-H. Liu, R.C. Longo,* University of Texas at Dallas*, D.J. Michalak,* Intel Corporation*, D.M. Pak, Y.J. Lee, J.X. Hsu, K.J. Cho, Y.J. Chabal*, University of Texas at Dallas

Recently, oxide-free and partially methoxy-terminated Si surfaces[1] have been developed as a novel platform for surface reactions because of their superior reactivity compared to hydrogen termination[2]. As a result, strong polar bonds such as Si-F could be stabilized on these surfaces. Since the electrical quality is critical for many applications (i.e. surface defects can degrade the device performance), we performed contactless surface recombination velocity measurements to examine the electronic quality of partially covered surfaces. Interestingly, we found that the carrier lifetime is significantly increased after fluorine termination, with the carrier lifetime 10 times higher than that of hydrogen terminated Si surfaces, approaching 1.5 ms. This anomalously long carrier lifetime can be explained either by a better surface passivation or by surface band bending effects. We therefore performed UPS and kelvin probe measurements to investigate the band structure of these surfaces after fluorine termination and found evidence for band bending. A potential model of a surface dipole layer induced band bending is supported by DFT calculations. Regardless of the mechanism controlling the recombination time, this method is well suited to explore the fluorination mechanism of H-terminated surfaces.

[1] D. Michalak, S. Amy, D. Aureau, M. Dai, A. Esteve, and Y. J. Chabal, *Nature Materials*, **9**, (2010)

[2] P. Thissen, T. Peixoto, R. Longo, W. Peng, W. Schmidt, K. Cho, and Y.J. Chabal, *JACS*, **134** (2012)

9:20am **SS+AS+EM+EN-ThM5 Molecular Functionalization of Semiconductor Surfaces: From Single Crystals to Quantum Dots***,* ***Stacey Bent***, Stanford University **INVITED**

Because the surfaces of small structures can dominate their properties, implementing functional nanoscale materials depends to a large extent upon understanding and controlling the surface reactivity. This talk will focus on studies of the adsorption of organic molecules at semiconductor surfaces, toward the ultimate goal of controlling the chemical and electrical properties of the substrate. We will describe model studies of molecular functionalization on both flat and nanostructured surfaces. The presentation will begin by examining adsorption on the Ge(100)-2×1 surface. Using a combination of experimental (infrared spectroscopy, X-ray photoelectron spectroscopy) and theoretical (density functional theory calculation, Monte Carlo simulation) methods, we will show how the molecular structure as well as the identity of the reactive moieties of organic molecules can affect the product distribution upon adsorption. We will then present results of a study in which the organic ligands bonded to semiconductor quantum dots (QDs) are used to tune the electronic properties of the QDs. We will describe experimental and theoretical studies of the effects of such interface engineering on the band gap and relative band positions in lead sulfide (PbS) QDs. These ligand-exchanged quantum dots are tested in multilayer colloidal QD solar cells, and the results show that molecular functionalization can be used to achieve enhanced photogenerated carrier collection in the devices.

11:00am **SS+AS+EM+EN-ThM10 Periodic Trends in the Hydrogen Elimination Thermal Decomposition Reaction on Si(100)-2×1: Linear and Branched Alkyl Halides, Alcohols, and Amines***,* ***Andrew Pohlman****, K.L. Romolino, N.J. Burgener, S.M. Casey*, University of Nevada

The hydrogen elimination thermal decomposition reaction was studied on the Si(100)-2×1 surface using temperature programmed desorption mass spectrometry (TPDMS) and electronic structure methods for a selection of linear and branched alkyl halides, alcohols, and primary amines. Desorption activation energies and pre-exponential factors were determined using several analysis techniques from TPDMS spectra and compared to calculations based on ab initio canonical transition state theory using density functional theory (DFT). Values for activation energies and pre-exponential factors for dissociative desorption are compared within an adsorbate class based on a varying ratio of available alpha:beta:gamma hydrogens for elimination. Kinetic parameters are also compared between classes of adsorbates for general structure-activity periodic trends. TPDMS experiments reveal desorbing masses consistent with hydrogen elimination in all cases; however, the different elimination channels remain convoluted. Rate constants for each desorption channel were calculated using DFT and used to determine branching ratios for each dissociative desorption reaction. Reaction barrier trends are consistent with previous reports; however, numerical values were found to be much lower when considering inter-dimer reaction mechanisms.

*** Morton S. Traum Award Finalist**

11:20am **SS+AS+EM+EN-ThM11 Diffusion of Arsenic Oxides During the Atomic Layer Deposition of Metal Oxide Films on GaAs(100) Surfaces**, ***Alex Henegar***, *T. Gougousi*, University of Maryland, Baltimore County

It is known that native oxides of III-V semiconductors are consumed during atomic layer deposition using certain subsets of precursors. It was believed these surface oxides were completely removed during the first few deposition cycles because once the surface was covered by a coalesced film the native oxides would be protected. It has been observed, however, that native oxide consumption in systems such as ALD TiO_2 on GaAs(100) and InAs(100) proceeds continuously well after the surface is completely covered. Therefore there must be a transport mechanism that continuously moves these oxides through the developing film in order to interact with the precursor at the surface and be removed.

The aim of this work was to find unequivocal evidence of the transport mechanism needed for continuous oxide removal during ALD at typical processing conditions. ALD processes using metal organics and H_2O were used to deposit TiO_2, Al_2O_3 and HfO_2 films on GaAs(100). The experiments were designed so as to decouple the native oxide consumption from the native oxide transport and provide convincing evidence for the existence of this unacknowledged thus far mechanism. We will provide results that solidify the hypothesis that native oxide diffusion is a critical component in the complete and continuous removal of the interfacial layer.

11:40am **SS+AS+EM+EN-ThM12 Ultrafast Non-Equilibrium Effects in Ti Overlayers on P-Type GaAs(100) Investigated by Femtosecond XUV Photoemission Spectroscopy**, ***Mihai E. Vaida***, University of California, Berkeley, *S.R. Leone*, University of California, Berkeley and Lawrence Berkeley National Laboratory

Time resolution, surface sensitivity and element specificity are technical ingredients required to investigate ultrafast photoinduced processes and charge localization at semiconductor surfaces. All these requirements are fulfilled by a new experimental apparatus that consists of a tunable femtosecond high harmonics XUV source, a pump-probe setup, and an ultra-high vacuum surface science chamber for surface preparation and investigation.

The present contribution focuses on the charge carrier dynamics at the surface of a bare p-type GaAs(100) as well as Ti overlayers on p-type GaAs(100). The charge transfer between the bulk and the surface of the bare GaAs(100) is produced by the pump laser pulse at the central wavelength of 800 nm and is investigated by monitoring the surface photovoltage through the shift of the Ga 3d photoemission peak with the XUV probe laser pulse as a function of the pump-probe time delay. A transient shift of the Ga 3d photoemission peak to lower binding energy at early pump-probe time delay, with a magnitude of 0.3 eV, is observed and is attributed to transport of the electrons from the bulk to the surface. Upon increasing the pump-probe time delay, a restoration of the Ga 3d peak is observed, which corresponds to the recombination of the positive and negative carriers.

When a Ti overlayer is deposited on the p-type GaAs(100) surface, a Schottky diode is formed. If the 800 nm pump laser pulse has sufficient intensity to produce a photoemission process via multi-photon excitation, non-equilibrium effects occur at the Ti-GaAs interface independently from the presence of the surface photovoltage. In this case, positive charges accumulate at the surface and are not effectively screened by the electrons coming from the bulk, and the Schottky diode is transiently driven into a reversed bias mode. The formation of the reverse bias Schottky diode, which is studied in real time with the XUV probe laser pulse by monitoring the Ti Fermi level photoemission shift as a function of the pump-probe time delay will be presented and discussed.

12:00pm **SS+AS+EM+EN-ThM13 Improving the Quality of p-type AlGaN Layers by Reactive-ion Etching**, ***Joy McNamara***, *K.L. Phumisithikul, A.A. Baski, M.A. Reshchikov,* Virginia Commonwealth University, *J. Marini, F. Shahedipour-Sandvik*, SUNY Polytechnic Institute

AlGaN layers prepared by metal-organic chemical vapor deposition, with varying composition of Al (6 – 17%), were studied using the surface photovoltage (SPV) technique. Previous SPV studies on both *n* and *p*-type GaN allowed us to calculate the value of the surface band bending, by applying a thermionic model to explain the transfer of charges over the near surface barrier in various conditions (air, vacuum, and for a wide range of temperatures, T = 80 – 600 K). [1,2] The band bending was estimated to be 1.0 eV and – 2.0 eV, for *n*-type GaN and *p*-type GaN, respectively. SPV measurements on *p*-type AlGaN layers were expected to have similar behaviors to their *p*-type GaN counterparts. However, numerous measurements showed that this was not the case. The SPV transients (upon turning on or off the excitation source) showed significantly slower transients and smaller values than expected from the thermionic model. Moreover, the restoration of the band bending, as indicated by the restoration of the SPV signal to its dark value, did not occur within a reasonable amount of time. The data could not be fit by the thermionic model, and thus we were unable to calculate the band bending. We attribute the slow transients and lack of restoration to a defective surface region which interferes with thermionic processes. To verify this assumption, the top 40 nm of the AlGaN layer was etched using a reactive-ion etch (RIE). After etching, the SPV behavior exhibited substantially different behavior. Fast transients and close-to-thermionic behavior was recovered. Additionally, the effect of annealing the samples after etching provided even closer values to what is predicted by the thermionic model. From this study, it can be concluded that a defective, near surface region is inhibiting the transfer of holes over the near surface barrier under illumination, and hole trapping may be occurring during restoration. In both cases, this behavior cannot be modeled by theory. Etching removes the defective layer, and reveals a region of presumably higher quality as evidenced by the subsequent thermionic behavior.

[1] M. A. Reshchikov, M. Foussekis, and A. A. Baski. *J. Appl. Phys*. **107**, 113535 (2010).

[2] M. Foussekis, J. D. McNamara, A. A. Baski, and M. A. Reshchikov, *Appl. Phys. Let.***101**, 082104 (2012).

Thin Film
Room: 114 - Session TF+EM+NS+PS+SM-ThM

Plasma ALD and Nano-applications
Moderator: Christophe Vallee, LTM, Univ. Grenoble Alpes, CEA-LETI, Richard Vanfleet, Brigham Young University

8:00am **TF+EM+NS+PS+SM-ThM1 Atomic Layer Deposition of Silicon Dielectrics: Precursors, Processes, and Plasmas**, ***Dennis Hausmann***, Lam Research Corporation **INVITED**

As the dimensions of modern semiconductor devices continue to shrink below the current 14 nm technology node, novel processes for the deposition of highly conformal, low temperature, silicon based dielectrics will be needed for applications that include sidewall spacers, barriers, and patterning layers. Atomic layer deposition (ALD) is an ideal method for achieving the high conformality and has been used in high volume manufacturing (HVM) to deposit high-k dielectric materials (HfO_2, ZrO_2, etc.) for several technology generations. Plasma assisted ALD is the best known method to meet low temperature ($<500^0$C) requirements and is now being used for depositing conformal silicon dielectrics such as silicon oxide (SiO_2) and silicon nitride (Si_3N_4).

In this presentation, we discuss the current state of the art of precursors, plasmas, and process conditions required to deposit conformal silicon dielectrics by plasma ALD. Theoretical and experimental data will be presented in order to explain the observed reaction characteristics for the plasma ALD of silicon oxide (SiO_2), silicon nitride (Si_3N_4), and the lack (so far) of silicon carbide (SiC). Generic to all ALD processes is the high cost of the precursors relative to traditional chemical vapor deposition (CVD); in the case of silicon dielectric ALD, this is exacerbated by the relative low “reactivity to cost ratio” of available silicon precursors. Although plasmas enable low temperature deposition, they pose challenges for achieving isotropic film properties over the complex topography on today’s semiconductor devices.

8:40am **TF+EM+NS+PS+SM-ThM3 ALD Dielectrics for Power Electronics**, ***Veena Misra***, NCSU **INVITED**

Owing to a high critical electric field and high electron mobility, wide band gap materials such as GaN and SiC are being sought for high voltage power electronics applications. In the case of GaN devices, the reliability continues to be a challenge to must be addressed before successful commercialization. In our work, different dielectrics deposited by Atomic Layer Deposition (ALD) have been investigated for improving the threshold voltage stability and dynamic reliability of AlGaN/GaN based MOSHFETs. A novel pulsed-IV-based methodology was developed and demonstrated to be applicable for detecting both shallow and deep traps and implemented on evaluating different high-k and low-k ALD dielectrics. Using physics-based simulation models and experimental data, it was demonstrated that the leakage at the surface of the AlGaN, whether through the passivation dielectric bulk or the dielectric/AlGaN interface, must be minimized to restrict the formation of a “virtual gate” and minimize current collapse. It was also found that an optimal passivation dielectric must create a high density of shallow interface donor traps to quicken the de-trapping of electrons from the “virtual gate” and the recovery of the channel underneath. Combining simulation and experimental results, an optimal set

of ALD dielectrics for a reliable gate stack and access-region passivation regions, respectively, was determined and will be discussed. In the area of SiC devices, low inversion channel mobility, caused high density of interface states (Dit) at SiO2/SiC interface, limits the wide adoption of SiC MOS devices. Atomic Layer Deposition offers key advantages in the area of gate dielectrics such as good film quality, low substrate damage, superior uniformity, precise thickness control, and low process temperature. Additionally, deposited SiO2 enables interface engineering to independently control the interface properties. To enhance the channel mobility and maintain good overall gate dielectric properties, a thin layer of a different dielectric material can be inserted to improve interface properties and high quality deposited SiO2 can be used as the bulk gate dielectric. We have demonstrated a novel interface engineering technique utilizing ultra thin lanthanum silicate (LaSiOx) at the SiC/dielectric interface and ALD SiO2 as the bulk gate dielectric. The lanthanum silicate interface engineering dramatically improves the mobility of 4H-SiC metal oxide semiconductor field effect transistors (MOSFETs) and is attributed to the large driving force of La_2O_3 to react with SiO_2.

9:20am **TF+EM+NS+PS+SM-ThM5 $Pb(Zr_xTi_{1-x})O_3$ Magnetoelectric Tunnel Junctions for Magnetoelectric RAM (MeRAM) Memory Applications**, *D. Chien, X. Li, K. Wong, P. Khalili, K. Wang, **Jane P. Chang***, University of California at Los Angeles

As existing memory systems approach fundamental limitations, ultra-thin uniform conformal PZT films are needed for next-generation ultralow-power voltage-controlled non-volatile magnetoelectric RAM (MeRAM) memory devices. By utilizing the magnetoelectric effect, where an electric field or voltage can be used to control the magnetization switching (instead of current), the writing energy can be reduced, resulting in increased memory density (Amiri, P.K. et al., Journal of Applied Physics, 2013). Previous research has shown that the voltage-controlled magnetic anisotropy (VCMA) effect increases with the capacitance of the stack (Kita, K. et al., Journal of Applied Physics, 2012). Therefore, integrating an ultra-thin PZT film (having a dielectric constant 1-2 orders of magnitudes higher than currently used MgO) into the tunneling oxide layer will enhance the VCMA coefficient, allowing for a lower voltage to switch the magnetization of the free magnetic layer and thus decreasing the write energy.

Using atomic layer deposition (ALD), a surface-reaction controlled process based on alternating self-limiting surface reactions, an ultra-thin film of PZT can be synthesized with precise control of the film thickness and elemental composition (Zr/Ti = 52/48). ALD PZT thin films were synthesized by depositing alternating layers of PbO, ZrO_2, and TiO_2 layers using $Pb(TMHD)_2$, $Zr(TMHD)_4$, and $Ti(O{\cdot}i\text{-}Pr)_2(TMHD)_2$ as metal precursors and H_2O as the oxidant. The number of local cycles and global cycles were regulated to achieve the desired stoichiometry and thickness, respectively. The bottom layers of Ta/CoFeB (free magnetic layer)/MgO were sputtered, the PZT film with thickness of 1.7 nm was deposited by ALD, the top layers of MgO/CoFeB (fixed magnetic layer)/Ta/Pt were sputtered, and the entire stack was annealed at 200ºC for 30 minutes in order to fabricate PZT magnetoelectric tunnel junctions (MEJs).

The perpendicular magnetic anisotropy (PMA) of the bottom free magnetic CoFeB layer was verified via superconducting quantum interference device (SQUID) magnetometer, confirming that the ALD PZT deposition process is a viable method for synthesizing PZT MEJs. The tunnel magnetoresistance (TMR) was measured to be 50%, demonstrating a promising read-out process. Due to the integrated ALD PZT layer in the tunneling barrier, the VCMA coefficient of PZT MEJ devices is expected to be double that measured for CoFeB/MgO/CoFeB devices (ξ = 37 fJ/V·m) (Zhu, J. et al., Physical Review Letters, 2012).

9:40am **TF+EM+NS+PS+SM-ThM6 Plasma-Assisted ALD of High-Quality Molybdenum Oxide Films**, ***Martijn Vos**, B. Macco, N.F.W. Thissen, A.A. Bol, W.M.M. Kessels*, Eindhoven University of Technology, Netherlands

In this contribution we present a novel plasma-assisted atomic layer deposition (ALD) process to deposit high-quality molybdenum oxide films, with a high growth per cycle (GPC) over a wide temperature range of 50 °C to 350 °C. This process complements existing (thermal) ALD MoO_x processes, which are less suited for deposition at low temperature, due to low GPC and contamination. A decent deposition process is of importance as MoO_x films have received great interest due to their remarkable optoelectronic and catalytic properties and find their use in many applications, including solid state lithium batteries, gas sensors, and more recently solar cells.

A variety of deposition techniques exists for the deposition of MoO_x, such as evaporation, sputtering, chemical vapor deposition and ALD. While many of the applications of MoO_x films can benefit from the merits of ALD, i.e. conformality and digital thickness control, only few ALD processes are known from literature [1, 2]. Recently bis(tert-butylimido) bis(dimethyamido) molybdenum ($(NtBu)_2(NMe_2)_2Mo$) appeared as a promising precursor for ALD of MoO_x films, using O_3 as oxidant [2].

The plasma-assisted ALD process we report on uses $(NtBu)_2(NMe_2)_2Mo$ and O_2 plasma and shows a relatively high GPC between 0.70 Å and 0.93 Å for amorphous films deposited at temperatures up to 250 °C. In comparison, the analogous O_3 process is featured by a low GPC of 0.17 Å at 150 °C. For deposition temperatures above 250 °C polycrystalline growth was observed, accompanied by an increase in GPC to 1.88 Å for 350 °C. From Rutherford backscattering measurements it was determined that the C and N content in the films is below the detection limit (3 at.% and 2 at.% respectively) for all deposition temperatures, which demonstrates the high-quality of the films (while the aforementioned O_3 process resulted in 9.2 at.% N). Furthermore the O/Mo ratio was found to be just below 3, indicative of oxygen vacancies, which are common for MoO_x films and can lead to an increased conductivity, which is beneficial for many applications. Additional material properties such as band gap, work function and surface morphology will also be discussed and finally an outlook to the application of this ALD process in silicon solar cells will be given.

[1] M. Diskus *et al.*, J. Mater. Chem. **21** (2011) 705

[2] A. Bertuch *et al.*, J. Vac. Sci. Technol. **32** (2014) 01A119

11:00am **TF+EM+NS+PS+SM-ThM10 Status and Prospects of Plasma-Assisted Atomic Layer Deposition**, ***Harm Knoops***, Oxford Instruments Plasma Technology, UK, *W.M.M. Kessels*, Eindhoven University of Technology, Netherlands **INVITED**

Plasma-assisted atomic layer deposition (ALD) or plasma ALD has established itself as a prominent branch in ALD processing and a wide range of plasma ALD processes are currently available. Due to the complexity of plasmas, plasma ALD is different from thermal ALD in various aspects. Even though the main relevant species in plasmas have been identified,[1] the effects of plasma chemistry and plasma-surface interaction need further study. In this contribution an overview on the status of plasma ALD is given and the key prospects for plasma ALD are highlighted.

Regarding the current understanding of plasma ALD, three subjects will be treated. First the basic plasma species (i.e., radicals, electrons, ions, and photons) and their role in plasma ALD will be discussed. For instance, potential damage to the surface from photons, but also cases where plasma species can repair defects (e.g., N_2 plasmas on GaN surfaces).[2] Second plasma chemistry and potential poisoning or inhibition processes will be treated, which can play a big role in the ALD of nitrides and conductive films. Third, dissociation in the plasma of reaction products can lead to redeposition effects which can have a large influence on for instance SiN_x and TaN_x ALD.

Several topics will be discussed regarding the prospects for plasma ALD. Even though plasma ALD provides additional possibilities, many cases exist where material properties or cycle times are still unsatisfactory and advances in reactor design such as the capability to provide additional energy in the form of a controlled ion bombardment are needed. In addition, advanced processing schemes such as 3-step ABC ALD cycles can be beneficial as shown by ALD of noble metals at low deposition temperatures (e.g., Pt ALD).[3] Whether metal films initially grow as continuous films or as nanoparticles (as well as the particle size), will depend on the chemistry, the surface energy, and the growth temperature. Recently, plasma ALD has shown to allow ALD of Ag by spatial ALD at high pressure.[4] This case shows that more understanding of the plasma is needed because of an unexpected decreased growth at long plasma exposures (presumably caused by NH_3 poisoning). In general, increasing control of the plasma and understanding of the relevant processes at the surface and in the plasma will be key to further develop plasma ALD.

[1] Profijt et al., *JVST A***29**, 050801 (2011)

[2] Chen et al., *Phys. Status Solidi A* (2014) / DOI 10.1002/pssa.201431712

[3] Mackus et al., *Chem. Mater.***25**, 1769 (2013)

[4] Van den Bruele et al., *JVSTA***33**, 01A131 (2015)

11:40am **TF+EM+NS+PS+SM-ThM12 A Novel Plasma-Enhanced ALD Process for HfO_2 using $HfCp(NMe_2)_3$ and O_2 Plasma**, ***Akhil Sharma**, V. Longo, A.A. Bol, W.M.M. Kessels*, Eindhoven University of Technology, The Netherlands

In atomic layer deposition (ALD) the associated precursor chemistry has a large effect on the quality and properties of the deposited thin films. The most commonly used hafnium precursor for ALD of HfO_2 is $HfCl_4$. This precursor is not ideal for all applications due to possible chlorine contamination and the generation of corrosive by-products during the ALD process. Organometallic precursors such as $Hf(NtMe)_4$ promise to be a better choice but they typically suffer from a limited thermal stability. In

this context, $HfCp(NMe_2)_3$ might offer a better alternative because of its higher thermal stability. However, while using H_2O as oxygen source in a thermal ALD process it yields a low growth rate[1]. This creates an opportunity for studying this precursor in combination with other oxygen sources. In this work, we report on the development of a novel plasma-enhanced ALD (PE-ALD) process using $HfCp(NMe_2)_3$ in combination with an O_2 plasma to deposit HfO_2 thin films. To our knowledge, to date, the PE-ALD for this precursor has not been reported in the literature.

Our results show that the PE-ALD process offers significant advantages over the reported thermal ALD process such as a high growth rate, reduced deposition temperature, shorter cycle time and good control over composition of the deposited films. In contrast to the thermal ALD process using $HfCp(NMe_2)_3$ and water[1], the PE-ALD process has resulted into a wide ALD temperature range (150-400°C) with significantly higher growth per cycle values (1.1Å/cycle) and shorter cycle times which ultimately improves the wafer throughput. The level of impurities were found to decrease with increasing the deposition temperature as concluded from XPS and ERD analyses. The concentrations of residual carbon and hydrogen reduced from 1.0 at% to 0.2 at% and 3.4 at% to 0.8 at%, respectively, by increasing the deposition temperature from 200°C to 400°C. Moreover, RBS studies showed an improvement in stoichiometry of HfO_2 thin films with increase in deposition temperature resulting in a Hf/O ratio of ~0.5 at 400°C. Furthermore, GI-XRD measurements detected a strong transition from amorphous (300°C) to fully crystallized films (400°C), consisting of a mixture of monoclinic, tetragonal and cubic phases. These results therefore have demonstrated that PE-ALD using $HfCp(NMe_2)_3$ and O_2 plasma is a promising and viable alternative to the thermal ALD process producing high quality HfO_2 thin films over a wider temperature range and with faster cycle times.

1. Consiglio et al, J. Vac. Sci. Technol. A 30(1), 2012

12:00pm **TF+EM+NS+PS+SM-ThM13 Conductive Hafnium Nitride Layers By Plasma-Assisted Atomic Layer Deposition***, Saurabh Karwal,*
B.L. Williams, W.M.M. Kessels, M. Creatore, Eindhoven University of Technology, The Netherlands

Transition metal nitrides (TMNs) have gained much attention in the semiconductor industry due to their characteristics such as copper and lithium diffusion barriers, metal-like behaviour (i.e. low resistivity) and high hardness, mechanical strength and chemical inertness. Among TMNs, hafnium nitride exhibits a low bulk resistivity of 33 μΩcm and highest negative Gibbs free energy of formation (HfN: -88.2, TiN: -80.4, TaN: -60.3 kcal/mol) and hence could serve as novel material for several applications, such as diffusion barrier and gate electrode in microelectronics, and reflective back contact for CIGS solar cells.

Conductive hafnium nitride thin films were deposited by inductively coupled plasma (ICP)- assisted atomic layer deposition using a heteroleptic metalorganic hafnium precursor, tris(dimethylamino)cyclopentadienylhafnium $CpHf(NMe_2)_3$ [TDMACpH] and H_2-or N_2- fed plasmas serving as co-reactants. The effects of the substrate temperature, plasma chemistry and plasma exposure time have been investigated in terms of growth-per-cycle (GPC), chemical, electrical and morphological properties of the deposited layer. It has been observed that highly resistive (0.75 Ωcm) Hf_3N_4 thin films are obtained via an A-B type ALD cycle (TDMACpH/N_2 –fed plasma) with a GPC of 0.035 nm/cycle. Furthermore, a limited abstraction of the ligands leads to a residual carbon content in the layer of 7%.

Instead, conductive films (1.8×10^{-3} Ωcm) are achieved upon the application of an A-B-C ALD cycle where an intermediate H_2- fed plasma exposure step is included between the TDMACpH exposure and the N_2-fed plasma step, with a GPC of 0.045 nm/cycle. This intermediate step is found to be responsible for a more efficient removal of the precursor ligands and for the reduction of Hf^{4+} state to Hf^{3+} state, essential for guaranteeing electron conductivity. This transition of chemical and electrical properties of the deposited thin films is also accompanied by a change in crystallographic properties from amorphous (A-B ALD cycle) to conductive cubic HfN (A-B-C ALD cycle), as revealed by grazing incidence X-ray diffraction.

Contact: s.karwal@tue.nl

2D Materials Focus Topic
Room: 212C - Session 2D+EM+MG+NS+SS+TF-ThA

Heterostructures of 2D Materials
Moderator: Stefan Förster, Martin-Luther-Universität Halle-Wittenberg, Michael Naguib, Oak Ridge National Laboratory

2:20pm **2D+EM+MG+NS+SS+TF-ThA1 Dielectrics Layer Deposition on 2D Materials by Functionalization with Polar Titanyl Phthalocyanine**, ***JunHong Park***, UC San Diego, *S. Fathipour,* University of Notre Dame, *I.J. Kwak,* UC San Diego, *H.C.P. Movva,* UT-Austin, *S. Vishwanath, H. Xing,* Cornell University, *S.K. Banerjee,* UT-Austin, *A.C. Seabaugh,* University of Notre Dame, *A.C. Kummel*, University of California at San Diego

Several novel designs for beyond CMOS devices have emerged using two-dimensional semiconductors. These devices require deposition of thin insulators on 2D semiconductors or between two sheets of 2D semiconductors. However, 2D semiconductors are nearly inert surfaces thereby making uniform nucleation of oxide growth challenging preventing scaling of the insulator thickness. A new technique has been developed to employ a monolayer of ordered metal phthalocyanines (MPc) on 2D semiconductors directly as a nucleation layer for growth of ALD dielectric. TiOPc monolayers were deposited on HOPG surfaces and WSe_2 by organic molecular beam epitaxy. TiOPc forms a monolayer with only few defects, and the crystal structure of monolayer has four-fold symmetry in a 1.6 x 1.6 nm grid on both HOPG and WSe_2. Observation of bright protrusions on each O-TiPc indicates that each O-TiPc in the monolayer is directed outward to vacuum. After exposure O-TiPc monolayer to 5 cycles ALD pulse (tri-methyl-aluminum (TMA)+H_2O), insulating aluminum oxide was deposited uniformly on TiOPc/HOPG. After formation of AlO_x on TiOPc/HOPG, the band gap of surface increases from 1.7 eV to 3.4 eV, while the conductance decreased. A metal-oxide-TiOPc-graphene capacitor has the lower thickness and the higher capacitance value than any reported graphene MOSCAPs. In the dual gated graphene FET with 40 cycles of AlO_x, TiOPc assisted AlO_x shows very low leakage current. Employing the TiOPc seeding layer also can be expanded to other TMD materials. The bottom gated WSe_2 FET was fabricated. On the bottom gated WSe2 FET, the TiOPc monolayer was deposited, then 50 cycle of AlO_x was deposited via ALD. In this dual gated WSe_2 FET, the leakage current of the AlO_x is measured as ~0.05 pA/μm^2 at 0.5 VTG. As a control, 20 cycles of Al_2O_3, and 140 cycles of HfO_2 were deposited on bare WSe_2. The leakage current of the TiOPc assisted 50 cycle Al_2O_3 oxide is 3 orders of magnitude lower than $HfO_2/Al_2O_3/WSe_2$, consistent with a high nucleation.

2:40pm **2D+EM+MG+NS+SS+TF-ThA2 Direct Probing of the Electronic Structure of Bilayer Homo- and Hetero-Structures and Tracking their Evolution with Interlayer Twist-Angle**, ***Nader Zaki***, *P. Yeh, W. Jin, R.M. Osgood, Jr.*, Columbia University

2D atomic layer materials such as graphene and transition-metal dichalcogenides such as MoS_2 have garnered much interest over the last few years due to their surprising electronic properties. For example, graphene possesses an exceptionally high mobility while monolayer MoS_2 possesses a direct bandgap with an exceptionally high light-matter interaction. One of the directions the 2D materials community is now pursuing is one in which these materials are combined together by way of vertical stacking in order to fabricate custom layered structures with potentially rich physics and unique device properties. Naturally, determining the electronic structure of these custom assembled structures is a necessary task to understanding their electronic behavior. While the electronic structure of the constituent materials have already been studied for monolayer form, the electronic structure of the stacked structures has only recently started to be deciphered. This talk will report on the direct determination of the electronic structure of two bilayer systems: twisted bilayer MoS_2 and twisted graphene/MoS_2. Using LEEM, µLEED, and µARPES, the stack quality, stack orientation, and stack electronic structure are directly probed and resolved with few μm and higher spatial resolution. To be discussed will be the evolution of the electronic structure with twist angle and its implications on the electronic properties of the respective homo- and hetero-structures.

3:00pm **2D+EM+MG+NS+SS+TF-ThA3 *In Situ* Microscopy on 2D Materials: Heterostructures, Nanostructures, Novel Materials Systems**, ***Peter Sutter***, University of Nebraska - Lincoln **INVITED**

Two-dimensional (2D) materials, such as graphene, hexagonal boron nitride, and a family of metal dichalcogenides have fascinating properties and show promise for applications. The broad exploration and use of these materials depends on the development of scalable synthesis methods, and of a fundamental understanding of their properties. I will discuss recent advances in understanding the synthesis, processing, and properties of 2D materials derived primarily from in-situ surface imaging.

In-situ microscopy provides the basis for creating complex heterostructures of different 2D materials, such as graphene and hexagonal boron nitride, and for studying atomically precise graphene nanostructures. Real-time imaging yields quantitative information on the growth and processing of new classes of 2D materials, such as metal dichalcogenide semiconductors. Finally, the combination of in-situ microscopy with synchrotron-based spectroscopy represents a unique approach for exploring the electronic band structure of 2D materials.

Our results illustrate that in-situ microscopy can be a powerful tool for realizing and probing the unique characteristics of two-dimensional materials.

4:00pm **2D+EM+MG+NS+SS+TF-ThA6 Direct Growth of Graphene/h-BN(0001) Multilayer Heterostructures for Novel Device Applications**, *S. Driver, D. Beatty, B. Olanipekun, S. Reid,* ***Jeffry Kelber***, University of North Texas

We report the direct layer-by-layer growth of h-BN(0001) multilayers on Co(0001) by atomic layer epitaxy (ALE), and the direct growth of graphene multilayers on h-BN(0001) by molecular beam epitaxy (MBE). For the first time, this allows the growth of graphene/BN heterostructures with graphene and BN thicknesses controlled with atomic precision, and with all graphene and BN layers in azimuthal registry. Such control is a prerequisite for many proposed spintronic and electronic applications that emphasize charge or spin transport perpendicularly through the heterojunction. Further, the growth by direct, scalable methods without physical transfer, is essential for industrial development of such devices. h-BN(0001) multilayers have been deposited on Co(0001)/Al_2O_3(0001), using a BCl_3/NH_3 ALE process at 600 K. X-ray photoelectron spectroscopy (XPS) indicates B:N atomic ratios of 1:1 with negligible Cl contamination or reaction with the metallic substrate. Low energy electron diffraction (LEED) data indicate BN domain sizes of ~ 300 A or greater, with the lattice in registry with that of the Co(0001) substrate. LEED data also indicate BN domains larger than those of the Co substrate, suggesting BN overgrowth of Co domain boundaries. The XPS-derived average BN film thickness scales linearly with the number of BCl_3/NH_3 cycles, and the lack of Co oxidation after ambient exposure of a BN bilayer indicates that these films are macroscopically continuous over the 1 cm x 1 cm sample size. Graphene formation on h-BN(0001) was achieved using MBE with a graphite rod source, with deposition carried out at 800 K. LEED data show the expected 6-fold LEED pattern in exact registry with that of the h-BN(0001)/Co(0001) substrate. XPS C 1s spectra indicate a C 1s binding energy near 284.5 eV and with the expected pi-to-pi* transition. A heterojunction consisting of ~ 3 monolayers (ML) graphene/3 ML h-BN on Co(0001) proved stable in vacuum to at least 1000 K, indicating the adaptability of this growth process to a variety of industrial applications. Other recent results indicate the adaptability of this process to other substrates, such as Ru(0001) or $CoSi_2$(111). These developments make possible a variety of spin filters, spin valves, and tunneling transistors proposed on the basis of close BN/graphene lattice matching, but not readily achievable with physically transferred films.

Acknowledgements: This work was supported by CSPIN, a MARCO/DARPA STARnet Center, under tasks 2381.001

and 2381.003, and by a UNT ROP grant. Peter Dowben and Jian-Ping Wang are acknowledged for stimulating and informative discussions.

4:20pm **2D+EM+MG+NS+SS+TF-ThA7 Al_2O_3 on Black Phosphorus by Atomic Layer Deposition: An *in situ* Interface S tudy**, ***Hui Zhu***, *S. McDonnell, X. Qin, A. Azcatl, L. Cheng, R. Addou, J. Kim,* UT-Dallas, *P.D. Ye,* Purdue University, *R.M. Wallace*, UT-Dallas

Black phosphorus ("black-P") is considered to be an appealing 2D material because of its novel properties and potential application in few-layer transistor structures.[1,2,3] However, a clear challenge in the implementation of black-P is the strong hydrophilic[4] and oxidation[5] reactions during device processing and thereafter. Thus, efficient isolation layers are necessary for black-P to preserve its electronic properties. Al_2O_3[2] or HfO_2[6] dielectric layers deposited by atomic layer deposition (ALD) have been used as isolation layers in recent black-P transistors. In this work, three different samples oxidized by ambient air were investigated to understand the interfacial chemistry, and nucleation of atomic layer deposited Al_2O_3 on black-P using *in situ* X-ray photoelectron spectroscopy (XPS). This work suggests that exposing a sample that is initially free of phosphorus oxide to the ALD precursors does not result in detectable oxidation. However, when

the phosphorus oxide is formed on the surface prior to deposition, the black-P can react with both the surface adventitious oxygen contamination and the H_2O precursor at the deposition temperature of 200 °C. As a result, the concentration of the phosphorus oxide increases after both annealing and the atomic layer deposition process. The nucleation rate of Al_2O_3 on black-P is correlated with the amount of oxygen on samples prior to the deposition. The growth of Al_2O_3 follows a "substrate inhibited growth" behavior where an incubation period is required. *Ex situ* atomic force microscopy is also used to investigate the deposited Al_2O_3 morphologies on black-P where the Al_2O_3 tends to form islands on the exfoliated black-P simples.

This work was supported in part by the SWAN Center, a SRC center sponsored by the Nanoelectronics Research Initiative and NIST, the Center for Low Energy Systems Technology (LEAST), one of the six SRC STARnet Centers, sponsored by MARCO and DARPA, and the US/Ireland R&D Partnership (UNITE) under the NSF award ECCS-1407765.

Reference:

1 L. Li, Y. Yu, G.J. Ye, Q. Ge, X. Ou, H. Wu, D. Feng, X.H. Chen, and Y. Zhang, Nat. Nanotech. 9, 372 (2014).

2 H. Liu, A.T. Neal, Z. Zhu, Z. Luo, X. Xu, D. Tománek, and P.D. Ye, ACS Nano 8, 4033 (2014).

3 F. Xia, H. Wang, and Y. Jia, Nat. Comm. 5, 4458 (2014).

4 J.D. Wood, S.A. Wells, D. Jariwala, K. Chen, E. Cho, V.K. Sangwan, X. Liu, L.J. Lauhon, T.J. Marks, and M.C. Hersam, Nano Lett. 14, 6964 (2014).

5 A. Favron, E. Gaufrès, F. Fossard, P.L. Lévesque, Anne-Laurence, Phaneuf-L' Heureux, N.Y.-W. Tang, A. Loiseau, R. Leonelli, S. Francoeur, and R. Martel, arXiv:1408.0345 (2014).

6 N. Haratipour, M.C. Robbins, and S.J. Koester, arXiv:1409.8395 2 (2014).

4:40pm **2D+EM+MG+NS+SS+TF-ThA8 Topological Winding Number Change and Broken Inversion Symmetry in a Hofstadter's Butterfly**, ***Marc Bockrath***, UC Riverside

Recently several research groups have demonstrated accurate placement of graphene on hexagonal BN (hBN) with crystallographic alignment. Due to the resulting superlattice formed in the graphene/hBN heterostructures, an energy gap, secondary Dirac Points, and Hofstadter quantization in a magnetic field have been observed. Using aligned layer transfer we are able to produce graphene/hBN heterostructures with ~1 degree alignment accuracy, and measure the transport properties of the resulting systems. We observe an additional π Berry's phase shift in the magneto-oscillations when tuning the Fermi level past the secondary Dirac points, originating from a change in topological winding number from odd to even when the Fermi-surface electron orbit begins to enclose the secondary Dirac points. At large hole doping inversion symmetry breaking generates a distinct hexagonal pattern in the longitudinal resistivity versus magnetic field and charge density. This results from a systematic pattern of replica Dirac points and gaps, reflecting the fractal spectrum of the Hofstadter butterfly.

5:00pm **2D+EM+MG+NS+SS+TF-ThA9 Compliant Substrate Epitaxy: Au on MoS_2**, ***Yuzhi Zhou***, *C. Daryl*, UC Berkeley

The heteroepitaxial growth of Au on MoS_2, a layered van der Waals bonded dichalcongenide, is analyzed. It is argued that the weak coupling between the layers in the dichalcogenides enables the first substrate layer to deform elastically almost independently from the substrate layers below, and hence enables epitaxial growth for a larger mismatch than might otherwise be expected. Linear, continuum elasticity theory and density functional theory are used to show that a {111} oriented Au film is the preferred over an {001} oriented Au film, despite the fact that the {111} orientation leads to a much higher elastic strain. During the initial stages of growth, the {111} orientation is favored over the {001} orientation due to its lower surface and interfacial energies. As the Au film grows thicker, the elastic relaxation of the first layer of the substrate leads to a reduction in the elastic energy of the growing film. This reduces the elastic energy difference between the {001} and {111} orientations enabling the {111} orientation to remain stable for all film thicknesses. This work is supported by the Director, Office of Science, Office of Basic Energy Sciences, Division of Materials Sciences and Engineering, of the U.S. Department of Energy under Contract No. DE-AC02-05CH11231.

5:20pm **2D+EM+MG+NS+SS+TF-ThA10 Direct Synthesis of 2D van der Waals Heterostructures**, ***Judy Cha***, Yale University **INVITED**

Two-dimensional (2D) chalcogenides have gained renewed interest due to their interesting electrical properties such as topological insulator surface states in Bi_2Se_3 and hydrogen evolution catalytic activities in MoS_2. Our ability to thin them down to a single layer and their anisotropic bonding nature opens up possibilities for novel heterostructures where we can tailor their electronic properties. I will present one-step, scalable heterostructure synthesis method to synthesize these chalcogenide nanostructures and examine their electronic transport properties. Intercalation into 2D materials will be considered as a novel way to design 2D heterostructures, in which the optical and electrical properties of the host 2D materials can drastically change. I will also discuss ways to control the alignment of molecular layers in these 2D chalcogenides, which exploits stress and strain built in the film during the growth. Electron tomography will be used to reconstruct the 3D structure of vertically oriented molecular layers in MoS_2 thin films. In the second part of the talk, I will present synthesis and electronic properties of SnTe topological crystalline insulator nanoplates. Although SnTe is cubic and not a layered material, large SnTe nanoplates expanding hundreds of microns in lateral dimension with ~ 100 nm in thickness are possible. I will discuss effects of substrates and growth conditions to promote thin film growth of non-layered materials.

Additive Manufacturing/3D Printing Focus Topic
Room: 211A - Session AM+EM+MS+TF-ThA

Additive Fabrication for Electronic Devices and Systems
Moderator: Jim Fitz-Gerald, University of Virginia, Gregory Whiting, Palo Alto Research Center

2:20pm **AM+EM+MS+TF-ThA1 Additive Printing for Flexible Electronic Devices**, *A.C. Pierre*, ***Ana Claudia Arias***, University of California at Berkeley **INVITED**

The area of printed electronics has been focused on the use of new classes of semiconducting and conducting materials in two main applications, displays and photovoltaics. Both applications require materials long-term stability, long shelf life as well the need for patterning and deposition over large areas. Over the past 10 years significant progress in the performance of printable materials has been reported including highly efficient solar cells, light emitting diodes and thin film transistors with mobilities as high as 10 cm^2/Vs. The work is highly motivated by the potential for high through put, high volume, low cost manufacturing. While large area electronics continues to be a good application for printed flexible devices, wearable medical devices, which benefit from new form factors, represent a good shift in direction of research in the field. Wearable medical sensors have the potential to play an essential role in the reduction of health care costs as they encourage healthy living by providing individuals feedback on personal vital signs and enable the facile implementation of both in-hospital and in-home professional health monitoring. In printed flexible electronics however, there are no standards for materials set, device models and fabrication methods. This lack of standards slows down design of new systems and the success of the technology as a whole. In this talk, I will review the state of the art of devices produced by printing and introduce a blade coating method that yields highly homogeneous flexible thin films that are applied to LEDS, photodiodes and TFTs. The application of these devices as building blocks for flexible electronics systems will also be discussed.

3:00pm **AM+EM+MS+TF-ThA3 Digital Microassembly for High-performance Printed Electronics**, ***Eugene Chow***, *J.P. Lu, G.L. Whiting, D.K. Biegelsen, S. Raychaudhuri, A.R. Völkel, J. Veres, P. Maeda, I. Matei, S. Nelaturi, L.S. Crawford*, Palo Alto Research Center (PARC) **INVITED**

Digitally printing micro-scale pre-fabricated building blocks instead of simpler materials enables an alternative route to printed electronics and opens up fundamentally new manufacturing capabilities. However, existing printing technologies do not provide the required accuracy and orientation control to print such micro objects. We will describe a demonstration of the fundamental process steps of such an electronic chip printer based on electrographic manipulation and xerographic concepts.

4:00pm **AM+EM+MS+TF-ThA6 3D Printed Bionic Nanomaterials**, ***Michael McAlpine***, University of Minnesota **INVITED**

The ability to three-dimensionally interweave biology with nanomaterials could enable the creation of bionic devices possessing unique geometries, properties, and functionalities. The development of methods for interfacing high performance devices with biology could yield breakthroughs in regenerative medicine, smart prosthetics, and human-machine interfaces. Yet, most high quality inorganic materials: 1) are two dimensional, 2) are hard and brittle, and 3) require high crystallization temperatures for maximally efficient performance. These properties render the corresponding devices incompatible with biology, which is: 1) three dimensional, 2) soft, flexible, and stretchable, and 3) temperature sensitive. These dichotomies are solved by: 1) using 3D scanning and printing for hierarchical, interwoven, multiscale material and device architectures, 2) using

nanotechnology as an enabling route for overcoming mechanical discrepancies while revealing new effects due to size scaling, and 3) separating the materials synthesis and 3D printed assembly steps to enable conformal integration of high quality materials with biology. The coupling of 3D printing, novel nanomaterial properties, and 'living' platforms may enable next-generation nano-bio interfaces and 3D printed bionic nanodevices.

Spectroscopic Ellipsometry Focus Topic
Room: 112 - Session EL+AS+BI+EM-ThA

Optical Characterization of Nanostructures and Metamaterials

Moderator: Bernard Drevillon, LPICM-CNRS, Ecole Polytechnique, France, Mathias Schubert, University of Nebraska - Lincoln

2:20pm **EL+AS+BI+EM-ThA1 Electrostatic Coating with Ligandless Copper Nanoparticles**, ***Lance Hubbard***, *A.J. Muscat*, University of Arizona

Electroless deposition (ELD) produces conformal coatings at low temperatures. ELD occurs by chemical reduction of metal ions without an externally applied potential or catalyst layer. In this paper, we report on a nonaqueous ELD process that uses a charge compensator, but not a ligand or complexing agent. The weak electrostatic attachment of the charge compensator to the ions and particles in solution and the high pH conditions improve the driving force for metal deposition. Si(100) native oxide was hydroxylated and terminated with a self-assembled amine layer (4 mM (3-aminopropyl)-trimethoxysilane in methanol). Metal films were deposited by suspending samples in a bath made by dissolving Cu(II) chloride in ethylene glycol (reducing agent), and adding 1-butyl-3-methylimidazolium tetrafluoroborate as a charge compensator. The Cu particle ion shell is attracted to the positively charged amine groups at high pH depositing a thin metal film that is both continuous and cohesive. Annealing the coupons at 200°C in nitrogen promoted electrically conductive film formation. Electron microscopy images of the coated substrates showed a 80-95 nm thick film of 3 nm diameter particles. Four-point probe measurements of the films yielded electrical conductivities in the range 10^6-10^7 S/m (10-80% of bulk conductivty). The surface plasmon resonance (SPR) peak of the Cu nanoparticles in the bath and film was at 585 nm. Light scattering measurements and transmission electron microscopy (TEM) images yielded a size distribution of 3.1±1.56 nm. Scanning electron microsopy (SEM) images at various angles in relation to the films were taken to examine film morphology and thickness. Spectroscopic ellipsometry (SE) data were modelled with bulk, nanophase d-band transition, and SPR absorbances. The SE agreed well with UV-VIS results for the SPR and shows an increasing contribution from d-band transitions with increasing ionic liquid concentration. SEM and Fourier transform infrared (FTIR) spectroscopy were used to determine film thicknesses and chemistry.

2:40pm **EL+AS+BI+EM-ThA2 Using Plasmonic Effects to Design Ellipsometric Targets with Sub-Angstrom Resolution**, ***Samuel O'Mullane***, SUNY Polytechnic Institute, *J. Race, N. Keller,* Nanometrics, *A.C. Diebold*, SUNY Polytechnic Institute

For traditional ellipsometric targets, slightly changing the thickness of a layer or the index of refraction of a material results in a similarly small change in the observed spectra. If structures are designed to allow for plasmonic coupling, a slight change in those same parameters results in wildly different spectra. Specifically, localized plasmonic resonances in metallic grating structures allow for extraordinary sensitivity to parameters such as CD, sidewall angle and pitch.

Existing metallic grating structures are arrays of long, thin lines of copper that can be described using one dimension. The typical resolution for ellipsometric CD measurements on these structures ranges from nanometers to Ångströms. Because there is no confining second dimension, localized plasmons cannot be produced.

In order to obtain sub-Ångström resolution, additional structural modifications are required. This is achieved by adding a second metallic grating perpendicular to the original grating forming a cross-grating structure. Note that the added pitch and linewidth are an order of magnitude larger than the original parameters. This results in fully localized plasmonic resonances so that parameter variation on the order of tens of picometers could be detected through ellipsometric measurements. Making use of conical diffraction further increases the sensitivity to structural changes due to increased anisotropy.

These conclusions are the result of rigorous coupled wave-analysis (RCWA) simulations which were confirmed via finite element method (FEM) simulations. With both RCWA and FEM agreement, experimental confirmation is expected.

3:00pm **EL+AS+BI+EM-ThA3 Enhanced Temperature Stability of Slanted Columnar Thin Films by ALD Overcoating**, ***Alyssa Mock***, *D. Sekora, T. Hofmann, E. Schubert, M. Schubert*, University of Nebraska - Lincoln

The demand for thermally stable nanostructures continues to increase as nanotechnology becomes ever more prevalent in both commercial and research applications. The high surface area of nanostructured thin films is susceptible to degradation under extreme temperatures. Scanning electron microscopy (SEM) and Mueller Matrix Generalized Ellipsometry (MMGE) were used to observe optical and structural properties of a glancing angle deposited cobalt slanted columnar thin film (SCTF) over increased annealing temperature. We show that the use of atomic layer deposition (ALD) to conformally passivate the SCTF surface provides both physical scaffolding and thermal protection during the annealing process up to 475°C as no changes in the SEM or MMGE results were present.

3:20pm **EL+AS+BI+EM-ThA4 Vector Magneto-Optical Generalized Ellipsometry on Heat Treated Sculptured Thin Films: A Study of the Effects of Al_2O_3 Passivation Coatings on Magneto-Optical Properties**, ***Chad Briley***, *A. Mock,* University of Nebraska-Lincoln, *D. Schmidt,* National University of Singapore, *T. Hofmann, E. Schubert, M. Schubert*, University of Nebraska-Lincoln

We present the vector magneto-optical generalized ellipsometric (VMOGE) response[1] and model dielectric function (MDF) anisotropic hysteresis calculations[2] of ferromagnetic slanted columnar thin films under the effects of heat treatment up to 475° C. Directional hysteresis magnetization scans were performed with an octu-pole vector magnet at room temperature on Cobalt slanted columnar thin film samples grown by glancing angle deposition with and without Al_2O_3 conformal passivation overcoating done by atomic layer deposition. Analysis of the measured Mueller matrix ellipsometric data through a point-by-point best match model process determine the magneto-optical (MO) dielectric tensor. Three dimensional rendering of the anti-symmetric off-diagonal elements of the MO dielectric tensor displays anisotropic magnetic response of the thin film with the hard axis along the long axis of the columns. Data analysis reveals the preservation of anisotropic magneto-optical properties of the thin film with the passivated coating as compared to the non-passivated coating due to oxidation effects from heat treatment.

1) D. Schmidt, C. Briley, E. Schubert, and M. Schubert, Appl. Phys. Lett. **102**, 123109 (2013).

2) C. Briley, D. Schmidt, T. Hofmann, E. Schubert, and M. Schubert, Appl. Phys. Lett. **106**, 133104 (2015).

4:00pm **EL+AS+BI+EM-ThA6 Spectroscopic Ellipsometry for Critical Dimensions Analysis**, ***Vimal Kamineni***, GLOBALFOUNDRIES, *D. Dixit, S. O'Mullane,* SUNY Polytechnic Institute, *G. Iddawela, A. Vaid,* GLOBALFOUNDRIES, *A.C. Diebold*, SUNY Polytechnic Institute **INVITED**

In this talk an overview of the current applications of spectroscopic ellipsometry (SE) towards measuring the shape of nanostructures will be presented. The transition of the semiconductor industry from planar to 3D transistors has expanded the applications of ellipsometry. Ellipsometry measurements on the periodic nanoscale structures enable a diffraction based measurement technique referred to as scatterometry. The critical dimensions can be extracted by means of a regression on the diffracted light using rigorous coupled wave analysis (RCWA). RCWA is a Fourier-space method used to generate the optical response by slicing the periodic structure of interest and matching the boundary conditions to compute EM modes. This method is inherently dependent on *a priori* knowledge of the dielectric function of the materials that construct the nanostructures as well as the shape of the nanostructure obtained from reference metrology. Furthermore, time-to-solution is one of the main drawbacks of developing scatterometry applications due to the dependency on developing a robust model and for validating the model with reference metrology measurement. To address these challenges new methods such as signal response metrology (SRM) encompassing machine-based statistical learning and virtual reference metrology have been proposed. [1,2] These methods will be reviewed along with their benefits and limitations when applied to advanced 3D transistor structures. In addition, application of Mueller matrix ellipsometry measurements on strained grating structures (SiGe/Si) and block copolymer structures to determine the impact of strain and defectivity (bridging defects, wiggles, LER, etc.) on anisotropy coefficients will be presented, respectively. [3,4] Additionally, hybrid approaches will be

proposed in conjunction with complementary/supplementary metrology methods (CD-SEM, HRXRD and CD-SAXS). [5-7]

[1] S. Pandev et al., SPIE Proc. 9424 (2015).

[2] A. Vaid et al., SPIE Proc. 9424 (2015).

[3] G. R. Muthinti et al., SPIE Proc. 8681 (2013).

[4] D. J. Dixit et al., Journal of Micro/Nanolithography, MEMS, and MOEMS 14, 021102 (2015).

[5] A. Vaid et al., SPIE Proc. 8324 (2012).

[6] A. C. Diebold et al., Proceedings of SPIE 8681, 86810I (2013).

[7] Charles Settens et al., Journal of Micro/Nanolithography, MEMS, and MOEMS 13, 041408 (2014)

4:40pm **EL+AS+BI+EM-ThA8 Structural and Ellipsometric Analysis of the Topological Insulator Bi_2Se_3**, ***Avery Green***, SUNY Polytechnic Institute

Topological Insulator (TI) materials have been the subjects of increasing scientific interest in the last decade. Their spin-momentum locked Dirac cone surfaces and insulating bulks have resulted in new directions in physics research and new spintronic devices. Though these materials have been thoroughly described in theory, the experimental realization and measurement of these surface states has been problematic, due to various crystalline defects. Theory predicts that TI surface states are protected against local defects, but it is essential to study the effects of global perturbations caused by surface oxidation, stoichiometric aberrations, and significant structural defect densities. The aim of this study is to measure the time-dependent dielectric function of the Bi_2Se_3 surface and bulk in air, using a dual rotating compensator spectroscopic ellipsometer. These data are backed up with various metrological measurements (AFM, cross-sectional TEM, EDS) to confirm surface topology and oxide thickness. This analysis of optical properties and oxide formation will, in the future, be used to optimize the Bi_2Se_3 flake thickness identification process, and provide a control for further necessary structural analysis, as stated above.

5:00pm **EL+AS+BI+EM-ThA9 Visible Luminescence in the VLS Grown Self Ga Doped ZnS Nanostructures**, ***Arshad Bhatti***, *H. Hussain, M.A. Johar, S. Rehman, M.A. Shehzad, M.A. Hafeez*, COMSATS Institute of Information Technology, Pakistan

ZnS is a wide band gap semiconductor and thus offers fascinating opportunities for tailoring and tuning its bandgap states for photonic devices in visible region of the spectra. Ga introduced a strong red luminescence in ZnS. VLS mechanism was employed to synthesize ZnS nanowires using Ga as a catalyst and dopant simultaneously. The thickness of Ga ultrathin film was varied from 0.5 nm to 5 nm to observe the effect of Ga droplet size on the formation, lifetime and activation energies of defect states in the band gap. It was expected that Ga^{3+} would replace Zn^{2+} sites and dope ZnS, in addition, an impurity phase of Ga_2S_3 was also observed, whose content showed strong dependence of Ga thickness. It also shrunk the crystallinity of ZnS due to varied size of Ga^{3+}(76 pm) ions replacing Zn^{2+} (88 pm), which was observed in the shifts of major XRD reflections of ZnS. Incorporation of Ga introduced strong impurity states in the band gap of ZnS. It also affected the intrinsic defect states of ZnS, namely Zn and S vacancies (Please refer to Figure 1, which also shows the de-convoluted band gap broad band). In the PL spectra, blue (440 nm), yellow (560 nm), orange (600 nm) and red (680 nm) bands were attributed to S vacancies, Ga related defects, donor-acceptor recombination and Ga_2S_3, respectively. Photoluminescence excitation spectroscopy revealed strong absorbance at corresponding energies. A strong correlation of these states was observed in the temperature dependent PL measurements due to presence in their presence in the vicinity as the activation energies of these states matched the energy differences of corresponding states. The conductivity measurements also complimented the optical results. Time resolved PL demonstrated the lifetime of these states was between 0.5 ns to 1.5 ns and had somewhat significant effect of dopant concentration. Finally, Ga doped ZnS showed extremely efficient IR sensitivity.

Figure 1: The room temperature PL spectra of Ga doped ZnS nanowires synthesized with varied thickness of Ga: (a) 0.5 nm, (b) 1.0 nm, (c) 3.0 nm, and (d) 5.0 nm. The broad band between 450 nm to 750 nm has been de-convoluted to show contribution of various defect states (as mentioned in the Figure). These states were identified from the PLE spectrum.

5:40pm **EL+AS+BI+EM-ThA11 Can Front-Surface Metal Mirrors Be Protected from Oxidation by Vacuum Applied Polymer Films?**, ***David Allred***, *R.S. Turley*, Brigham Young University, *R.T. Perkins*, Utah Valley University

We have used variable-angle, spectroscopic ellipsometry to monitor secular changes in multilayers consisting of chemically active thin films, such as aluminum, deposited on dielectric-coated silicon wafers and protected by various vacuum-applied barrier layers. Ultrathin barrier layers included polymers such as parylene and rarely, sputtered inorganic films, such as silicon. Applications include the measurements of the oxidation of evaporated aluminum for use as a mirror in the VUV (vacuum ultraviolet) and the determination of the optical constants of materials such as Y_2O_3 potentially useful in VUV and XUV (extreme ultraviolet) optics.

Electronic Materials and Processing
Room: 211C - Session EM+EN-ThA

Materials for Light Management
Moderator: Michael Filler, Georgia Institute of Technology, Sang M. Han, University of New Mexico

2:20pm **EM+EN-ThA1 III-V Nanowires for Photonics and Solar Energy Applications**, ***Anna Fontcuberta i Morral***, EPFL, Switzerland **INVITED**

Semiconductor nanowires are filamentary crystals with a tailored diameter between few to few hundred nanometer. Their special shape and dimensions render them especially interesting for photonic applications. In my talk I will discuss several photonic applications of nanowires. I will start by showing how to modify light absorption and emission of nanowires by coupling them to plasmonic elements [1]. I will then follow by explaining the use of III-V nanowires for solar cell applications. I will show how, by choosing the adequate diameter and length, it is possible to obtain absorption cross-sections much larger than the nanowire physical size. This concentration effect can be used to increase the efficiency of nanowire-based solar cells and to reduce considerably the use of materials [2].

References

[1] A. Casadei et al , Scientific Reports 5, 7651 (2015)

[2] P. Krogstrup et al, Nature Photon. 7, 306 (2013) ; M. Heiss et al, Nanotech. 25, 014015 (2014)

3:00pm **EM+EN-ThA3 Formation of Wurtzite Phase by Si Doping and its Effect on the Optical Properties of GaAs Nanowires grown on Si Substrates by a Catalyst-free MBE-VLS Technique**, ***Marina Nakano***, *K. Sugihara, D. Ohori, K. Sakai,* Univ. of Miyazaki, Japan, *H. Amano, Y. Honda,* Univ. of Nagoya, Japan, *T. Ikari, A. Fukuyama*, Univ. of Miyazaki, Japan

GaAs nanowires (NWs) are expected to applying to optoelectronic devices. However, material properties have not been understood yet due to a presence of impurity and defect level related to an involved catalyst which was inevitable for growing nanowires. Recently, we succeeded in fabricating the catalyst-free GaAs NWs on a (111) Si substrates using a combination of molecular beam epitaxy and vapor-liquid-solid method [1]. The NW had two kinds of crystalline phases, a zinc-blend (ZB) and a wurtzite (WZ) structures [2]. We found the amount of WZ phase increased with increasing the amount of Si-doping by using high-resolution X-ray diffraction and transmission electron microscope [3]. In this study, we investigate the electronic band structure of Si-doped GaAs NWs by using a photoreflectance (PR) and a photoluminescence (PL) techniques and discuss the effect of Si-doping on the optical properties.

Three kinds of samples with different Si cell temperatures at 1015, 1065, and 1150ºC were grown. The average diameter and length of NWs were 60 nm and 35 mm, respectively. The amount of Si doping was evaluated by a carrier concentration estimated from a Hall measurement. The lowest hole concentration was 5.5×10^{17} cm^{-3} for the sample grown at 1015 ºc and increased about an order by increasing the cell temperature. PR and the PL emission light were carried at 4 K.

The crystallographic investigations showed that the amount of secondary WZ phase increased with increasing the Si-doping. Three critical energies were observed at 1.51, 1.49 and 1.43 Ev in the PR. The first two signals were observed for all samples and attributed to band to band and band to Si acceptor transitions, respectively. Since the signal at 1.43 Ev appeared only in high Si-doping sample with high amount of WZ phases, this is due to the band to band transition at the interface between the two different crystalline phases. In the PL spectra, three other emission peaks were observed at 1.46, 1.42 and 1.37eV. The intensities of these peaks changed for the samples with different cell temperature, these may be due to impurity and defect levels in nanowires. Si dopant itself as well as different crystal structure affect the electron transition. Since the interface transition observed at 1.43 Ev becomes dominant, emissions through such impurities were hidden for the sample with highest Si-doping. Temperature dependences of the PR and

PL spectra will be discussed for further understanding the effect of Si-doping.

[1] J. H. Paek et al., Phys. Stat. Sol. (c) 6, 1436 (2009).

[2] D. Spirkoska et al., Phys. Rev. B 80, 245325 (2009).

[3] A. Suzuki et al., Jpn. J. Appl. Phys. 54, 035001 (2015).

3:20pm **EM+EN-ThA4 Nanowire Enabled 3-Dimensional Band Engineering for Efficient Next Generation Solar Cells**, ***Esther Alarcon Llado***, Ecole Polytechnique Fédérale de Lausanne (EPFL), Switzerland, *O. Demichel,* Universite de Bourgogne, France, *A. Fonctuberta i Morral*, Ecole Polytechnique Fédérale de Lausanne (EPFL), Switzerland

Next generation photovoltaics (PV) aim to achieve large currents at high voltage by new materials and device concepts that overcome the main efficiency losses in traditional solar cells. Intermediate band solar cells (IBSCs) are a class of next generation PV where multi-energy levels in the semiconductor enable the scavenging of low energy photons and converting them into high voltage electrons. IBSCs have only been recently proven with highly mismatched alloys, however with very little efficiencies. The main challenge is the short lifetime of electrons at intermediate band states.

In this regard, the nanowire (NW) geometry offers potential advantages in the solar energy conversion process. Due to their richness in structure and morphology combined with doping and bandgap engineering, NWs provide an opportunity for new charge separation mechanisms.

In this work we propose a new IB-based solar cell design that is advantageously benefited from nanostructuring. We propose the use of core-shell heterostructures in order to reduce the optical coupling between the different band states in a three-level IBSC. Taking advantage of the intrinsic anisotropy of the nanowire geometry, the fundamental idea here is that excitons are separated by the heterostructure along the radial direction, while carrier extraction is performed along the axial direction. As a result, mid-gap recombination rate is reduced by several orders of magnitude.

On the other hand, it is known that optical resonances in NWs result into light self-concentrating effects that allow high absorption with reduced material. What's more, light resonances in NWs leave a very specific spatial distribution of light inside the nanostructure. By tuning the geometrical parameters of the NW, one can guide light around different regions in the NW depending on the photon energy. A combination of both electrical and morphological engineering, can lead to high efficiency PV.

4:00pm **EM+EN-ThA6 Effect of Internal Electric Field on the Miniband formation of Multi Quantum Well Solar Cell Structures Investigated by a Photoreflectance and a Photothermal Spectroscopy**, ***Tsubasa Nakamura***, *K. Matsuochi, T. Murakami, H. Suzuki,* University of Miyazaki, Japan, *K. Toprasertpong, M. Sugiyama, Y. Nakano,* The University of Tokyo, Japan, *T. Ikari, A. Fukuyama*, University of Miyazaki, Japan

Insertion of a multiple quantum-well (MQW) structure into the absorbing layer of solar cells is promising for accomplishing higher conversion efficiency. Recently, a MQW with a very thin barrier structure has been proposed to enhance the conversion efficiency [1]. The coupling of the wave functions between adjacent quantum wells causes a mini-Brillouin zone along the growth direction, which results in the formation of miniband. We have discussed carrier escaping mechanism in MQW by using photoreflectance (PR) and photothermal spectroscopy (PPT) and found that internal electric field in the QW region might affect the recombination probability [2]. In this study, we investigate the effect of internal electric filed on the miniband width.

Three kinds of MQW samples were grown by a metal-organic vapor phase epitaxy technique. Two GaAs p-i-n solar cell structure samples with MQWs in the i-layer were prepared. The doping levels in the p- and n-type layer were changed and this induced the different strength of the electric field in the absorbing layer. Another sample had GaAs n-n structures without any electric field in the absorbing layer. The thicknesses of the well barrier were changed from 2 to 6 nm for discussing the detailed miniband formation. PR and PPT measurements were carried out at room temperature. The miniband width was estimated from the difference of the peak energies of the PR modulus spectra. The lower and higher energy peak correspond to the energies of bottom and top of the miniband, respectively. The PPT method is used to detect the heat generated by non-radiative recombination of photo generated carriers. The miniband width was also calculated from the Gaussian decomposition technique of the observed PPT spectra [3].

Decrease of the miniband width by increasing the barrier width was observed for all samples. This is coincide with the theoretical prediction. The miniband width for n-n structure is considered to be larger than that of p-i-n structure. Applied electric filled may reduce the wave function overlapping between the adjacent wells. The increase of the miniband width by the electric field for the p-i-n structure sample was observed. However, the increase of the miniband widths for n-n structure could not be confirmed from the PR spectra. Since the PPT measurement is more sensitive for estimating the band edge transition, effect of the electric field may be more clearly observed by comparing the PR and PL spectra.

[1] Y. Wang, et al., J. Cryst. Growth 352, 194 (2012).

[2] T. Aihara et al., J. Appl. Phys. 116, 044509 (2014).

[3] T. Aihara et al., J. Appl. Phys. 117, 084307 (2015).

4:20pm **EM+EN-ThA7 Controlling Light Absorption with Nanophotonics**, ***Vivian Ferry***, University of Minnesota **INVITED**

Luminescent solar concentrators (LSCs) offer many advantages over traditional concentrator geometries. As opposed to concentrators that rely on tracking, LSCs operate under both direct and diffuse illumination and require the solar cell to only be efficient at a small range of wavelengths. In practice, most LSCs suffer losses from reabsorption of emitted light, non-unity quantum yields, and incomplete light guiding to the solar cell. Here we combine tunable lumophores based on quantum dot heterostructures with photonic designs to improve the concentration efficiency of LSCs and study light propagation within the device.

To achieve high concentration ratios it is critical to have high effective Stokes shifts, high quantum yields, and to reduce escape cone losses. We synthesized a series of core-shell nanocrystal lumophores that exhibit tunable emission. We show how the narrow emission bandwidth of these nanocrystals enables the use of a 1D photonic mirror on the top surface of the device, designed to admit incident sunlight and trap luminesced light from the nanocrystal. In combination, the concentration ratios from these devices exceed the performance of dyes with higher quantum yields but broader emission. Another approach to photonic LSCs is to restrict the angle of emission from the lumophores to promote coupling to the total internal reflection modes of the LSC. This talk will discuss designs for the latter approach and compare achievable concentration factors.

The second portion of the talk will discuss light management strategies for solid-state lighting, and the incorporation of plasmonic nanostructures to enhance light outcoupling from solid-state devices. This section of the talk will compare and contrast plasmonic structures for solar cells and solid-state lighting, and discuss ways that design rules should be adjusted for different materials systems.

5:20pm **EM+EN-ThA10 Symmetry-Breaking in Periodic Nanostructures for Enhanced Light Trapping in Organic Solar Cells**, ***Seok Jun Han***, *S. Ghosh, O.K. Abudayyeh, E.J. Martin, J.K. Grey, S.M. Han, S.E. Han*, University of New Mexico

In this study, we introduce a new light-trapping scheme for organic solar cells by systematically breaking the symmetry in periodic nanostructures on the bottom metal contact. To create symmetry-breaking metal nanostructures, we start by fabricating a mold from a crystalline silicon (c-Si) substrate. We intentionally misalign the etch mask with respect to [110] crystallographic orientation of the c-Si. Subsequently, silver is sputter-coated over the nanoscale recess created in the c-Si substrate to create the metal nanostructures, and an organic photoactive material, PCPDTBT, is spin-coated on the silver layer. The enhancement in light absorption is achieved at surface plasmon resonances at the polymer-metal interface. We demonstrate that surface plasmon band structure can be tailored by symmetry-breaking. In experiment, we increase the number of surface plasmon bands in the visible spectrum and locate the bands at the desired wavelengths by controlling the symmetry. In general, by patterning a flat film in symmetry-breaking structures, absorption is enhanced from 65% to 85% in a broad short wavelength spectrum. Moreover, the absorption spectrum is extended into long wavelengths by 20 nm. We expect that our low-cost, symmetry-breaking fabrication strategy would be scalable and lead to a manufacturable process for efficient light-trapping in organic photovoltaic devices.

5:40pm **EM+EN-ThA11 Symmetry-Breaking in Light-Trapping Nanostructures on Silicon**, ***Sang Eon Han***, *S.J. Han, S. Ghosh, T. Cai, B. Hoard, S.M. Han*, University of New Mexico

In thin-film photovoltaics, highly absorptive materials are conventionally used. However, these materials have achieved efficiencies that are not comparable to those of thick crystalline silicon (c-Si) photovoltaics and, in some cases, suffer from their toxicity and low supply. A viable solution to these problems would be to use c-Si for thin-film photovoltaics. However, thin c-Si films absorb sunlight weakly because of its indirect band gap and strong light-trapping should be provided to achieve high efficiency. For thin-film photovoltaics, nanoscale structures are typically involved for light trapping because the film thickness becomes comparable to the wavelength of sun light. While diverse nanostructures have been studied to break the light-trapping limit of geometric optics, known as the Lambertian limit, highly efficient nanostructures that can be easily manufactured have not been demonstrated. We have previously predicted that symmetry-breaking

in light-trapping periodic nanostructures on thin films can approach the Lambertian limit very closely. Herein, we will present how the systematic symmetry-lowering increases light-trapping in c-Si thin-film photovoltaics. We will demonstrate the experimental realization of such low-symmetry structures using simple wet etching methods on c-Si(100) wafers without any off-cut, tilt angle. Further, we will discuss the optical characterization of our fabricated structures on thin c-Si films.

Electronic Materials and Processing
Room: 210E - Session EM+MS-ThA

III-N Nitrides II
Moderator: Nikolaus Dietz, Georgia State University

2:20pm **EM+MS-ThA1 Accelerating Adoption of Wide Band Gap Semiconductors though Manufacturing Innovation**, ***John Muth***, North Carolina State University **INVITED**

As part of the national strategy for the United States to compete in the increasingly competitive global marketplace, a National Network for Manufacturing Innovation (NNMI) is being implemented to create a competitive and sustainable research-to-manufacturing infrastructure for U.S. Industry, academia and government to solve industry relevant problems.

PowerAmerica a $146 million dollar investment by the Department of Energy, Industry and the State of North Carolina is the second NMNI to be announced and with its industry and academic partners has initiated 20 projects focused on manufacturing wide band gap semiconductor devices and demonstrating their advantages in power electronic applications.

The mission of PowerAmerica is to develop advanced manufacturing processes to enable cost competitive, large-scale production of wide bandgap semiconductor-based power electronics, which allow electronic systems to be smaller, faster and more efficient than power electronics made from silicon. Innovations in manufacturing, improvements in reliability and demonstrations of system level advantages are important aspects of PowerAmerica's strategy to accelerate the adoption of wide band gap semiconductors into power electronics.

The number of systems that use power electronics between generation and use is about 20% today and is expected to grow to about 80% by 2030 a wide variety of technologies will be disrupted by the system advantages offered by wide band gap semiconductors. These include electric vehicles, motor drives, data centers, smart grid, photovoltaic and other renewable energy systems as well as niche applications in consumer electronics. In addition to the technical work performed in PowerAmerica a significant effort is being put towards workforce development and education. These efforts will prepare industry to compete in and the next generation of engineers and workers to lead the world into a brighter, more energy efficient world.

3:00pm **EM+MS-ThA3 InGaN/GaN Nanostructures for Efficient Light Emission and White Light Emitting Diodes**, *Y. Nakajima*, ***P. Daniel Dapkus***, *Y. Lin*, University of Southern California **INVITED**

InGaN/GaN quantum well LEDs that form the basis for efficient solid state lighting exhibit properties that limit the ultimate efficiency that can be achieved for this application. Among these deleterious properties are a high current efficiency decrease not related to heating – efficiency droop – and reduced efficiency in the green and yellow regions of the spectrum. It has been speculated that one of the causes for the droop and the reduced efficiency of green and yellow emitting diodes is the presence of piezoelectric fields that result from the growth of these structures on the polar (0001) plane of GaN.

In this work we report investigations of the formation of GaN nanostructures that are defined by non-polar and semi-polar planes that act as templates upon which quantum well active regions are formed. Nanorods, nanosheets, and nanostripe pyramids are described that are predominantly defined by {1-100}, {11-20}, and semi-polar planes and act as templates for the growth of InGaN/GaN multiple quantum well active regions. We describe the properties of blue LEDs formed on these templates and compare them to devices made on planar (0001) substrates.

Efficient green emitting LEDs and monolithic white light emitting LEDs require the extension of the range of efficient light emission in the InGaN / GaN materials system. We demonstrate high efficiency green and yellow light emitting multiple quantum well (MQW) structures grown on GaN nanostripe templates. The nanostripe dimensions range from 100 nm to 300 nm and have separations that range from 300 nm to 1 micron. Such small lateral dimensions are chosen to promote the elimination of threading dislocations from the structures. Nanostripes with various nonpolar and semi polar surfaces are grown with selective area growth on patterned c-plane GaN where the mask openings are oriented between the [10-10] and [11-20] directions. With stripes are aligned along the [10-10] and [11-20] directions, the sidewalls can be controlled to be nearly vertical or inclined and intersecting. Both shapes were examined and MQWs were grown on these different stripes. Photoluminescence (PL) measurement shows that MQWs grown on stripes with (10-11) surfaces and triangular shape emit the longest peak wavelength and have the best surface stability. Efficient PL emission peak wavelengths as long as 570 nm are realized on the triangular stripes with (10-11) surfaces by optimizing the MQW growth conditions for long wavelength emission. LED structures that utilize MQWs grown on nanostripes with (10-11) surfaces were fabricated to further demonstrate the viability of the approach.

4:00pm **EM+MS-ThA6 Tuning Bandgap Through Cation Ordering in New PV Materials**, ***Steve Durbin***, *R.A. Makin*, *N. Feldberg*, Western Michigan University, *J.P. Mathis*, *N. Senabulya*, *R. Clarke*, University of Michigan

There continues to be considerable interest in so-called earth abundant element compound semiconductors, of which we have multiple candidates at present. One material worth considering, $ZnSnN_2$, is properly termed a ternary heterovalent compound and is a member of the more general family of II-IV-V_2 semiconductors. It is analogous to InN, whereby pairs of indium atoms are replaced by a periodic arrangement of a Zn and Sn atom, and in that way is related to CIGS as that material corresponds to II-VI semiconductors. Although $ZnSnN_2$ is predicted to crystallize in an orthorhombic lattice with a bandgap of approximately 2.0 eV (calculations reported in the literature vary somewhat), we have observed that single crystal thin films grown by plasma-assisted molecular beam epitaxy are more likely to form in a wurtzitic lattice, with a lower electronic bandgap energy. In fact, we have recently observed both optical absorption and x-ray emission spectroscopy results on a series of films which agree with density functional theory calculations predicting a bandgap as small as 1 eV - the direct consequence of disorder in the cation sublattice. Careful tuning of the growth parameters enables the degree of order to be varied, and consequently the bandgap energy as well. This provides the intriguing possibility of tuning the bandgap through the growth process, as opposed to the traditional approach of alloying. The optimal bandgap energy of approximately 1.5 eV would therefore be an intermediate state between the two extremes.

4:20pm **EM+MS-ThA7 Comparison Studies of GaN Grown with Trimethylgallium and Triethylgallium for Optoelectronic Applications**, ***Mustafa Alevli***, Marmara University, Turkey, *A. Haider*, Bilkent University, Turkey, *N. Gungor*, Marmara University, Turkey, *S. Kizir*, *S. Alkis*, *A.K. Okyay*, *N. Biyikli*, Bilkent University, Turkey

Si is famous for the well-developed mature CMOS technology and a promising substrate for GaN due to its wafer size, low material cost, and possible integration with the CMOS. However, it is very difficult to deposit high-quality GaN films on Si due to its high deposition temperature which results in inter-diffusion at the GaN/Si interface and the relatively large lattice mismatch. Atomic layer deposition is a low temperature technique that can provide an alternative path for the deposition of GaN on Si.

In this study, GaN materials were grown at 200°C by two different kinds of metalorganic precursors, one by using trimethylgallium (TMG) and another by using triethylgallium (TEG) as gallium sources. It is reported that the carbon concentration was fifty times higher in the GaN films grown by TMG precursor than in that grown by TEG precursor. As it is going to be shown in this contribution, optical and electrical properties of Hollow cathode plasma-assisted atomic layer deposition of crystalline GaN films will be presented. When TMG pyrolyzes, it introduces more reactive CH_3 radicals in to the CVD reactor when it is compared to TEG precursor. It means that TMG enhances carbon incorporation in epitaxial film structure.

Spectroscopic ellipsometry studies on GaN films shows that refractive indices of GaN films increase when TMG was used as metalorganic precursor. The increase in the refractive index values indicates that the crystalline quality of GaN films improved with the use TMG. The change in the metalorganic precursor did not affect either the Bragg peak positions or crystalline phase of deposited GaN films. The grazing-incidence XRD patterns of both GaN films revealed that the films are polycrystalline with hexagonal wurtzite structure and are referring to (100), (101), (002), (102), (110), and (103) planes. The increase in the intensity and improvement in the FWHM value of the (002) peak also showed that the crystallinity improved for TMG grown GaN films. Further More,. The effect of alkyl precursors is also studied by a variety of characterization techniques Fourier Transform infrared reflectance, optical transmission, X-ray photoelectron spectroscopy, current-voltage characteristics of which the results will be discussed in detail.

This work is supported by TÜBİTAK project #114F002.

4:40pm **EM+MS-ThA8 Growth Control of InGaN Alloys and Nanostructures by Migration-Enhanced, Plasma-Assisted MOCVD**, ***Daniel Seidlitz***, *I. Senevirathna, Y. Abate, N. Dietz,* Georgia State University, *A. Hoffmann*, Technical University Berlin, Germany

This contribution will present results of the structural and optoelectronic properties of InN and InGaN alloys and nanostructures as a function of temperature, reactor pressure and the temporal injection of metalorganic precursors and plasma activated nitrogen species (e.g. N*/NH*/NH_x*).

Migration-enhanced plasma-assisted metal organic chemical vapor deposition (MEPA-MOCVD) is utilized for the growth of InN and InGaN layers and nanocomposites at growth temperatures in the range of 450°C and 700°C. The custom-built MEPA-MOCVD system consists of a showerhead reactor combined with a hollow cathode (HC) plasma source (Meaglow) powered by a high-frequency (13.56 MHz) RF generator with a output power up to 600W. The HC plasma source creates reactive nitrogen fragments, which afterglow region approaches the growth surface. Plasma emission spectroscopy (PES) is utilized for real-time information about the formation and concentration of plasma generated active species. Added provisions allow a spatial and temporal injection of both, nitrogen and metalorganic precursors and enable the control of the epitaxial layers and their composition during the growth process.

Ex-situ investigations by Atomic Force Spectroscopy (AFM) as well as Fourier Transform Infrared Reflectance (FTIR) and Raman spectroscopy assess structural and optoelectronic properties (e.g. surface roughness, high-frequency dielectric constant e_∞, film thickness, etc.) of the deposited InN and InGaN nanostructures.

Correlation of the in-situ obtained plasma characteristics with the ex-situ results of the structural and optical properties of the InN and InGaN nanostructures are provided, as well as correlations between plasma afterglow regime position above the growth surface and the epitaxial layer properties. The aim of these studies is to access the phase stability regime of indium-rich ternary group III-nitrides as a function of growth temperature, kinetic energy of plasma species, reactor pressure, and temporal and spatial precursor supply.

5:00pm **EM+MS-ThA9 GaN on Rare-earth Oxide Buffer –A New Player in GaN-on-Si Technology**, ***Rytis Dargis***, *A. Clark*, Translucent Inc.

We present the results of process development for GaN MOCVD epitaxial growth on Si using single crystal rare-earth oxide buffer layers. Advantage of this technological approach over traditional GaN-on-Si that uses a AlN nucleation buffer is the chemical isolation of the Si substrate from the group-III metals thereby preventing Si diffusion into the III-N layer. This removes one of the main breakdown failure modes being the silicon doped interface. Additionally, the relatively high breakdown electric field of rare-earth oxides (e.g. 4MV/cm for erbium oxide) can be used as part of the overall vertical breakdown thereby reducing the thickness of the III-N layer structure without impairment of electrical breakdown properties of a power device. This is important to the overall process since thinner GaN not only reduces MOCVD cycle time but results in lower stress in the structure. Additionally, thermal and chemical stability of the oxides opens up opportunity for implementation of a more flexible process for GaN-on-silicon including solutions used in GaN-on-sapphire.

Two types of the oxide buffers with thickness of 300 nm were grown of Si (111): single Er_2O_3 and double layer Er_2O_3-Sc_2O_3 structure were employed. Robustness and scalability of the oxide process make it suitable for manufacturing.

To validate the technology, the standard AlN-first process was used. GaN with thickness of 2 µm was grown in a state of the art 200mm manufacturing tool. It demonstrated excellent management of the stress in the structure with 25µm convex curvature, superior surface morphology (RMS = 0.56 nm, Z-range = 4.1 nm) and good crystal structure (GaN (002) FWHM = 561 arcsec, GaN (102) FWHM = 907 arcsec).

Our newly developed GaN-first MOCVD process, which is based on a typical GaN-on-sapphire process, uses nitridation and low temperature GaN buffer. During the growth, the upper part of the oxides is transformed into rare-earth nitride with lattice constant smaller than that of the oxide and consequently lower lattice mismatch to GaN (e.g. lattice constant mismatch between GaN and ScN is approximately -0.2%). The GaN layers with total thickness of 2.5 µm grown on the both types of the buffers exhibit smooth surface with RMS < 1 nm and Z-range <10 nm. The wafers exhibit good structural quality with X-ray diffraction GaN (002) peak FWHM of 540 arcsec and 684 arcsec for GaN on Er_2O_3 layer and Er_2O_3/Sc_2O_3 stack respectively. SIMS data shows no oxygen or rare-earth metal diffusion into the GaN.

5:20pm **EM+MS-ThA10 Plasma Enhanced Atomic Layer Deposition of Al_2O_3 on AlGaN/GaN High Electron Mobility Transistors**, ***Xiaoye Qin***, *R.M. Wallace*, University of Texas at Dallas

Metal insulator semiconductor AlGaN/GaN high electron mobility transistors (MISHEMTs) are promising for power device applications due to a lower leakage current than the conventional Schottky AlGaN/GaN HEMTs. Among a large number of insulator materials, Al_2O_3 dielectric layer, deposited by atomic layer deposition (ALD), is often employed as the gate insulator because of a large band gap (and the resultant high conduction band offset on AlGaN)[1], high breakdown field, conformal growth, and a relatively high dielectric constant. However, the thermal ALD Al_2O_3 does not passivate the surface effectively according to our previous work.[1–4] In this work, the half cycle study of plasma enhanced atomic layer deposited (PEALD) Al_2O_3 on AlGaN is investigated using *in situ* X-ray photoelectron spectroscopy (XPS), low energy ion scattering (LEIS) and *ex situ* electrical characterizations. A faster nucleation or growth is detected in PEALD than thermal ALD using an H_2O precursor. The PEALD Al_2O_3 layer decreases the gate leakage current as the ALD Al_2O_3. Importantly, the remote O_2 plasma oxidizes the AlGaN surface slightly at the initial stage, which passivates the surface and reduces the OFF-state leakage. This work demonstrates that PEALD is a useful strategy for Al_2O_3 growth on AlGaN/GaN devices.

This work was supported by the Asian Office of Aerospace Research and Development (AOARD) through the Air Force Office of Scientific Research (AFOSR) under Grant No. FA2386-14-1-4069.

Reference

[1] X. Qin, L. Cheng, S. McDonnell, A. Azcatl, H. Zhu, J. Kim, and R.M. Wallace, J. Mater. Sci. Mater. Electron. In press (2015).

[2] X. Qin, B. Brennan, H. Dong, J. Kim, C.L. Hinkle, and R.M. Wallace, J. Appl. Phys. **113**, 244102 (2013).

[3] X. Qin, A. Lucero, A. Azcatl, J. Kim, and R.M. Wallace, Appl. Phys. Lett. **105**, 011602 (2014).

[4] X. Qin, H. Dong, J. Kim, and R.M. Wallace, Appl. Phys. Lett. **105**, 141604 (2014).

Selective Deposition as an Enabler of Self-Alignment Focus Topic
Room: 210F - Session SD+AS+EM+PS-ThA

Process Development for Selective Deposition and Self-aligned Patterning
Moderator: John Ekerdt, The University of Texas at Austin, Chuck Winter, Wayne State University

2:20pm **SD+AS+EM+PS-ThA1 Surface Chemistry Related to Selective Deposition**, ***Suvi Haukka***, ASM Microchemistry Ltd., Finland, *J.W. Maes*, ASM Belgium **INVITED**

The shrinking device dimensions in semiconductor manufacturing call for new innovative processing approaches. One of these considered is selective deposition which has gained increasing interest among semiconductor manufacturers today. Selective deposition would be highly beneficial in various ways, for instance, it would allow a decrease in lithography and etch steps reducing the cost of processing and enable enhanced scaling in narrow structures making bottom up fill possible. Chemical vapor deposition (CVD) and especially atomic layer deposition (ALD) as very surface sensitive techniques are considered enabling techniques.

Selective deposition typically deals with a selective deposition method where, for instance, a metal layer is selectively deposited on metal surface over dielectric surface, or a dielectric layer is selectively deposited on hydrophilic polymer over a more hydrophobic polymer. In most of the selective deposition schemes of today the passivation is used for the surface on which no deposition is desired. The most known method is to use SAM´s (self-assembled monolayers) which are silicon compounds with long carbon chains. Besides the SAM passivation of surfaces also the clever selection of precursors with built-in selectivity in certain process conditions could be applied.

In this paper, the chemistry challenges in the various selective deposition approaches and passivation means are reviewed. In addition, results from the selective deposition of metal on metal over dielectric surface in a Cu capping application and from selective strengthening of DSA (direct self-assembly) layers are presented.

3:00pm **SD+AS+EM+PS-ThA3 Selective Deposition - The New Patterning Paradigm?**, ***Florian Gstrein***, Intel Corporation **INVITED**

Top-down patterning techniques based on optical lithography have made consumer electronics ever more powerful, ubiquitous and affordable. This is largely due to the ability of lithographic techniques to transfer trillions of mask features to wafers at defect densities approaching virtually zero in high-volume manufacturing. While the resolution of optical lithography tools is typically considered to be the main challenge for continued device scaling, it is actually accurate pattern placement, which has emerged as the biggest concern. Novel bottom-up patterning approaches such as selective deposition are needed to overcome shortcomings in pattern placement accuracy.

The talk will first outline the challenges patterning processes based on 193i pitch division and EUV lithography face in terms of alignment accuracy and how complementary patterning techniques such as selective deposition can reduce pattern placement errors. One of the great challenges of selective deposition is defect mitigation, especially as the sensitivity to killer defects increases as device dimensions scale. Defect mitigation requires a fundamental understanding of the chemical selectivity of surfaces. While molecules can recognize chemical functionality on a surface, selective deposition processes based on atomic layer deposition (ALD) or chemical vapor deposition (CVD) are exceedingly rare and largely limited to specific precursors and substrates. For metal deposition, inherent selectivity was achieved through judicious precursor ligand design. Experimental results will be presented in the context of a theoretical investigations aimed at calculating the kinetic barriers that govern the selectivity of metal deposition. The use of self-assembled monolayers (SAMs) as passivants and/or blocking layers for subsequent deposition is an attractive way of overcoming the non-selectivity of many CVD or ALD processes. Here, the critical parameters for selective blocking are choice of the terminal group, surface termination, carbon chain length, and proper precursor choice. Using SAMs, selective deposition of dielectrics with respect to a variety of surfaces was achieved. The talk will conclude with our vision of how defects can be mitigated: It comprises a fundamental understanding of the chemical nature of the surface, precursors with high kinetic barriers for defect formation, passivation of defect nucleation sites, and the removal of defects post deposition. Selective deposition, if properly resourced and developed, can provide powerful means to future scaling and is one way of ensuring that patterning will continue to support Moore's Law in the foreseeable future.

4:00pm **SD+AS+EM+PS-ThA6 Area-Selective Molecular Layer Deposition: Enhanced Selectivity via Selective Etching**, ***Richard Closser***, *D.S. Bergsman, F.H. Minaye Hashemi, S.F. Bent*, Stanford University

Recent developments in electronic devices are pushing toward smaller and smaller features of both metal and dielectric patterns, along with a desire to produce selectively deposited organic thin films on such patterns. Techniques that allow for a high degree of control over the thickness and conformality of organic thin films, such as molecular layer deposition (MLD), are ideal candidates to meet these selective deposition requirements. Using MLD, several types of thin film polymers can be deposited with angstrom-level control due to the sequential, self-limiting surface reactions resulting in monomer-by-monomer growth. Selectivity in the MLD polymer growth is then achieved by utilizing the chemical functionally between the solid substrate surface and the gas phase monomer precursors.

Previously, we have shown the ability to selectively deposit thin film polymers by MLD onto pre-patterned metal and dielectric substrates by utilizing a blocking layer of octadecylphosphonic acid (ODPA) self-assembled monolayers (SAMs) that deposits onto metals more readily than onto dielectric films. Although this process can prevent MLD for up to 6 nm of deposition, selectivity of polymer growth is lost for thicker films, and therefore we are exploring new methods for increasing the MLD selectivity. For the current studies, ODPA SAM is deposited onto a patterned metal/dielectric (Cu on SiO_2) substrate to act as the MLD blocking layer. Once the SAM is fully deposited, polyurea films are grown onto the substrate by MLD to a desired thickness which can be controlled by the number of monomer dose cycles used. An acid etchant is then used to remove the surface oxide of the metal along with the SAM layer while leaving intact the polymer film deposited onto the dielectric. X-ray photoelectron spectroscopy, Auger electron spectroscopy, and ellipsometry measurements show that this process removes undesired MLD film that was deposited on the metal. Studies on patterned substrates confirm selective polymer film growth onto the dielectric over the metal. The etchant removal technique thus increases the selectivity of MLD growth by more than an order of magnitude when compared to the SAM blocking layer alone. Due to the increased selectivity with the etching based process, selective deposition of MLD films as thick as 12 nm have been demonstrated. Atomic force microscopy results show slight surface roughening due to etching while the bulk of the metal/dielectric pattern remains intact. This increase in MLD selectivity should allow for novel applications of selective polymer film deposition.

4:20pm **SD+AS+EM+PS-ThA7 Nucleation and Steady State ALD of Metallic Tin Using $SnCl_4$ and a Silyl Pyrazine Reducing Agent**, ***Eric Stevens***, *M.B. Mousa, G.N. Parsons*, North Carolina State University

Metal atomic layer deposition (ALD) processes are typically limited to noble, high work-function metals where uniform nucleation and conformal growth can be problematic. Recent work suggests that 1,4-bis(trimethylsilyl)-1,4-dihydropyrazine (DHP) could be an effective reducing agent for deposition of metals with highly negative electrochemical potentials. This work investigates DHP as a potential reducing agent for tin metal ALD using tin (IV) chloride ($SnCl_4$).

Experiments were carried out in a custom-built, hot-wall reactor using N_2 carrier gas, an operating pressure of 1.3 Torr, and temperatures between 130 and 170°C. The DHP source was heated to 70°C to maintain a vapor pressure ~1.2 Torr. Initial films were deposited at 130°C on silicon using a $SnCl_4/N_2/DHP/N_2$ exposure sequence of 4/50/10/50 seconds, then analyzed ex-situ by X-ray photoelectron spectroscopy (XPS) with Ar depth profiling. In sputtering deeper into the film, XPS exhibited both Sn-Sn and Sn-O peaks at 485 and 486.7 eV, respectively, where a decrease in Sn-O and an increase in Sn-Sn peak intensities suggests native oxidation of the film upon exposure to air. Furthermore, 7% Cl and 19% N were found in the films after sputtering, presumably from an incomplete reaction and/or incorporation of reaction byproducts.

To better understand surface reactions and growth mechanisms, we characterized the ALD process at 130, 150, and 170°C using *in situ* quadrupole mass spectrometry (QMS) and quartz crystal microbalance (QCM). QCM analysis at 130 and 150°C showed continued growth with extended exposures, consistent with non-ALD growth. Deposition at 170 °C was more repeatable and more closely approached surface saturation. At 170°C, QCM showed a clear mass increase during the $SnCl_4$ dose and a corresponding mass decrease during the DHP dose, consistent with DHP removing Cl and reducing the Sn-Cl surface. Moreover, the QMS results showed peaks exclusively during DHP doses at m/z values of 80 (pyrazine) and 65, 93, 95 (trimethylsilyl chloride), which are the most probable byproducts of DHP reacting with a chlorinated surface.

Using gold-coated QCM crystals at 170°C, Sn growth proceeds slowly for the first ~150 ALD cycles, whereas growth on QCM crystals previously coated with Sn show a more rapid transition to steady-state growth (<20 cycles). We are currently investigating the nucleation on different substrates and how process conditions can be tuned to achieve selective deposition. Understanding the surface reaction and growth mechanisms of tin metal deposition using DHP could provide a foundation for deposition of metal thin-films that were previously unattainable.

4:40pm **SD+AS+EM+PS-ThA8 Determination of the Minimum Saturating Dose during Atomic Layer Deposition of Alumina and Titania on Si(100) and Si(100)-H**, *D. Dick,* University of Texas at Dallas, ***Joshua Ballard***, *J. Randall,* Zyvex Labs, *Y.J. Chabal*, University of Texas at Dallas

Atomic layer deposition (ALD) has become an important process step in semiconductor manufacturing, where the self-limiting nature of each step of the process permits atomic scale control over the ultimate layer thickness in addition to relatively fast processing with high pressure reactors. However, it has been shown that ALD can be used to selectively deposit material onto patterned surfaces, requiring not only saturation of each deposition cycle in desired areas but also suppression of deposition in those areas where it is undesirable. One mechanism for improving practical selectivity would be to find the minimum exposure that is saturates the growth where desired in order to avoid excess overall reaction probability in areas where inhibited growth is preferred.

To investigate this, we have examined the deposition in vacuum ("UHV ALD") of Al_2O_3 and TiO_2 with TMA and $TiCl_4$, respectively, on both hydrophobic, H-terminated Si(100) surfaces and hydrophilic OH-terminated Si(100) surfaces prepared by H_2O exposure of clean Si(100)-(2x1) surfaces. Surface reactions and relative coverages are determined by in-situ IR spectroscopy, and ex-situ XPS. We find that good selectivity can be achieved at 150°C. Preliminary data and calculations also suggest that an initial wetting layer of TMA on clean Si(100) promotes subsequent growth of TiO_2 or other high-k dielectrics. Finally, we will discuss how these findings have made it possible to develop a full multi-cycle process for a custom low-pressure ALD system equipped with scanning tunneling microscopy and atomic force microscopy.

5:00pm **SD+AS+EM+PS-ThA9 Selective Growth of GeSbTe Phase-Changing Materials Utilizing Self-Aligned Confined Structure**, ***ByungJoon Choi***, Seoul National University of Science and Technology, Republic of Korea, *T. Eom, C.S. Hwang*, Seoul National University, Republic of Korea

GST Phase changing material, typically GeTe–Sb_2Te_3 pseudo-binary solid solution, has been extensively studied for rewritable digital versatile optical disks or phase change random access memory (PcRAM), on account of the drastic change of its optical reflectivity or electrical resistivity between amorphous and crystalline phases. As the device size of PcRAM is scaled down, GST materials should be confined into the contact-plug for reducing its programming current, which cannot be achieved by any physical deposition method.

Among the various metal-organic (MO) precursors, the combination of $Ge(iBu)_4$, $Sb(iPr)_3$ and $Te(iPr)_2$ has been extensively studied for plasma enhanced chemical vapor depostion or its variant methods with plasma-activated H_2 gas as a reducing agent of the MO-precursors. Plasma-enhanced pulsed CVD was attempted using the precursor pulse sequence consisting of Sb–Te–Ge–Te cycles (each elemental cycle is composed of precursor injection and Ar + H_2 plasma reduction steps). The chemical composition of the films was appropriately controlled by the cycle ratio and sequence of each precursor pulse. The linear growth with the number of cycles was shown, and the GPC (growth-per-cycle, i. e. growth rate) was determined to be 0.73 nm/super-cycle from the slope at a wafer temperature of 200°C.

Strong substrate dependency can be utilized in the selective growth of GST material on a TiN contact-plug formed in the SiO_2 inter-layer dielectric (ILD). Higher selectivity (difference of GPC) between TiN contact-plug and SiO_2 ILD layer was achieved by pulsed CVD with increasing the amount of $Te(iPr)_2$ injection. The reason for the selective growth was believed to have originated from the adverse interference of the residual gas (unreacted $Te(iPr)_2$ or its derivatives) to the chemical adsorption of Sb nuclei on the SiO_2 surface, which functions as a nucleation site for further GST growth. It was reported that amide-based Ge precursors also showed strong selectivity at a particular temperature, enabling Sb and Te precursors to be chemisorbed on the Ge seed layer, which could be utilized for selective growth of GST.

The most feasible explanation for the substrate-dependent growth behavior of the GST film is the electron donation from the substrate, which would enhance the precursor decomposition and removal of ligands from the adsorbed precursor molecules. The nucleation and growth behaviors of the GST films were studied on Si substrates with various nucleation or buffer layers. It turned out that the types of substrates have a crucial impact on the nucleation behaviors and the chemical composition of the film.

5:20pm **SD+AS+EM+PS-ThA10 Toward an All- Vapor Process for Area Selective Atomic Layer Deposition**, ***FatemehSadat Hashemi***, *S.F. Bent*, Stanford University

Modern electronic devices containing planar and 3-D structures utilize a number of metal/dielectric patterns in both the front and back end. The scaling of next generation electronic devices makes achieving these patterns increasingly difficult and motivates the development of novel processing methods. One such method−area selective deposition−has the opportunity to play an important role in significantly reducing process complexities associated with current top-down fabrication of patterned structures by eliminating some of the deposition and etching steps that are time-consuming and expensive.

Atomic layer deposition (ALD) is a good choice for area selective deposition because its chemical specificity provides a means to achieve selectivity on a spatially patterned substrate. Area selective ALD, reported previously by several groups, requires improvements for the process to be compatible with current device fabrication goals. Most previous studies of area selective ALD have achieved deposited thicknesses on the order of only a few nanometers and the selectivity was generally obtained by passivation of the surface using self-assembled monolayers (SAMs) in the regions where ALD was not desired. Existing methods are usually performed by dipping the substrates into a solution containing the SAM-forming molecules for several hours. A more desirable all-vapor process would require vapor delivery of the SAMs. This method would provide better SAM coverage on porous or three-dimensional structures, potentially decreasing the required deposition time for the passivation layer, and allowing the SAM passivation step to be integrated with the rest of the ALD process.

In this work, we investigate area selective dielectric-on-dielectric deposition by selectively depositing organic alkanethiol SAM as the blocking layer on metal parts of a metal/dielectric (Cu/SiO_2) pattern. We compare area-selective ALD achieved by introduction of the thiolate SAM in both the solution and vapor phase. We show that while in both cases the SAM can prevent subsequent deposition of metal oxide dielectric films via ALD, vapor deposition provides stronger passivation in a shorter exposure process on the metal. We also report results on regenerating the thiol SAM protecting layer from the vapor phase between ALD cycles and show that this approach is effective in improving the blocking properties of the SAM on Cu. This strategy provides the ability to significantly improve selective deposition of dielectrics. Moreover, it is a significant step toward an all-vapor process for area selective deposition, opening up the possibility for new applications in next generation electronic devices.

5:40pm **SD+AS+EM+PS-ThA11 Selective Deposition of ALD Metal oxides and Metal Thin Films by Fab-Friendly Surface Treatments**, ***Kandabara Tapily***, *K.-H. Yu, S. Consiglio, R. Clark, D. O'Meara, C. Wajda, G. Leusink*, TEL Technology Center, America, LLC

For the last 5 decades, the semiconductor industry has relied on the continued scaling down of the device feature size in order to improve performance and increase bit density according to Moore's law. However, with the delay in implementation of extreme ultraviolet lithography (EUV) in high volume manufacturing,[1] patterning beyond the 14 nm technology node is getting extremely difficult to manage due to the overlay control and the increase in manufacturing cost due to multi-layer alignments. In order to keep reducing the device feature size, new patterning solutions are needed such as selective deposition and selective etching of materials. Atomic layer deposition (ALD) has emerged as one of the leading film deposition techniques as a result of the semiconductor device scaling.[2] ALD provides excellent film control, uniformity and high conformality. ALD is highly surface reaction driven and it is possible to modify the substrate surface to activate or deactivate growth on selected area hence selective-area ALD (SA-ALD). Selective-area ALD can simplify and reduce the high manufacturing cost associated with highly aggressive patterning schemes by eliminating certain lithography steps. Thin films can now be selectively deposited or removed from a desired area. Most selective-area ALD studies in the literature are conducted with the use of self-assembled monolayers (SAMs) in order to deactivate or activate growth on certain areas.[3-5] SAMs are thin organic films that form spontaneously in tightly packed oriented molecules on solid surfaces. A key enabler of SAMs is the ability to turn these organic layers into patterned layers. However, thermal stability and the slow formation process into well packed layer are some of the major drawbacks of SAMs.[5]

In this study, a non SAMs based approach was used to inhibit ALD growth of metals and metal oxides. Using different surface treatments, it was observed the growth of the ALD thin films can be modulated, see Fig.1 and Fig.2 respectively. ALD Al_2O_3 growth was suppressed by a combination of the vapor HF and cyclical low temperature plasma hydrogen treatment and deposition. Additionally, ALD TaN growth was also inhibited by the use of a combination trimethylsilane (TMS) and dimethylamine (DMA) treatment of the surface prior to ALD deposition.

Reference

1. J. Beynet, et al, *Proc. SPIE*, 7520, 75201J (2009).

2. S. M. George, *Chem. Rev.***110**, 111 (2010).

3. ChaMarra K et al. *Nanotechnol*,***3***, 114 (2012).

4. J. C. Love et al., *Chem. Rev.*,**105**, 1103 (2005).

5. A. J. M. Mackus et al, *Nanoscale*, **6**, 10941 (2014).

Surface Science
Room: 113 - Session SS+AS+EM+EN-ThA

Atomistic Modeling of Surface Phenomena & Semiconductor Surfaces and Interfaces - II
Moderator: Talat Rahman, University of Central Florida

2:20pm **SS+AS+EM+EN-ThA1 Ideas Old and New Applied to Non-Ideal Surface Adsorption and Reaction**, ***William Schneider***, University of Notre Dame **INVITED**

Free energies of adsorption are arguably the most elementary quantities in heterogeneous catalysis. These free energies depend on the surface and adsorbate (reactant, intermediate, or product) of interest, system temperature and adsorbate coverage. The free energy represents a balance between the energetic driving force for creating bonds between an adsorbate and a surface and the entropic cost of moving an adsorbate from a fluid phase to a surface. Standard density functional theory (DFT) approaches generally begin by optimizing the location of an adsorbate on a surface, computing a binding energy, and approximating the internal, translational, and configurational contributions to the free energy. In this work we examine the reliability of standard approximations and describe easily

applied improvements that give reliable free energy estimates. We describe applications to adsorption at metal surfaces and in the pores of zeolites.

3:00pm **SS+AS+EM+EN-ThA3 Insights into the Oxidation of Stepped Cu Surfaces using Multiscale Investigations**, *Q. Zhu, W.A. Saidi, **Judith Yang***, University of Pittsburgh

Surface defects can induce non-canonical oxidation channels on metal surfaces that may lead to the formation of novel nanostructures. Recently, in situ environmental transmission electron microscopy (ETEM) experiments showed that the oxidation of stepped Cu surfaces promotes the formation of a flat metal-oxide interface through Cu adatoms detachment from steps and diffusion across the terraces. To bridge the gap between experiments and theory, we are investigating Cu oxidation using a multiscale computational approach. Our previous MD simulations based on a reactive force field (ReaxFF) demonstrated that the oxidation of stepped Cu(100) takes place on the upper terrace at a faster rate than the lower terrace due to a preferable oxygen diffusion from the lower to upper terraces. We have extended this study using first-principles density functional theory (DFT) and kinetic Monte Carlo (KMC), and performed a systematic study of all stepped Cu surfaces with a low Miller index. The DFT results show that the oxygen diffusion trend varies with the surface type, where in most cases the oxygen ascending diffusion is more favored. This result is confirmed also with ReaxFF MD and KMC simulations. The MD simulations, with a fine-tuned ReaxFF force field parametrization, have also indicated that oxygen adatoms on the upper terrace can enhance the interlayer Cu atom mass transport. These theoretical simulations provide essential fundamental understanding of the experimentally observed smoothing of the Cu surface during in situ oxidation.

3:20pm **SS+AS+EM+EN-ThA4 Reconciling Complimentary Analyses of Epitaxial Growth: Role of Transient Mobility for para-Hexaphenyl on Mica**, ***Josue Morales-Cifuentes**, T.L. Einstein,* University of Maryland, College Park, *A. Pimpinelli*, Rice University

In studies of epitaxial growth, a major goal is to assess the size of the smallest stable cluster (with $i + 1$ monomers, where i is the critical nucleus size). This is accomplished by analyzing either the capture zone distribution (CZD), the scaling of incident flux F to the density of stable islands N or the island-size distribution (ISD). For CZD, generalized Wigner distributions (GWD) have proven useful, [1,2] with successful applications to, non-comprehensively: polar-conjugated molecule Alq_3 on passivated Si(100), self-assembled Ge/Si(001) nanoislands and para-Hexaphenyl (6P) films on amorphous mica. [3] We concentrate on the last, for which the Winkler group found that $i \approx 3$.

Scaling of N usually follows $N \propto F^{\alpha}$, where α is the growth exponent. For 6P films, a difference in scaling behaviors at small and large F is attributed to DLA and ALA dynamics (i.e. $i = 5 \pm 2$, and $i = 7 \pm 2$, respectively). [4] This discrepancy motivates our current work, where transient mobility effects modify scaling non-trivially. [5]

Consider that monomers begin in a (ballistic) hot precursor state before thermalizing (random walk). The competing times of ballistic monomers becoming thermalized vs. being captured by an island naturally define a "thermalization" scale for the system. We obtain an analytic solution and elaborate on the physical meaning behind the energies and dimensionless parameters used. Novel scaling regimes are retrieved for which power-law scaling applies, with non-monotonic crossovers between them and the growth exponent exclusively dependent on i. Applying the model to the 6P films results in good agreement for the scaling and the activation energies: experimental values of the activation energies of 0.26eV (high-T) and 0.04eV (low-T) match model predictions of 0.3eV (high-T) and 0.04eV (low-T). Furthermore, the high-flux regime is interpreted not as ALA (attachment-limited aggregation) or HMA (hot monomer aggregation) but rather as an intermediate scaling regime related to DLA (diffusion-limited aggregation). Lastly, we discuss a simplifying approximation for the model and connections to some capture zone distribution considerations of α. [6]

[1] T.L. Einstein, A. Pimpinelli, D. González, J. Cryst. Growth 401, 67 (2014)

[2] T.L. Einstein, A. Pimpinelli, D. González, and J. R. Morales-Cifuentes, Proc. CCP2014, J. Phys.: Conf. Series (2015), in press.

[3] T. Potocar, G. Lorbek, D. Nabok et al. 2011 Phys. Rev. B 83 075423

[4] L. Tumbek & A. Winkler, Surf. Sci. 606, L55 (2012)

[5] J. R. Morales-Cifuentes, T. L. Einstein, and A. Pimpinelli. Phys. Rev. Lett. 113, 246101(2014)

[6] J. R. Morales-Cifuentes, T. L. Einstein, and A. Pimpinelli (in preparation)

4:00pm **SS+AS+EM+EN-ThA6 Probing 2-DEG at InN Surface by Electrolyte-Gated Raman Spectroscopy**, *E. Alarcon Llado,* Ecole Polytechnique Fédérale de Lausanne (EPFL), Switzerland, ***Tommaso Brazzini***, Lawrence Berkeley Lab, University of California, Berkeley, *J.W. Ager*, Lawrence Berkeley National Laboratory (LBNL)

Indium nitride has attracted much attention as its narrow bandgap (~0.67eV) expands the range of the direct gaps of the group III-N alloys into the visible and near-IR and thus offers an outstanding potential for solar energy conversion and optoelectronic applications. However, experimental demonstration of high efficiency In-rich III-V pn rectification junctions has been hampered by the existence of an intrinsic interface electron accumulation layer, which seems to persist regardless of surface treatment. The large capacitance of the Helmholtz double layer that forms on a surface of an object in contact with an electrolyte allows the 2-DEG at the surface of InN to be tuned and even depleted. Using this effect, we demonstrated the first pn rectification behavior in InN.[1]

In addition, the 2-DEG accumulation layer affects not only the electrical properties, but also has brought many controversies in the interpretation of optical experiments. Raman spectroscopy probes not only the lattice dynamics in a crystal, but also the electronic structure and free carriers. In particular, the interaction between the free electrons at the surface and the longitudinal optical (LO) phonon in InN has been addressed by several studies. However some questions still remain.

In this work, we present an in-situ micro-Raman study that confirms the presence of a surface related Raman mode in InN and shows its interaction with accumulated electrons at the surface. Electrolyte gated Raman spectroscopy (EGRS) on InN layers was performed in order to modulate and in-situ probe the surface electron accumulation region in InN. A reversible shift of the LO phonon with the applied gate potential is found (see figure 1). The peak position and shift depends on the probing light energy, however it is independent of bulk doping. We explain these findings by Martin's double scattering mechanism and bandgap narrowing at the surface tuned by the gate voltage. InN nanocolumns were also investigated by EGRS. The LO mode lies at higher frequencies in all nanocolumn samples. This fact corroborates the nature of the scattering mechanism, which is strongly dependent on the surface orientation. In summary, our results clearly demonstrate the surface origin of this feature and allow the fundamental study and understanding of the electronic structure of InN.

1.Alarcón-Lladó, E. et al. PN junction rectification in electrolyte gated Mg-doped InN. Appl. Phys. Lett. 99, 102106 (2011).

4:20pm **SS+AS+EM+EN-ThA7 Surface Termination of Single Crystal Bi_2Se_3 Investigated by Low Energy Ion Scattering**, ***Weimin Zhou**, J.A. Yarmoff*, UC Riverside

Bismuth Selenide (Bi_2Se_3) is a prototypical topological insulator (TI) with a two-dimensional layered structure that enables clean and well-ordered surfaces to be prepared by cleaving. Although some surface structure studies have concluded that the cleaved surface is terminated with Se, as is expected from the bulk crystal structure, there are other reports that show either a Bi- or mixed-termination [1]. Low Energy Ion Scattering (LEIS) and low energy electron diffraction (LEED) are used here to compare surfaces prepared by *ex-situ* cleaving, *in-situ* cleaving and Ar^+ ion bombardment and annealing (IBA) in ultra-high vacuum. Surfaces prepared by *in-situ* cleaving always have a sharp 1x1 LEED patterns and are Se-terminated. Surfaces prepared by IBA show a transition from Bi- to Se-termination with increasing annealing temperature. Samples inserted into the vacuum chamber following *ex-situ* cleaving have much dimmer LEED patterns, show surface contamination with Auger electron spectroscopy, and could be terminated either with Se or Bi. The angular dependence of LEIS spectra, which is sensitive to the surface atomic structure, doesn't indicate any substantial differences between surfaces prepared by IBA or *in-situ* cleaving. Ion scattering simulations using Kalypso are compared to experimental angular data to obtain more details about the structure. Exposure of clean surfaces to gaseous species will also be discussed in an effort to determine the surface chemical reactions responsible for the termination change.

[1] X. He, W. Zhou, Z. Y. Wang, Y.N. Zhang, J. Shi, R.Q. Wu and J.A. Yarmoff, Phys. Rev. Lett. **110**, 156101 (2013).

4:40pm **SS+AS+EM+EN-ThA8 Real-Time Imaging with Atomic-level Spatial Resolution of Silicon Oxidation**, ***Bryan Wiggins**, L.G. Avila-Bront, R. Edel, S.J. Sibener*, University of Chicago

The investigation of the initial stages of molecular oxygen adsorption on Si(111)-7x7 with real-time and real-space visualization will be discussed in this presentation. We will present the first results from a newly built supersonic molecular beam paired with a scanning probe microscope instrument. The system is designed with an oil free differentially pumped supersonic beam and has a custom scanning probe microscope with the surface plane normal to the beam. This geometric arrangement allows us to

perform real-time and real-space *in-situ* experiments. This study consists of exploring the potential energy surface for molecular oxygen adsorption on Si(111)-7x7. The questions that are being addressed are fundamental for issues relating to semiconductor oxidation as well as being of direct relevance to semiconductor processing. The site-specific locations of molecular oxygen reactivity on Si(111)-7x7 surfaces are not clear and remains a topic of current discussion. Recent spectroscopic studies show that by controlling the molecular beam energy (E_k) one can activate different adsorption pathways for molecules on surfaces. However, the effect of collimated and energy-selected beams impacting the surface at different incident angles has not been observed *in-situ* at the local molecular level until now. We will show high-resolution spatial images of the initial stages of oxygen adsorption on Si(111)-7x7 at different beam energies. The comparison of Si(111)-7x7 oxidation *via* thermal oxygen versus the specific adsorption sites that arise at different beam energies will also be discussed. The results indicate that using supersonic beams in this matter may provide enhanced control of semiconductor oxidation chemistry.

5:00pm **SS+AS+EM+EN-ThA9 Surface Band-Bending Upon Oxidation of Wurtzite and Zincblende InAs Depending on Surface Orientation and atomic Structure**, ***Rainer Timm***, *M. Hjort, J. Knutsson, O. Persson, A. Troian, S. Lehmann, K.A. Dick, A. Mikkelsen*, Lund University, Sweden

InAs is known to typically show n-type behavior with an electron accumulation layer at the surface. Many studies have been performed for evaluating to which extend this behavior is due to adsorbates such as a native oxide layer, or to specific surface orientations and reconstructions of clean InAs. InAs nanowires (NWs) add an extra degree of complexity, since they can exist both in zincblende and wurtzite crystal structure, typically exhibiting unintended switching between both stacking orders during epitaxial growth. During recent years, a strong debate has been going on about how far such crystal phase mixing influences the conductivity of InAs NWs and therewith their suitability for high-mobility device application [1]. A staggered band alignment with band offsets in the range of up to 0.1 eV between zincblende and wurtzite conduction band edges has been reported, based on transport measurements in ambient atmosphere [2]. In contrast, our recent study of clean and unreconstructed InAs NW surfaces based on scanning tunneling microscopy and spectroscopy (STM/S) in ultrahigh vacuum showed aligned conduction band edges for zincblende [110[and wurtzite [11-20[surfaces [3].

Here, we present a systematic study of surface band-bending upon cleaning and oxidation of various InAs surfaces, including purely zincblende or purely wurtzite NWs, obtained by synchrotron-based X-ray photoemission spectroscopy (XPS). We were able to clean all investigated InAs surfaces from their native oxide by annealing them in the presence of atomic hydrogen [3]. Different rates of cleaning and re-oxidation were observed for the different surfaces. Even more importantly, from the energy shifts of the investigated core-levels upon oxidation, varying between 0.1 and 0.3 eV for various surfaces, we obtained significant differences in oxide-induced surface band-bending for different surface orientations. We will compare our XPS results with the atomic and local electronic structure of the specific surfaces as obtained by STM/S [4]. Our results indicate that the band alignment along InAs heterostructures, and therewith the transport properties of InAs NWs, depend on the surface orientation, composition, and atomic structure rather than the crystal phase of the specific InAs segments.

[1] Thelander *et al.*, Nano Lett. **11**, 2424 (2011)

[2] Dayeh *et al.*, Adv. Funct. Mater. **19**, 2102 (2009)

[3] Hjort *et al.,* ACS Nano **12**, 12346 (2014)

[4] Knutsson *et al.*, ACS Appl. Mater. Interfaces **7**, 5748 (2015)

5:20pm **SS+AS+EM+EN-ThA10 Control of Oxygen Defect Surface Injection in ZnO via Sub-Monolayer Sulfur Adsorption**, ***Ming Li***, *E. Seebauer*, University of Illinois at Urbana-Champaign

Native oxygen defects within metal oxide semiconductors such as ZnO affect the material's performance in applications for photovoltaics, nanoelectronics, gas sensing, and photocatalysis. Previous work in this laboratory has shown that the semiconducting metal oxides surfaces can be used to manipulate the concentrations and spatial distributions of bulk oxygen defects, particularly oxygen vacancies. The interaction chemistry between bulk point defects and reactive sites on semiconductor surfaces is comparable in richness to the reactions of surfaces with gases. The present work discusses a novel mechanism of controlling oxygen defect injection in c-plane ZnO(0001) through surface active sites blocking with sub-monolayer sulfur adsorption. Oxygen diffusion rates were measured by exposing single-crystal ZnO to isotopically labeled oxygen ($^{18}O_2$) gas. Sulfur was deposited controllably via an electrochemical cell and characterized *in situ* by Auger Electron Spectroscopy (AES). The resulting diffusion profiles were measured by secondary ion mass spectrometry (SIMS). Kinetic parameters were extracted by fitting the diffusion profiles with a previously derived mass transport model. The preliminary data shows that sulfur adsorption decreases the oxygen defect injection rate by roughly three times through affecting the injection flux, which points to a site blocking model. Subsequent temperature and pressure dependence study will help us gain insights into detailed injection kinetic pathways.

5:40pm **SS+AS+EM+EN-ThA11 Investigation of the Role of Electronic Defects and Grain Boundaries in Sputter Deposited CdS/CdTe Junctions and Solar Cells**, ***Mohit Tuteja***, University of Illinois at Urbana Champaign, *P. Koirala,* University of Toledo, *J. Soares,* University of Illinois at Urbana Champaign, *R. Collins,* University of Toledo, *A. Rockett*, University of Illinois at Urbana Champaign

Device quality CdS/CdTe heterostructures and completed solar cells (~12% efficient) have been studied using low-temperature photoluminescence (PL) as a function of temperature (82-295 K) and laser excitation power (0.02-2 mW). The CdS/CdTe junctions were grown on transparent conducting oxide covered soda lime glass using rf-sputter deposition. It was found that the luminescence shifts from being dominated by sub-gap defect-mediated emission at lower excitation powers to near band edge excitonic emission at higher excitation powers. The effect of copper (Cu) used in making back contacts was studied in connection with the CdS/CdTe junction PL. It was found that the presence of Cu suppresses the sub-band gap PL emissions. This effect was concluded to be due either to Cu occupying cadmium vacancies (V_{Cd}) or forming acceptor complexes with them. This points to a potential role of Cu in plugging sub-band gap recombination routes and hence increasing charge separation ability of the device. An energy band diagram is presented indicating various observed transitions and their possible origins.

2D Materials Focus Topic
Room: 212C - Session 2D+EM+IS+NS+PS+SP+SS-FrM

Surface Chemistry of 2D Materials: Functionalization, Membranes, Sensors
Moderator: Peter Sutter, University of Nebraska - Lincoln, Judy Cha, Yale University

8:20am **2D+EM+IS+NS+PS+SP+SS-FrM1 Chemically Modifying Graphene for Surface Functionality**, ***Paul Sheehan***, *S. Tsoi, S.C. Hernández, S.G. Walton, T.L. Reinecke, K.E. Whitener, J.T. Robinson,* Naval Research Laboratory, *R. Stine*, Nova Research

Graphene has many superlative properties that may be tailored for specific applications, or even enhanced, through chemical functionalization. Chemical functionalization dramatically changes almost every critical property of graphene, changing it from opaque to transparent, from diamagnetic to ferromagnetic, from electron rich or electron poor, from electrically conducting to insulating (and back again!). This extensive control suggests that chemically modified graphene may aid applications from flexible sensors to surface engineering. I will discuss how stacks of 2D materials can control the dominant surface forces—van der Waals,[1] acid-base interactions, electrostatic interactions, etc.—and so surpass conventional methods of preparing surfaces with, for example, self-assembled monolayers. I will also briefly address goals as diverse as biosensing[2] or sloughing off chemical warfare agents.[3]

[1] ACS Nano, **2014**, *8* (12), pp 12410–12417

[2] BioTechniques, Vol. 57, No. 1, July 2014, pp. 21–30

[3] ACS Nano. 2013 Jun 25;7(6):4746-55.

8:40am **2D+EM+IS+NS+PS+SP+SS-FrM2 Structural Phase Stability Control of Monolayer $MoTe_2$ with Adsorbed Atoms and Molecules**, ***Yao Zhou***, *E.J. Reed*, Stanford University

Of the Mo- and W- dichalcogenide monolayers, $MoTe_2$ is particularly interesting because it exhibits a small energy difference (approximately 31 meV per $MoTe_2$) between its semiconducting 2H phase and metallic 1T' crystal structures. This feature makes it particularly interesting for potential phase change applications.

We study the adsorption of some common atoms and molecules onto monolayer $MoTe_2$ and the potential for adsorption to induce a phase change between the semiconducting 2H and metallic 1T' crystal structures of the monolayer. Using density functional theory with spin orbit and van der Waals energy contributions, we determined the most energetically favorable adsorption positions and orientations on the two phases of monolayer $MoTe_2$. We then obtained the formation energies for these adsorption reactions and found that atomic adsorption generally favors 1T' metallic phases while molecular adsorption favors semiconducting 2H phases. A possible application of this work may be the chemical stabilization of a preferred phase during the growth process.

Further, we consider the $Mo_xW_{1-x}Te_2$ alloy monolayers that exhibit even smaller energy difference between phases. Our calculations indicate that it may be possible to engineer an alloy ($0<x<0.5$) such that specific molecules will induce a phase change to 1T' while other molecules studied stabilize the 2H phase, which suggests that alloying may provide some molecular selectivity. This potentially provides the basis for molecular sensing applications due to the large electronic contrast between 2H and 1T' phases.

9:00am **2D+EM+IS+NS+PS+SP+SS-FrM3 Selective Nanochemistry on Graphene/Silicon Carbide: Substrate Functionalization and Polycyclic Aromatic Hydrocarbons Formation**, ***Patrick Soukiassian***, CEA, France **INVITED**

Graphene & silicon carbide (SiC) are advanced semiconductors having figures of merit scaling well above those of well-established ones [1,2]. Understanding/mediating SiC and graphene surfaces & interfaces properties are of central importance toward functionalization and applications. As a 2D material, graphene is a single atomic layer of carbon atoms in a *sp2* bonding configuration. Therefore, functionalization remains challenging since interacting too strongly with the graphene atomic layer may change its bonding configuration and properties. Instead, interacting with the SiC substrate offers an alternative approach. The 1st case of hydrogen-induced metallization of a semiconductor surface has been shown for a 3C-SiC(001) surface [3]. Here, combining investigations using advanced experimental techniques such as STM/STS, vibrational & 3rd generation synchrotron radiation-based photoelectron spectroscopies together with state-of-art calculations will be presented and discussed. It includes: i) the 1st evidence of H/D-induced nanotunnel opening at a semiconductor sub-surface shown here for SiC [4]. Depending on H coverage, these nanotunnels could either be metallic or semiconducting. Dangling bonds generated inside the nanotunnels offer a promising template to capture atoms or molecules. These features open nano-tailoring capabilities towards advanced applications in electronics, chemistry, storage, sensors or biotechnology. Understanding & controlling such a mechanism open routes towards selective surface/interface functionalization of epitaxial graphene [4]. ii) The role of H interaction with graphene on SiC dust grains in polycyclic aromatic hydrocarbons (PAH) formation in the interstellar space with a possible route toward prebiotic roots of life in the universe [5].

1–W. Lu, P. Soukiassian, J. Boeckl "*Graphene: fundamentals and functionalities*" **MRS Bull. 37**, 1119 (2012)

2–P. Soukiassian "*Will graphene be the material of the 21th century?*" **MRS Bull. 37**, 1321 (2012)

3-V. Derycke, P. Soukiassian, F. Amy, Y.J Chabal, M. D'angelo, H. Enriquez, M. Silly, "*Nanochemistry at the atomic scale revealed in hydrogen-induced semiconductor surface metallization*", **Nature Mat.2**, 253 (2003)

4–P. Soukiassian, E. Wimmer, E. Celasco, Cl. Giallombardo, S. Bonanni, L. Vattuone, L. Savio, A. Tejeda, M. Silly, M. D'angelo, F. Sirotti, M. Rocca "*Hydrogen-induced nanotunnel opening within semiconductor subsurface*" **Nature Com. 4**, 2800 (2013)

5–P. Merino, M. Švec, J.I. Martinez,P. Jelinek, P. Lacovig, M. Dalmiglio, S. Lizzit, P. Soukiassian, J. Cernicharo, J.A. Martin-Gago "*Graphene etching on SiC grains as a path to interstellar PAHs' formation*" **Nature Com. 5**, 3054 (2014)

9:40am **2D+EM+IS+NS+PS+SP+SS-FrM5 Intrinsic Wettability of Graphene**, ***Haitao Liu***, Department of Chemistry, University of Pittsburgh

Graphene and graphite are long believed to be hydrophobic. Here we show that a clean graphitic surface is in fact mildly hydrophilic [1]. We find that an as-prepared graphene sample is hydrophilic with a water contact angle of ca. 40°. Upon exposure to ambient air, the water contact angle gradually increased to ca. 60° within 20 min and plateaued at ca. 80° after 1 day. Infrared (IR) spectroscopy and X-ray photoelectron spectroscopy (XPS) showed that airborne hydrocarbon adsorbed onto the graphene surface during this process. Both thermal annealing and controlled UV/O_3 treatment removed the hydrocarbon contaminants, which was accompanied by a concurrent decrease in the water contact angle. Our findings show that graphene is more hydrophilic than previously believed and suggest that the reported hydrophobic nature of graphene is due to unintentional hydrocarbon contamination from ambient air.

Reference

[1] Zhiting Li; et al.; Nature Materials, 12, 925-931, (2013)

10:00am **2D+EM+IS+NS+PS+SP+SS-FrM6 Au-doped Graphene As a Promising Electrocatalyst for the Oxygen Reduction Reaction in Hydrogen Fuel Cells: Prediction from First Principles**, ***Sergey Stolbov***, University of Central Florida, *M. Alcantara Ortigoza*, Tuskegee University

One of the main obstacles hindering large scale practical application of hydrogen fuel cells is a prohibited cost of the Pt (or Pt-based) catalysts for the oxygen reduction reaction (ORR) on the fuel cell cathode. In this work, we consider Au-doped graphene as an alternative to Pt for facilitating ORR. Our first-principles calculations show that Au atoms incorporated into graphene di-vacancies form a thermodynamically and electrochemically stable structure. Furthermore, calculation of the binding energies of the ORR intermediates reveals that Au-C bonding makes the C atoms neighboring to Au optimally reactive for ORR. The calculated ORR free energy diagrams suggest that the Au-graphene structures have an ORR onset potential as high as that of Pt. We also demonstrate that the linear relation among the binding energy of the reaction intermediates assumed in a number of works on computational high-throughput material screening does not hold, at least for this none purely transition-metal material.

10:20am **2D+EM+IS+NS+PS+SP+SS-FrM7 Spontaneous Deposition of Palladium Nanoparticles on Graphene through Redox Reaction**, ***Xiaorui Zhang***, *W. Ooki, Y.R. Kosaka, T. Kondo, J. Nakamura*, University of Tsukuba, Japan

Due to its unique properties such as huge surface area and excellent conductivity, graphene becomes great interesting for supporting noble metal catalysts. Some noble metals such as palladium, platinum, gold nanoparticles was reported to be able to spontaneous deposition on as-synthesized reduced graphene oxide with external reducing agent-free

recently. Yet the mechanism of spontaneous deposition of metals on graphene has not been clarified until now. In the present research, we spontaneously deposited palladium nanoparticles on as-synthesized reduced graphene oxide in H_2O medium without external reducing agent. It was found that the deposited amount of palladium varied with pH, meanwhile, the bivalent Pd^{2+} precursor was reduced to metallic palladium, and graphene was oxidized simultaneously with an increasing of its oxygen functional groups. The atomic ratio of the deposited Pd and the increased O in rGO located in a range from 1 to 2. As reducing agent-free, the mechanism on spontaneous redox deposition of metal nanoparticles on graphene was proposed, firstly, an efficient adsorption of metal precursor on graphene is a prerequisite which is determined by their electrical charges and adjusted by pH. Secondly, a positive galvanic potential between metal precursor and graphene is necessary for metal spontaneous deposition.

10:40am **2D+EM+IS+NS+PS+SP+SS-FrM8 Gradient Electrochemical Response of Template Synthesized Thickness Sorted MoS_2 Nanosheets for Cellular Level Free Radical Detection**, ***Ankur Gupta***, *T. Selvan, S. Das, S. Seal*, University of Central Florida

The human body is a complex system capable of defending in adverse conditions. A classic example of such complex process is balanced equilibrium production between pro-oxidant and antioxidant in cells. However, when this equilibrium is disturbed, production of free radicals such as superoxide and nitric oxide strengthen, and causes serious cellular damages. Furthermore, myeloperoxidase (MPO) is released during the oxidative burst. This MPO combines with hydrogen peroxide (H_2O_2) and Cl^- and generate hypochlorous acid (HOCl). This is a short-lived and powerful diffusible oxidant strong oxidizer and could react with O^{2-} to produce $OH^.$. Therefore, in physiological condition HOCl has a major role as a potent microbicidal agent in the immune defense; however, during the oxidative burst HOCl not only damage healthy tissue and generate radicals that are extremely reactive. Therefore, monitoring of the production of free radicals at the cellular level is important for diagnostic purpose. Over past years, several material have been used to develop sensors for free radical detection such as cerium oxide nanoparticles, MoS_2 nanosheets and nanoparticles. However, detection of free radicals at cellular level is still a challenge.

In this attempt, layered molybdenum disulfide (MoS_2) were synthesized via hydrothermal method. SBA-15 polymer template were utilized during hydrothermal process to grow MoS_2 around it to develop porosity. After the hydrothermal synthesis and washing, polymer template was removed by dissolving it in isopropanol which leaves high surface area layered MoS_2 crystal. Wet chemical exfoliation of MoS_2 were carried out in aqueous solution of Pluronic^{Ó} F-127 having hydrophobic and hydrophilic chains. Pluronic^{Ó} F-127 was used to bring down the buoyant density of MoS_2. Non-templated nanosheets were synthesized as control. The exfoliated solution were centrifuged at 3000 rpm to remove large particle and supernatant was collected for density gradient ultracentrifugation (DGU). Separation of different thickness layers is carried out by DGU. Thickness sort MoS2 nanosheets were characterized using AFM, XPS, HRTEM, Raman and UV-Vis spectroscopy for structural and chemical analysis. XPS, HETEM and EFTEM analysis of nanosheets have illustrate the sulfur deficiency at the edges of the nanosheets. MoS2 nanosheets were deposited on glassy carbon electrode for cyclic-voltammetry and chronoamperometry measurements. Higher sensitivity and repeatability were demonstrated by nanosheets prepared via template method as compared to control for reactive oxygen and nitrogen species, and HOCl.

11:00am **2D+EM+IS+NS+PS+SP+SS-FrM9 Methanol Synthesis on Defect-Laden Single-Layer MoS_2 Supported on Cu(111): Results of a First Principles Study**, *D. Le*, ***Takat B. Rawal***, *T.S. Rahman*, University of Central Florida

Despite being found to be the preferred structure in single layer MoS_2, the sulfur vacancy row does not facilitate alcohol synthesis from syngas [1] because its narrow size limits adsorption, diffusion, and formation of possible intermediates. On the Cu(111) surface, strong interactions between MoS_2 and Cu are expected to reduce the corrugations caused by sulfur vacancy rows, resulting in a larger exposure of vacancies to adsorbates which could enhance the catalytic activity of the row towards alcohol synthesis from syngas. Based on the results of our density functional theory (DFT) simulations utilizing the DFT-D3 correction for accounting the van der Waals interactions, we show that: (1) there is a significant charge transfer from the Cu(111) surface to MoS_2, enhancing its catalytic properties, (2) the binding energies of CO and dissociated H_2 increase by 0.3 eV in comparison to that on unsupported MoS_2, indicating stronger interactions, and (3) the barriers for forming intermediate species in alcohol synthesis process reduce significantly in comparison to that on unsupported MoS_2. On the basis of these energetics, we conclude the Cu(111) substrate promotes methanol synthesis from syn gas on single-layer MoS_2 with a vacancy row. We will also present the energetic pathways for the formations of other reaction products such as methane, formaldehyde, and water, as well as that of (the reverse) water gas-shift reaction.

[1] D. Le, T. B. Rawal, and T. S. Rahman, *J. Phys. Chem. C***118**, 5346 (2014).

*This work is supported in part by the U.S. Department of Energy under grant DE-FG02-07ER15842

11:20am **2D+EM+IS+NS+PS+SP+SS-FrM10 The Happy Marriage of Graphene and Germanium: Graphene Achieves Exceptional Conductivity and Protects Germanium from Oxidizing**, ***Richard Rojas Delgado***, University of Wisconsin-Madison, *F. Cavallo*, University of New Mexico, *R.M. Jacobberger, J.R. Sanchez Perez, D. Schroeder, M.A. Eriksson, M.S. Arnold, M.G. Lagally*, University of Wisconsin-Madison

The properties of graphene (G) make it an outstanding candidate for electronic-device applications, especially those that require no band gap but a high conductance. The conductance, involving both carrier mobility and carrier concentration, will depend critically on the substrate to which G is transferred. We demonstrate an exceptionally high conductance for G transferred to Ge(001) and provide an understanding of the mechanism.[1] Essential in this understanding is an interfacial chemistry consisting of Ge oxide and suboxide layers that provide the necessary charges to dope the graphene sheet, and whose chemical behavior is such that one can obtain long-term stability in the conductance. In contrast, when high-quality G is grown directly on Ge (100), (111), or (110), the conductance is unexceptional, but oxidation of the surface is significantly delayed and slowed, relative to both clean Ge and Ge with G transferred to its surface . [2,3] We fabricate Hall bars in G transferred to Ge and G grown using atmospheric-pressure CVD with methane precursors . X-ray photoelectron spectroscopy (XPS) is used to investigate the oxide in all stages of the measurements. The sheet resistance and Hall effect are measured from 300K to 10K for transferred and grown samples. Values of mobility and carrier concentration are extracted. It appears we have reached the highest combination of mobility and carrier concentration in graphene (suspended or supported) for temperatures from 10 to 300K. The implication is that the primary mechanisms for scattering charge in the G, roughness and a non-uniform electrostatic potential due to fixed charges, have limited effect when the substrate is oxidized Ge. Finally the subsequent oxidation kinetics of Ge (001) are compared for graphene directly grown on Ge and for graphene transferred to Ge. XPS shows that for graphene grown on Ge(001) the interface is oxide-free and remains so over long periods of time. For graphene transferred to Ge(001) the interface contains stoichiometric and substoichiometric oxides. The thickness of these oxides increases with time, but quite slowly. Using spatially resolved XPS, we propose a model of diffusion limited oxidation initiated at edges of the graphene.

Research supported by DOE.

[1]Cavallo, Francesca, et al. "Exceptional Charge Transport Properties of Graphene on Germanium." *ACS nano* 8.10 (2014): 10237-10245.

[2] R. M. Jacobberger, et al. "*Oriented Bottom-Up Growth of Armchair Graphene Nanoribbons on Germanium." Nature Comm*., under review.

[3] R. Rojas, et. al "Passivation of Ge by Graphene.", in process.

Electronic Materials and Processing
Room: 211C - Session EM+AS+EN+NS-FrM

Nanoparticles for Electronics and Photonics
Moderator: Jessica Hilton, Mantis Deposition, Joseph G. Tischler, U.S. Naval Research Laboratory

8:20am **EM+AS+EN+NS-FrM1 Elimination of Bias-stress Effect in Ligand-free Quantum Dot Field-effect Transistors**, ***Matt Law***, UC Irvine **INVITED**

Colloidal quantum dot (QD) solids are the subject of active research with applications emerging in light-emitting diodes, field-effect transistors, and solar cells. In this talk, I describe the use of atomic layer deposition (ALD) infilling to engineer the surfaces and interfaces of PbSe QD films in order to produce high-performance QD field-effect transistors (FETs) that completely lack bias-stress effect (i.e., drain current transients caused by charge trapping near the dielectric/channel interface). This ALD “matrix engineering” approach includes steps designed to manage ligand concentrations, passivate surface states, and arrest ionic motion within the films, resulting in the first high-mobility (~14 $cm\ V^{-1}\ s^{-1}$), environmentally stable, and transient-free PbX QD transistors. Two bias-stress mechanisms in QD FETs are identified and discussed. The implications of these mechanisms for the operation of QD solar cells is highlighted.

9:00am **EM+AS+EN+NS-FrM3 Ultra High Sensitive CO Sensors with Less Overhead: Influence of Doping Methods and Dopants on the CO Sensitivity of Cu, Pt and Pd Doped SnO_2 Pellets**, ***Karthik Tangirala***, *M.A. Olvera*, CINVESTAV-IPN, Mexico

In this work, we report the synthesis, characterization and manufacturing of Cu, Pt and Pd doped SnO_2 pellets with ultra high sensitivities for CO atmospheres. To the best of our knowledge, we have accounted for the first time the ultra high CO sensitivities for Cu doped than Pt and Pd doped SnO_2 pellets. In order to obtain high sensitivities, we have employed novel methods, which are the mixture of chemical and physical synthesis methods. Non-spherical SnO_2 structures were prepared via two chemical synthesis routes using Urea (R1) and ammonia (R2) as precipitation agents. The resultant SnO_2 powders were doped with transition metal, Cu, and noble metals like Pt and Pd via two doping methods D1 and D2. In D1, the powders were bulk doped and then ball milled, whereas in D2, the powders were ball milled and then surface doped. All the powders obtained were later pressed using manual pressing machine to manufacture the SnO_2 pellets. The effect of synthesis routes, doping methods and dopants, on the structural, morphological and also on CO sensing were studied by different characterization techniques and reported with their detailed explanations. Interestingly, the Cu-SnO_2 pellets manufactured from the powders obtained by method D1R1, showed highest sensitivity around 1783 due to various reasons like uniform and small particle size, necks formation, inter-particle conductance and high oxygen adsorption due to stacking faults. All the reasons mentioned above were demonstrated by comparing the established sensor theory with our different experimental results obtained using XRD, Raman, SEM, HRTEM and sensitivity analysis.

9:20am **EM+AS+EN+NS-FrM4 Selective Nucleation of Quantum Dots on Spontaneously Nanopatterned Surfaces**, ***Davide Del Gaudio***, *S. Huang, L. Aagesen, K. Thornton, R.S. Goldman*, University of Michigan, Ann Arbor

Controlled lateral ordering of self-assembled semiconductor quantum dots (QDs) is desirable for a wide range of solid-state applications, including solar cells, lasers, and telecom devices. To date, lateral alignment of QDs has been demonstrated for multilayers of QDs.[1]

In these cases, the first layer of QDs is isotropically distributed; subsequently, during the growth of QD stacks, the accumulation of anisotropic strain often results in lateral QD alignment. However, a significant remaining question concerns the *direct* influence of spontaneous surface patterning on the selective nucleation of QDs.

In this work, we use a combined experimental-computational approach to directly examine correlations between buffer surface morphology and QD nucleation. For this purpose, we exploit a surface instability induced by the anisotropy of the surface diffusion constant of ad-atoms (the Ehrlich-Schwöbel effect[2]) which leads to the formation of elongated ripples, often termed “mounds”. For epitaxial growth of InAs QDs on GaAs, Ye et al. reported a preference for in-plane QD alignment along the mound lengths[1]. Here, our one-dimensional phase-field model reveals a preference for QD nucleation in regions of positive curvature,[3] such as on the sides of the mounds and/or in the “valleys” between the mounds. In our experiments, we explore the formation of InAs QDs on AlGaAs mounds using various substrate temperatures and indium exposure times.

We explore the use of fixed geometry indium evaporation as an approach to restrict QD nucleation to one side of the AlGaAs mounds, resulting in the formation of 1D QD chains.[4] Specifically, for substrate temperature of 580°C, a high density of AlGaAs mounds is observed along [0-11]. For 3 monolayer (ML) of InAs deposition, we achieved selective positioning of QDs, with an average diameter of 16nm, on one side of the mounds.

We will discuss the influence of the As species (As2 vs As4) and growth interrupts on the size, density, and spatial arrangement of QDs. We will also present a detailed analysis of the surface instabilities that induce ripple formation, and the As adsorption kinetics, which lead to the anisotropic nucleation.

References

[1] W. Ye, S. Hanson, M. Reason, X. Weng, and R. S. Goldman. (2005). *J. Vac. Sci. Technol.* B **23**, 1736-1740.

[2] Schwöbel, R. L., & Shipsey, E. J. (1966). *J. App. Phys.*, **37**(10), 3682–3686.

[3] Seol, D. J., Hu, S. Y., Liu, Z. K., Chen, L. Q., Kim, S. G., & Oh, K. H. (2005) *J. Appl. Phys.*, **98**(4), 044910.

[4] Arciprete, F., Placidi, E., Magri, R., Del Gaudio, D., Patella, F. (2013) *J. Mat. Res.***28**(23), 3201–3209

9:40am **EM+AS+EN+NS-FrM5 Tailor-made Gas Phase based Nanoparticles with Functional Properties**, ***Gert ten Brink***, *B. Kooi, G. Palasantzas*, University of Groningen, The Netherlands **INVITED**

Using a home modified Mantis dedicated nanocluster© source we have the possibility to produce nanoparticles (NPs) of a great variety of materials with relatively small size dispersion and with properties that can be novel and different from their bulk counterpart. The system works on the principle of inert gas condensation and magnetron sputtering. We have produced a whole range of different NPs with size and motif control.

Covalent bonded NPs, in particular carbon;

Metallic NPs: Cu[1], Fe, Mg, Mo, Co, Al, Ag, Nb, Ti, Pd;

Semiconductor NPs, in particular Ge;

Bimetallic NPs: MgNi, MoCu, MgTi with several compositions;

Ternary alloy NPs, e.g. GeSbTe with several compositions and with amorphous and crystallinity control.

The particles can be deposited on most surfaces provided they have good vacuum compatibility.

The applications range from novel:

Wetting phenomena; Cu NPs covered surfaces giving rose petal effect[2];

Bimetallic Mo-Cu NPs which are bulk immiscible but in NPs fully miscible[3];

Bimetallic NPs for hydrogen storage[4]: MgNi, MgTi, MgCu;

Magnetic NPs: Fe-Fe_3O_4 core-shell particles for medical applications.

1. Brink, G. H. ten, Krishnan, G., Kooi, B. J. & Palasantzas, G. Copper nanoparticle formation in a reducing gas environment. *J. Appl. Phys.* **116,** 104302 (2014).

2. Ten Brink, G. H., Foley, N., Zwaan, D., Kooi, B. J. & Palasantzas, G. Roughness controlled superhydrophobicity on single nanometer length scale with metal nanoparticles. *RSC Adv.* **5,** 28696–28702 (2015).

3. G. Krishnan, M.A. Verheijen, G.H. ten Brink, G. Palasantzas, B.J. Kooi, Tuning structural motifs and alloying of bulk immiscible Mo-Cu bimetallic nanoparticles by gas-phase synthesis, *Nanoscale* **5**, 5375-5383 (2013).

4. Krishnan, G. *et al.* Synthesis and exceptional thermal stability of Mg-based bimetallic nanoparticles during hydrogenation. *Nanoscale* **6***,* 11963-11970 (2014).

10:20am **EM+AS+EN+NS-FrM7 A New Surfactant for Directed Deposition of Carbon Nanomaterials**, ***Hanna Nilsson***, University of Maryland, *L. de Knoop,* Chalmers University, *J. Ticey, B. Meany, Y. Wang,* University of Maryland, *E. Olsson,* Chalmers University, *J. Cumings*, University of Maryland

We show the results of using a new surfactant, ammonium laurate (AL), to suspend and deposit carbon nanostructures. In a recent publication[1], we show that multi-walled carbon nanotubes (MWCNTs) can be suspended in AL with much better shelf stability as compared with the common surfactant sodium dodecyl sulfate (SDS). AL differs from SDS only by the choice of ionic species, but the deposition process with AL is more reliable and cleaner than with SDS. We use a process of producing a charged self-assembled monolayer on the substrate and then exposing the substrates to the aqueous surfactant solution of MWCNTs to achieve directed deposition of clean individual MWCNTs, which can then be used for fabrication of individual nanotube devices. In addition to these results, we show results for single-walled carbon nanotubes (SWCNTs) in AL, which show that nanotubes deposited from AL have lower electrical contact resistance as compared to those deposited from SDS. Photoluminescence results also show that SWCNTs with specific chirality are preferentially suspended in AL, which may present a separation and purification pathway. We will also present extensions of the work to single and few layer graphene sheets, where AL can be used to make clean depositions from aqueous solution onto sensitive substrates.

(1) Nilsson, H. M.; Meany, B.; Ticey, J.; Sun, C.-F.; Wang, Y.; Cumings, J. Ammonium Laurate Surfactant for Cleaner Deposition of Carbon Nanotubes. *Langmuir* **2015**, *31*, 6948-6955.

10:40am **EM+AS+EN+NS-FrM8 Compositional Control and Doping Uniformity in Spray Pyrolyzed CZTS Nanoparticles and Films**, ***Stephen Exarhos***, *A. Alvarez, J. Hernandez, L. Mangolini*, University of California - Riverside

An innovative and scalable synthesis approach to the formation of stoichiometric Cu_2ZnSnS_4 (CZTS) nanocrystals has been developed using aerosol spray pyrolysis. This quaternary phase material is a potential replacement for currently commercialized semiconductors such as CdTe and CIGS that are used in photovoltaic devices. However, sustainability and environmental issues threaten long-term viability of these materials. Based upon earth abundant constituents and low chemical toxicity, CZTS, with a

reported bandgap of ~1.5 eV[1], appears to be a superior alternative to these other materials. Additional research and development is necessary to increase the efficiency of CZTS-based cells from the current record (12.6% by Wang *et al*.[2]) to the >18% necessary to be considered commercially viable. Our work demonstrates the controllable, cost-effective, and reproducible synthesis of high-quality CZTS nanoparticles and films. A modified spray pyrolysis method involving decomposition of copper, zinc, and tin diethyldithiocarbamate precursors allows uniform incorporation of dopants (such as sodium) that are known to increase crystal grain growth during nanoparticle sintering[3]. Once formed, the nanoparticles are deposited onto a substrate from a methanol dispersion using an "ink-spray" process with an argon-driven airbrush. To form an efficient absorber layer in a photovoltaic device, the coating is then annealed in a sulfur-vapor atmosphere resulting in a thin film with uniformly large crystal grain morphology throughout the film thickness (~1-2 µm). The deposited films are characterized with respect to crystalline phase, stoichiometry, and overall film quality. Further preliminary results regarding the formation of $Cu_2ZnSn_{(1-x)}(IV)_xS_4$ by means of this processing approach will be reported.

[1] H. Wang. "Progress in Thin Film Solar Cells Based on Cu_2ZnSnS_4," International Journal of Photoenergy 2011 (2011).

[2] Wang, Wei, Mark T. Winkler, *et al*. "Device Characteristics of CZTSSe Thin-Film Solar Cells with 12.6% Efficiency." Advanced Energy Materials 4, no. 7 (2014).

[3] Johnson, M., S. V. Baryshev, *et al*. "Alkali-Metal-Enhanced Grain Growth in Cu2ZnSnS4 Thin Films." Energy & Environmental Science 7, no. 6 (2014): 1931–38.

Authors Index

Bold page numbers indicate the presenter

— A —

Aagesen, L.: EM+AS+EN+NS-FrM4, 73
Abate, Y.: EM+MS-ThA8, 66; EM+MS-ThM2, **50**
Abbas, A.: EN+AS+EM+NS+SE+SS+TF-MoM10, 8
Abbott, D.H.: AM+EM+MS+TF-WeM3, 34
Abe, Y.: EM-WeA2, **42**
Abel, A.J.: EN+AS+EM+SE+SS-TuM5, **22**
Abelson, J.R.: SD+AS+EM-ThM2, 54
Abudayyeh, O.K.: EM+EN-ThA10, 64; SE+EM+EN-MoA4, **17**
Adams, D.P.: TF+AS+EM+EN+MN-WeA3, 44; TF+AS+EM+EN+MN-WeA4, **44**
Addou, R.: 2D+EM+IS+MC+NS+SP+SS-WeA8, 38; 2D+EM+MG+NS+SE+SM+SS+TF-ThM6, **46**; 2D+EM+MG+NS+SS+TF-ThA7, 60
Afanas'ev, V.: EM-ThM13, 53; EM-WeA12, 43
Afsari, S.: 2D+EM+MG+NS+SE+SM+SS+TF-ThM2, 46
Agarwal, S.: PS+EM-MoA8, 16
Agasie, R.: EM-WeM6, 36
Ager, J.W.: EN+AS+EM+SE+SS-TuM10, **22**; SS+AS+EM+EN-ThA6, 69
Aghaee, M.: TF+EM+MI+MS-TuM4, **24**
Akaishi, A.: 2D+EM+IS+MC+NS+SP+SS-WeA12, 39
Alarcon Llado, E.: EM+EN-ThA4, **64**; EN+AS+EM+SE+SS-TuM2, 22; SS+AS+EM+EN-ThA6, 69
Alcantara Ortigoza, M.: 2D+EM+IS+NS+PS+SP+SS-FrM6, 71
Aldridge, T.V.: EN+EM+NS+SE+SS+TF-TuA9, 28
Alevli, M.: EM+MS-ThA7, **65**; EM+MS-ThM1, 50
Alkis, S.: EM+MS-ThA7, 65
Allred, D.D.: EL+AS+BI+EM-ThA11, **63**
Almeida, C.R.: EM-TuP17, **32**
Alvarez, A.: EM+AS+EN+NS-FrM8, 73
Alvarez, D.: EM+NS+PS-MoA7, 12; EM+NS+PS-MoA8, **12**
Alverez, D.: EM+NS+PS-MoM4, 5
Amano, H.: EM+EN-ThA3, 63
Anand, B.X.: EN+AS+EM+NS+SE+SS+TF-MoA1, 13
Anderson, T.J.: EM+AS+MS+SS-WeA12, 41; EM+AS+MS+SS-WeA7, 40
Andrei, E.: EM-TuP27, 33
Antunez, P.D.: EN+AS+EM+NS+SE+SS+TF-MoM2, 7
Araidai, M.: EM-TuP10, **31**; EM-TuP11, 31; EM-TuP12, 31
Aretouli, K.E.: 2D+EM+MG+NS+SE+SM+SS+TF-ThM5, 46
Arias, A.C.: AM+EM+MS+TF-ThA1, **61**
Arnold, M.S.: 2D+EM+IS+NS+PS+SP+SS-FrM10, 72
Arwin, H.: EL+EM+EN-ThM13, 50
Avila-Bront, L.G.: SS+AS+EM+EN-ThA8, 69
Aydil, E.S.: EN+AS+EM+NS+SE+SS+TF-MoA9, **14**
Aydogan, P.: EN+AS+EM+NS+SE+SS+TF-MoM9, 7
Azcatl, A.: 2D+EM+MG+NS+SS+TF-ThA7, 60

— B —

Babar, S.: SD+AS+EM-ThM2, 54
Bagley, J.: EM-WeM11, 36
Baklanov, M.: EM-ThM11, 53; EM-ThM13, 53; EM-ThM5, 52; EM-WeA12, 43; EM-WeA3, **42**
Ballard, J.: SD+AS+EM+PS-ThA8, **67**
Banerjee, S.K.: 2D+EM+IS+MC+NS+SP+SS-WeA7, 38; 2D+EM+MG+NS+SS+TF-ThA1, 60; EM-TuM5, **21**
Baneton, J.: PS+EM-MoA9, **16**
Bao, W.: 2D+EM+IS+MC+NS+SP+SS-WeA11, 39
Barnes, T.M.: EN+AS+EM+NS+SE+SS+TF-MoM10, 8
Barroso, D.: 2D+EM+MC+MS+NS-MoA10, 9; 2D+EM+MG+NS+SE+SM+SS+TF-ThM1, **46**
Bartels, L.: 2D+EM+MC+MI+NS+SP+SS+TF-TuA4, 26; 2D+EM+MC+MS+NS-MoA10, 9; 2D+EM+MG+NS+SE+SM+SS+TF-ThM1, 46
Bartynski, R.A.: EM-TuP27, 33
Baski, A.A.: SS+AS+EM+EN-ThM13, 57
Baxter, J.B.: EN+AS+EM+NS+SE+SS+TF-MoA5, **14**; EN+AS+EM+SE+SS-TuM5, 22
Bayindir, Z.: EM-WeA1, 42
Beach, J.D.: EN+AS+EM+NS+SE+SS+TF-MoM10, 8
Beams, R.: 2D+EM+NS+PS+SP+SS+TF-MoM4, 1
Bearden, B.E.: EN+AS+EM+NS+SE+SS+TF-MoA1, 13
Beatty, D.: 2D+EM+MG+NS+SS+TF-ThA6, 60
Beeby, S.: EM+AS+SS-MoA1, 10
Belkadi, A.: EM+AS+SS-MoM1, 3; EM-TuP2, **30**
Benck, J.D.: EN+AS+EM+SE+SS-TuM3, 22
Bent, S.F.: SD+AS+EM+PS-ThA10, 68; SD+AS+EM+PS-ThA6, 67; SS+AS+EM+EN-ThM1, 55; SS+AS+EM+EN-ThM5, **56**
Bergsman, D.S.: SD+AS+EM+PS-ThA6, 67
Bermudez, V.M.: 2D+EM+NS+PS+SP+SS+TF-MoM1, 1
Bhansali, S.: EM-TuP8, 31
Bhattacharya, P.: EN+EM+NS+SE+SS+TF-TuA4, 27
Bhatti, A.S.: EL+AS+BI+EM-ThA9, **63**
Biegelsen, D.K.: AM+EM+MS+TF-ThA3, 61
Bielefeld, J.D.: EM-WeA7, **43**
Birol, T.: EM+AS+SS-MoA5, 11
Biyikli, N.: EM+MS-ThA7, 65; EM+MS-ThM1, 50; EM+MS-ThM13, 51
Blackwell, J.: EM-WeA7, 43
Blatz, J.: EM-TuP21, **32**
Bleuse, J.: 2D+EM+MC+MI+NS+SP+SS+TF-TuA11, 26
Bockrath, M.W.: 2D+EM+MG+NS+SS+TF-ThA8, **61**
Bojarski, S.: EM-WeA7, 43
Bol, A.A.: TF+EM+NS+PS+SM-ThM12, 58; TF+EM+NS+PS+SM-ThM6, 58
Bolat, S.: EM+MS-ThM13, **51**
Bolt, P.J.: EN+AS+EM+NS+SE+SS+TF-MoM8, 7
Bonilla, J.: EM-TuM4, 20
Booth, J.C.: EM+AS+SS-MoA5, 11
Borguet, E.: 2D+EM+MG+NS+SE+SM+SS+TF-ThM2, 46
Bottoms, W.R.: EM+MN+PS-TuA1, **27**
Bowman, S.R.: EM+MS-ThM12, 51
Boyd, A.: 2D+EM+NS+SS+TF-TuM10, 20
Boyer, N.: TF+AS+EM+EN+MN-WeA12, **45**
Brady, P.: EM+AS+SS-MoM1, 3; EM+AS+SS-MoM6, 3
Brandt, A.: EM+NS+PS-MoA9, 13
Brazzini, T.: SS+AS+EM+EN-ThA6, **69**
Breckenfeld, E.: AM+EM+MS+TF-WeM6, **34**
Briley, C.: EL+AS+BI+EM-ThA4, **62**
Brink, M.: PS+EM-MoA4, 15
Britto, R.: EN+AS+EM+SE+SS-TuM3, 22
Brooks, A.: 2D+EM+MG+NS+SE+SM+SS+TF-ThM1, 46
Brown, C.G.: EM+MS-ThM12, 51
Bruce, R.L.: PS+EM-MoA4, 15
Budak, S.: EM-TuP18, 32
Burgener, N.J.: SS+AS+EM+EN-ThM10, 56
Burghaus, U.: 2D+EM+MG+NS+SE+SM+SS+TF-ThM10, 47

— C —

Cabrera, W.: SD+AS+EM-ThM10, 55
Cabrini, S.: EM+MS-ThM5, **51**
Cai, T.: EM+EN-ThA11, 64
Cairns, E.: EN+AS+EM+SE+SS-TuM13, 23
Caldarella, G.: PS+EM-MoA9, 16
Cameron, D.C.: TF+EM+MI+MS-TuM4, 24
Carlin, J.-F.: EL+EM+EN-ThM6, 49
Carpick, R.W.: EM-WeM13, 36
Caruso, A.N.: EM-ThM3, 52
Casey, S.M.: SS+AS+EM+EN-ThM10, 56
Castaneda, H.: 2D+EM+NS+PS+SP+SS+TF-MoM3, 1
Cavallo, F.: 2D+EM+IS+NS+PS+SP+SS-FrM10, 72
Cha, J.: 2D+EM+MG+NS+SS+TF-ThA10, **61**
Chabal, Y.J.: EN+AS+EM+NS+SE+SS+TF-MoA1, 13; SD+AS+EM+PS-ThA8, 67; SD+AS+EM-ThM10, **55**; SS+AS+EM+EN-ThM2, 56; SS+AS+EM+EN-ThM4, 56
Chagarov, E.: EM+NS+PS-MoA9, 13; EM-WeM3, 35; EM-WeM4, **35**; EN+AS+EM+NS+SE+SS+TF-MoM1, 6
Chakthranont, P.: EN+AS+EM+SE+SS-TuM3, 22
Chalker, P.R.: EM+AS+SS-MoA1, 10
Chambers, S.A.: EM+AS+SS-MoM11, 4
Chandhok, M.: EM-WeA7, 43
Chang, A.S.: EM-TuP26, 33
Chang, J.P.: TF+EM+NS+PS+SM-ThM5, **58**
Chang, M.: EM+NS+PS-MoM4, 5
Chang, T.: EM-WeM6, 36
Charbon, E.: 2D+EM+MC+MS+NS-MoA6, 9
Charipar, N.: AM+EM+MS+TF-WeM6, 34
Chen, C.: EN+EM+NS+SE+SS+TF-TuA9, 28
Chen, J.-R.: SD+AS+EM-ThM1, 54
Chen, K.-S.: 2D+EM+MC+MS+NS-MoA9, 9
Chen, M.W.: 2D+EM+MG+NS+SE+SM+SS+TF-ThM11, **47**
Chen, W.C.: EM-TuP16, **32**
Chen, X.G.: EL+EM+EN-ThM5, 48
Chen, Z.: EN+EM+NS+SE+SS+TF-TuA9, 28
Cheng, G.: 2D+EM+NS+PS+SP+SS+TF-MoM8, 2

Cheng, L.: 2D+EM+MG+NS+SS+TF-ThA7, 60
Chervin, C.N.: EN+EM+NS+SE+SS+TF-TuA7, 28
Chhowalla, M.: 2D+EM+MC+MI+NS+SP+SS+TF-TuA11, 26
Chi, X.: EL+EM+EN-ThM3, 48
Chien, D.: TF+EM+NS+PS+SM-ThM5, 58
Chin, M.: EM+AS+SS-MoM9, 4
Chintalapalle, R.V.: EN+AS+EM+NS+SE+SS+TF-MoA8, 14
Cho, E.: 2D+EM+MC+MS+NS-MoA9, 9
Cho, K.J.: SS+AS+EM+EN-ThM2, 56; SS+AS+EM+EN-ThM4, 56
Choi, B.D.: EN+AS+EM+NS+SE+SS+TF-MoM6, 7
Choi, B.J.: SD+AS+EM+PS-ThA9, **68**
Choi, E.C.: EM-TuP5, 30
Choi, S.: EM-WeA1, 42
Chopra, S.: SD+AS+EM-ThM11, 55
Chopra, T.P.: SS+AS+EM+EN-ThM2, **56**
Choudhury, F.: EM-ThM11, **53**
Chow, E.M.: AM+EM+MS+TF-ThA3, **61**
Clark, A.: EM+MS-ThA9, 66
Clark, R.: EM+NS+PS-MoA3, **12**; SD+AS+EM+PS-ThA11, 68
Clarke, J.: EM-ThM10, 53; EM-WeA7, 43
Clarke, R.: EM+MS-ThA6, 65; EM-TuP26, 33
Clemens, B.M.: SE+EM+EN-MoA5, **17**
Clement, T.J.: AM+EM+MS+TF-ThM3, **47**
Clendenning, S.: EN+EM+NS+SE+SS+TF-TuA9, 28
Closser, R.G.: SD+AS+EM+PS-ThA6, **67**
Cola, B.A.: EM+AS+SS-MoA4, **10**
Coley, W.: 2D+EM+MG+NS+SE+SM+SS+TF-ThM1, 46
Collins, R.: SS+AS+EM+EN-ThA11, 70
Conley, Jr., J.F.: EM+AS+SS-MoM10, 4
Consiglio, S.: SD+AS+EM+PS-ThA11, 68
Cormier, P.-A.: SE+EM+EN-MoA3, 17
Cornaby, S.: TF+AS+EM+EN+MN-WeA12, 45
Cotta, M.: EM-TuP17, 32
Cramer, H.: EM+MS-ThM10, 51
Crawford, L.S.: AM+EM+MS+TF-ThA3, 61
Creatore, M.: TF+EM+MI+MS-TuM4, 24; TF+EM+NS+PS+SM-ThM13, 59
Creighton, R.: TF+AS+EM+EN+MN-WeA12, 45
Crumlin, E.J.: EN+EM+NS+SE+SS+TF-TuA10, 28
Culter, P.H.: EM+AS+SS-MoM5, 3
Cumings, J.: EM+AS+EN+NS-FrM7, 73
Cunningham, F.: EM-TuP9, 31

— D —

Dai, R.C.: EL+EM+EN-ThM4, 48
Dai, S.: EM-TuP1, 30
Dalmau-Mallorqui, A.: EN+AS+EM+SE+SS-TuM2, 22
Daniels, K.M.: 2D+EM+NS+SS+TF-TuM10, **20**
Dapkus, P.D.: EM+MS-ThA3, **65**
Darakchieva, V.: EL+EM+EN-ThM6, 49
Dargis, R.: EM+MS-ThA9, **66**
Daryl, C.: 2D+EM+MG+NS+SS+TF-ThA9, 61
Das, S.: 2D+EM+IS+NS+PS+SP+SS-FrM8, 72
Dash, P.: EM-WeA9, **43**
Dauskardt, R.H.: EM-ThM4, **52**; TF+EM+MI+MS-TuM12, 25
Davis, R.: EM+AS+MS+SS-WeA3, 40
Davis, R.C.: EM-WeM11, 36; TF+AS+EM+EN+MN-WeA12, 45; TF+AS+EM+EN+MN-WeA9, **44**
Davis, R.F.: EM+AS+MS+SS-WeA4, 40
Davydov, A.V.: 2D+EM+NS+PS+SP+SS+TF-MoM4, 1
de Knoop, L.: EM+AS+EN+NS-FrM7, 73
de la Barrera, S.: 2D+EM+NS+PS+SP+SS+TF-MoM9, **2**
de Marneffe, J.-F.: EM-ThM11, 53; EM-ThM13, 53; EM-WeA12, 43
De Temmerman, G.: PS+EM-MoA10, 16
Dean, C.R.: 2D+EM+MC+MS+NS-MoA1, **9**
Debaille, V.: PS+EM-MoA9, 16
Del Gaudio, D.: EM+AS+EN+NS-FrM4, **73**
del Pozo, S.: AM+EM+MS+TF-WeM5, 34
Demichel, O.: EM+EN-ThA4, 64
Dervaux, J.: SE+EM+EN-MoA3, 17
Deutsch, T.: EN+AS+EM+SE+SS-TuM12, 23
Dick, D.: SD+AS+EM+PS-ThA8, 67; SD+AS+EM-ThM10, 55
Dick, K.A.: SS+AS+EM+EN-ThA9, 70
Dickens, PM.: AM+EM+MS+TF-ThM10, **48**
Diebold, A.C.: EL+AS+BI+EM-ThA2, 62; EL+AS+BI+EM-ThA6, 62
Diercks, D.R.: EN+AS+EM+NS+SE+SS+TF-MoM10, 8
Diest, K.: EM+AS+SS-MoM9, 4
Dietz, N.: EM+MS-ThA8, 66; EM+MS-ThM2, 50; EM+MS-ThM4, **51**
Dimoulas, A.: 2D+EM+MG+NS+SE+SM+SS+TF-ThM5, **46**
Ding, Y.: TF+EM+MI+MS-TuM12, **25**
Ding, Z.J.: EL+EM+EN-ThM4, 48
Diniz, J.A.: EM-TuP17, 32
Diroll, B.T.: EN+AS+EM+NS+SE+SS+TF-MoA5, 14
Dixit, D.: EL+AS+BI+EM-ThA6, 62
Doeff, M.: EN+EM+NS+SE+SS+TF-TuA1, **27**
Dogan, I.: PS+EM-MoA8, **16**
Domask, A.C.: EM-TuM3, 20
Doscher, H.: EN+AS+EM+SE+SS-TuM12, 23
Downey, B.: EM+AS+MS+SS-WeA9, **41**
Drevillon, B.: EL+EM+EN-ThM1, **48**
Driver, S.: 2D+EM+MG+NS+SS+TF-ThA6, 60
Droopad, R.: EM+NS+PS-MoA7, 12; EM+NS+PS-MoM3, 5; EM+NS+PS-MoM4, 5
Duan, J.: EM-TuP27, 33
Dubois, G.: EM-ThM4, 52
Duerloo, K.-A.: 2D+EM+MC+MS+NS-MoA3, 9
Dumcenco, D.: 2D+EM+IS+MC+NS+SP+SS-WeA2, 38; 2D+EM+MG+NS+SE+SM+SS+TF-ThM11, 47
Dumenco, D.: 2D+EM+MC+MS+NS-MoA6, 9
Durand, W.: PS+EM-MoA4, 15
Durbin, S.M.: EM+MS-ThA6, **65**
Durham, D.: EM-WeM13, 36

— E —

Eddy, Jr., C.R.: EM+AS+MS+SS-WeA7, **40**; EM+MS-ThM12, 51
Edel, R.: SS+AS+EM+EN-ThA8, 69
Edmonds, M.: EM+NS+PS-MoA7, 12; EM+NS+PS-MoM4, **5**
Eichfeld, S.M.: 2D+EM+MG+NS+SE+SM+SS+TF-ThM6, 46; 2D+EM+NS+PS+SP+SS+TF-MoM9, 2
Eichhorn, B.: EN+EM+NS+SE+SS+TF-TuA10, 28
Einstein, T.L.: SS+AS+EM+EN-ThA4, 69
Eizenberg, M.: EM+NS+PS-MoM3, 5
Ekerdt, J.: SD+AS+EM-ThM11, **55**
Ellinger, C.R.: EM+AS+SS-MoA9, 11
Ellison, C.: PS+EM-MoA4, 15
Empante, T.: 2D+EM+MG+NS+SE+SM+SS+TF-ThM1, 46
Endicott, L.: EM-TuP26, 33
Engelmann, S.U.: PS+EM-MoA4, 15
Engstrom, J.R.: SD+AS+EM-ThM1, **54**
Eom, T.: SD+AS+EM+PS-ThA9, 68
Eriksson, M.A.: 2D+EM+IS+NS+PS+SP+SS-FrM10, 72
Exarhos, S.: EM+AS+EN+NS-FrM8, **73**

— F —

Falta, J.: 2D+EM+MG+NS+SE+SM+SS+TF-ThM12, 47
Fathipour, S.: 2D+EM+MG+NS+SS+TF-ThA1, 60
Feenstra, R.: 2D+EM+NS+PS+SP+SS+TF-MoM9, 2
Feigelson, B.N.: 2D+EM+NS+PS+SP+SS+TF-MoM1, **1**; 2D+EM+NS+PS+SP+SS+TF-MoM3, 1; EM+AS+MS+SS-WeA12, 41
Feldberg, N.: EM+MS-ThA6, 65
Feldman, L.: EM-TuP27, 33
Feng, H.: SE+EM+EN-MoA9, **18**
Fennie, C.J.: EM+AS+SS-MoA5, 11
Ferguson, I.: EM+MS-ThM2, 50; EM+MS-ThM4, 51
Fernandes, G.E.: EM+AS+SS-MoM9, 4
Fernando, N.: EM+NS+PS-MoA10, **13**
Ferry, V.E.: EM+EN-ThA7, **64**
Fiori, G.: 2D+EM+MC+MS+NS-MoA6, 9
Flege, J.I.: 2D+EM+MG+NS+SE+SM+SS+TF-ThM12, 47
Foad, M.A.: EM+NS+PS-MoA2, 12
Fonctuberta i Morral, A.: EM+EN-ThA4, 64; EN+AS+EM+SE+SS-TuM2, 22
Fong, K.D.: EN+AS+EM+SE+SS-TuM3, 22
Fontcuberta i Morral, A.: EM+EN-ThA1, **63**
Fordham, J.L.: EN+AS+EM+NS+SE+SS+TF-MoA5, 14
Förster, S.: 2D+EM+MG+NS+SE+SM+SS+TF-ThM12, **47**
Frau, E.: EN+AS+EM+SE+SS-TuM2, **22**
Fredrickson, G.H.: PS+EM-MoA1, 15
Frégnaux, M.: 2D+EM+MC+MI+NS+SP+SS+TF-TuA11, 26
Freitag, R.: EM+MS-ThM10, 51
Freitas, J.A.: EM+MS-ThM12, 51
Frijters, C.: EN+AS+EM+NS+SE+SS+TF-MoM8, 7
Fuhrer, M.: 2D+EM+IS+MC+NS+SP+SS-WeA11, 39; 2D+EM+NS+PS+SP+SS+TF-MoM3, 1
Fukuyama, A.: EM+EN-ThA3, 63; EM+EN-ThA6, 64
Funke, S.: 2D+EM+NS+SS+TF-TuM11, 20; 2D+EM+NS+SS+TF-TuM6, **19**
Furdyna, J.: 2D+EM+NS+PS+SP+SS+TF-MoM9, 2

— G —

Galindo, J.: EN+AS+EM+NS+SE+SS+TF-MoM5, 7
Gao, F.: SS+AS+EM+EN-ThM3, **56**
Gapp, N.: SE+EM+EN-MoA4, 17
Garcia-Caurel, E.: EL+EM+EN-ThM13, 50
Gardner, D.S.: EN+EM+NS+SE+SS+TF-TuA9, **28**
Garfunkel, E.: EM-TuP27, 33
Gash, A.E.: TF+AS+EM+EN+MN-WeA11, 44
Gaskill, D.K.: 2D+EM+NS+PS+SP+SS+TF-MoM3, 1; 2D+EM+NS+SS+TF-TuM10, 20

Gaulding, E.A.: EN+AS+EM+NS+SE+SS+TF-MoA5, 14
George, S.M.: TF+EM+MI+MS-TuM5, 24
Ghaffar, F.: EM+AS+SS-MoA2, 10
Ghosez, P.: EM+AS+SS-MoA5, 11
Ghosh, G.: EM-WeM10, 36; EM-WeM12, 36; EM-WeM5, **35**
Ghosh, S.: EM+EN-ThA10, 64; EM+EN-ThA11, 64; EM-TuM4, 20
Giamini, S.A.: 2D+EM+MG+NS+SE+SM+SS+TF-ThM5, 46
Giardini, S.: EM+AS+SS-MoM9, 4
Ginger, D.S.: EN+AS+EM+NS+SE+SS+TF-MoA7, 14
Girolami, G.S.: SD+AS+EM-ThM2, 54
Giugliano, M.: 2D+EM+NS+SS+TF-TuM2, 19
Goeke, R.S.: EM-WeM1, **34**
Goian, V.: EM+AS+SS-MoA5, 11
Goldberger, J.: 2D+EM+NS+PS+SP+SS+TF-MoM10, **2**
Goldenberg, E.: EM+MS-ThM1, 50
Goldman, R.S.: EM+AS+EN+NS-FrM4, 73; EM-TuP26, 33
Gomez, M.: 2D+EM+MC+MI+NS+SP+SS+TF-TuA4, **26**
Gong, J.B.: EL+EM+EN-ThM4, **48**
Gonon, P.: EM-WeM2, 35
Gonzales, J.M.: 2D+EM+IS+MC+NS+SP+SS-WeA1, 38
Goovaerts, E.: 2D+EM+NS+SS+TF-TuM2, **19**
Gopalan, V.: EM+AS+SS-MoA5, 11
Gordon, J.M.: EM+AS+SS-MoM4, 3
Gordon, M.: PS+EM-MoA6, **16**
Gordon, R.: SD+AS+EM-ThM3, **54**
Gorham, R.: AM+EM+MS+TF-WeM1, 34
Goswami, R.: EM+MS-ThM12, 51
Gougousi, T.: SS+AS+EM+EN-ThM11, 57
Grandjean, N.: EL+EM+EN-ThM6, 49
Grant, J.T.: SE+EM+EN-MoA7, 17
Greber, T.: 2D+EM+MG+NS+SE+SM+SS+TF-ThM12, 47
Green, A.: EL+AS+BI+EM-ThA8, **63**
Greenlee, J.D.: EM+AS+MS+SS-WeA12, **41**
Greg Hearn, G.: 2D+EM+NS+SS+TF-TuM6, 19
Grey, J.K.: EM+EN-ThA10, 64
Grill, A.A.: EM-ThM1, **52**
Grob, F.: TF+EM+MI+MS-TuM3, 23
Gstrein, F.: SD+AS+EM+PS-ThA3, **67**
Gu, F.: 2D+EM+IS+MC+NS+SP+SS-WeA11, 39
Guglietta, G.W.: EN+AS+EM+NS+SE+SS+TF-MoA5, 14
Guillorn, M.: PS+EM-MoA4, 15
Guillot, S.: EN+EM+NS+SE+SS+TF-TuA3, **27**
Gungor, N.: EM+MS-ThA7, 65
Gunlycke, D.: 2D+EM+NS+SS+TF-TuM1, **19**
Guo, J.-H.: EN+AS+EM+SE+SS-TuM13, 23
Guo, X.: EM-TuP22, 33; EM-WeA12, **43**
Guo, Y.: EM+NS+PS-MoA5, 12
Gupta, A.: 2D+EM+IS+NS+PS+SP+SS-FrM8, **72**
Gupta, R.: EM-WeM10, 36
Gupta, S.: EM+MS-ThM10, **51**
Gurunathan, R.L.: EM-TuM3, 20
Gustafson, J.L.: EN+EM+NS+SE+SS+TF-TuA9, 28

— H —

Hacker, N.: EM-ThM5, 52
Hafeez, M.A.: EL+AS+BI+EM-ThA9, 63
Haglund, A.V.: EM-TuP1, 30
Hahn, C.J.: EN+AS+EM+SE+SS-TuM3, 22
Haider, A.: EM+MS-ThA7, 65; EM+MS-ThM1, **50**
Haight, R.A.: EN+AS+EM+NS+SE+SS+TF-MoM1, 6; EN+AS+EM+NS+SE+SS+TF-MoM2, 7
Haislmaier, R.: EM+AS+SS-MoA5, 11
Hall, S.: EM+AS+SS-MoA1, 10
Halls, M.D.: SD+AS+EM-ThM10, 55; SS+AS+EM+EN-ThM2, 56
Hamers, R.J.: EN+EM+NS+SE+SS+TF-TuA3, 27
Hammer, R.: 2D+EM+MG+NS+SE+SM+SS+TF-ThM12, 47
Han, S.E.: EM+EN-ThA10, 64; EM+EN-ThA11, **64**
Han, S.J.: EM+EN-ThA10, **64**; EM+EN-ThA11, 64
Han, S.M.: EM+EN-ThA10, 64; EM+EN-ThA11, 64; EM-TuM4, **20**; SE+EM+EN-MoA4, 17
Hannah, E.C.: EN+EM+NS+SE+SS+TF-TuA9, 28
Harker, M.: TF+AS+EM+EN+MN-WeA12, 45
Hartman, J.: EM+MS-ThM10, 51
Hashemi, F.H.: SD+AS+EM+PS-ThA10, **68**
Hassan, V.: EM+NS+PS-MoA2, 12
Haukka, S.: SD+AS+EM+PS-ThA1, **66**
Hausmann, D.M.: TF+EM+NS+PS+SM-ThM1, **57**
Hayes, G.: SE+EM+EN-MoA5, 17
Hearn, G.: 2D+EM+NS+SS+TF-TuM11, 20
Heinlein, E.: EM+NS+PS-MoA8, 12
Hellstern, T.R.: EN+AS+EM+SE+SS-TuM3, 22
Hemminger, J.C.: EN+AS+EM+SE+SS-TuM6, 22
Henderson, W.A.: EN+EM+NS+SE+SS+TF-TuA4, 27
Henegar, A.J.: SS+AS+EM+EN-ThM11, **57**
Henry, G.: EM+MS-ThM10, 51
Henry, P.: EM-ThM3, 52
Heo, J.: EM-TuM10, 21
Heo, S.: EN+AS+EM+NS+SE+SS+TF-MoM6, **7**
Hernandez, J.: EM+AS+EN+NS-FrM8, 73
Hernández, S.C.: 2D+EM+IS+NS+PS+SP+SS-FrM1, 71; 2D+EM+NS+PS+SP+SS+TF-MoM1, 1
Hersam, M.C.: 2D+EM+MC+MS+NS-MoA9, 9
Herzinger, C.M.: EL+EM+EN-ThM6, 49
Hickey, R.: EM+NS+PS-MoA10, 13
Hight Walker, A.: 2D+EM+NS+PS+SP+SS+TF-MoM8, 2
Hinkle, C.L.: 2D+EM+IS+MC+NS+SP+SS-WeA8, 38
Hite, J.K.: 2D+EM+NS+PS+SP+SS+TF-MoM1, 1; 2D+EM+NS+PS+SP+SS+TF-MoM3, 1; EM+AS+MS+SS-WeA7, 40; EM+MS-ThM12, **51**
Hjort, M.: SS+AS+EM+EN-ThA9, 70
Hoard, B.: EM+EN-ThA11, 64
Hobart, K.D.: EM+AS+MS+SS-WeA12, 41; EM+AS+MS+SS-WeA7, 40
Hobbs, M.: TF+AS+EM+EN+MN-WeA4, 44
Hodges, D.R.: EN+AS+EM+NS+SE+SS+TF-MoM5, **7**
Hoffmann, A.: EM+MS-ThA8, 66
Hofmann, D.C.: AM+EM+MS+TF-ThM5, **48**
Hofmann, T.: EL+AS+BI+EM-ThA3, 62; EL+AS+BI+EM-ThA4, 62; EL+EM+EN-ThM6, 49
Holleitner, A.W.: 2D+EM+NS+SS+TF-TuM11, 20
Holmes, R.: EM+NS+PS-MoA8, 12
Holmlid, L.: EN+AS+EM+SE+SS-TuM1, 21
Holzwarth III, C.W.: EN+EM+NS+SE+SS+TF-TuA9, 28
Homola, T.: TF+EM+MI+MS-TuM4, 24
Honda, Y.: EM+EN-ThA3, 63
Hong, B.Y.: EM-TuP5, 30
Hou, M.: EM+AS+MS+SS-WeA8, **41**
Hourani, R.: SD+AS+EM-ThM10, 55
Howell, R.: EM+MS-ThM10, 51
Hsiao, C.N.: EM-TuP16, 32
Hsu, J.X.: SS+AS+EM+EN-ThM4, 56
Hsu, K.: EM-WeM6, **36**
Hu, K.: EM+NS+PS-MoA1, **11**
Hu, L.: 2D+EM+IS+MC+NS+SP+SS-WeA11, 39
Huang, C.: 2D+EM+MG+NS+SE+SM+SS+TF-ThM1, 46
Huang, S.: EM+AS+EN+NS-FrM4, 73
Hubbard, L.R.: EL+AS+BI+EM-ThA1, **62**; EM-TuP14, 32
Hughart, D.R.: EM-WeM1, 34
Hussain, H.: EL+AS+BI+EM-ThA9, 63
Hwang, C.S.: SD+AS+EM+PS-ThA9, 68

— I —

Iannaccone, G.: 2D+EM+MC+MS+NS-MoA6, 9
Ichikawa, A.: 2D+EM+IS+MC+NS+SP+SS-WeA12, 39
Iddawela, G.: EL+AS+BI+EM-ThA6, 62
Ikari, T.: EM+EN-ThA3, 63; EM+EN-ThA6, 64
Ikeda, N.: TF+EM+MI+MS-TuM6, 24
Illiberi, A.: EN+AS+EM+NS+SE+SS+TF-MoM8, **7**
Isaacson, S.G.: EM-ThM4, 52
Isarraraz, M.: 2D+EM+MC+MS+NS-MoA10, 9
Islam, S.M.: EM+MS-ThM3, 50
Iverson, B.D.: TF+AS+EM+EN+MN-WeA12, 45

— J —

Jacobberger, R.M.: 2D+EM+IS+NS+PS+SP+SS-FrM10, 72
Jain, .: EM+NS+PS-MoM2, 5
Jamieson, S.: EM-WeM11, 36
Jan, A.: SE+EM+EN-MoA5, 17
Janakiraman, S.: EN+AS+EM+NS+SE+SS+TF-MoA6, 14
Jang, J.E.: EM+AS+SS-MoA3, **10**; EM-TuP7, 30
Jaramillo, T.F.: EN+AS+EM+SE+SS-TuM3, **22**
Jariwala, D.: 2D+EM+MC+MS+NS-MoA9, 9
Järrendahl, K.: EL+EM+EN-ThM13, 50
Jayaraman, S.: EM-TuM12, **21**
Jena, D.: 2D+EM+NS+PS+SP+SS+TF-MoM9, 2; EM+MS-ThM3, 50
Jezewski, C.: EM-WeA7, 43
Jiang, H.: EL+EM+EN-ThM5, 48
Jiang, X.: EM+AS+SS-MoA10, 11
Jin, G.: EL+EM+EN-ThM10, **49**; EL+EM+EN-ThM12, 49
Jin, W.: 2D+EM+MG+NS+SS+TF-ThA2, 60; EN+EM+NS+SE+SS+TF-TuA9, 28
Job, N.: PS+EM-MoA9, 16
Joghee, P.: EM+AS+SS-MoM9, 4
Johansson, P.: TF+EM+MI+MS-TuM4, 24
Johar, M.A.: EL+AS+BI+EM-ThA9, 63
Johnson, K.: EM+NS+PS-MoA8, 12
Johnson, N.: EN+AS+EM+NS+SE+SS+TF-MoM9, **7**
Jones, J.G.: SE+EM+EN-MoA7, 17
Joseph, E.A.: PS+EM-MoA4, 15
Joshi, S.: EM+AS+SS-MoM1, 3; EM-TuP2, 30

Ju, H.X.: EN+AS+EM+NS+SE+SS+TF-MoA7, **14**; EN+AS+EM+SE+SS-TuM13, 23
Jung, H.: SD+AS+EM-ThM12, 55
Jung, S.: EM-TuM10, 21
Junquera, J.: EM+AS+SS-MoA5, 11

— K —

Kabir, N.: EM-WeA7, 43
Kachian, J.: EM+NS+PS-MoA1, 11; EM+NS+PS-MoM4, 5
Kaiser, D.: EM-TuM4, 20
Kakalios, J.: EN+AS+EM+NS+SE+SS+TF-MoA9, 14
Kalanyan, B.: 2D+EM+NS+PS+SP+SS+TF-MoM4, **1**
Kalyanikar, M.: EM-TuP27, 33
Kamba, S.: EM+AS+SS-MoA5, 11
Kamineni, V.M.: EL+AS+BI+EM-ThA6, **62**
Kaminski, P.M.: EN+AS+EM+NS+SE+SS+TF-MoM11, 8
Kamiya, K.: EM-TuP12, 31
Kang, H.J.: EN+AS+EM+NS+SE+SS+TF-MoM6, 7
Kang, M.: EM+AS+SS-MoM9, 4
Karim, A.: 2D+EM+MC+MI+NS+SP+SS+TF-TuA7, **26**
Karwal, S.: TF+EM+NS+PS+SM-ThM13, **59**
Kaspar, T.C.: EM+AS+SS-MoM11, **4**
Kassalen, P.: EM-WeM10, 36
Kaufman-Osborn, T.: EM+MS-ThM3, 50; EM-WeM3, **35**
Kava, D.: EN+AS+EM+NS+SE+SS+TF-MoM5, 7
Kawase, A.: EN+AS+EM+SE+SS-TuM13, 23
Kazior, T.: EM+MN+PS-TuA3, **27**
Kelaidis, N.: 2D+EM+MG+NS+SE+SM+SS+TF-ThM5, 46
Kelber, A.: 2D+EM+MG+NS+SS+TF-ThA6, **60**
Keller, N.: EL+AS+BI+EM-ThA2, 62
Kemal Okyay, A.: EM+MS-ThM1, 50
Kent, T.: EM+NS+PS-MoA7, 12; EM+NS+PS-MoM3, 5; EM+NS+PS-MoM4, 5
Kessels, W.M.M.: TF+EM+NS+PS+SM-ThM10, 58; TF+EM+NS+PS+SM-ThM12, 58; TF+EM+NS+PS+SM-ThM13, 59; TF+EM+NS+PS+SM-ThM6, 58
Khalili, P.: TF+EM+NS+PS+SM-ThM5, 58
Khan, A.A.: EM+AS+SS-MoA2, 10
Kibsgaard, J.: EN+AS+EM+SE+SS-TuM3, 22
Kim, H.: 2D+EM+MC+MI+NS+SP+SS+TF-TuA11, 26; AM+EM+MS+TF-WeM6, 34; EM+MS-ThM3, **50**; EM+NS+PS-MoA9, 13; EM-TuP15, **32**; SD+AS+EM-ThM12, 55
kim, H.J.: EM+NS+PS-MoM1, 4
Kim, H.-J.: SD+AS+EM-ThM12, 55
Kim, H.S.: PS+EM-MoA3, 15
Kim, J.: 2D+EM+MG+NS+SE+SM+SS+TF-ThM1, 46; 2D+EM+MG+NS+SS+TF-ThA7, 60
Kim, K.: EM-TuP15, 32
Kim, K.B.: EM+AS+SS-MoM9, 4
Kim, S.: EM-TuP7, 30
Kim, S.K.: EM+NS+PS-MoM1, **4**
Kimes, W.A.: 2D+EM+NS+PS+SP+SS+TF-MoM4, 1
King, M.: EM+MS-ThM10, 51
King, S.W.: EM+AS+MS+SS-WeA3, **40**; EM-ThM10, 53; EM-ThM11, 53; EM-ThM12, 53; EM-ThA3, 52; EM-TuP21, 32; EM-TuP22, 33; EM-WeA12, 43; EM-WeA7, 43; EM-WeM10, 36; EM-WeM12, 36; EM-WeM5, 35
Kis, A.: 2D+EM+IS+MC+NS+SP+SS-WeA2, 38; 2D+EM+MG+NS+SE+SM+SS+TF-ThM11, 47
Kitano, M.: TF+EM+MI+MS-TuM6, **24**
Kizir, S.: EM+MS-ThA7, 65; EM+MS-ThM1, 50
Klee, V.: 2D+EM+MG+NS+SE+SM+SS+TF-ThM1, 46
Knight, S.: EL+EM+EN-ThM6, **49**
Knoops, H.C.M.: TF+EM+NS+PS+SM-ThM10, **58**
Knutsson, J.: SS+AS+EM+EN-ThA9, 70
Koehler, A.D.: EM+AS+MS+SS-WeA7, 40
Koirala, P.: SS+AS+EM+EN-ThA11, 70
Kolmakov, A.: 2D+EM+NS+PS+SP+SS+TF-MoM8, 2
Kolodzey, J.: EM+NS+PS-MoA10, 13
Kondo, T.: 2D+EM+IS+NS+PS+SP+SS-FrM7, 71
Konstantinidis, S.: SE+EM+EN-MoA3, 17
Kooi, B.: EM+AS+EN+NS-FrM5, 73
Kooi, S.: EM+AS+SS-MoM9, 4
Kosaka, Y.R.: 2D+EM+IS+NS+PS+SP+SS-FrM7, 71
Kotter, D.: EM+AS+SS-MoM1, 3
Kourkoutis, L.F.: EM+AS+SS-MoA5, 11
Kozen, A.C.: EN+EM+NS+SE+SS+TF-TuA11, **28**
Krenner, H.: 2D+EM+MC+MS+NS-MoA10, 9
Krysak, M.: EM-WeA7, 43
Kub, F.J.: EM+AS+MS+SS-WeA12, 41; EM+MS-ThM12, 51
Kucukgok, B.: EM+MS-ThM4, 51
Kühne, P.: EL+EM+EN-ThM6, 49
Kummel, A.C.: 2D+EM+IS+MC+NS+SP+SS-WeA7, 38; 2D+EM+MG+NS+SS+TF-ThA1, 60; EM+MS-ThM3, 50; EM+NS+PS-MoA1, 11; EM+NS+PS-MoA7, 12; EM+NS+PS-MoA9, 13; EM+NS+PS-MoM3, 5; EM+NS+PS-MoM4, 5; EM-WeM3, 35; EM-WeM4, 35; EN+AS+EM+NS+SE+SS+TF-MoM1, **6**; EN+AS+EM+NS+SE+SS+TF-MoM2, 7
Kuo, S.Y.: EM-TuP16, 32
Kuusipalo, J.: TF+EM+MI+MS-TuM4, 24
Kwak, I.J.: 2D+EM+IS+MC+NS+SP+SS-WeA7, **38**; 2D+EM+MG+NS+SS+TF-ThA1, 60
Kwon, J.: EN+AS+EM+SE+SS-TuM6, **22**

— L —

Lagally, M.G.: 2D+EM+IS+NS+PS+SP+SS-FrM10, 72
Lai, F.I.: EM-TuP16, 32
Lanford, W.A.: EM-ThM3, 52
Lanigan, D.: EN+AS+EM+NS+SE+SS+TF-MoA10, 15
Lansford, J.: EM-WeA1, 42
LaRoche, J.: EM+MN+PS-TuA3, 27
Lau, K.K.S.: EN+AS+EM+NS+SE+SS+TF-MoA6, 14
Laughlin, K.: EM-WeM11, **36**
Lauhon, L.: 2D+EM+MC+MS+NS-MoA9, 9
Law, M.: EM+AS+EN+NS-FrM1, **72**
Le, D.: 2D+EM+IS+NS+PS+SP+SS-FrM9, 72
Lee, C.: 2D+EM+MG+NS+SE+SM+SS+TF-ThM1, 46
Lee, C.H.: EM+AS+SS-MoA5, 11
Lee, D.H.: EN+AS+EM+NS+SE+SS+TF-MoM6, 7
Lee, E.: EM-TuM10, 21
Lee, H.I.: EN+AS+EM+NS+SE+SS+TF-MoM6, 7
Lee, J.: EM-TuM10, 21
Lee, J.D.: EM-TuP14, 32
Lee, J.U.: EM+NS+PS-MoM8, **6**
Lee, K.: EM-TuM10, 21
Lee, S.: EM-TuM10, 21
Lee, S.I.: TF+EM+MI+MS-TuM1, **23**
Lee, S.-Y.: EM+AS+SS-MoA7, **11**
Lee, W.C.: EM-TuP5, **30**
Lee, W.K.: 2D+EM+MC+MI+NS+SP+SS+TF-TuA3, **26**
Lee, Y.: EM-WeA1, 42
Lee, Y.-B.: SD+AS+EM-ThM12, 55
Lee, Y.C.: EM-TuP16, 32
Lee, Y.J.: SS+AS+EM+EN-ThM4, 56
Lehmann, S.: SS+AS+EM+EN-ThA9, 70
Leighton, C.: EN+AS+EM+NS+SE+SS+TF-MoA9, 14
Leijtens, T.: EN+AS+EM+NS+SE+SS+TF-MoA3, **13**
Leite, M.: 2D+EM+NS+PS+SP+SS+TF-MoM8, 2
Lenahan, P.M.: EM-ThM12, 53
Leone, S.R.: SS+AS+EM+EN-ThM12, 57
Lerner, P.B.: EM+AS+SS-MoM5, **3**
Leusink, G.: SD+AS+EM+PS-ThA11, 68
Li, A.-P.: 2D+EM+IS+MC+NS+SP+SS-WeA9, **39**
Li, J.: EN+AS+EM+NS+SE+SS+TF-MoM10, **8**
Li, M.: EN+AS+EM+NS+SE+SS+TF-MoA9, 14; SS+AS+EM+EN-ThA10, **70**
Li, S.: EN+AS+EM+NS+SE+SS+TF-MoA5, 14
Li, W.: EM-ThM13, 53
Li, W.Q.: EL+EM+EN-ThM5, **48**
Li, X.: TF+EM+NS+PS+SM-ThM5, 58
Li, Y.: 2D+EM+MC+MS+NS-MoA3, **9**
Li, Y.L.: SE+EM+EN-MoA1, **17**
Lima, L.P.B.: EM-TuP17, 32
Lin, F.: EN+EM+NS+SE+SS+TF-TuA1, 27
Lin, S.: EM+AS+SS-MoM10, **4**
Lin, Y.: EM+MS-ThA3, 65
Lin, Y.-C.: 2D+EM+MG+NS+SE+SM+SS+TF-ThM6, 46; 2D+EM+NS+PS+SP+SS+TF-MoM9, 2
Lin, Y.H.: EM-TuP26, 33
Linford, M.R.: EM-WeM11, 36
Lionti, K.: EM-ThM4, 52
Liu, C.: PS+EM-MoA4, 15
Liu, G.: EM-TuP27, 33
Liu, H.: 2D+EM+IS+NS+PS+SP+SS-FrM5, **71**; EM-WeA1, 42; EM-WeA11, 43
Liu, L.-H.: EN+AS+EM+NS+SE+SS+TF-MoA1, 13; SD+AS+EM-ThM10, 55; SS+AS+EM+EN-ThM4, 56
Liu, Q.: EN+EM+NS+SE+SS+TF-TuA10, 28
Liu, S.Y.: EL+EM+EN-ThM5, 48
Liu, W.: EM-TuP26, 33
Liu, X.: 2D+EM+MC+MS+NS-MoA9, 9; 2D+EM+NS+PS+SP+SS+TF-MoM9, 2
Liu, Y.: EN+EM+NS+SE+SS+TF-TuA9, 28
Lo, C.: EM+NS+PS-MoA2, 12
Long, J.W.: EN+EM+NS+SE+SS+TF-TuA7, 28
Long, R.: EM+AS+MS+SS-WeA11, 41
Longo, R.C.: SS+AS+EM+EN-ThM2, 56; SS+AS+EM+EN-ThM4, 56
Longo, V.: TF+EM+NS+PS+SM-ThM12, 58
López Sánchez, O.: 2D+EM+MC+MS+NS-MoA6, **9**
Lopez-Sanchez, O.: 2D+EM+MG+NS+SE+SM+SS+TF-ThM11, 47

Lu, D.: EM+AS+SS-MoM6, 3; EN+EM+NS+SE+SS+TF-TuA4, 27
Lu, I.: 2D+EM+MC+MS+NS-MoA10, 9; 2D+EM+MG+NS+SE+SM+SS+TF-ThM1, 46
Lu, J.P.: AM+EM+MS+TF-ThA3, 61
Lu, N.: EM+MS-ThM4, 51
Lucas, S.: SE+EM+EN-MoA3, 17
Lunt, B.M.: EM-WeM11, 36
Luo, Z.: EM+AS+SS-MoA1, 10

— M —

Ma, Z.: EM-WeM6, 36
Macco, B.: TF+EM+NS+PS+SM-ThM6, 58
Madisetti, S.: EM+NS+PS-MoA1, 11; EM-WeM3, 35
Maeda, P.: AM+EM+MS+TF-ThA3, 61
Maes, J.W.: SD+AS+EM+PS-ThA1, 66
Magbitang, T.P.: EM-ThM4, 52
Magnusson, R.: EL+EM+EN-ThM13, **50**
Maher, M.: PS+EM-MoA4, 15
Makin, R.A.: EM+MS-ThA6, 65
Malko, A.V.: EN+AS+EM+NS+SE+SS+TF-MoA1, 13
Mancheno-Posso, L.: EM+NS+PS-MoM2, **5**
Mandrus, D.: EM-TuP1, 30
Mangolini, L.: EM+AS+EN+NS-FrM8, 73
Mannequin, C.: EM-WeM2, 35
Manno, M.: EN+AS+EM+NS+SE+SS+TF-MoA9, 14
Marinella, M.: EM-WeM1, 34
Marini, J.: SS+AS+EM+EN-ThM13, 57
Marinov, K.M.: 2D+EM+IS+MC+NS+SP+SS-WeA2, **38**
Marks, T.J.: 2D+EM+MC+MS+NS-MoA9, 9
Markus, I.: EN+EM+NS+SE+SS+TF-TuA1, 27
Marot, L.: PS+EM-MoA10, 16
Marquez-Velasco, J.: 2D+EM+MG+NS+SE+SM+SS+TF-ThM5, 46
Martin, E.J.: EM+EN-ThA10, 64
Martinez, J.: 2D+EM+MC+MI+NS+SP+SS+TF-TuA4, 26
Mashaal, H.: EM+AS+SS-MoM4, **3**
Maslar, J.E.: 2D+EM+NS+PS+SP+SS+TF-MoM4, 1
Mastro, M.A.: EM+MS-ThM12, 51
Matei, I.: AM+EM+MS+TF-ThA3, 61
Mathis, J.P.: EM+MS-ThA6, 65
Mathys, D.: PS+EM-MoA10, 16
Matsuochi, K.: EM+EN-ThA6, 64
Matsuyama, H.: 2D+EM+IS+MC+NS+SP+SS-WeA12, 39
Maydannik, P.S.: TF+EM+MI+MS-TuM4, 24
McAlpine, M.: AM+EM+MS+TF-ThA6, **61**
McDonnell, S.: 2D+EM+IS+MC+NS+SP+SS-WeA8, 38; 2D+EM+MG+NS+SS+TF-ThA7, 60
McGehee, M.D.: EN+AS+EM+NS+SE+SS+TF-MoA3, 13
McIntyre, P.: EM+NS+PS-MoM3, 5
McIntyre, P.C.: EM+AS+MS+SS-WeA11, 41; EM+NS+PS-MoA1, 11; EM+NS+PS-MoA2, 12; TF+EM+MI+MS-TuM6, 24
McNamara, J.D.: SS+AS+EM+EN-ThM13, **57**
Meany, B.: EM+AS+EN+NS-FrM7, 73
Meinel, K.: 2D+EM+MG+NS+SE+SM+SS+TF-ThM12, 47
Mende, P.: 2D+EM+NS+PS+SP+SS+TF-MoM9, 2
Merche, D.: PS+EM-MoA9, 16
Meyer, J.R.: EM+MS-ThM12, 51
Meysing, D.M.: EN+AS+EM+NS+SE+SS+TF-MoM10, 8
Michael, M.K.: SE+EM+EN-MoA1, 17
Michalak, D.J.: EM-WeA7, 43; SD+AS+EM-ThM10, 55; SS+AS+EM+EN-ThM4, 56
Mikkelsen, A.: SS+AS+EM+EN-ThA9, 70
Miller, B.: 2D+EM+NS+SS+TF-TuM11, 20
Minaye Hashemi, F.H.: SD+AS+EM+PS-ThA6, 67
Miskovsky, N.M.: EM+AS+SS-MoM5, 3
Misra, V.: TF+EM+NS+PS+SM-ThM3, **57**
Mitrovic, I.Z.: EM+AS+SS-MoA1, **10**
Mitzi, D.B.: EN+AS+EM+NS+SE+SS+TF-MoM1, 6
Miyazoe, H.: PS+EM-MoA4, **15**
Mock, A.: EL+AS+BI+EM-ThA3, **62**; EL+AS+BI+EM-ThA4, 62
Moddel, G.: EM+AS+SS-MoM1, **3**; EM+AS+SS-MoM3, 3; EM-TuP2, 30
Mohimi, E.: SD+AS+EM-ThM2, **54**
Mohney, S.E.: EM-TuM3, **20**
Moinpour, M.: EM-WeA7, 43
Moon, B.K.: EN+EM+NS+SE+SS+TF-TuA9, 28
Mooney, P.: EM+AS+MS+SS-WeA1, **40**
Morales-Cifuentes, J.R.: SS+AS+EM+EN-ThA4, **69**
Mork, F.: EN+AS+EM+NS+SE+SS+TF-MoA9, 14
Morris, E.: AM+EM+MS+TF-WeM1, **34**
Moskovkin, P.: SE+EM+EN-MoA3, 17
Moten, R.: EM-TuP9, 31
Mousa, M.B.: SD+AS+EM+PS-ThA7, 67
Movva, H.C.P.: 2D+EM+IS+MC+NS+SP+SS-WeA7, 38; 2D+EM+MG+NS+SS+TF-ThA1, 60
Mowll, T.R.: 2D+EM+NS+PS+SP+SS+TF-MoM2, **1**
Mueller, T.: 2D+EM+NS+SS+TF-TuM3, **19**
Muller, D.A.: EM+AS+SS-MoA5, 11
Mundy, J.A.: EM+AS+SS-MoA5, 11
Murakami, T.: EM+EN-ThA6, 64
Murari, N.: EM+AS+SS-MoM10, 4
Murphy, N.R.: EN+AS+EM+NS+SE+SS+TF-MoA8, 14; SE+EM+EN-MoA7, 17
Murphy, R.D.: TF+AS+EM+EN+MN-WeA3, **44**
Murray, C.B.: EN+AS+EM+NS+SE+SS+TF-MoA5, 14
Muscat, A.J.: EL+AS+BI+EM-ThA1, 62; EM+NS+PS-MoM2, 5; EM-TuP14, **32**
Mutch, M.: EM-ThM12, **53**
Muth, J.F.: EM+MS-ThA1, **65**
Myers, A.: EM-WeA7, 43
Myers-Ward, R.L.: 2D+EM+NS+SS+TF-TuM10, 20

— N —

Nagase, M.: TF+EM+MI+MS-TuM6, 24
Naghibi, S.: 2D+EM+MG+NS+SE+SM+SS+TF-ThM1, 46
Naguib, M.: 2D+EM+MG+NS+SE+SM+SS+TF-ThM3, **46**
Nakajima, Y.: EM+MS-ThA3, 65
Nakamura, J.: 2D+EM+IS+MC+NS+SP+SS-WeA12, **39**; 2D+EM+IS+NS+PS+SP+SS-FrM7, 71
Nakamura, T.: EM+EN-ThA6, **64**
Nakano, M.: EM+EN-ThA3, **63**
Nakano, Y.: EM+EN-ThA6, 64
Nallan, H.: SD+AS+EM-ThM11, 55
Nam, J.G.: EN+AS+EM+NS+SE+SS+TF-MoM6, 7
Nandasiri, M.I.: EN+EM+NS+SE+SS+TF-TuA4, **27**
Narasimhan, M.: TF+AS+EM+EN+MN-WeA1, **44**
Nath, A.: 2D+EM+NS+PS+SP+SS+TF-MoM3, 1
Nechay, B.: EM+MS-ThM10, 51
Negara, M.: EM+AS+MS+SS-WeA11, **41**; EM+NS+PS-MoM3, 5
Nelaturi, S.: AM+EM+MS+TF-ThA3, 61
Nelson, C.: SE+EM+EN-MoA4, 17
Nelson, S.F.: EM+AS+SS-MoA9, **11**
Nemanich, R.: EM+AS+MS+SS-WeA3, 40
Nepal, N.: EM+AS+MS+SS-WeA7, 40
Nesladek, M.: 2D+EM+NS+SS+TF-TuM2, 19
Ngo, T.: SD+AS+EM-ThM11, 55
Nguyen, A.: 2D+EM+MC+MS+NS-MoA10, 9; 2D+EM+MG+NS+SE+SM+SS+TF-ThM1, 46
Nguyen, T.D.: EM-ThM3, 52
Nichols, M.: EM-ThM10, 53
Nie, Y.: EM+AS+SS-MoA5, 11
Nilsson, HM.: EM+AS+EN+NS-FrM7, **73**
Nishi, Y.: EM-ThM10, 53; EM-ThM11, 53; EM-ThM13, 53; EM-TuP21, 32; EM-TuP22, 33; EM-WeA12, 43; EM-WeM6, 36
Niu, Y.: EL+EM+EN-ThM10, 49; EL+EM+EN-ThM12, **49**
Noh, J.H.: EM-TuP1, 30
Nordell, B.J.: EM-ThM3, 52
Nunley, T.N.: EM+NS+PS-MoA10, 13
Nyakiti, L.O.: 2D+EM+NS+PS+SP+SS+TF-MoM3, 1

— O —

O'Mullane, S.: EL+AS+BI+EM-ThA6, 62
Obata, H.T.: EM-TuP17, 32
O'Brien, L.: EN+AS+EM+NS+SE+SS+TF-MoA9, 14
Oh, I.K.: SD+AS+EM-ThM12, 55
O'Hayre, R.: EM+AS+SS-MoM9, 4
Ohori, D.: EM+EN-ThA3, 63
Oktyabrsky, S.: EM+NS+PS-MoA1, 11; EM-WeM3, 35
Okyay, A.K.: EM+MS-ThA7, 65; EM+MS-ThM13, 51
Olafsson, S.: EN+AS+EM+SE+SS-TuM1, **21**
Olanipekun, B.: 2D+EM+MG+NS+SS+TF-ThA6, 60
Oleynik, I.I.: 2D+EM+IS+MC+NS+SP+SS-WeA1, 38
Olsen, C.: EM+NS+PS-MoA2, 12
Olsson, E.: EM+AS+EN+NS-FrM7, 73
Olvera, M.A.: EM+AS+EN+NS-FrM3, 73
O'Meara, D.: SD+AS+EM+PS-ThA11, 68
O'Mullane, S.: EL+AS+BI+EM-ThA2, **62**
Ong, E.W.: 2D+EM+NS+PS+SP+SS+TF-MoM2, 1
Ooki, W.: 2D+EM+IS+NS+PS+SP+SS-FrM7, 71
Opasanont, B.: EN+AS+EM+SE+SS-TuM5, 22
Orloff, N.D.: EM+AS+SS-MoA5, 11
Orlowski, M.K.: EM-WeM10, **36**; EM-WeM12, 36; EM-WeM5, 35
Orzali, T.: 2D+EM+NS+PS+SP+SS+TF-MoM4, 1
Osgood, Jr., R.M.: 2D+EM+MG+NS+SS+TF-ThA2, 60
Osgood, R.M.: EM+AS+SS-MoM9, **4**
Ossikovski, R.: EL+EM+EN-ThM13, 50
Ovchinnikov, D.: 2D+EM+IS+MC+NS+SP+SS-WeA2, 38
Ozgit-Akgun, C.: EM+MS-ThM1, 50; EM+MS-ThM13, 51

— P —

Padhi, D.: EM-WeA9, 43
Pak, D.M.: SS+AS+EM+EN-ThM4, 56

Pakbaz, H.: EM-ThM5, **52**
Pala, I.R.: EN+EM+NS+SE+SS+TF-TuA7, 28
Palasantzas, G.: EM+AS+EN+NS-FrM5, 73
Paquette, M.M.: EM-ThM3, **52**
Paradiso, S.: PS+EM-MoA1, **15**
Parameshwaran, V.: SE+EM+EN-MoA5, 17
Parameswaran, L.: EM+AS+SS-MoM9, 4
Park, G.S.: EN+AS+EM+NS+SE+SS+TF-MoM6, 7
Park, J.B.: EN+AS+EM+NS+SE+SS+TF-MoM6, 7
Park, J.H.: 2D+EM+IS+MC+NS+SP+SS-WeA7, 38; 2D+EM+MG+NS+SS+TF-ThA1, **60**; SS+AS+EM+EN-ThM4, **56**
Park, J.W.: PS+EM-MoA3, 15
Park, S.: EM-TuM10, **21**
Park, S.P.: EM+MS-ThM3, 50; EM+NS+PS-MoA9, **13**
Park, W.: EM+AS+SS-MoM6, **3**
Parke, J.: EM+MS-ThM10, 51
Parker, J.F.: EN+EM+NS+SE+SS+TF-TuA7, 28
Parsons, G.N.: SD+AS+EM+PS-ThA7, 67
Parzinger, E.: 2D+EM+NS+SS+TF-TuM11, 20
Patel, A.M.: EN+AS+EM+SE+SS-TuM5, 22
Pearson, T.: EM-WeM11, 36
Pei, D.: EM-ThM10, **53**
Pei, L.: TF+AS+EM+EN+MN-WeA12, 45
Peixoto, T.: SD+AS+EM-ThM10, 55
Pelz, B.: EM+AS+SS-MoM1, 3; EM+AS+SS-MoM3, **3**
Pena-Hueso, A.: EN+EM+NS+SE+SS+TF-TuA3, 27
Peng, W.N.: EN+AS+EM+NS+SE+SS+TF-MoA1, **13**; SS+AS+EM+EN-ThM4, 56
Peretti, M.W.: AM+EM+MS+TF-WeM3, **34**
Periasamy, P.: EM+AS+SS-MoM9, 4
Perkins, R.T.: EL+AS+BI+EM-ThA11, 63
Perriot, R.: 2D+EM+IS+MC+NS+SP+SS-WeA1, 38
Persson, O.: SS+AS+EM+EN-ThA9, 70
Phumisithikul, K.L.: SS+AS+EM+EN-ThM13, 57
Piallat, F.: EM-WeA10, **43**
Pierangelo, A.: EL+EM+EN-ThM1, 48
Pierre, A.C.: AM+EM+MS+TF-ThA1, 61
Pimpinelli, A.: SS+AS+EM+EN-ThA4, 69
Piqué, A.: AM+EM+MS+TF-WeM6, 34
Plombon, J.: EM-WeA7, 43
Pohlman, A.J.: SS+AS+EM+EN-ThM10, **56**
Poodt, P.: EN+AS+EM+NS+SE+SS+TF-MoM8, 7; TF+EM+MI+MS-TuM3, 23
Porter, L.M.: EM+AS+MS+SS-WeA4, **40**; EM-WeM4, 35
Preciado, E.: 2D+EM+MC+MS+NS-MoA10, **9**; 2D+EM+MG+NS+SE+SM+SS+TF-ThM1, 46
Pudasaini, P.R.: EM-TuP1, **30**
Pujar, S.P.: SD+AS+EM-ThM10, 55
Purohit, S.S.: EM-ThM3, 52
Pyzyna, A.: PS+EM-MoA4, 15

— Q —

Qi, J.: EM+AS+SS-MoA10, **11**; EM-TuP6, 30
Qin, X.: 2D+EM+MG+NS+SS+TF-ThA7, 60; EM+MS-ThA10, **66**

— R —

Race, J.: EL+AS+BI+EM-ThA2, 62
Rack, P.D.: EM-TuP1, 30
Raes, M.: PS+EM-MoA9, 16
Rahman, T.S.: 2D+EM+IS+NS+PS+SP+SS-FrM9, 72; 2D+EM+NS+SS+TF-TuM5, 19
Rajagopalan, R.: TF+EM+MI+MS-TuM10, **24**
Ralph, J.F.: EM+AS+SS-MoA1, 10
Ramos, C.: EM+NS+PS-MoA8, 12
Randall, C.: TF+EM+MI+MS-TuM10, 24
Randall, J.: SD+AS+EM+PS-ThA8, 67
Rangan, S.: EM-TuP27, **33**
Rawal, T.B.: 2D+EM+IS+NS+PS+SP+SS-FrM9, **72**
Raychaudhuri, S.: AM+EM+MS+TF-ThA3, 61
Reed, E.J.: 2D+EM+IS+NS+PS+SP+SS-FrM2, 71; 2D+EM+MC+MS+NS-MoA3, 9
Reese, M.O.: EN+AS+EM+NS+SE+SS+TF-MoM10, 8
Reeves, J.B.: SE+EM+EN-MoA5, 17
Reeves, R.V.: TF+AS+EM+EN+MN-WeA11, **44**; TF+AS+EM+EN+MN-WeA3, 44; TF+AS+EM+EN+MN-WeA4, 44
Rehman, S.: EL+AS+BI+EM-ThA9, 63
Reid, S.: 2D+EM+MG+NS+SS+TF-ThA6, 60
Reinecke, T.L.: 2D+EM+IS+NS+PS+SP+SS-FrM1, 71
Renaldo, K.: EM+MS-ThM10, 51
Renault, O.J.: 2D+EM+MC+MI+NS+SP+SS+TF-TuA11, **26**
Reniers, F.A.B.: PS+EM-MoA9, 16
Reshchikov, M.A.: SS+AS+EM+EN-ThM13, 57
Reshotko, M.: EM-WeA7, 43
Ribton, C.N.: AM+EM+MS+TF-WeM5, **34**
Robertson, J.: 2D+EM+IS+MC+NS+SP+SS-WeA7, 38; EM+NS+PS-MoA5, **12**
Robinson, J.A.: 2D+EM+MG+NS+SE+SM+SS+TF-ThM6, 46; 2D+EM+NS+PS+SP+SS+TF-MoM9, 2; EM+NS+PS-MoM5, **6**
Robinson, J.T.: 2D+EM+IS+NS+PS+SP+SS-FrM1, 71; 2D+EM+MC+MI+NS+SP+SS+TF-TuA3, 26
Robinson, Z.R.: 2D+EM+NS+PS+SP+SS+TF-MoM1, 1; 2D+EM+NS+PS+SP+SS+TF-MoM2, 1
Rockett, A.: EN+AS+EM+NS+SE+SS+TF-MoM9, 7; SS+AS+EM+EN-ThA11, 70
Rojas Delgado, R.: 2D+EM+IS+NS+PS+SP+SS-FrM10, **72**
Rokholt, J.A.: EM+AS+MS+SS-WeA4, 40
Rolison, D.R.: EN+EM+NS+SE+SS+TF-TuA7, **28**
Romolino, K.L.: SS+AS+EM+EN-ThM10, 56
Rothschild, M.: EM+AS+SS-MoM9, 4
Routkevitic, D.: TF+EM+MI+MS-TuM5, 24
Rowley, J.T.: TF+AS+EM+EN+MN-WeA12, 45
Rubloff, G.W.: EN+EM+NS+SE+SS+TF-TuA11, 28
Rusydi, A.: EL+EM+EN-ThM3, 48
Ryan, E.: EM-TuP21, 32; EM-TuP22, 33

— S —

Saadi, M.: EM-WeM2, 35
Sahu, B.: EM+NS+PS-MoA1, 11; EM+NS+PS-MoA9, 13; EM-WeM3, 35
Saidi, W.A.: SS+AS+EM+EN-ThA3, 69
Sakai, K.: EM+EN-ThA3, 63
Salagaj, T.: EM+AS+MS+SS-WeA4, 40
Sampat, S.C.: EN+AS+EM+NS+SE+SS+TF-MoA1, 13
Sana, C.O.: EN+AS+EM+NS+SE+SS+TF-MoM5, 7
Sanchez Perez, J.R.: 2D+EM+IS+NS+PS+SP+SS-FrM10, 72
Sanders, D.: PS+EM-MoA4, 15
Sandoval, T.E.: SS+AS+EM+EN-ThM1, **55**
Sangwan, V.: 2D+EM+MC+MS+NS-MoA9, 9
Sanne, A.M.: 2D+EM+IS+MC+NS+SP+SS-WeA7, 38
Sardashti, K.: EM+MS-ThM3, 50; EM+NS+PS-MoA1, 11; EN+AS+EM+NS+SE+SS+TF-MoM1, 6; EN+AS+EM+NS+SE+SS+TF-MoM2, **7**
Satpathy, S.: 2D+EM+NS+PS+SP+SS+TF-MoM9, 2
Sauter, A.J.: EN+AS+EM+NS+SE+SS+TF-MoA6, 14
Sbrockey, N.M.: EM+AS+MS+SS-WeA4, 40
Schlom, D.G.: EM+AS+SS-MoA5, **11**
Schmidt, D.: EL+AS+BI+EM-ThA4, 62; EL+EM+EN-ThM3, **48**
Schneider, W.F.: SS+AS+EM+EN-ThA1, **68**
Schöche, S.: EL+EM+EN-ThM6, 49
Schreiber, D.K.: EM+AS+SS-MoM11, 4
Schroeder, D.: 2D+EM+IS+NS+PS+SP+SS-FrM10, 72
Schubert, E.: EL+AS+BI+EM-ThA3, 62; EL+AS+BI+EM-ThA4, 62
Schubert, M.: EL+AS+BI+EM-ThA3, 62; EL+AS+BI+EM-ThA4, 62; EL+EM+EN-ThM6, 49
Schülein, F.J.R.: 2D+EM+MC+MS+NS-MoA10, 9
Schwarz, A.: EN+EM+NS+SE+SS+TF-TuA4, 27
Seabaugh, A.C.: 2D+EM+MG+NS+SS+TF-ThA1, 60
Seal, S.: 2D+EM+IS+NS+PS+SP+SS-FrM8, 72
Sedghi, N.: EM+AS+SS-MoA1, 10
Seebauer, E.: SS+AS+EM+EN-ThA10, 70
Seidlitz, D.: EM+MS-ThA8, **66**; EM+MS-ThM2, 50
Sekora, D.: EL+AS+BI+EM-ThA3, 62
Selvan, T.: 2D+EM+IS+NS+PS+SP+SS-FrM8, 72
Senabulya, N.: EM+MS-ThA6, 65
Senegor, R.: EM-WeA2, 42
Senesky, D.G.: EM+AS+MS+SS-WeA8, 41
Senevirathna, I.: EM+MS-ThA8, 66
Seo, S.: SD+AS+EM-ThM12, **55**
Shahedipour-Sandvik, F.: SS+AS+EM+EN-ThM13, 57
Shahriar, S.: EN+AS+EM+NS+SE+SS+TF-MoM5, 7
Shamim, A.: EM+AS+SS-MoA2, **10**
Sharma, A.: TF+EM+NS+PS+SM-ThM12, **58**
Sharma, K.: TF+EM+MI+MS-TuM5, **24**
Sheehan, P.E.: 2D+EM+IS+NS+PS+SP+SS-FrM1, **71**; 2D+EM+MC+MI+NS+SP+SS+TF-TuA3, 26
Shehzad, M.A.: EL+AS+BI+EM-ThA9, 63
Shen, K.M.: EM+AS+SS-MoA5, 11
Shin, J.H.: EM-TuP7, **30**
Shiraishi, K.: EM-TuP10, 31; EM-TuP11, 31; EM-TuP12, 31
Shirakawa, H.: EM-TuP11, 31; EM-TuP12, **31**
Shohet, J.L.: EM-ThM10, 53; EM-ThM11, 53; EM-ThM13, 53; EM-TuP21, 32; EM-TuP22, 33; EM-WeA12, 43; EM-WeM6, 36
Shu, J.: EM-WeA1, **42**; EM-WeA11, 43
Shumlas, S.L.: 2D+EM+MG+NS+SE+SM+SS+TF-ThM2, 46
Sibener, S.J.: SS+AS+EM+EN-ThA8, 69
Siddiqui, S.: EM+NS+PS-MoA1, 11; EM+NS+PS-MoA9, 13
Simsek, E.: 2D+EM+NS+SS+TF-TuM1, 19

Singam, S.K.R.: 2D+EM+NS+SS+TF-TuM2, 19
Singh, A.: EM-TuP8, **31**
Singh, K.: EM-WeA7, 43
Sinno, T.: EM-TuM4, 20
Sivapragasam, N.: 2D+EM+MG+NS+SE+SM+SS+TF-ThM10, **47**
Smolin, Y.Y.: EN+AS+EM+NS+SE+SS+TF-MoA6, **14**
Smyth, C.M.: 2D+EM+IS+MC+NS+SP+SS-WeA8, **38**
Snook, M.: EM+MS-ThM10, 51
Snyders, R.: SE+EM+EN-MoA3, **17**
Soares, J.: SS+AS+EM+EN-ThA11, 70
Soroush, M.: EN+AS+EM+NS+SE+SS+TF-MoA6, 14
Soukiassian, G.: 2D+EM+IS+NS+PS+SP+SS-FrM3, **71**
Spence, J.: EM-TuP9, **31**
Sperling, B.A.: 2D+EM+NS+PS+SP+SS+TF-MoM4, 1
Spiegelman, J.: EM+NS+PS-MoA8, 12
Spurgeon, S.R.: EM+AS+SS-MoM11, 4
Sridhara, K.: 2D+EM+NS+PS+SP+SS+TF-MoM1, 1
Sridhara, KS.: 2D+EM+NS+PS+SP+SS+TF-MoM3, **1**
Srivathanakul, S.: EM-WeA11, 43
Stergiopoulos, V.: PS+EM-MoA9, 16
Stevens, E.: SD+AS+EM+PS-ThA7, **67**
Stewart, E.: EM+MS-ThM10, 51
Stine, R.: 2D+EM+IS+NS+PS+SP+SS-FrM1, 71
Stoica, V.A.: EM-TuP26, 33
Stolbov, S.: 2D+EM+IS+NS+PS+SP+SS-FrM6, **71**
Stranick, S.J.: 2D+EM+NS+PS+SP+SS+TF-MoM4, 1
Streller, F.: EM-WeM13, **36**
Strongin, D.R.: 2D+EM+MG+NS+SE+SM+SS+TF-ThM2, 46
Sugihara, K.: EM+EN-ThA3, 63
Sugiyama, M.: EM+EN-ThA6, 64
Sullivan, K.T.: TF+AS+EM+EN+MN-WeA11, 44
Sun, L.: SE+EM+EN-MoA7, **17**
Sun, Z.: EM-WeA1, 42; EM-WeA11, **43**
Sutter, P.W.: 2D+EM+MG+NS+SS+TF-ThA3, **60**
Sutto, T.: AM+EM+MS+TF-WeM6, 34
Suzer, S.: 2D+EM+MC+MS+NS-MoA4, **9**; EN+AS+EM+NS+SE+SS+TF-MoM9, 7
Suzuki, H.: EM+EN-ThA6, 64
Syed, A.: EM+AS+SS-MoA2, 10
Sylvestre, A.: EM-WeM2, 35
Syme, D.B.: TF+AS+EM+EN+MN-WeA12, 45

— T —

Tadjer, M.J.: EM+AS+MS+SS-WeA7, 40
Takato, M.: EM-TuP11, **31**
Takeuchi, I.: EM+AS+SS-MoA5, 11
Tang, K.: EM+NS+PS-MoA1, 11; EM+NS+PS-MoM3, **5**
Tangirala, V.K.: EM+AS+EN+NS-FrM3, **73**
Tanyeli, I.: PS+EM-MoA10, **16**
Tapily, K.: SD+AS+EM+PS-ThA11, **68**
Tekcan, B.: EM+MS-ThM13, 51
ten Brink, G.H.: EM+AS+EN+NS-FrM5, **73**
Teplyakov, A.V.: SS+AS+EM+EN-ThM3, 56
Terryn, H.: PS+EM-MoA9, 16
Thenuwara, A.C.: 2D+EM+MG+NS+SE+SM+SS+TF-ThM2, 46
Thiesen, P.H.: 2D+EM+NS+SS+TF-TuM11, **20**; 2D+EM+NS+SS+TF-TuM6, 19
Thimsen, E.: EN+AS+EM+NS+SE+SS+TF-MoA10, **15**
Thissen, N.F.W.: TF+EM+NS+PS+SM-ThM6, 58
Thissen, P.: SS+AS+EM+EN-ThM2, 56
Thornton, K.: EM+AS+EN+NS-FrM4, 73
Ticey, J.: EM+AS+EN+NS-FrM7, 73
Tieckelmann, R.: 2D+EM+NS+PS+SP+SS+TF-MoM4, 1
Timm, R.: SS+AS+EM+EN-ThA9, **70**
Tokei, Z.: EM-ThM5, 52
Tomalia, D.A.: EN+EM+NS+SE+SS+TF-TuA4, 27
Tompa, G.S.: EM+AS+MS+SS-WeA4, 40
Toprasertpong, K.: EM+EN-ThA6, 64
Torregrosa, I.G.: EN+AS+EM+SE+SS-TuM5, 22
Torres, J.: EM-WeA7, 43
Trautmann, M.: 2D+EM+MG+NS+SE+SM+SS+TF-ThM12, 47
Trinh, B.: SD+AS+EM-ThM2, 54
Troian, A.: SS+AS+EM+EN-ThA9, 70
Tsai, H.: PS+EM-MoA4, 15
Tseng, F.: 2D+EM+NS+SS+TF-TuM1, 19
Tsipas, P.: 2D+EM+MG+NS+SE+SM+SS+TF-ThM5, 46
Tsoi, S.: 2D+EM+IS+NS+PS+SP+SS-FrM1, 71
Tsoutsou, D.: 2D+EM+MG+NS+SE+SM+SS+TF-ThM5, 46
Turkot, R.: EM-WeA7, 43
Turkowski, V.: 2D+EM+NS+SS+TF-TuM5, **19**
Turley, R.S.: EL+AS+BI+EM-ThA11, 63
Turner, J.: EN+AS+EM+SE+SS-TuM12, 23
Tuteja, M.: SS+AS+EM+EN-ThA11, **70**
Tutt, L.W.: EM+AS+SS-MoA9, 11
Tutuc, E.: EM+NS+PS-MoM10, **6**
Tyagi, P.: 2D+EM+NS+PS+SP+SS+TF-MoM2, 1

— U —

Uecker, R.: EM+AS+SS-MoA5, 11
Uher, C.: EM-TuP26, 33
Usrey, M.: EN+EM+NS+SE+SS+TF-TuA3, 27

— V —

Vaid, A.: EL+AS+BI+EM-ThA6, 62
Vaida, M.E.: SS+AS+EM+EN-ThM12, **57**
Valentin, M.: 2D+EM+MC+MI+NS+SP+SS+TF-TuA4, 26
Vallee, C.: EM-WeM2, **35**
van de Sanden, M.C.M.: PS+EM-MoA10, 16; PS+EM-MoA8, 16
van den Bruele, F.: TF+EM+MI+MS-TuM3, **23**
van der Zande, A.M.: 2D+EM+NS+PS+SP+SS+TF-MoM5, **2**
Vanfleet, R.: TF+AS+EM+EN+MN-WeA12, 45
Varaksa, N.: TF+EM+MI+MS-TuM5, 24
Vargas, M.: EN+AS+EM+NS+SE+SS+TF-MoA8, **14**
Ventrice, Jr., C.A.: 2D+EM+NS+PS+SP+SS+TF-MoM2, 1
Veres, J.: AM+EM+MS+TF-ThA3, 61
Verma, A.: EM-WeM12, **36**
Vernisse, L.: 2D+EM+MG+NS+SE+SM+SS+TF-ThM2, **46**
Veyan, J.-F.: SD+AS+EM-ThM10, 55
Vishwanath, S.: 2D+EM+IS+MC+NS+SP+SS-WeA7, 38; 2D+EM+MG+NS+SS+TF-ThA1, 60; 2D+EM+NS+PS+SP+SS+TF-MoM9, 2
Vitiello, J.: EM-WeA10, 43
Voiry, D.: 2D+EM+MC+MI+NS+SP+SS+TF-TuA11, 26
Völkel, A.R.: AM+EM+MS+TF-ThA3, 61
Volksen, W.: EM-ThM4, 52
von Son, G.: 2D+EM+MC+MS+NS-MoA10, 9; 2D+EM+MG+NS+SE+SM+SS+TF-ThM1, 46
Vora, A.: PS+EM-MoA4, 15
Vos, M.F.J.: TF+EM+NS+PS+SM-ThM6, **58**
Vukajlovic, J.: EN+AS+EM+SE+SS-TuM2, 22
Vurgaftman, I.: EM+MS-ThM12, 51
Vyas, A.: EM-WeA2, 42

— W —

Wabiszewski, G.: EM-WeM13, 36
Wajda, C.: SD+AS+EM+PS-ThA11, 68
Wakrim, T.: EM-WeM2, 35
Wallace, R.M.: 2D+EM+IS+MC+NS+SP+SS-WeA8, 38; 2D+EM+MG+NS+SE+SM+SS+TF-ThM6, 46; 2D+EM+MG+NS+SS+TF-ThA7, 60; EM+MS-ThA10, 66
Walls, J.M.: EN+AS+EM+NS+SE+SS+TF-MoM10, 8; EN+AS+EM+NS+SE+SS+TF-MoM11, **8**
Walrath, J.C.: EM-TuP26, **33**
Walter, J.: EN+AS+EM+NS+SE+SS+TF-MoA9, 14
Walter, T.N.: EM-TuM3, 20
Walton, S.G.: 2D+EM+IS+NS+PS+SP+SS-FrM1, 71
Wambold, R.A.: EM-TuP6, **30**
Wan, J.: 2D+EM+IS+MC+NS+SP+SS-WeA11, **39**
Wang, C.P.: EN+EM+NS+SE+SS+TF-TuA9, 28
Wang, F.: 2D+EM+MC+MI+NS+SP+SS+TF-TuA9, **26**
Wang, H.: EM-WeM11, 36
Wang, J.: EL+EM+EN-ThM3, 48
Wang, K.: TF+EM+NS+PS+SM-ThM5, 58
Wang, Y.: EM+AS+EN+NS-FrM7, 73
Wang, Z.P.: EL+EM+EN-ThM4, 48
Ward, T.Z.: EM-TuP1, 30
Wathuthanthri, I.: EM+MS-ThM10, 51
Wattendorf, M.D.: EN+EM+NS+SE+SS+TF-TuA7, 28
Webb, S.: EM+NS+PS-MoA8, 12
Weeks, S.L.: PS+EM-MoA8, 16
Weerakkody, A.D.: EM+AS+SS-MoA1, 10
Weisel, G.J.: EM-TuP6, 30
Wells, S.: 2D+EM+MC+MS+NS-MoA9, 9
Wheeler, V.D.: 2D+EM+NS+PS+SP+SS+TF-MoM1, 1
Whitener, K.E.: 2D+EM+IS+NS+PS+SP+SS-FrM1, 71; 2D+EM+MC+MI+NS+SP+SS+TF-TuA3, 26
Whiting, G.L.: AM+EM+MS+TF-ThA3, 61
Whitwick, M.B.: 2D+EM+MG+NS+SE+SM+SS+TF-ThM11, 47
Wicker, R.B.: AM+EM+MS+TF-WeM12, **34**
Widdra, W.: 2D+EM+MG+NS+SE+SM+SS+TF-ThM12, 47
Wie, J.U.: EM-TuP5, 30
Wiggins, B.: SS+AS+EM+EN-ThA8, **69**
Williams, B.L.: TF+EM+NS+PS+SM-ThM13, 59
Willis, B.G.: EM+AS+SS-MoA10, 11; EM-TuP6, 30

Willman, J.T.: 2D+EM+IS+MC+NS+SP+SS-WeA1, **38**
Willson, G.: PS+EM-MoA4, 15
Wilt, D.M.: SE+EM+EN-MoA4, 17
Winter, C.H.: SD+AS+EM-ThM5, **54**
Winter, R.: EM+NS+PS-MoM3, 5
Wixforth, A.: 2D+EM+MC+MS+NS-MoA10, 9
Wolden, C.A.: EN+AS+EM+NS+SE+SS+TF-MoM10, 8
Wolf, S.: EM+NS+PS-MoA7, **12**; EM+NS+PS-MoM4, 5
Womack, G.: EN+AS+EM+NS+SE+SS+TF-MoM11, 8
Wong, A.: EM-TuP1, 30
Wong, K.: TF+EM+NS+PS+SM-ThM5, 58
Wood, J.D.: 2D+EM+MC+MS+NS-MoA9, **9**
Wrench, J.S.: EM+AS+SS-MoA1, 10
Wrobel, J.W.: SE+EM+EN-MoA1, 17
Wu, S.: 2D+EM+NS+PS+SP+SS+TF-MoM9, 2
Wurstbauer, U.: 2D+EM+NS+SS+TF-TuM11, 20

— X —

Xenogiannopoulou, E.: 2D+EM+MG+NS+SE+SM+SS+TF-ThM5, 46
Xiao, J.: EN+EM+NS+SE+SS+TF-TuA4, 27
Xiao, Z.: EM-TuP18, **32**; EM-TuP9, 31
Xing, G.H.: EM-TuM1, **20**
Xing, H.: 2D+EM+IS+MC+NS+SP+SS-WeA7, 38; 2D+EM+MG+NS+SS+TF-ThA1, 60; 2D+EM+NS+PS+SP+SS+TF-MoM9, 2
Xu, J.: EM+AS+SS-MoM9, 4
Xu, X.D.: 2D+EM+NS+PS+SP+SS+TF-MoM9, 2
Xue, P.: EM-ThM13, **53**; EM-WeA12, 43

— Y —

Yamamoto, T.: EM-TuP10, 31
Yang, C.: EM-WeA2, 42
Yang, J.C.: SS+AS+EM+EN-ThA3, **69**
Yao, Y.: EM+AS+MS+SS-WeA4, 40
Yarmoff, J.A.: SS+AS+EM+EN-ThA7, 69
Yarrington, C.D.: TF+AS+EM+EN+MN-WeA3, 44
Yatzor, B.: EM-WeA1, 42
Yazyev, O.V.: 2D+EM+IS+MC+NS+SP+SS-WeA3, **38**
Ye, P.D.: 2D+EM+MC+MS+NS-MoA7, **9**; 2D+EM+MG+NS+SS+TF-ThA7, 60
Ye, Y.F.: EN+AS+EM+SE+SS-TuM13, **23**
Yeh, P.: 2D+EM+MG+NS+SS+TF-ThA2, 60
Yeom, G.Y.: PS+EM-MoA3, 15
Yin, X.: 2D+EM+NS+SS+TF-TuM12, **20**
Yoo, C.: SD+AS+EM-ThM12, 55
Yoo, H.: EM-WeA7, 43
Yoon, J.: SD+AS+EM-ThM12, 55
Yoshida, N.: EM+NS+PS-MoA1, 11; EM+NS+PS-MoA9, 13; EM+NS+PS-MoM4, 5
You, L.: EL+EM+EN-ThM3, 48
Young, A.F.: 2D+EM+MC+MI+NS+SP+SS+TF-TuA1, **26**
Young, J.: EN+AS+EM+SE+SS-TuM12, **23**
Yu, K.-H.: SD+AS+EM+PS-ThA11, 68
Yu, Y.: EN+EM+NS+SE+SS+TF-TuA10, **28**
Yuan, S.: EM+AS+SS-MoM1, 3
Yulaev, A.: 2D+EM+NS+PS+SP+SS+TF-MoM8, **2**
Yun, D.H.: PS+EM-MoA3, **15**

— Z —

Zaki, N.: 2D+EM+MG+NS+SS+TF-ThA2, **60**
Zeng, Y.: EM-TuM3, 20
Zhang, C.W.: EL+EM+EN-ThM5, 48
Zhang, D.: EM+NS+PS-MoA10, 13
Zhang, G.: EM-WeA1, 42
Zhang, L.: EM+NS+PS-MoA2, **12**
Zhang, W.: SD+AS+EM-ThM1, 54
Zhang, X.: EN+AS+EM+NS+SE+SS+TF-MoA9, 14
Zhang, X.R.: 2D+EM+IS+NS+PS+SP+SS-FrM7, **71**
Zhang, Z.: SD+AS+EM-ThM11, 55
Zhang, Z.M.: EL+EM+EN-ThM4, 48
Zhao, L.: EM-WeM6, 36
Zheng, H.: EM-ThM13, 53; EM-TuP21, 32; EM-TuP22, **33**
Zhernokletov, D.: EM+AS+MS+SS-WeA11, 41
Zhou, W.: SS+AS+EM+EN-ThA7, **69**
Zhou, Y.: 2D+EM+IS+NS+PS+SP+SS-FrM2, **71**; 2D+EM+MG+NS+SS+TF-ThA9, **61**
Zhu, H.: 2D+EM+IS+MC+NS+SP+SS-WeA8, 38; 2D+EM+MG+NS+SE+SM+SS+TF-ThM6, 46; 2D+EM+MG+NS+SS+TF-ThA7, **60**
Zhu, J.F.: EN+AS+EM+NS+SE+SS+TF-MoA7, 14; EN+AS+EM+SE+SS-TuM13, 23
Zhu, Q.: SS+AS+EM+EN-ThA3, 69
Zhu, Y.: EM+AS+SS-MoA5, 11
Zimmerman, D.T.: EM-TuP6, 30
Zollner, S.: EM+NS+PS-MoA10, 13
Zuilhof, H.: SD+AS+EM-ThM10, 55